The Dissertation Committee for Christopher Luk Hoy Certifies that this is the approved version of the following dissertation:

Development of Femtosecond Laser Endoscopic Microsurgery

Committee:

Adela Ben-Yakar, Supervisor

Matthew J. Hall

Paul S. Ho

Konstantin V. Sokolov

James W. Tunnell

Development of Femtosecond Laser Endoscopic Microsurgery

by

Christopher Luk Hoy, B.S.M.E.; M.S.E.

Dissertation

Presented to the Faculty of the Graduate School of
The University of Texas at Austin
in Partial Fulfillment
of the Requirements
for the Degree of

Doctor of Philosophy

The University of Texas at Austin
May 2011

Dedication

This dissertation is dedicated to Katherine Aisling O'Suilleabhain – for her inexhaustible patience, love, and understanding, even if I didn't always understand it myself.

It is also dedicated to my family – for the tools I needed to get this far and the sense of humor required to enjoy it.

Acknowledgements

I would like to thank the many people who helped me in completing this work. Particularly, I would like to thank Dr. Adela Ben-Yakar for introducing me to the field of biomedical optics and for providing support and guidance throughout the course of my research. Additionally, I would like to thank my lab-mates for providing both insight and levity whenever it was needed. The friendships made in this lab and throughout the graduate program will remain invaluable to me.

I also would like to acknowledge our collaborators, in particular: Drs. Olav Solgaard, Wibool Piyawattanametha, and Hyejun Ra at Stanford University for providing the micro scanning mirrors; Dr. James Kobler at Massachusetts General Hospital for providing original ideas and critical guidance throughout my laryngeal microsurgery research; and Dr. Kazunori Hoshino at the University of Texas at Austin for assistance in wire bonding the micro scanning mirrors used in both probes.

Development of Femtosecond Laser Endoscopic Microsurgery

Publication No._____

Christopher Luk Hoy, PhD
The University of Texas at Austin, 2011

Supervisor: Adela Ben-Yakar

Femtosecond laser microsurgery has emerged as a remarkable technique for precise ablation of biological systems with minimal damage to their surrounding tissues. The combination of this technique with nonlinear optical imaging provides a means of microscopic visualization to guide such surgery *in situ*. A clinical endoscope capable of image-guided femtosecond laser microsurgery will provide physicians a means for cellular-level microsurgery with the highest precision.

This dissertation focuses the development of a miniaturized fiber-coupled probe for image-guided microsurgery, towards future realization as a clinical endoscope. The first part of the dissertation describes the development of an 18-mm diameter probe. This development includes delivery of femtosecond laser pulses with pulse energy in excess of 1 μJ through air-core photonic bandgap fiber, laser beam scanning by a microelectromechanical system scanning mirror, and development of a new image reconstruction methodology for extracting increased temporal information during Lissajous beam scanning. During testing, the 18-mm probe compares favorably with the state-of-the-art as a microscopic imaging tool and we present the first known demonstration of cellular femtosecond laser microsurgery through an optical fiber.

The second part of the dissertation explores further refinement of the design into a streamlined package with 9.6 mm diameter and improved imaging resolution. Study of

the optical performance through analytical and computer-aided optical design indicates that simple custom lenses can be designed that require only commercial-grade manufacturing tolerances while still producing a fully aberration-corrected microsurgical endoscope. With the 9.6-mm probe, we demonstrate nonlinear optical imaging, including tissue imaging of intrinsic signals from collagen, using average laser powers 2-3× lower than the current state-of-the-art. We also demonstrate the use of the 9.6-mm probe in conjunction with gold nanoparticles for enhanced imaging and microsurgery through plasmonics.

Finally, in the third part of this dissertation, we detail bench-top development of a new clinical application for combined femtosecond laser microsurgery and nonlinear optical imaging: the treatment of scarred vocal folds. We show the utility of femtosecond laser microsurgery for creating sub-epithelial voids in vocal fold tissue that can be useful for enhancing localization of injectable biomaterial treatments. We demonstrate that a single compact fiber laser system can be utilized for both microsurgery and imaging. Furthermore, the proposed clinical technique is shown to be achievable with parameters (e.g., pulse energy, focused spot size) that were found to be attainable with fiber-coupled probes while still achieving ablation speeds practical for clinical use.

Table of Contents

List of Tables

List of Figures

Chapter 1: Introduction

Almost since their inception, lasers have been put to use as versatile biological cutting tools. The invention of the laser in 1960 excited biologists and clinicians alike with the prospect of a surgical tool capable of creating targeted damage with diffraction-limited precision [1,2]. Quickly thereafter, a variety of laser surgery applications were developed, ranging in scale from sub-cellular dissection of organelles [3-5] and chromosomes [6] to bulk tissue ablation of eyes [7], skin [8], and teeth [9]. Over the next forty years, the surgical applications of lasers grew and matured, leading to an abundance of discoveries in cell biology [10] and clinical applications throughout medicine, where acceptance has been particularly strong in ophthalmology [11], dermatology [12], and otolaryngology [13].

The development of clinical laser techniques has centered on continuous wave (cw) and nanosecond or longer pulsed lasers. These conventional laser surgery techniques rely predominantly on linear absorption of laser light because the laser intensities are generally too low to induce appreciable nonlinear interaction at practical average powers. Owing to the linear absorption mechanism, photodamage from these lasers is highly wavelength-dependent and thermal in nature [14]. This wavelength dependence can be exploited to create a tissue-selective effect. However it can also result in non-deterministic cutting effects when cutting heterogeneous tissue and can limit efficacy in transparent or low-absorbing samples. Similarly, though laser heating has been used to great effect clinically for both cauterization of laser incisions and tissue welding [15], the diffusion of heat away from the laser focal volume can lead to collateral damage outside the focal volume and may lead to scarring in biological tissues. While both wavelength-dependence and heating can be mitigated or exploited, the linear absorption of laser light throughout the laser-tissue interaction volume leads to increased damage outside the focal volume along the laser path. This lack of axial confinement ultimately limits their precision inside thicker specimens. With the development of femtosecond-pulsed laser

sources in the early 1980s, biologists and clinicians were given access to new predominantly non-thermal regimes of photodamage, which have increased surgical precision to the diffraction limit and beyond.

Thus far, the clinical potential of femtosecond laser microsurgery has barely begun to be realized. One of the major technological barriers to the adoption of this technology is the current lack of a means to flexibly deliver the laser light to clinical sites in or on the patient. The goal of this dissertation is to detail my recent efforts towards developing a clinical tool capable of delivering femtosecond laser pulses to medical regions of interest for both microsurgery and microscopic visualization of the microsurgery site.

The following chapters will first review the underlying mechanisms behind both microsurgery and nonlinear microscopy with femtosecond laser pulses, as well as their clinical applications and current state of development. Next, we will explore the unique design considerations and constraints that dictate the options for clinical development before discussing the construction and testing of an initial microsurgery and microscopy probe. With the insight gained from this first device, we will then cover the in-depth design, development, and demonstration of a smaller microsurgery and microscopy probe that improves upon the earlier device. Lastly, the dissertation will summarize recent work in developing a new clinical application for fiber-delivered femtosecond laser surgery: the treatment of scarred vocal folds for voice restoration.

Chapter 2: Background

Before delving into the detailed development of a femtosecond laser microsurgical endoscope, it is helpful to review both the underlying physics and the scope of femtosecond laser applications in surgery. This chapter will begin by discussing the mechanisms through which femtosecond lasers can create microsurgical effects in tissue. This section is followed by a review of the phenomena that can limit the lasers' surgical efficacy and therefore must be avoided or mitigated. Next, I provide a discussion of the current scope of clinical and pre-clinical applications of femtosecond laser surgery to establish the motivation for creating a clinical femtosecond laser surgical endoscope. Lastly, this chapter will cover nonlinear optical imaging, which can provide a means of visualization for surgical guidance that also utilizes femtosecond laser pulses. In addition to the mechanisms behind the nonlinear optical imaging techniques, this section will cover recent efforts to develop nonlinear optical endoscopes for diagnostic imaging. This discussion introduces many of the design considerations that will also impact the development of a femtosecond laser surgical endoscope.

2.1: MECHANISMS OF FEMTOSECOND LASER SURGERY

Surgery with focused femtosecond lasers is triggered by the generation of an initial population of free electrons through a combination of multiphoton ionization and band-gap (Zener) tunneling [16,17]. These ionization pathways are nonlinearly dependent on the local light intensity and thus the region of free electron generation is highly-localized in three dimensions within the focal volume. The free electrons may then act as seed electrons for avalanche ionization, shown in Figure 2.1, wherein an initial free electron is accelerated by the incident laser field and collides with a bound valence electron, thus ionizing the bound electron through impact ionization. This doubling process can then repeat, causing a cascade, until termination of the laser pulse or total

ionization of the valence electron population. The final density of this exponentially growing number of free electrons determines the precise mechanism of damage, which can be dominated by photochemical effects, thermoelastic bubble nucleation, or optical breakdown. Each of the three mechanisms are summarized in Table 2.1 and will be discussed briefly below, while the interested reader can find further details in the work of Vogel *et al*. [17] and Joglekar *et al*. [16].

Table 2.1. Review of femtosecond laser microsurgery mechanisms.

Damage mechanism	**Photochemical Damage**	**Thermoelastic Stress Confinement**	**Optical Breakdown**
Intensity threshold	0.26×10^{12} W/cm^2	5.1×10^{12} W/cm^2	6.54×10^{12} W/cm^2
Electron density at threshold	2.1×10^{13} cm^{-3} One free electron in the focal volume	0.24×10^{21} cm^{-3} Induced thermal stress overcomes the tensile strength of water	1.0×10^{21} cm^{-3} Critical electron density for optical breakdown
Description	Free electrons participate in chemical reactions to form destructive reactive oxygen species and lead to breaking of chemical bonds.	Thermalization of the plasma occurs faster than the acoustic relaxation time. Confinement of thermal stresses leads to formation of nano-scale transient bubbles.	Damage is created by high pressure and high temperature plasma and by the accompanying shock wave and cavitation bubble.
Pulse repetition rate	> 1 MHz A large number of pulses is required. For practical reasons high repetition rate lasers are preferable.	< 1MHz Bubble lifetime is 100-500ns. We need avoid heat accumulation and long lasting bubble formation.	

Adapted from Ben-Yakar and Bourgeois [18].

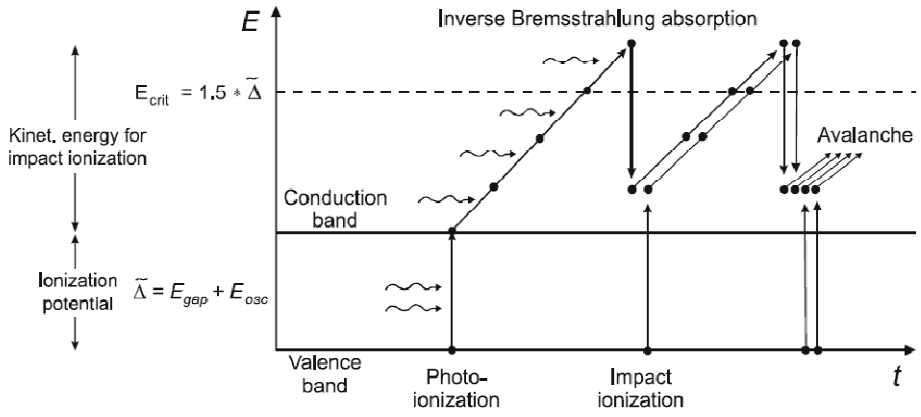

Figure 2.1. Illustration of nonlinear ionization pathways in dielectric materials with ultrafast laser pulses. Valence electrons can be ionized directly through either multiphoton ionization or bandgap tunneling (not shown). Further free electrons are generated through repeated cycles of impact ionization. This avalanche ionization leads to the exponential growth of free electrons. Figure adapted from [17].

Photochemical damage can occur at relatively low irradiances. Vogel *et al.* theoretically modeled that photochemical effects may begin at peak laser irradiances as low as 0.26 TW/cm^2 [17], which corresponds to one free electron generated in the focal volume of a 1.3 NA objective lens per pulse(1). In the photochemical damage pathway, energetic free electrons may either (1) cause damage through disassociation of water molecules, leading to the creation of reactive oxygen species (ROS) that can destroy cellular components [19], or (2) participate directly in the bond breaking of other cellular

(1) Unless otherwise specified, the threshold irradiances provided here assume 100 fs pulses with 800 nm center wavelength focused into water by a 1.3 NA lens, in accordance with the model used in Vogel *et al* [17]. Peak irradiance damage thresholds in the femtosecond regime have been shown to be only weakly dependent on these parameters, however.

components [20]. It is also possible that non-ionizing multiphoton absorption may aid photochemical damage in structures such as DNA, where the simultaneous absorption of three near-infrared (NIR) photons may be sufficient to cause direct bond breaking due to the widely observed single-photon absorption peak for 260 nm [21]. Because creation of appreciable photochemical damage requires a large number of relatively low energy pulses, high-repetition rate (~100 MHz) femtosecond oscillators are required to create useful damage in a reasonable amount of time.

Thermoelastic damage can occur at peak laser irradiances exceeding approximately 5.1 TW/cm^2. In this regime, thermalization of the free electrons leads to rapid, confined heating inside the focal volume. The subsequent thermoelastic stresses generated therein lead to the formation of transient nanoscale bubbles [17]. Bubble lifetimes near the nucleation threshold are on the order of tens to hundreds of nanoseconds. Because the thermalization of the electrons occurs over four orders of magnitude faster than the characteristic thermal diffusion time, temperature effects are well confined and it is the nucleation and expansion of the nanoscale bubble that is responsible for damage in this regime. For femtosecond laser surgery in this regime, amplified laser systems at lower repetition rates are used, both due to the higher pulse energies required and the need to prevent accumulative pulse effects from increasing the extent of damage.

Lastly, damage due to optical breakdown can occur when laser irradiances above 6.5 TW/cm^2 are delivered and the critical free electron density of ~10^{21} cm^{-3} can be met and exceeded. At this point, the plasma at the focal volume becomes highly absorbing and the remaining pulse energy acts primarily to increase the plasma energy density. In this ablation regime, the rapid ionization of the focal volume is accompanied by formation of a cavitation bubble and emission of a shock wave, which may induce mechanical damage to the target that extends beyond the focal volume. While optical breakdown can also be induced using up to nanosecond pulse durations, seed electrons for avalanche ionization generally must be provided by linear heating and thermionic

emission. Because femtosecond laser pulses can produce their own seed electrons through multiphoton ionization, ablation with femtosecond laser pulses can be conducted in the bulk of transparent and minimally-absorbing materials, such as the transparent tissues of the eye.

Each of the aforementioned damage mechanism relies on the same rapid generation of free electrons via the nonlinear optical interaction with matter described earlier. As a result of the nonlinear mechanism, femtosecond laser damage has been generally shown to exhibit only a weak dependence on wavelength. Specifically, Stuart *et al*. found the threshold for fused silica to be approximately 2 J/cm^2 (~5 TW/cm^2) for a 1053 nm 400 fs pulse and approximately 1 J/cm^2 (~3.3 TW/cm^2) for a 526 nm 300 fs pulse [22]. Similarly, Schaffer *et al*. found only a 10% discrepancy between the ablation thresholds of both fused silica and calcium fluoride when studying 110 fs laser pulses at both 800 nm and 400 nm wavelength [23]. In biological tissue, Olivé *et al*. found the damage threshold of porcine cornea to lie between 1.5 and 2.2 J/cm^2 (~15 and 22 TW/cm^2) for 100fs pulses with wavelengths between 800 nm and 1450 nm, excepting at 1150 nm and 1200 nm, which the authors attribute to instability in their laser system at these wavelengths [24]. This relatively weak wavelength dependence of the ablation threshold not only results in increased consistency when cutting heterogeneous tissues but also allows for tuning of the laser wavelength into the near infrared (NIR). This NIR wavelength range is often referred to as the “therapeutic window” because the low absorption of blood and water at these wavelengths allow for deeper penetration than for ultraviolet or visible light.

Nanosecond-pulsed lasers can also be wavelength tuned to limit their linear absorption and, with sufficiently tight focusing and large enough pulse energies, can achieve optical breakdown through nonlinear absorption. However, due to the relatively low peak intensities of nanosecond pulses compared with femtosecond pulses, nonlinear ablation in the nanosecond regime requires several orders of magnitude more energy [17]. This excess energy is imparted to the tissue as heat and via mechanical stress waves,

both of which contribute significant collateral tissue damage outside of the focal volume [14].

2.2: FUNDAMENTAL LIMITATIONS TO PENETRATION DEPTH AND PRECISION

The high peak intensities of ultrashort laser pulses enable the nonlinear interaction with tissue that permits confined ablation inside bulk tissue. However these high peak intensities also introduce unwanted nonlinear effects that can limit the maximum penetration depth and precision of ablation. The two critical nonlinear phenomena that introduce limitations or constraints are self-focusing and self-phase modulation in the presence of group velocity dispersion. These phenomena will be explained in this section, with a focus on how they pertain to an endoscopic system and suggestions on how to avoid or mitigate these effects through careful selection of laser parameters and focusing conditions.

2.2.1: Self-focusing

When using femtosecond laser pulses for microsurgery within bulk tissue, the primary limitation to the maximum ablation depth and precision is ultimately the phenomenon of self-focusing. Self-focusing with femtosecond laser pulses occurs when the intense laser pulses create a spatial variation in the refractive index profile via the nonlinear index of refraction, n_2, and the Kerr effect [25,26]. The Kerr effect arises from the third order nonlinear susceptibility and is thus present to some degree in all materials. As a result, the index of refraction in a Kerr medium is given by

$$n = n_0 + n_2 I(r,t), \tag{2.1}$$

where n is the total index of refraction, n_0 is the linear index of refraction, and $I(r,t)$ is the irradiance as a function of beam radius, r, and time, t. Representative values for n_2 are approximately 5.4×10^{-16} cm^2/W for water at 804 nm [27] and 2.0×10^{-15} m^2/W for porcine cornea at 1030 nm [28]. Thus for irradiances delivered during femtosecond laser ablation, the nonlinear component of the refractive index becomes significant and spatially

varying, creating the effect of a positive lens. See Figure 2.2 for illustration. For a collimated laser beam propagating in a dielectric Kerr medium, the self-focusing effect competes with diffraction, with the two phenomena balancing each other when peak power of the pulse is approximately [29]

$$P_{cr} = \frac{0.471\lambda^2}{\pi n_0 n_2}, \tag{2.2}$$

where P_{cr} is the critical power for self-focusing and λ is wavelength. Beyond this critical power, self-focusing dominates and the pulse begins to collapse and focuses before the geometric focus.

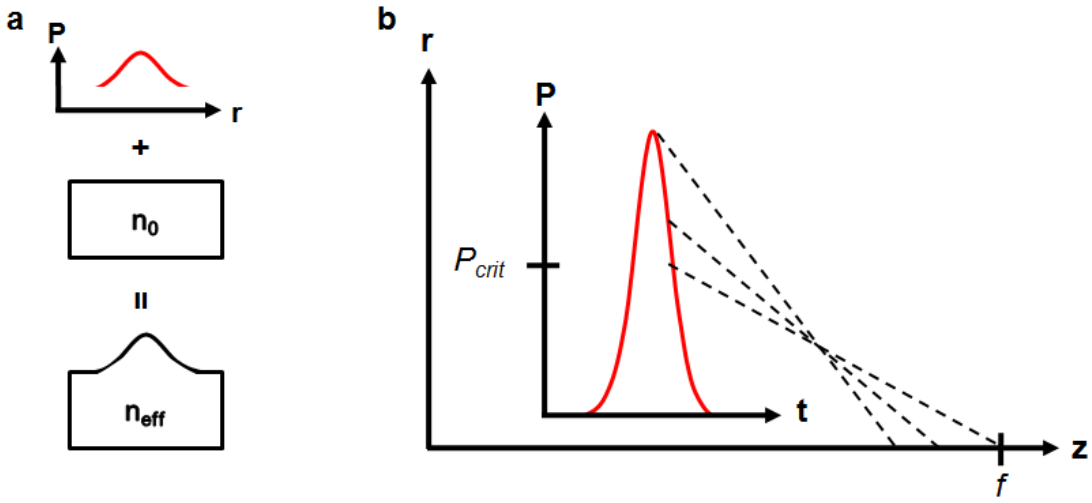

Figure 2.2. Illustration of self-focusing of ultrashort laser pulses. a The spatial variation of intensity within a laser pulse leads to a modification of the effective refractive index. This transient modification creates an effective positive lens. **b** During the temporal evolution of the pulse, the varying peak power leads to a varying focal length, thus creating an elongated focus or filament.

For focused pulses the critical power is approximately the same, where the distance to beam collapse is simply shifted by the lens transformation. Due to the

temporal evolution of the pulse, self-focusing laser pulses exhibit a “moving focus” [29], wherein the low intensity front and tail of the pulse will focus toward the geometric focus whilst the high-intensity peak of the pulse will focus earlier. In practical cases, such catastrophic self-focusing is often arrested by a combination of factors, such as plasma defocusing from generated free electrons, self-phase modulation and subsequent dispersion reducing pulse intensity, and reduction of pulse energy due to scattering and absorption in turbid media [30]. Nevertheless, self-focusing effects can lead to material modification both leading up to and behind the geometric focus when intense pulses are focused inside bulk material [31-34].

When focusing inside scattering tissue, increasing laser energy is required to reach the damage threshold at the focus as the focus is moved deeper into the tissue, due to attenuation following the Beer-Lambert law. Thus as depth is increased, the peak power of the incoming laser pulses are exponentially increased until $P >> P_{cr}$ and catastrophic self-focusing shifts the focus significantly shallower than the targeted depth. Fortunately, several approaches can be taken to limit the effects of self-focusing in surgical applications.

First, because self-focusing depends only on the peak power of the pulse, utilization of a smaller diameter focal spot can help avoid self-focusing while still achieving optical breakdown. For Corning 0211 glass, which has a critical power at 800 nm of approximately 1.5 MW, Schaffer *et al*. found self-focusing effects to be negligible when focusing with numerical apertures (NA) above 0.9 [35]. The critical power in this study was very similar to the critical power of 1.2 MW found by Miclea *et al*. for porcine cornea at 1030 nm [28]. It should be noted, however, that while higher NA can help to avoid the onset of self-focusing, it can also lead to increased spherical aberrations when focusing deep into tissue without use of immersion fluid to match the index of refraction of the tissue [36]. Spherical aberration enlarges the focal volume, particularly in the axial direction, degrading the confinement of ablation.

Second, for pulse durations below approximately 10 ps, optical breakdown occurs without significant free electron recombination during the pulse and the threshold fluence becomes only weakly dependent on pulse duration [17,22]. In practice, this weak dependence implies that increasingly shorter pulse durations will serve to increase self-focusing, without a commensurate decrease in ablation threshold. For example, a 100 fs pulse[(2)] with a $sech^2$ temporal profile, a critical power of 1.2 MW is achieved with only 140 nJ pulse energy, while a 1 ps pulse can contain 1.4 µJ of energy before reach the same peak power. Thus pulse durations on the order of hundreds of femtoseconds to 1 picosecond may be useful to avoid self-focusing effects while preserving damage confinement.

Lastly, pulse-to-pulse incubation effects can provide a reduced damage threshold when multiple pulses are delivered during ablation at repetition rates in the kHz regime and above. Subsequently, a series of pulses can used to create optical breakdown in bulk tissue while keeping the individual pulse peak power well below the critical power for self-focusing.

To summarize, to maximize the practical ablation depth with ultrashort pulsed lasers, it is beneficial to (1) maximize the focusing numerical aperture while (2) utilizing pulse durations in the hundreds of femtoseconds or low single picoseconds, and (3) using repetition rates in the hundreds of kilohertz where pulse-to-pulse accumulation effects can be utilized without introducing heating or significantly increasing procedure time.

2.2.2: Group velocity dispersion and self-phase modulation

The key to inducing the desired nonlinear absorption for ablation lies in generating very large peak laser intensities, usually through the temporal confinement of light into ultrashort laser pulses. Naturally, the efficiencies of nonlinear interactions suffer as pulse durations become longer. Processes that stretch the laser pulse duration,

---

[(2)] Note that all pulse durations in this document are measured at the full width at half maximum (FWHM).

referred to broadly as dispersion, are common during the propagation of ultrashort laser light through optical systems and can decrease the efficiency and precision of femtosecond laser microsurgery.

The most significant sources of dispersion in an ultrafast optical system are usually forms of group velocity dispersion (GVD). GVD occurs when the velocity of light exhibits a dependence on the wavelength of the light, causing the different spectral components in a single laser pulse to travel at different speeds. Shorter laser pulses necessarily contain greater spectral bandwidth so that, when all spectral components are in phase, interference among the spectral components leads to a short pulse in the time domain. This relationship between minimum pulse duration and minimum spectral bandwidth is dictated by Fourier transform theory, where the limiting condition is referred to as the transform limit and given by

$$(\Delta\tau)(\Delta\nu) = C_B, \tag{2.3}$$

where $\Delta\tau$ is the FWHM of the pulse duration, $\Delta\nu$ is the FWHM of the spectral frequency bandwidth, and C_B is the transform limited time-bandwidth product, which depends on the temporal pulse shape. For the sech^2 envelope common to passively mode-locked laser sources, C_B = 0.315; for Gaussian envelopes common to actively mode-locked sources, C_B = 0.441. Thus a 100 fs sech^2 pulse at a center wavelength of 800 nm will have a minimum of 9.4 nm FWHM bandwidth.

The relatively large spectral bandwidth of ultrashort pulses makes them susceptible to GVD, which arises primarily from either material dispersion or waveguide dispersion. In material dispersion, the dependence of an optical material's refractive index on the wavelength of light results in the various wavelengths inside the spectral bandwidth traveling at different speeds, and thus elongating the pulse temporally. Waveguide dispersion occurs when light propagates through a waveguide with a diameter size approaching the wavelength of the light. Under these conditions, the confinement conditions of each spectral component, including their propagation constants, *k*, vary.

Because $k = 2\pi/\lambda$, this variation in propagation speed with k leads to GVD. Material dispersion in most optical materials leads to longer wavelength components traveling faster than shorter wavelengths in what is termed "normal" or "positive" dispersion. Waveguide dispersion, in contrast, often shifts shorter wavelengths ahead of longer wavelengths through "anomalous" or "negative" dispersion. A positively or negatively dispersed pulse is said to be "chirped".

Importantly, the dominant effects of both material and waveguide dispersion in the majority of femtosecond laser systems produce a linear phase shift across the spectrum of the pulse, and higher-order phase shifts are usually small. Thus positive and negative dispersion of equal magnitude (but opposite sign) can be combined to recover a transform limited pulse duration at the point of interest, in the absence of any higher order dispersion effects. One can commonly compensate for dispersion through the use of either prism pair or grating pair pulse chirping systems, for example.

Through the optical Kerr effect, described earlier, the speed of light can also depend on the instantaneous pulse intensity for high peak power laser pulses. In this case, the change in the local speed of light during the propagation of the pulse can create a phase shift across the pulse. Because optical phase is defined as $\Phi \equiv \omega t - kz$ and $k \equiv n\omega/c$,

$$\omega(t) = \frac{\partial \Phi}{\partial t} \approx \omega_0 - \frac{\omega_0 n_2}{c} \frac{\partial I}{\partial t} z . \tag{2.4}$$

Heuristically, this means that a rapid change in phase results in a shift to higher and lower frequencies. When the temporal envelope of the pulse is a peak function, like the common sech^2 or Gaussian functions, the second term in the right-hand side of Eq. (2.4) leads to a shift to longer wavelengths at the leading edge of the pulse and a shift to shorter wavelengths at the trailing edge of the pulse. This phenomenon is referred to as self-phase modulation (SPM). Because new spectral bandwidth is being created during SPM, the onset of SPM alongside GVD can result in accelerated pulse broadening in media with normal dispersion until the peak power is no longer sufficient for SPM. In this manner, SPM can lead to nonlinear dispersion properties, particularly in conventional

optical fiber where GVD is nearly always present and high peak powers arise due to spatial confinement. This nonlinearity of the dispersion makes pre-compensation with a pulse chirping system extremely difficult and thus SPM must be avoided in delivering high peak power ultrashort laser pulses through normally dispersive media for microsurgery.

Because SPM depends on peak pulse intensity, similar to self-focusing, the means for avoiding self-focusing can also be applied to avoid the effects of SPM as well. Self-phase modulation is primarily a concern during beam propagation, however, since it is the action of GVD during the propagation of a high-bandwidth pulse that reduces pulse intensity. As a result, SPM is most commonly managed by avoiding propagation of intense optical pulses in materials with appreciable n_2 whenever possible. Alternatively, if a pulse will be propagated through a material with a large GVD of known sign (i.e. either positive or negative dispersion), then the pulse can be pre-dispersed in the opposite manner such that the peak intensity of the pulse is small during propagation to the sample, but restored to its original level near the sample. This technique of pulse duration management, often termed “pre-chirping”, is covered in more detail in Chapter 4.

2.3: APPLICATIONS OF FEMTOSECOND LASER SURGERY

In comparison with nanosecond-pulsed and cw laser ablation of biological tissues, numerous early studies of femtosecond laser ablation have found improvements in the ablated surface quality and decreased regions of collateral damage [37-40]. These qualities, coupled with the ability to create confined damage within bulk tissue, have spurred interest in the use of femtosecond lasers as clinical tools for surgery in a variety of applications and tissue types. In this section, we will highlight several major areas of clinical and pre-clinical development to establish the motivation for developing a flexible femtosecond laser microsurgery tool.

2.3.1: Ophthalmology

By far, the most significant clinical development and acceptance of femtosecond laser surgery has occurred in the field of ophthalmology, specifically in the application of "blade-free" femtosecond laser-assisted in situ keratomileusis (fs-LASIK). In conventional LASIK surgery, a microkeratome is used to cut a thin flap of a thickness of several hundred microns or less on the cornea. This flap is then pulled back to expose the underlying stroma, at which point an excimer laser is used to ablate the corneal stroma, reshaping it to correct aberrations and improve visual acuity. In fs-LASIK, the femtosecond laser is used to create the flap instead of a microkeratome, thereby improving uniformity and predictability of flap thickness and reducing the incidence of complications [41,42]. A comparison of a fs-LASIK flap and a traditional LASIK flap is provided in Figures 2.3**a** and 2.3**b**. First clinically demonstrated in 2003 [41] and marketed by IntraLase Corp., the fs-LASIK procedure has gained wide-spread acceptance with femtosecond lasers being used in 30% of all LASIK procedures by 2006 [43]. Recently, several other commercial femtosecond laser systems have been developed for ophthalmology [44] and fs-LASIK remains the most widely-accepted clinical adaptation of femtosecond laser surgery. This successful translation may be because fs-LASIK (1) targets a region of interest that is easily accessible without the need for fiber optic delivery, (2) capitalizes on the femtosecond laser's strength of making precise cuts within transparent bulk tissue, which uniquely enables the femtosecond laser to replace the microkeratome, (3) provides significant enough improvement in outcome to offset the additional cost, and (4) integrates into a pre-existing laser surgery procedure which avoids major changes in the way the surgical tool interfaces with the patient or with the physician, speeding development and acceptance.

In addition to the success of fs-LASIK, and in large part because of this success, a number of other ophthalmological applications for femtosecond lasers are currently being pursued. Among these, the use of femtosecond lasers for keratoplasty (corneal

transplantation) has undergone rapid development and entered clinical practice [45]. In keratoplasty, either a partial thickness (anterior or posterior lamellar keratoplasty) or the entire thickness (penetrating keratoplasty) is removed from the patient's cornea and replaced by tissue from a donor eye. For this procedure, femtosecond lasers have been demonstrated to cut the tissue in both donor and recipient eyes in ex-vivo animal and human studies since 2003 [46], in in-vivo animal studies since 2006 [47], and in-vivo in human patients since 2007 [48]. Compared to a conventional blade, femtosecond lasers offer the advantages of high-reproducibility of cut dimensions and the ability to more easily cut increasingly complex shapes [49,50] for increased donor-to-recipient tissue surface interaction. Examples are shown in Figures 2.3**d** and 2.3**e**. Recent studies indicate that femtosecond laser-assisted keratoplasty can result in improved wound healing time [51] and reduced astigmatism [48]. Interested readers may find more details about the use of femtosecond lasers in specific types of keratoplasty in the review by Soong and Malta [52] and the references therein.

A number of other ophthalmological applications of femtosecond laser surgery are either being developed or are in the early stages of clinical acceptance. These applications include the use of femtosecond lasers to:

- create intracorneal tunnels for the implantation of PMMA ring segments [41,53-56],
- excise segments of corneal tissue for diagnostic corneal biopsy [57,58]
- produce arcuate cuts inside the cornea to correct astigmatism [59]
- cut planes inside the eye to increase deformability for treatment of presbyopia (Figure 2.3**c**) [60-63]
- create pockets for intracorneal implantation of keratoprosthesis [64]
- cut the capsule to provide access to the lens (capsulotomy) and segment the lens during cataract treatment [65].

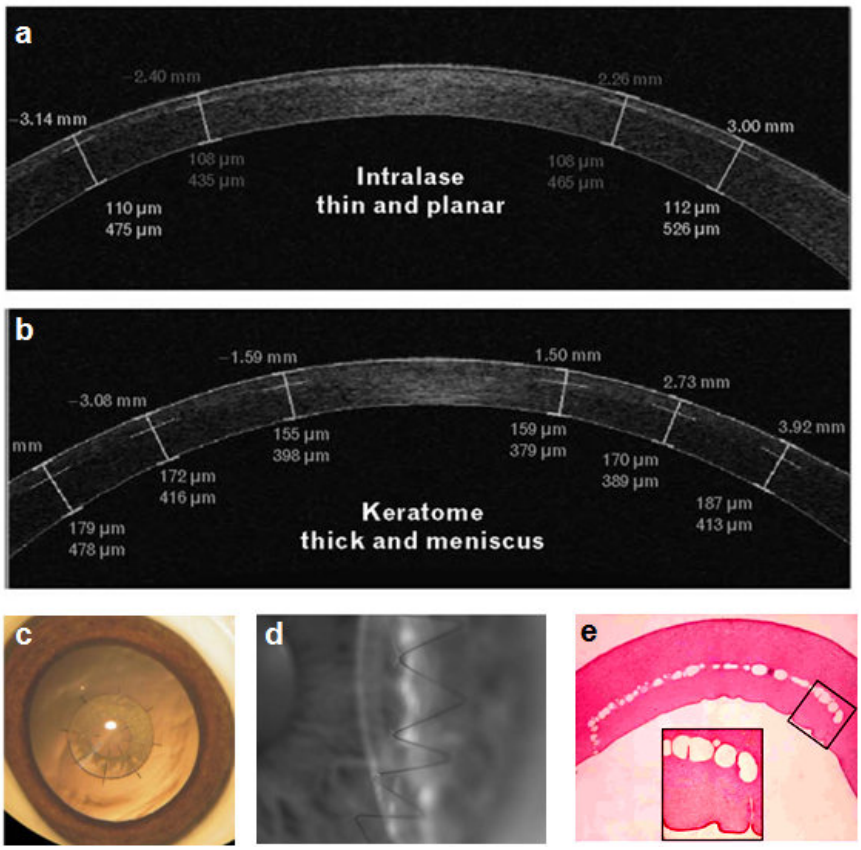

Figure 2.3. Representative images of ophthalmic femtosecond laser microsurgery applications. Optical coherence tomography images of LASIK flaps created with, **a**, the IntraLase femtosecond laser and, **b**, a conventional keratome [42]. The flap is the superficial layer on the cross-section shown. Note that the IntraLase flap is thinner with better uniformity of thickness. **c** Light microscopy image of the spoked-wheel pattern cut in the bulk of the lens to produce "gliding planes" in the proposed presbyopia treatment [61]. **d** Light microscopy image of a donor cornea seated in the eye with a "zig-zag" interface created by a femtosecond laser [50]. **e** Histological section of a posterior lamellar graft cut in a porcine cornea [46]. Note that in the applications shown in **c**-**e**, the femtosecond laser has enabled complex and/or sub-surface ablations not practical with conventional methods.

In these applications, with the exceptions of the proposed presbyopia treatment and cataract lens segmentation, the femtosecond laser is being used to replace mechanical

cutting tools, thereby increasing precision and repeatability while reducing the frequency of complications.

2.3.2: Soft tissue ablation outside of ophthalmology

In addition to ophthalmological applications, femtosecond laser microsurgery techniques have been investigated in other soft tissues. In skin, early bench-top studies have indicated that femtosecond lasers can ablate dermal tissue without any observable collateral damage to surrounding tissue [66,67]. Frederickson *et al*. investigated surface ablation of excised rat dermis and found that thermal damage effects were avoided when using fewer pulses delivered to the focal spot and energies close to the ablation threshold [66]. Conversely, delivery of 35 pulses at 10 Hz repetition rate and pulse energy over ten times the threshold energy led to thermal damage extending 30 µm in this case [66]. The authors propose that this small amount of thermal damage could be intentionally induced to provide hemostasis for in vivo ablation of the dermis, though superficial ablation with thermal collateral damage of this scale is also achievable with less expensive conventional laser sources.

Though dermal tissues are highly scattering compared to the tissues of the eye, several studies have also demonstrated confined sub-surface femtosecond laser ablation in the epithelium and dermis without causing damage to the superficial cellular structure [34,67,68]. Specifically, Tse *et al*. succeeding in ablating porcine skin up to 1 mm below the tissue surface as verified by acoustic wavefield measurements [34]. The conditions used in this study resulted in significant self-focusing effects, however, greatly degrading the axial confinement of the laser damage as evidenced by bubble formation detected above and below the focal plane. Further study is warranted to explore the optimum conditions for maximum ablation depth in the absence of self-focusing.

Aside from these initial bench-top investigations, there has been limited development of dermatological applications for femtosecond laser ablation, despite the potential for improved wound healing, reduced scar formation, and improved cosmetic

results. Though intended for use with excised tissue, recent studies by Huang and Guo demonstrated the successful use of ablation with femtosecond laser pulses to separate layers of excised dermis for use in skin grafts [69,70]. This laser surgery method demonstrated improved precision over manual layer separation which reduced tissue waste and allowed many layers to be separated from a single strip of donor dermal tissue.

In addition to dermal tissue, several studies investigated clinical application of femtosecond neurosurgery in the late 1990s [39,71], culminating in the design of a hollow stereotactic probe for delivery of femtosecond laser pulses into the human brain [72,73]. The probe utilizes concentric hollow tubes to deliver the laser light and steer the focused beam through a cylindrical focal plane around the probe. It is unclear if development of the probe ever progressed to clinical trials. Several applications within neurosurgery have been suggested, such as ablation in the third ventricle to relieve hydrocephalus, partial ablation of the thalamus to relieve tremors associated with Parkinson's disease, or the resection of small tumors [39]. More recently, the Schaffer group at Cornell University has demonstrated the use of femtosecond laser ablation to delay and attenuate seizure propagation in mouse models of focal epilepsy [74]. Despite the early interest and development, femtosecond laser ablation of neural tissues is still in infancy. With increasing availability of femtosecond laser systems and further development of femtosecond laser microsurgical tools, new applications may develop as neurosurgeons gain wider access to this technology.

2.3.3: Hard tissue ablation

In addition to ablation of soft tissues, femtosecond lasers have found numerous applications in ablation of bone and teeth as well. Dental applications of laser ablation have been widely pursued and a number of techniques have achieved a limited degree of clinical acceptance [75]. The driving force behind the development of non-contact laser dental tools has been the desire to avoid the pain and patient discomfort associated with conventional dentistry tools. Laser dental tools can also provide the potential for

material-selective ablation by exploiting differences in absorption spectra, thereby limiting the removal of healthy tissue [76,77]. Initially, development of laser dentistry tools was hampered by the heating of dental pulp leading to tooth necrosis [78]. Even with the use of Er:YAG lasers, which typically emit at 2.94 µm, which have greatly reduced heating for ablation of dentin and enamel [79], the increased procedure time required for laser dentistry has limited acceptance [80]. Conventional dental laser systems are also unable to provide the quality of surface finish required for some procedures, such as the preparation of crown stumps [75]. Lastly, many lasers and conventional diamond burr rotary instruments have been shown to produce micro cracks during material removal, which can weaken the tooth and increase susceptibility to future dental caries [81-83].

Encouragingly, early studies of femtosecond laser ablation of both dentine and enamel have found a greatly reduced thermal load while eliminating the formation of micro cracks [40,84-86]. Notably, Rode *et al.* measured the intrapupal temperature of a tooth during 200 s of surface ablation by ~100 fs NIR pulses at 1 kHz repetition rate [85]. The authors found that, while the increase in pupal temperatures could exceed the damage threshold of 5.5 ºC [78], the use of air cooling at 5 l/min or higher kept pupal heating at safe levels. By comparison, Neev *et al*. found a negligible temperature increase below 2.5 ºC at the back of a 1-mm thick dentin slab during ablation with similar pulses at 10 Hz [40]. These results suggest that when using repetition rates in the kilohertz regime or above, care must still be taken to ensure safe internal temperature levels are not exceeded. When paired with a cooling mechanism, repetition rates in the tens to hundreds of kilohertz are still desirable to achieve satisfactory procedure times. Using a 45 kHz repetition rate, Niemz *et al*. demonstrated ablation rates comparable to Er:YAG lasers and slow-speed mechanical drills [87]. Use of newer fiber laser systems operating at hundreds of kilorhertz repetition rate should decrease procedures times even further.

While the use of femtosecond pulsed lasers for dental ablation can reduce the cracking and thermal loading associated with conventional laser systems, the weak

wavelength dependence of femtosecond laser ablation threshold means that much of the inherent selectivity between caries (cavities) and healthy dentin is lost. To regain this selectivity, Serbin *et al.* have proposed a means of monitoring the spectra from the plasma created during optical breakdown to identify the material being ablated, which could be tied into a feedback mechanism to control the laser exposure [88].

In addition to teeth, femtosecond lasers have been applied to hard tissue ablation of bone. The use of lasers in lieu of mechanical tools for bone surgery is attractive because of the potential for increased precision and the potential to access surgical sites with less invasiveness. Compared with conventional lasers, the lack of hemostasis that accompanies femtosecond laser ablation may provide fewer complications in bone surgery compared to procedures in more vascularized tissues.

Using conventional lasers, laser ablation of bone is predominantly accompanied by thermal damage, often evidenced by carbonization, and, in the case of pulsed lasers, the generation of significant mechanical stress waves [14]. A delay in the onset of wound healing has been noted in conventional laser ablation of bone and attributed to the thermal damage zone [89]. In addition, acoustic stresses can lead to localized cracking and potentially cause hearing damage in laser surgeries of the middle ear bones [90], an area in which laser ablation has great potential due to the high precision and non-contact nature of laser tools.

Early studies of femtosecond laser ablation in bone and nail tissue showed no observable thermal damage or cracking, as shown in Figure 2.4 [40,91]. Furthermore, in a detailed examination of extracellular and intracellular enzymatic activity on cultured bone tissue after ablation with femtosecond and nanosecond laser pulses, Girard *et al.* observed a dramatic decrease in enzyme denaturation using femtosecond laser pulses [92]. Spectroscopic analysis of the surface of pure hydroxyapatite (a major bone constituent) also showed no change in chemical composition after near-threshold ablation with femtosecond laser pulses [93]. Despite the observed reduction in collateral damage effects, however, a slight delay in wound healing has still been observed in mouse skulls

ablated with femtosecond lasers when compared to mechanical tools [94]. In the middle ear, bench-top studies have found femtosecond lasers to improve ablation surface quality for stapedotomy while reducing thermal and mechanical collateral damage compared to conventional lasers [95-97].

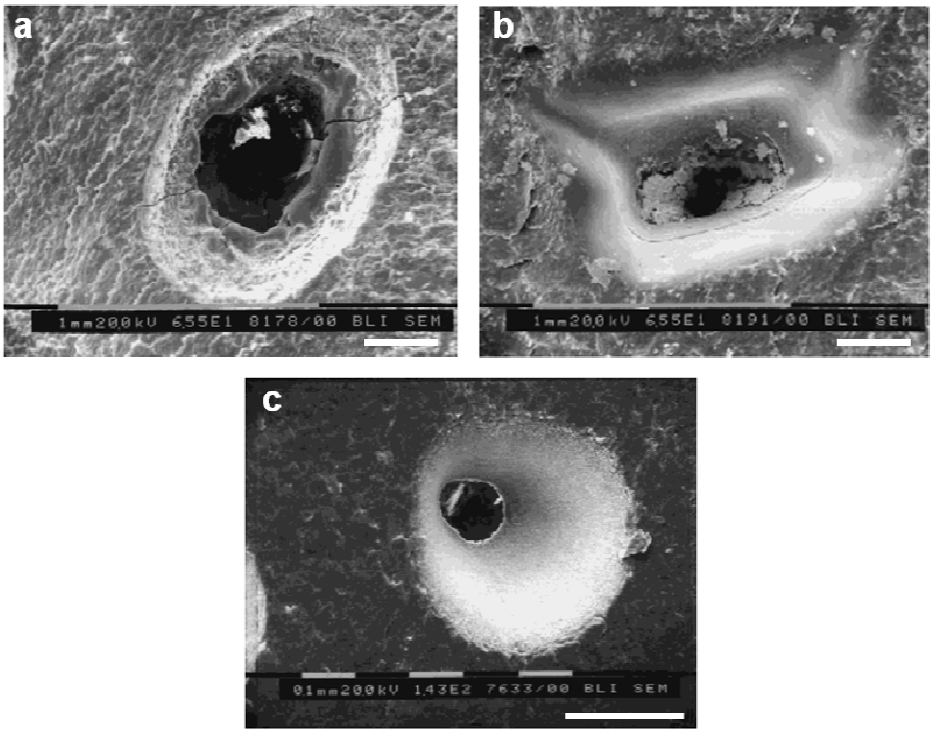

Figure 2.4. Scanning electron micrographs of laser ablation in human nail bed. Craters ablated with 100 pulses using (**a**) Ho:YSGG (λ = 2,080 nm, τ = 250 µs) and (**b**) XeCl (λ = 308 nm, τ = 15 ns) using 8-24 J/cm^2 with a 1 mm^2 focal spot (exact fluence per pulse is not reported) **c** Crater ablated with 100 Ti:sapphire (λ = 1,053 nm, τ = 350 fs) laser pulses at 2 J/cm^2 with a 0.2 mm^2 spot size.. Note that the thermally affected areas and cracking noticeable in **a** are not found in **b** or **c**. Adapted from [91]. Scale bars are 250 µm.

For practical clinical use, femtosecond lasers must be able to provide material removal at speeds comparable to conventional techniques. Several studies have found the

rate of ablation per pulse achieved by femtosecond lasers in hard tissue to be approximately 1 µm/pulse when using near 2 J/cm^2 peak fluence at a 10 Hz repetition rate [40,91,95], compared to rates of approximately 2 µm/pulse, 7 µm/pulse, and 30 µm/pulse found in human nail for Ho:YSGG, XeCl, and Er:YAG lasers, at 4 Hz repetition rate and peak fluences of approximately 24 J/cm^2, 12 J/cm^2, and 16 J/cm^2, respectively [91]. Table 2.3 provides a summary of the comparison of these lasers and their measured ablation parameters from Neev *et al*. [91]. In this study, the authors created craters in human nail using irradiation with 100 pulses at varying fluences for each laser system. They then reported the ablation rate in µm/pulse as the depth of each crater divided by 100 pulses. Similarly, the ablation efficiency in µm/mJ was calculated by dividing the ablation rate by the pulse energy in milliJoules. These metrics are relevant for laser drilling, as they reflect the accumulated depth that be drilled and how much energy is required.

From this study, the Er:YAG laser (2940 nm wavelength, 250 µs pulse) appears the best choice for applications which require high ablation speeds but do not have stringent requirements on cracking and morphology. The femtosecond laser pulses from the Ti:sapphire system (1053 nm wavelength, 350 fs pulse) achieved the highest ablation efficiency, implying that very little energy was wasted as heat or mechanical shock wave. However, in Figure 2.4**b**, the craters created by the XeCl laser (308 nm wavelength, 15 ns pulse) appeared to match the quality of the femtosecond laser-created craters while providing a seven-fold increase in ablation rate for the parameters investigated. The comparable ablation quality indicates that nanosecond laser pulses in the near-ultraviolet (UV) can suffice for precise superficial ablation of hard tissue. Indeed, the excellent surface quality during superficial ablation is why excimer lasers similar to the XeCl laser remain the tool of choice for reshaping the corneal stroma during LASIK, despite the use of femtosecond lasers to create the Bowman's flap to expose the corneal stroma. However, the ablation efficiency of the nanosecond XeCl pulses was found to be an order of magnitude lower than the femtosecond Ti:sapphire pulses. The excess energy in the

nanosecond XeCl laser ablation is converted into shock waves [98], which can be damaging to hearing in otological applications and may make Ti:sapphire lasers a more appropriate tool for ablation in the middle ear.

While the femtosecond laser proved to provide the slowest per pulse ablation rate in the study discussed above, the slightly lower per pulse ablation rate of femtosecond lasers can be overcome with higher repetition rates and correspondingly higher average powers. Liu and Niemz investigated using femtosecond lasers to cut through femoral bone using a pulse repetition rate of 40 kHz [99]. Based on these experiments, the authors estimate that a cut through the femur for knee replacement surgery would take approximately 20 minutes. While the authors cite this speed as meeting clinical expectations, further increases in procedure time can be gained through further increasing the pulse repetition rate. For clinical femtosecond laser microsurgery, a repetition rate in the hundreds of kilohertz range would be optimal for maximizing ablation speed while still avoiding effects of thermal accumulation.

Table 2.2. Summary of human nail ablation with pulsed lasers from Neev *et al*. [91].

Laser	Er:YAG	Ho:YSGG	XeCl	Ti:sapphire
Wavelength	2940 nm	2080 nm	308 nm	1053 nm
Pulse Duration	250 µs	250 µs	15 ns	350 fs
Repetition Rate	4 Hz	4 Hz	4 Hz	10 Hz
Spot Size	1 mm^2	1 mm^2	1 mm^2	0.4 mm^2
Maximum Ablation Rate (100 Pulses)	30 µm/pulse	2 µm/pulse	7 µm/pulse	1 µm/pulse
Peak Fluence at Maximum Ablation Rate	16 J/cm^2	24 J/cm^2	12 J/cm^2	3 $J/cm^{2\,(1)}$
Maximum Ablation Efficiency	0.5 µm/mJ	0.05 µm/mJ	0.1 µm/mJ	1 µm/mJ
Peak Fluence at Maximum Ablation Efficiency	8 J/cm^2	24 J/cm^2	12 J/cm^2	1 $J/cm^{2\,(1)}$
Crater Morphology	Slightly rough walls, cracks forming in deep craters	Rough walls, tapering with depth, cracks and melt debris present	Smooth walls, no visible cracking or melting	Smooth walls, no visible cracking or melting

(1) Ablation rate with the Ti:sapphire laser was only studied at 1 J/cm^2 and 3 J/cm^2 in this study. Maximum ablation rate and other metrics are defined in text.

Very recently, femtosecond lasers have been investigated as a means to treat kidney stones via laser lithotripsy of urinary calculi [100]. In this study, Qiu *et al*. found that very high energy (640 µJ) femtosecond pulses focused with 0.40 NA could ablate urinary calculi in a bench-top microscope. Compared to nanosecond laser lithotripsy with a Ho:YAG laser, the femtosecond laser produced debris that was one to two orders of magnitude smaller and greatly reduced the mechanical shock waves generated in the calculi. Recently the authors have presented ablation of calculi using a hollow core multimode fiber [101]. The fiber has an inner core on the order of 1 mm in diameter and can deliver ~200 fs pulses with pulse energies of at least 700 µJ [102]. While the delivery of such high energy pulses can be beneficial for developing flexible endoscopic microsurgery applications, the modal quality, dispersion, and attenuation of this fiber are all highly sensitive to bending, which may prove difficult to manage in clinical practice.

The clinical applications discussed in this chapter, both proposed and realized, take advantage of an increased precision and/or the ability to create confined effects inside bulk tissue. To capitalize on the benefits of increased precision or target structures in bulk tissue, the microsurgery must have a means of guidance. The next subsection will discuss optical means for guiding and imaging femtosecond laser microsurgery.

2.3.4: Laser-based guidance and monitoring

Full realization of the precision of femtosecond lasers for microsurgery requires a means of surgical guidance and/or feedback. To this end, a number of optical guidance methods have been proposed and implemented. The primary methods of guidance include laser-induced breakdown spectroscopy (LIBS) [88,103], optical coherence tomography (OCT) [68,97,104], and nonlinear optical interactions such as second harmonic generation (SHG) [105,106] and two-photon excited fluorescence (TPEF) [107].

Laser-induced breakdown spectroscopy analyzes the spectrum of the plasma spark created during ablation to identify the ablated material components. In so doing, LIBS provides molecularly sensitive information about the targeted material and can

indicate whether the laser is currently ablating the desired structure. Because LIBS is a spectroscopy method, and not an imaging technique, a conventional means of imaging is still required for guiding the surgical laser beam. Also, attenuation of the plasma spark inside bulk tissue decreases the utility of LIBS for ablation inside turbid tissue structures.

Optical coherence tomography is an imaging technique that can provide depth-resolved tissue information with microscopic detail. It relies upon the backscattering of laser light for signal generation and thus provides morphological information about the sample. Penetration depth of OCT is up to 2 mm in scattering tissue [108], deep enough to cover all anticipated femtosecond laser microsurgery applications, and Fourier-domain OCT systems are capable of providing real-time imaging during ablation [68].

Nonlinear optical techniques such as SHG and TPEF can utilize the femtosecond microsurgical laser at reduced pulse energies to induce the nonlinear optical phenomena of SHG and TPEF, respectively. By scanning the laser beam, images of the surgical site can be created with sub-cellular detail. Because both SHG and TPEF signals are material dependent, these techniques can provide both molecular *and* morphological detail, while potentially using the same microsurgical laser. Because nonlinear optical imaging provides image guidance with spatial resolution equal to the surgical laser and enables development of a compact single-laser system, the incorporation of SHG and TPEF into femtosecond laser microsurgical systems is an attractive option [109,110]. We will now explore the underlying mechanisms and fundamentals of these two nonlinear optical imaging techniques.

2.4: MECHANISMS OF NONLINEAR OPTICAL IMAGING

Though nonlinear optical imaging can broadly apply to a wide range of techniques including third harmonic generation and coherent anti-Stokes Raman scattering (CARS), here we limit discussion to SHG and TPEF microscopy, which provide stronger signals and can be easily realized with a single laser source. Traditionally, this laser source is a femtosecond laser oscillator, which can provide the

ultrashort pulse durations (and therefore peak intensities) required for efficient nonlinear interactions while operating at fast enough repetition rates to enable practical imaging speeds.

Two-photon excited fluorescence microscopy is a form of laser scanning fluorescence microscopy capable of imaging to depths in excess of 1 mm in the absence of strong scattering [111,112]. In laser scanning fluorescence microscopy, a focused laser spot is scanned in a sample to excite fluorescence and the detected emission is reconstructed to create an image of the sample. In conventional systems, a pinhole is usually placed in the back image plane in the detection pathway to reject emission light generated from outside of the focal volume. This arrangement is referred to as a confocal microscope and the use of the pinhole provides depth-sectioning of the sample so that clear images can be obtained from inside the sample. In addition to rejecting out-of-focus emission, the confocal pinhole also rejects emission light that has scattered while exiting the tissue, thus limiting the imaging depth in scattering samples. In TPEF microscopy, ultrashort laser pulses are used to excite fluorophores by near-simultaneous absorption of two photons, shown in Figure 2.5. Because two-photon absorption uses two photons of lower energy to overcome the bandgap in a fluorophore, wavelengths in the NIR can be used to excite many commonly used fluorophores. Just as in femtosecond laser microsurgery, the use of NIR wavelengths provides TPEF microscopy with depth penetration superior to that of single-photon fluorescence techniques. Furthermore, because two-photon absorption depends quadratically on the incident light intensity, the excitation is three-dimensionally confined to the focal volume where the intensity is highest, similar to the confinement of damage in FLMS as illustrated in Figure 2.6. In TPEF microscopy, this confinement provides inherent optical sectioning for high-resolution three-dimensional (3D) imaging without the use of a pinhole. Because all emission light can be assumed to originate from the focal volume, all scattered light can be collected while out-of-focus photobleaching and photochemical damage are greatly reduced.

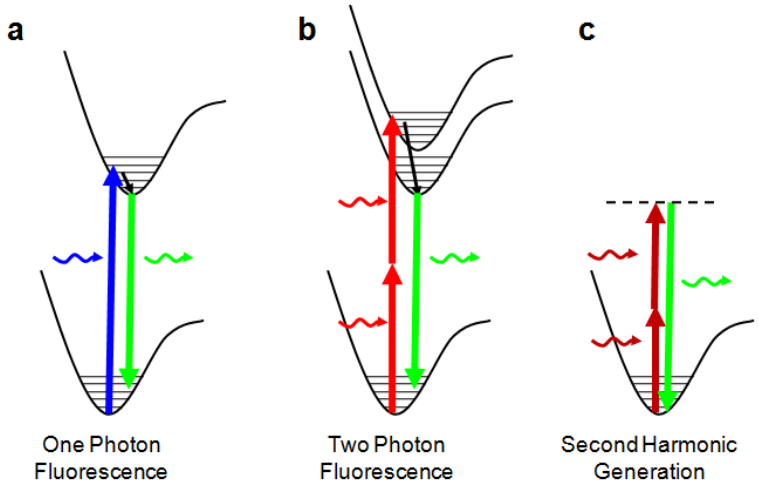

Figure 2.5. Simplified Jablonski Diagrams for two-photon excited fluorescence and second harmonic generation. As opposed to single-photon excitation, shown in **a**, the process of two-photon excitation, shown in **b**, utilizes two lower-energy photons to overcome the energy bandgap. Second harmonic generation, shown in **c**, is a nonlinear scattering process that does not involve an electronic transition between energy states.

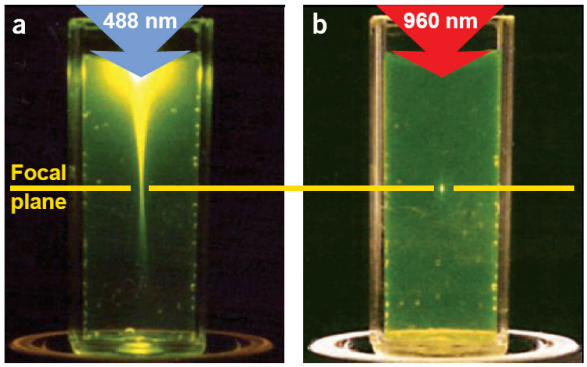

Figure 2.6. Comparison of excitation confinement in two-photon versus single-photon fluorescence. Single-photon excitation, **a**, exhibits significant out-of-focus excitation which leads to blurring and increased photodamage. Out-of-focus excitation is dramatically reduced in two-photon excitation, **b**, where the nonlinear dependence on intensity for results in a three-dimensionally confined excitation volume. Figure adapted from [113].

In addition, TPEF microscopy systems can also be used to image SHG [113,114]. SHG is a degenerate case of sum frequency generation, in which two electromagnetic waves interact with a material possessing a second-order nonlinear susceptibility ($\chi^{(2)}$) to create a third wave with a frequency equal to the sum of the frequencies of the incoming waves. In SHG, signal wave interacts with itself in the presence of the nonlinear material to create a new wave at half the original wavelength, shown in Figure 2.5**c**. This process is analogous to the creation of a single fluorescent emission photon from two-photon absorption; however SHG is a coherent process, producing a signal that is polarization dependent and anisotropically emitted in the forward direction. Nevertheless, the backscattered SHG signal can be detected to create images of certain biological structures such as collagen fibers and other types of connective tissue. A more rigorous discussion on the generation and collection of second-harmonic signals from biological sources can be found in [115]. Due to the dependence on $\chi^{(2)}$, SHG exhibits a quadratic dependence on laser intensity similar to TPEF and thus provides similar depth-sectioning capability. Images of SHG can provide information about morphology in the extracellular matrix, where there are fewer endogenous fluorophores, which makes SHG imaging a good complement to TPEF microscopy. In practice, SHG microscopy is often performed concurrently with TPEF microscopy and many systems do not distinguish between the two signals.

Both TPEF and SHG microscopy can provide valuable diagnostic information when used to image biological tissue, and commercial clinical two-photon microscopes have recently become available from JenLab GmbH (Jena, Germany). In addition to morphological information, excitation of endogenous fluorophores (autofluorescence) can be used to visualize other diagnostic indicators, such as the metabolic rate [116]. Specifically, recent studies have found that TPEF and SHG microscopy can be a powerful tool for early cancer diagnostics and staging by imaging cellular autofluorescence and observing changes in morphology and signal intensity [116-121].

Furthermore, the use of molecularly-specific targeted contrast agents can be used to identify a host of known disease indicators for imaging with TPEF microscopy [122,123]. The use of contrast agents has also be used to provide additional functional information, such as neural activity in the brain [124,125], as well as anatomical information, such as vascular pathways [126-128], which enable a wide range of diagnostic applications.

2.5: DEVELOPMENTS IN NONLINEAR OPTICAL ENDOSCOPY

Though there exists no previous demonstration of endoscopic development of femtosecond laser microsurgery systems, miniaturized and fiber-coupled nonlinear optical imaging systems have been developed since 2001 [129]. Initially, the primary impetus for development was neurological research [130-135], though recently probes have been developed toward clinical examination of diseased tissue as well [136-142]. For comparison, Table 2.3 presents a summary of imaging capabilities of various miniaturized two-photon microscopy devices found in literature. Table 2.3 also includes the two image-guided microsurgery probes presented in this dissertation for ready comparison of these probes with the current state of the art. Though using a variety of different optical designs, the miniature microscopes in Table 2.3 exhibit similar optical resolutions, generally about 1-2 μm laterally and 10-20 μm axially. This resolution provides these microscopes with the ability to resolve some sub-cellular detail with basic depth-sectioning capability. Collection efficiency is of paramount importance in these devices where intrinsic fluorophore signals are weak and fiber-coupling of scattered light is often inefficient. Given similar resolutions and frame rates between two devices, the power used to image a given sample listed in Table 2.3 can provide a comparison of relative collection efficiencies.

Table 2.3. Summary of imaging capabilities of published miniature fiber-coupled nonlinear optical microscopy probes.

Reference, Year	Resolution, lat. × ax. [µm]	FOV [µm]	Frame Rate [Hz]	Imaging Power Used [mW]	Sample Imaged
[129], 2001	NR	140[(a)]	2	NR	
[131], 2004	3.2 × 20.0	320	NR	30	Pollen
[132], 2005	1.2 × 9.8	215	2	15-80	Fluorescently-labeled blood vessels
[136], 2006	2.0 × 20.0	220	2.6	10	2.2 µm beads
[137], 2007	NR × 10.0	140 × 85[(a)]	0.03[(b)]	40	Fluorescently-labeled cancer tissue
				1.8	10 µm beads
[133], 2007	NR	80 × 20	5	30-40	Pollen
[134], 2008	1.0 × 7.7	200	25	1	10 µm beads
				25	500 nm beads
				150-200	Fluorescently-labeled rat brain tissue
[138], 2008	1.0 × 14.5	475	1.8	15	1 µm beads
				30	Fluorescently-labeled rat kidney tissue
[109], 2008	1.6 × 16.4	310	10	8.2	1 µm beads
				9.0	Pollen
[139], 2008	0.6 × 4.7	420	0.77 - 0.013	NR	
[140], 2009	1.6 × 11.4	160	3.3	15	Fluorescently-labeled pig cornea tissue
				55	SHG from rat tail tendon
[141], 2009	2.0 × NR	200	0.25	13	6 µm beads
[135], 2009	1.3 × 10.3	295 × 100	15 - 1	27	Labeled mouse vasculature
[143], 2011	1.3 × 9.9	130 × 100	7	20	SHG from rat tail tendon
				10	1 µm beads
				9.8	Pollen

NR = Not Reported. [(a)]Estimated from published images. [(b)]Estimated from reported 7 lines/second acquisition rate for 256 × 256 pixel image. Values in grey correspond to image-guided microsurgery probes presented in this dissertation.

Because TPEF and SHG microscopy are laser scanning microscopy techniques, any nonlinear optical endoscope must incorporate some form of laser beam scanning, either outside of the miniaturized system (proximally) or inside of it (distally). Proximal scanning can be achieved by scanning the laser beam onto a coherent fiber bundle, in which each fiber acts as a pixel to deliver the scanning pattern coherently to the miniature optics. This technique has been widely-demonstrated in confocal endoscopes [144-148]. Though proximal scanning through a fiber bundle eliminates the need for a miniaturized scanning mechanism and can allow for a relatively large field of view (FOV), the resolution is inherently limited by the fiber spacing. Furthermore, for femtosecond laser pulses, the single-mode fibers that make up the bundle limit the pulse energy that can be delivered before self-phase modulation leads to increased GVD and pulse distortion, as previously discussed. Though two-photon endoscopes based upon fiber bundles have been demonstrated, their cellular imaging performance has been limited [131].

As an alternative, several distal scanning methods have been developed including resonant vibration of the laser delivery fiber via a piezoelectric device [129,132,134,136], and, more recently, scanning of the laser beam by a microelectromechanical systems (MEMS) scanning mirror [133,135,137]. An endoscope design utilizing a rotational MEMS micro motor has also been demonstrated recently [149]. This design, common among OCT endoscopes, utilizes a small motor to rotate a prism after the objective lens to sweep a cylindrical FOV. The use of post-objective scanning in a miniaturized system requires a low-NA objective lens, however, which greatly reduces resolution and collection efficiency while greatly increasing the laser energy required at the sample.

While fiber-tip scanning has been implemented since the earliest TPEF probe designs, this scanning method can lead to off-axis aberrations due to the scanning of diverging light through stationary optics. In contrast, MEMS scanning mirrors can be used to scan a collimated laser beam, much as a pair of galvanometric scanning mirrors is used in a table-top two-photon microscope. As an additional advantage, MEMS scanners can theoretically be driven either in resonance, for large deflection angles at low driving

voltages, or off resonance, where slow scanning speeds and accurate positioning can be used for conventional raster scanning. Precise static and off-resonance displacement is valuable for FLMS applications, where the microsurgery laser may need to be targeted to arbitrary locations within the FOV. One drawback of MEMS scanning mirrors can be the low reflectivity of bare silicon, 33% at 760 nm [150]. Though reflectivity can be enhanced with metal deposition onto the mirror surface, the use of fiber scanning mechanisms in lieu of a scanning mirror will always provide the highest laser energy efficiency.

Aside from miniaturization of a scanning mechanism, efficient collection of fluorescent emission is another critical challenge in miniature fiber-coupled TPEF devices. For simplicity, some designs collect emitted light through the same fiber used to deliver the excitation laser [136,137]. While using a single fiber allows for very compact designs, the small NAs and small core sizes make the delivery fibers poor collectors of scattered light. This problem is also exacerbated in designs that use fiber-tip scanning, where fast scanning and large deflections will also impair collection of the scattered light. Similarly, in MEMS-based systems, losses due to poor mirror reflectivity are incurred again on the collection of the emission light. To address this issue, systems have been designed which incorporate either dual-core fibers [136,137,151], separate collection fibers [132,134], or even miniaturized detectors mounted in the probe [129]. Of these solutions, dual-core fibers maintain the most compact design; however the collection-core sizes are currently limited to approximately 165 µm, which still limits collection efficiency compared to large-core multimode collection fibers. The probe-mounted PMT used in Helmchen *et al*. avoids loss of signal due to fiber coupling and transmission [129]; however this limits the degree to which the system can be miniaturized, which is crucial to many applications. In the following chapter, we will explore the design criteria and constraints for miniaturized nonlinear optical microscopes in further detail and discuss the unique constraints inherent in designing for delivery of high-energy ultrashort laser pulses for microsurgery.

Because these nonlinear optical microscopy probes utilize fiber delivery of femtosecond laser pulses, the numerous design solutions outlined above can often be applied when designing a femtosecond laser microsurgery endoscope. In addition to the design considerations present when using low energy pulses for imaging, the use of amplified femtosecond laser pulses for microsurgery introduces an additional set of design criteria which are required to manage material damage, SPM, and self-focusing phenomena. The following chapter will discuss all of the design considerations that play a role in developing a nonlinear imaging-guided femtosecond laser microsurgery endoscope.

Chapter 3: Design Considerations of Femtosecond Pulse Laser Endoscopes

There are several important design criteria for developing a femtosecond laser microsurgical endoscope. First, such a device requires tight laser focusing at the sample to enable optical breakdown at practical laser pulse energies and to maximize the lateral and axial imaging resolution. Second, navigation and surgical guidance requires a large field of view relative to the features under investigation. Third, high scanning speeds are desired in clinical applications to mitigate patient motion artifacts and decrease microsurgery time. Lastly, efficient light collection is needed to collect weak fluorescent signals from intrinsic fluorophores and attenuating tissue.

While the aforementioned criteria are broadly applicable to clinical laser scanning microscopy systems, the use of amplified femtosecond laser pulses required for microsurgery entails further challenges to ensure that ultrashort pulses of sufficient intensity are delivered to the sample. Chief among these challenges is the need to manage group velocity dispersion (GVD) while avoiding self-phase modulation (SPM) and material damage. This chapter will first address the selection of optical components and basic optical layout, followed by an in-depth look at how the optical design dictates the imaging and surgery performance through determination of the focused spot size and the maximum field of view.

3.1: Selection of Optical Components and Basic Optical System Design

A nonlinear image-guided femtosecond laser microsurgery endoscope requires at least four specific key optical components. First, the system requires a fiber optic to deliver the femtosecond laser pulses. Second, a laser beam scanning device is required to enable TPEF and SHG microscopy and may also be used to scan the surgery laser. Third, an objective lens is needed to create the highly confined laser intensities required for

successful nonlinear imaging and femtosecond laser ablation. Lastly, a flexible means of efficiently collecting the emitted TPEF and SHG signal is needed. This section will address the selection of each component and discuss their role in determining the performance of the system.

3.1.1: Fiber optic for delivery of ultrashort pulses and collection of emitted light

Flexibly decoupling the microsurgical endoscope from the optical table requires the use of fiber optics for delivery of the laser light and collection of the fluorescent emission. Though the original design of Helmchen *et al*. [129] succeeded in utilizing a miniature photomultiplier tube (PMT) to detect fluorescence rather than an optical fiber, the current sizes of such devices prevent their use in a clinical endoscopy application.

As stated in the previous chapter, conventional single-mode fibers present difficulties in nonlinear optical imaging due to the onset of SPM complicating dispersion management. Specifically, Jung and Schnitzer calculated that SPM becomes significant after only 1.3 cm of single-mode fiber when delivering a 100-fs pulse of just 1 nJ pulse energy [130]. Fibers with larger core sizes can be used, however, in conventional fibers, an increase in core size leads to a greater number of transverse modes traveling through the fiber. Increased transverse mode content increases the diffraction-limited focused spot size of the laser beam and thus degrades resolution while increasing the pulse energy required for microsurgery.

Microstructured fibers have been created which utilize periodic air holes parallel to the fiber core to create a photonic crystal structure, altering the propagation dynamics of the laser beam. Examples of such fibers are shown in Figure 3.1. One such design (Figure 3.1**b**) allows for single-mode propagation inside an increased core diameter (approximately 15-35 µm versus 2-10 µm for a conventional single-mode fiber). Even with the increased core size, however, appreciable SPM occurs for pulses just below 10 nJ after 1 meter of propagation [152]. An alternative to increasing the core size to reduce SPM is to reduce the n_2 of the guiding material. To this end, hollow-core fibers have been

created, shown in Figure 3.1**c**, that utilize photonic microstructuring to create a photonic bandgap. This bandgap confines the laser light to an air-filled hollow core, which can be single-mode guiding [153].

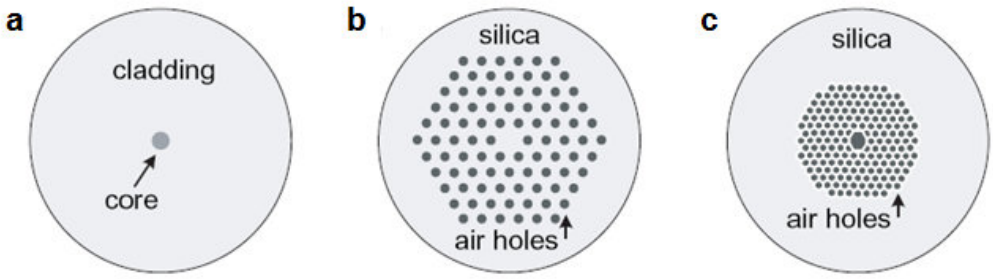

Figure 3.1. Illustrative comparison of single-mode laser delivery fibers. a. Conventional single-mode glass optical fiber consists of a glass core and cladding which guide light by total internal reflection. **b.** Large mode area photonic crystal fiber uses air holes to create a photonic crystal structure, enabling the propagation of a single transverse mode with a larger mode field diameter. **c.** Hollow-core fiber utilizes a photonic bandgap to guide light inside a hollow core, usually filled with air. Illustrations adapted from Fu and Gu [154].

To avoid SPM and enable delivery of high energy (> 100 nJ) amplified femtosecond pulses for microsurgery, we have chosen to implement a single-mode air-core photonic bandgap fiber (PBF) guiding in the range of 750 - 800 nm (Air-6-800, NKT Photonics A/S), with a zero-dispersion wavelength near 755 nm.

Because this specific fiber relies on a photonic bandgap structure to guide the light, the spectral bandwidth of guidance is fairly narrow and thus cannot be used for collection of visible TPEF or SHG emission light. Therefore a separate dedicated collection fiber is required in addition to the laser delivery fiber. While the use of a second fiber slightly increases the size and complexity of the miniaturized system, the use of a separate collection fiber enables optimization of this fiber for collection of scattered visible light at low intensities, which can dramatically improve the total system collection

efficiency. For this purpose, a large-core plastic optical fiber (NT02-551, Edmund Optics Inc.) was chosen as the dedicated collection fiber for its large 2 mm core size, 0.5 numerical aperture and relatively low attenuation of visible light between 400 nm and 600 nm.

3.1.2: Laser beam scanning mechanism

Nonlinear optical imaging and high-speed microsurgery require a means of fast laser beam scanning. By selecting an air-core PBF as the laser delivery fiber, we have precluded the use of proximal scanning through a coherent fiber bundle and distal scanning must be implemented through a miniaturized scanning mechanism. Though, hypothetically, a bundle of air-core PBF could be created, scanning of the microsurgery laser would likely result in damaging the proximal end of the fiber bundle, destroying the coupling efficiency. As previously addressed, the current two best options for distal scanning are fiber-tip scanning by piezoelectric actuators (Figure 3.2**a**) and beam scanning by reflective MEMS scanning mirrors (Figure 3.2**b**). We also considered other options, including rotational scanning by a micromotor and acousto-optic scanning. Post-objective rotational scanning with a micromotor, as demonstrated by Liu *et al*. [149], was deemed impractical due to the required low NA. Suitably small acousto-optic scanners, if they could be fabricated, would be difficult to employ due to the depolarized nature of the light exiting the PBF and the spatio-temporal distortions to the pulse that can arise in such scanners [155].

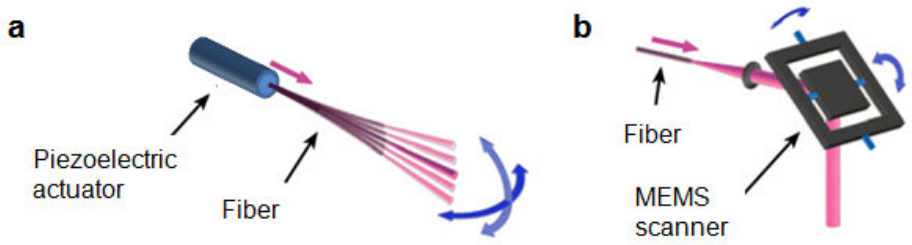

Figure 3.2. Illustration of piezoelectric fiber actuator and MEMS micromirror laser beam scanning mechanisms. a. A piezoelectric tube can house the fiber to sweep the fiber tip in two directions. Usually the motion of each axis is coupled to create a spiral scanning pattern. **b.** A MEMS micromirror can be used to provide two-axis scanning of a reflected laser beam. Illustrations adapted from Flusberg *et al*. [156].

Both fiber-tip actuators and MEMS micromirrors have inherent advantages and disadvantages. Piezoelectric fiber-tip actuators possess the advantages of compactness and high optical efficiency. Because these devices do not rely upon any reflection, the optical path can be entirely parallel to the axis of the device, which helps to reduce overall optical system dimensions while also avoiding any reflective losses. These devices must be driven on their mechanical resonance, however, which prevents the use of raster scanning or off-axis targeting of a microsurgery beam. In fact, nearly all applications of piezoelectric fiber scanners in nonlinear microscopy have relied upon modulated sinusoidal voltage signals to drive the fiber tip in a circular spiral pattern for best actuation. While effective, this scanning pattern requires the measurement and compensation of the angular phase lag of the fiber tip to remove twisting artifacts from the image during reconstruction [134,136]. Lastly, fiber-tip scanning results in scanning a diverging beam of light, which for large deflections can induce off-axis aberrations [156]. The alternative is to attach a small collimating lens to the end of the fiber [157], however this greatly increases the moving mass, thus slowing the scanning speed and leading to more significant vibration of the total optical assembly.

MEMS scanning mirrors provide an attractive alternative by easily scanning collimated light and offering potential off-resonance actuation. As previously mentioned, the drawback of these devices lies primarily in the space required to house and package them. Current two-axis micromirror dies are generally between 2 × 2 mm^2 to 3.5 × 3.5 mm^2 in size and must be mounted such that light can be reflected off the mirror surface towards the focusing optics. Because of their size, MEMS scanning mirrors can often become the limiting factor for overall miniaturization of an endoscope.

For use in the femtosecond laser microsurgery endoscope, we received two-axis gimbaled MEMS scanning micromirrors fabricated from silicon-on-insulator (SOI) by the Solgaard Group at Stanford University. The devices rely upon electrostatic comb banks to drive two orthogonal axes of rotation. Their design provides the potential for off-resonance deflection and static beam steering which may expand the future utility of the endoscope.

3.1.3: Layout of optical system

We built the remaining optical system around the fiber and MEMS scanning mirror we have chosen. Figure 3.3 presents a schematic diagram of the optical system. First, a lens collimates the laser light exiting the fiber. For this purpose, we have chosen to use a gradient index (GRIN) rod lens. GRIN lenses utilize a radially varying refractive index to focus light instead of curved surfaces. As a result, GRIN lenses can be manufactured down to very small outer diameters (< 1 mm) with elongated cylindrical shapes that ease packaging and alignment. These two virtues are critical for fiber collimation where we wish to keep the diameter of the collimation assembly as small as possible.

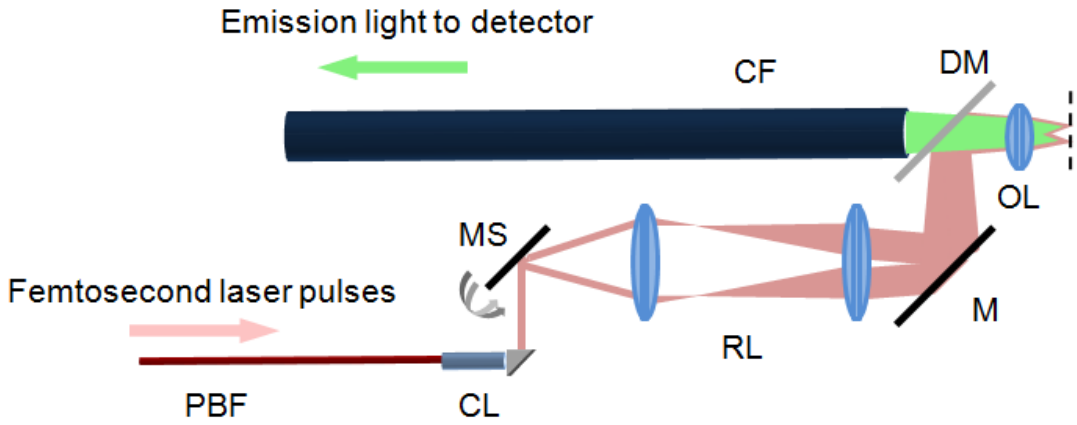

Figure 3.3. Schematic of the optical system chosen for the femtosecond laser microsurgery endoscope. Amplified and unamplified femtosecond laser pulses are delivered through an air-core photonic bandgap fiber (PBF). The laser light is then collimated by a GRIN collimating lens (CL) before being reflected to the MEMS scanning mirror (MS). The scanning mirror scans the laser beam through a relay lens pair (RL), off a silver mirror (M) and a dichoric mirror (DM), to the back aperture of a miniaturized objective lens (OL). Emitted TPEF or SHG signal from the focal plane is then collected by the objective lens and transmitted by the dichroic mirror to the large-core plastic optical collection fiber (CF) to be transmitted to a photodetector (not shown).

The vast majority of previously demonstrated nonlinear optical endoscopes have also relied upon GRIN lenses for objective lenses as well, for the reasons mentioned above. There are two important disadvantages to GRIN lenses. First, while extremely easy to package, GRIN lenses tend to exhibit appreciable spherical aberration which ultimately limit their resolution to near twice the diffraction limit [156]. Second, the gradient index focusing mechanism causes their principle plane to be set back behind the back aperture of the lens, especially at moderate to high numerical apertures. This configuration has the consequence of reducing the working distance of GRIN lenses relative to traditional spherical or aspherical lenses of similar NA and diameter. Still, working distances around 200 µm are common for most GRIN lenses near 0.5 NA and 2

mm outer diameter, enabling access to many tissues of interest and approaching the practical imaging depth of most published nonlinear optical endoscopes.

Alternatively, a number of manufacturers now offer molded glass aspherical lenses with diameters down ~ 2 mm and numerical apertures of 0.6 or higher. For this project, both GRIN and aspherical miniature objective lenses were investigated and will be discussed in greater detail in subsequent chapters.

Having chosen to use a separate fiber for the efficient collection of emitted light, the optical system then requires a means for separating the collection light pathway from the excitation/microsurgery light pathway and directing the collected light into the collection fiber. The most straightforward way to discriminate between the two pathways is by wavelength with a dichoric mirror, as the emitted light will be generated at approximately half the wavelength of the excitation light and will have ample spectral separation.

Since one of the strengths of nonlinear imaging techniques is the ability to collect and use all emitted light regardless of scattering, it is critical that the collection pathway be designed to collect as much scattered light as possible. The simplest way to achieve this with small diameter optics is to use high NA collection optics, in this case a fiber, and to place the optics as close to the objective lens as possible. This condition necessitates placing the dichroic mirror directly behind the objective lens and allowing the dichroic mirror to pass the emitted light to the collection fiber placed directly behind it.

The maximization of the field of view was among the chief design goals identified earlier. While achieving this goal, we will need, first, to maintain a useful imaging resolution over the full angular scanning range of the MEMS scanning mirrors, and, second, to place the dichroic mirror and collection fiber in close proximity to the objective lens for efficient collection of scattered light. This need then requires that the MEMS scanning mirror be separated from the objective lens by at least the size of the dichroic mirror. If the scanning mirror is etched onto a 3.5 mm square die and we

generously assume a dichroic mirror of equal size can be fabricated, the path length from the scanning mirror surface to the back aperture of the objective lens can be no smaller than roughly 4.75 mm. For a common 1.8 mm GRIN lens with a clear aperture of 1.26 mm (such as the LGI830 from Newport, Inc.), this distance dictates that optical scanning angles must be kept well below 7.5º half angle to avoid scanning off the clear aperture of the objective lens. Since MEMS scanning mirrors commonly achieve maximum optical scanning half angles over 10º, this simple configuration clearly limits our maximum achievable field of view.

To overcome this conflict and maximize both collection and FOV simultaneously, while maintaining a uniform resolution across the FOV, we have chosen to employ a relay lens system to image the scanning mirror plane to the back aperture of the objective lens. Such lenses are common in bench-top laser scanning microscopes, though they have frequently been eschewed in miniaturized systems to avoid complicating alignment and packaging. Several miniaturized nonlinear imaging microscopes have utilized multi-pitch GRIN lenses or GRIN lens assemblies [135,158]. In GRIN rod lenses, an infinitely long lens would guide light in a sinusoidal fashion such that the light periodically focused and collimated within the lens. The number of periods of the sinusoid that light will experience in the GRIN lens is referred to as the "pitch". Thus a single-pitch or higher GRIN lens will have at least one focus inside of the lens. Such internal foci must be avoided in a microsurgery probe to avoid nonlinear effects such as SPM and self-focusing near the focus and to prevent damage to the lens. Indeed, König *et al*. observed luminescence originating from the interior of a 0.97-pitch GRIN lens when delivering femtosecond laser pulses at 0.12 J/cm^2 per pulse, which they attributed to material damage [159]. To avoid such damage and unwanted nonlinear effects, any intermediary focus in the optical system must be located in air, where the breakdown threshold is high and the n_2 is low. To achieve this, we have chosen to use a simple two lens relay system using two positive lenses separated by their combined focal lengths. This arrangement has the added advantage of acting as a beam expander. The active area of MEMS

scanning mirrors is often smaller than the back aperture size of miniaturized objective lens candidates by roughly a factor of 2. The possibility of beam expansion allows for increasing the beam diameter after the scanning mirror to utilize more of the objective lens aperture and thus increase resolution. The choice of expansion ratio ultimately dictates the trade-off between resolution and field of view in such a system. The design aspects controlling this optimization are discussed in the following section.

3.2: OPTICAL DESIGN FOR MINIATURE LASER SCANNING MICROSCOPES

In laser scanning imaging systems, arguably two of the most important indicators of optical performance are the field of view (FOV) and the lateral resolution, δ_{xy}. These two parameters can be combined to compare imaging systems on a normalized basis using the concept of the number of resolvable spots [160], N, where

$$N \equiv \frac{\mathrm{FOV}}{\delta_{\mathrm{xy}}}. \tag{3.1}$$

For basic projection systems consisting simply of a laser beam deflected optically by some scanning device and impinging on a screen, N can be expressed on an angular basis as

$$N_{proj} \equiv \frac{\theta}{\partial\theta}, \tag{3.2}$$

where θ is the total optical scan angle from the scanning device and $\partial\theta$ is the full angle angular beam divergence. All angles are expressed in radians. Assuming an overfilled scanning device, the divergence can be approximated as

$$\partial\theta \cong \frac{\lambda}{D}, \tag{3.3}$$

where λ is the illumination wavelength and D is the aperture diameter of the scanning device[3]. Thus we see for simple projection systems, the number of resolvable spots is given simply by

$$N_{proj} \cong \frac{\theta D}{\lambda}. \tag{3.4}$$

Equation (3.4) illustrates that the factors dictating the maximum number of resolvable spots is determined by the scanning device and the wavelength of the illumination. This result can be applied broadly to a wide range of laser scanning optical systems because the product θD is the optical (Lagrange) invariant of the system [161]. As such, θD is a constant of the optical system unaffected by the addition of any static refractive or reflective optical elements to the beam path. Thus: (1) given the assumption that the scanning device is over-filled, and (2) in the absence of any diffraction or aberration from any additional optical elements, the number of resolvable spots in any laser scanning system is dictated by the performance of the beam scanner and the wavelength of illumination.

Approaching this concept in another way, remember that the limiting aperture of an optical system constitutes the aperture stop and is the only element that contributes diffraction effects to the propagation of the beam [162]. Thus for an assumption of an over-filled scanning device, the scanning device can be assumed to be the limiting aperture. Therefore the device determines the optical invariant for the rest of the optical system.

Equation (3.4) provides accurate characterization of simple laser projection systems and can be useful in comparing scanning devices. For real laser scanning

---

[3] Occasionally, Equation 3.3 is multiplied by a factor of 1.22, corresponding to diffraction from a circular aperture. Most often, this factor is ignored in literature and is ignored here for easy comparison with literature.

microscopy systems, however, the assumptions that the scanner is the dominating source of diffraction and that the scanner is completely overfilled are often incorrect. Equation (3.4) has been applied to report the maximum number of resolvable spots in several published miniaturized laser scanning microscope systems [141,163,164] and is useful in comparing the scanning devices used in each case, however analysis of the performance of these systems clearly shows that the equation is not intended to properly model the systems in question. Thus, to properly model the imaging conditions of the femtosecond laser microsurgery endoscope and guide the design process, it is necessary to derive the number of resolvable spots for the optical system of the endoscope.

In bench-top systems, commonly used galvanometric scanning mirrors can achieve many thousands of resolvable spots, and thus the mirrors are often underfilled, while the beam is expanded significantly to overfill the back aperture of the objective lens. Overfilling the back aperture of the objective sacrifices achieving the maximum N in favor of maximizing imaging resolution. For the femtosecond laser microsurgery probe, the choice is less clear and there exist two different generalized scenarios to consider. Namely, one in which the MEMS scanning mirror provides the limiting aperture of the system and another in which the limiting aperture belongs to the objective lens. These scenarios presume that the relay lenses are of large enough diameter that neither of them constitutes the limiting aperture. The assumption is reasonable as the relay lens apertures must be designed to be sufficiently large to permit scanning of the beam. The generalized case can be derived, which applies whether the scanner or the objective are the limiting aperture. To begin, the maximum FOV from Eq. (3.2) can be expressed as

$$\mathrm{FOV} \approx f\theta_{obj} = \frac{f\theta_{mirror}}{M}, \tag{3.5}$$

by using the paraxial and thin lens approximations, where f is the focal length of the objective lens and θ_{obj} and θ_{mirror} are the full scan angles at the back aperture of the objective lens and at the MEMS mirror, respectively, in radians. Here, M is the effective magnification of the relay lens pair. The two-photon microscopy resolution (full width at half-maximum, or FWHM) can be given by

$$\delta_{xy} \approx \frac{\mathrm{K}_1 \lambda}{2\sqrt{2} NA}, \tag{3.6}$$

where $\sqrt{2}$ factor accounts for the difference in FWHM of the intensity-squared distribution from that of the intensity distribution and K_1 is a correction factor accounting for the diffraction experienced by a Gaussian laser beam [165]. The K_1 parameter is given by

$$\mathrm{K}_1 = \frac{0.75}{D_{beam}/D_{aperture}}, \quad \text{for } D_{beam}/D_{aperture} < 0.5, \tag{3.7}$$

and

$$\mathrm{K}_1 = 1.036 - \frac{0.058}{D_{beam}/D_{aperture}} + \frac{0.156}{\left(D_{beam}/D_{aperture}\right)^2}, \quad \text{for } D_{beam}/D_{aperture} > 0.4. \tag{3.8}$$

Here, D_{beam} is the $1/e^2$ diameter of the beam waist at the limiting aperture, $D_{aperture}$ is the diameter of the limiting aperture [165], and we define the limiting aperture as the aperture stop of the system, or the aperture that provides the largest truncation ratio. The quotient $D_{beam}/D_{aperture}$ is the truncation ratio.

Again using the paraxial approximation, we can rewrite the focusing numerical aperture of the optical system, as

$$\mathrm{NA} \approx \frac{D_{aperture}^{objective}}{2f} \quad \text{or} \quad \frac{M\,D_{aperture}^{mirror}}{2f}, \tag{3.9}$$

depending on whether the objective lens or the MEMS mirror is the limiting aperture, respectively. Equation (3.9) has the added assumption that the lens is focusing in air, and can be multiplied by the index of refraction of the immersion fluid if one is used. When the mirror constitutes the limiting aperture of the optical system, the aperture that dictates the NA of the optical system is given by the projection of the MEMS mirror aperture at the objective lens.

In the case of under-filled apertures where the truncation ratio is less than 0.5, the laser beam diameter defines the resolution of the system. By substituting Eqs. (3.7) and (3.9) into Eq. (3.6), we can rewrite the resolution as

$$\delta_{xy} \approx \frac{0.75\lambda f}{\sqrt{2}D_{beam}^{objective}} = \frac{0.75\lambda f}{\sqrt{2}MD_{beam}^{mirror}}, \tag{3.10}$$

where $D_{beam}^{objective}$ and D_{beam}^{mirror} are the beam size on the objective and mirror, respectively. By substituting Eqs. (3.5) and (3.10) into Eq. (3.1), we find that the number of resolvable spots for the case of under-filling simplifies to

$$N \approx \frac{1.89 \cdot D_{beam}\theta}{\lambda}. \tag{3.13}$$

Here Eq. (3.13) is generalized such that D_{beam} and θ correspond to either the values at the objective lens or the scanning mirror. From Eq. (3.13), we see that the scanning device still defines the number of resolvable spots by defining the maximum scanning angle. In

the case of under-filling, however, the beam waist at the scanning device replaces the scanner diameter.

In the case of greater truncation ratios ($D_{beam}/ D_{aperture} > 0.4$), the derivation of maximum number of resolvable spots achievable follows the same steps but does not reduce to a compact form due to the nonlinear nature of Eq. (3.8).

Finally, for the limiting case of uniform aperture illumination ($D_{beam}/ D_{aperture} \rightarrow \infty$), we find that N can be expressed as

$$N \cong \frac{1.37 \cdot D_{aperture}}{\lambda}, \tag{3.14}$$

where $D_{aperture}$ and θ correspond to either the values at the objective lens or the scanning mirror depending which one is the limiting aperture. Note that Eq. (3.14) is very nearly the relationship for a simple projection system multiplied by the $\sqrt{2}$ factor for two-photon excitation. Because inherent in Eq. (3.13) is the requirement that the Gaussian beam be no larger than half the diameter of the aperture at the aperture stop, Eq. (3.14) shows that uniformly filling the aperture can increase N at least 45% compared with under-filling. In practice, however, the over-filling of the limiting aperture to achieve a uniform illumination with a Gaussian beam results in significant energy loss from the laser beam and a compromise must be made.

It is useful to note that the diffraction-limited axial resolution can also be predicted through similar means, where

$$\delta_z \approx \frac{\mathrm{K}_2 \lambda}{4NA^2\sqrt{2}} = \frac{\mathrm{K}_2 \lambda}{2^{5/2} NA^2}, \tag{3.15}$$

$$\mathrm{K}_2 = \frac{1.27}{\left(D_{beam}/D_{aperture}\right)^2}, \text{ for } D_{beam}/D_{aperture} < 0.5, \tag{3.16}$$

and

$$K_2 = 3.5 + \frac{0.33}{D_{beam}/D_{aperture}} - \frac{0.73}{\left(D_{beam}/D_{aperture}\right)^2} + \frac{0.52}{\left(D_{beam}/D_{aperture}\right)^3},$$

for $D_{beam}/D_{aperture} > 0.4$. (3.17)

From these equations, we see that the axial resolution is much more sensitive to the degree of truncation on the scanning device. As with the lateral resolution, these equations also hold if the objective lens is the limiting aperture, where the truncation ratio at the scanner is replaced with the truncation ratio at the objective lens.

From the discussion above, it is clear that when designing a laser scanning microscopy system, the scanning device determines the upper bound on the number of resolvable spots achievable in the system. Once this parameter is fixed by the size of the beam on the scanning device, the remaining optics can be chosen with the goals of (1) selecting the desired combination of FOV and resolution, as dictated by *N*, and (2) avoiding the introduction of aberrations, which would degrade *N*.

When a relay lens pair is used to provide magnification between the scanning device and the objective lens, these basic design constraints allow significant freedom in the choice of an objective lens. In the case of the femtosecond laser microsurgery probe, the desired objective lens will have: high NA and large clear aperture for maximum collection efficiency, small total diameter for miniaturization, and a working distance sufficient so as to not limit the maximum imaging and ablation depths of the device.

Chapter 4: Development of an 18-mm Diameter Image-Guided Microsurgery Probe

As a first step towards development of a clinical femtosecond laser microsurgical endoscope, we set out to develop a preliminary device to act as the proof of concept. The goals of this first device were (1) to test the critical components, such as the air-core fiber and MEMS scanning mirrors, as part of a miniaturized optical system; (2) to demonstrate femtosecond laser microsurgery for the first time through a fiber-coupled micro optical system, and (3) to experimentally investigate the factors limiting both microsurgery and imaging performance. This chapter will summarize the independent characterizations of the air-core fiber and MEMS mirror, followed by a summary of the fully packaged system and a detailed description of the Lissajous image reconstruction algorithm developed for nonlinear imaging. The chapter will conclude with a characterization of the performance of both the individual optical components and combined system, and lastly successful demonstration of the cellular imaging and microsurgery capabilities of the completed device.

4.1: Component Characterization

4.1.1: Characterization of air-core photonic bandgap fiber

As previously noted, the nonlinear absorption mechanisms at the heart of both femtosecond laser microsurgery and nonlinear optical imaging are sensitive to pulse duration. The air-core PBF propagates the laser light through air and thus introduces extremely low material dispersion. However, waveguide dispersion is still present and can introduce significant anomalous dispersion to the pulse. As a result, laser pulses far from the minimally dispersive wavelengths of the fiber can have their pulse duration stretched by an order of magnitude or more during propagation through as short as one

meter of PBF. We therefore characterized the key features of the fiber and specifically measured the pulse duration, collimated beam profile, and wavelength spectrum of pulses with various center wavelengths after propagating through one meter of fiber.

In our experiments throughout this chapter, we used laser light from either a Ti:sapphire oscillator or a chirped pulse amplifier (CPA). The Ti:sapphire oscillator (Mai Tai, Spectra Physics) is a wavelength tunable source delivering pulses near 100 fs at a repetition rate of 80 MHz and 1 Watt average power. Its high repetition rate and wavelength tunability make this laser well-suited for nonlinear imaging. Microsurgery in the high-density plasma regimes requires amplified laser pulses to initiate optical breakdown. For this purpose, we utilize pulses from the CPA (Spitfire, Spectra Physics). The CPA system also delivers pulses near 100 fs and 1 Watt average power, but at a much lower repetition rate of 1 kHz providing pulses as large as 1 mJ in energy. The wavelength of the CPA has a narrow tuning range and is therefore kept at a nominal center wavelength of 780 nm.

The air-core PBF chosen for our femtosecond laser microsurgery endoscope has a good transmission range from 750 nm to 800 nm, which covers the wavelength of the CPA and determines the range of wavelengths that can be used for imaging from the Ti:sapphire oscillator. The fiber exhibits a near-zero-dispersion wavelength near 755 nm, above which the fiber is increasingly anomalously dispersive. The fiber is single-mode guiding with a core size of 6 μm. We created a scanning electron micrograph of the tip of this fiber to illustrate the microstructured design, shown in Figure 4.1.

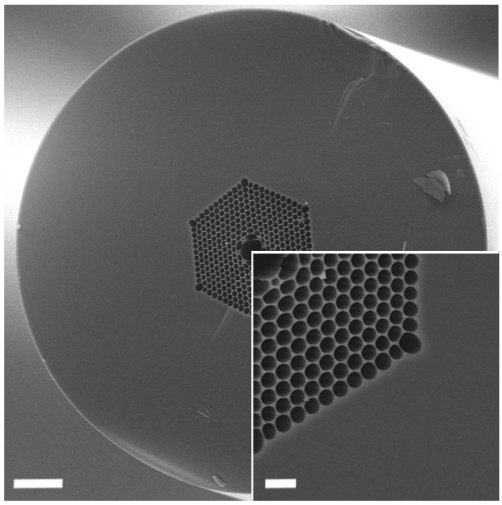

Figure 4.1. Scanning electron micrograph of the air-core photonic bandgap fiber. The fiber consists of a 125 µm-diameter silica cladding with a periodic air-hole microstructure creating a photonic crystal in the center. A larger central air hole in the crystal with 6 µm diameter acts as a single-mode waveguide. A high magnification view in the inset shows detail of the microstructure. Scale bars are 15 µm and 3 µm (inset).

Using a flipping mirror we could select and direct either laser beam to a 10× objective lens with 0.25 NA for coupling into the fiber. By under-filling the coupling lens, we matched its effective numerical aperture to the 0.17 NA of the fiber to maximize the coupling efficiency. At the fiber exit, the laser light was collimated using a 0.23-pitch GRIN lens with 1.8 mm diameter (LGI830-1, Newport, Inc.). This lens is similar to the small diameter GRIN lenses suitable for use in a fully miniaturized endoscopy system.

Using this fiber coupling arrangement, we first measured the overall transmission efficiency for two different lengths of fibers; 0.72 m and 5.92 m. The large difference in fiber lengths was chosen to isolate the effects of coupling efficiency and attenuation. Table 4.1 summarizes their transmission efficiencies for laser pulses from the Ti:sapphire oscillator at 755 nm and 780 nm, as well as from the CPA at 780 nm. The overall transmission efficiency, T, is a function of the coupling efficiency, η_c, the attenuation coefficient, α, and the length, L, where

$$T = \eta_c 10^{(-\alpha L/10)}, \tag{4.1}$$

and α is in units of dB/m. The parameters η_c and α can be found using the transmission measurements in Table 4.1 and solving Eq. (4.1) simultaneously for the two lengths at each wavelength. This procedure yields a measured attenuation coefficient of approximately 0.3 dB/m and a coupling efficiency between 64% and 69%. The error estimated from propagation of measurement uncertainty is approximately ± 0.08 dB/m on α and ± 3.5 % on η_c. The fiber manufacturer specifies the attenuation coefficient as "< 0.4 dB/m" for the wavelength range measured, in good agreement with the measured values. These measurements also illustrate that the both laser systems can be coupled into and out of the PBF equally well with this arrangement.

Table 4.1. Fiber coupling and attenuation measurements.

Laser	Wavelength [nm]	Fiber Length [m]	Total Transmission [%]	Attenuation Coefficient [dB/m]	Coupling Efficiency [%]
Ti:Sapphire Oscillator	755	0.72	61	0.33	65
		5.92	41		
Ti:Sapphire Oscillator	780	0.72	66	0.31	69
		5.92	45		
CPA	780	0.72	61	0.30	64
		5.92	43		

To measure pulse dispersion, we built a homemade interferometric autocorrelator similar to Ranka *et al*. [166] utilizing a GaAsP photodiode as a nonlinear signal transducer to measure the pulse durations before and after propagation through one meter of PBF. Autocorrelation measurements were taken directly from the collimated beam emerging from the collimating GRIN lens. Representative autocorrelation traces are shown in Figures. 4.2 and 4.3, while Figure 4.4 summarizes pulse duration measurements before and after the fiber for relevant wavelengths throughout the fiber bandwidth. The

fiber was found to exhibit a minimum amount of dispersion at a center wavelength of 753 nm, where a 120 fs input pulse resulted in a 150 fs output pulse after one meter of fiber propagation. At a center wavelength of 780 nm, a 140 fs input pulse was found to have been stretched by over a factor of 20× to 3.2 ps.

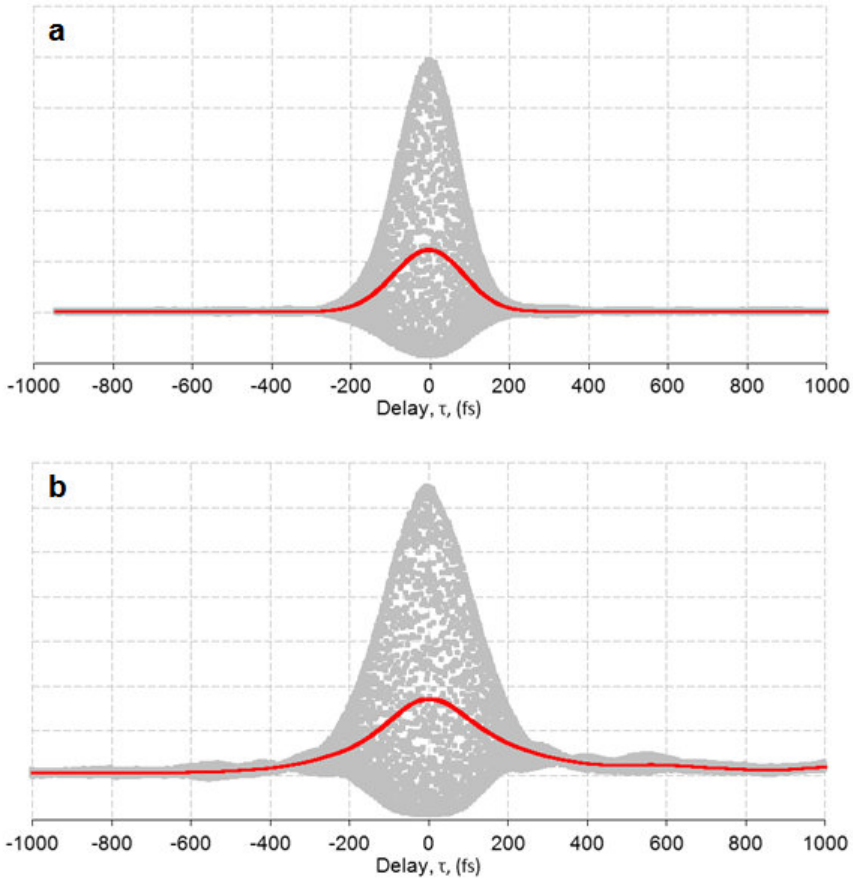

Figure 4.2. Autocorrelation traces near the zero dispersion wavelength of the PBF. a An interferometric autocorrelation trace (grey) and the running average (red) for a 753 nm wavelength pulse of 120 fs duration FWHM, prior to propagating through the PBF. **b** The corresponding trace for a 753 nm pulse after propagating through 1 meter of PBF, in which the pulse duration remains relatively short at 150 fs. The Ti:sapphire oscillator was used to produce the laser for both traces.

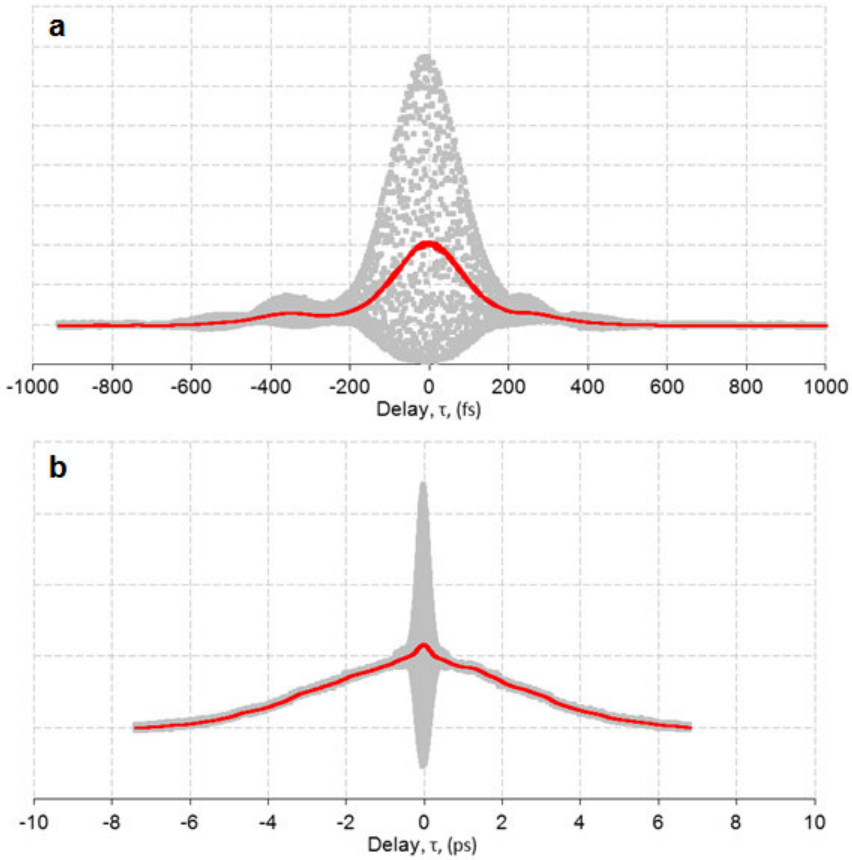

Figure 4.3. Autocorrelation traces before and after the PBF at 780 nm. a An interferometric autocorrelation trace (grey) and the running average (red) of a 780 nm wavelength pulse of 140 fs duration, prior to propagating through the PBF. **b** The corresponding trace for a 780 nm pulse after propagating through 1 meter of PBF. Here the pulse duration has stretched considerably due to group velocity dispersion, to a length of 3.2 ps. Note change in scale between **a** and **b**. The Ti:sapphire oscillator was used to produce the laser for both traces. The small side-lobes in **a** are low energy features in the pulse shape that arose from the laser oscillator at this wavelength.

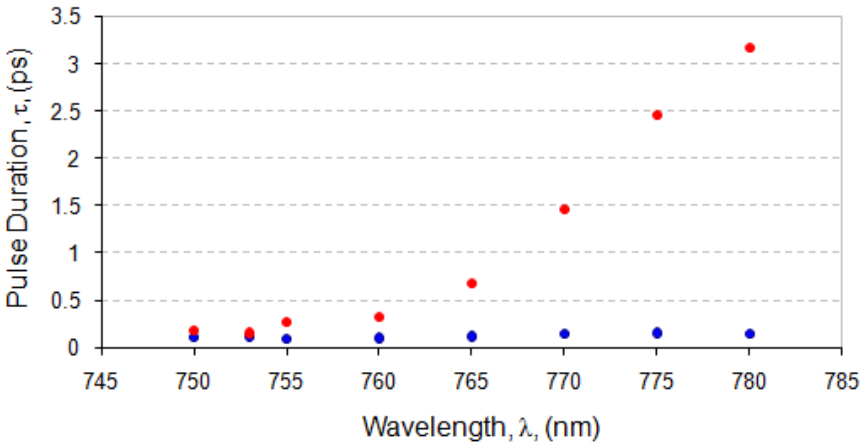

Figure 4.4. Summary of autocorrelation measurements before and after propagation through one meter of PBF using pulses from the Ti:sapphire oscillator. The blue data points represent the measured pulse duration before propagation through the fiber, while the red data points indicate the measured pulse duration after the fiber. The fiber exhibits minimal dispersion near a center wavelength of 753 nm. Above 753 nm, the fiber is anomalously dispersive with dispersion increasing monotonically up to 780 nm, the highest wavelength tested.

All autocorrelation measurements were made assuming a sech^2 pulse shape and using the corresponding deconvolution factor of 1.54. For clarity in analyzing heavily chirped pulses (see, for example, Figure 4.3**b**), the fringe-averaged trace is calculated using a running average. Averaging yields a close approximation of the amplitude trace by removing the effects of interference. Estimated measurement uncertainty is ± 10 fs.

The manufacturer specifications for this fiber list a zero dispersion wavelength near 755 nm and report dispersion increasing with wavelength to a dispersion coefficient, D_λ, of approximately 390 ps/km/nm at 780nm. The dispersion coefficient can be converted to the effective group delay dispersion (GDD) of the fiber by

$$\text{GDD} = -\frac{\lambda^2 L}{2\pi c} D_\lambda , \tag{4.2}$$

where λ is the center wavelength of the laser, c is the speed of light, and L is the length of fiber. For one meter of the air-core fiber at a center wavelength of 780 nm, the predicted GDD is 126,000 fs^2. The measured GDD can be calculated using

$$\left|\mathrm{GDD}\right| = \frac{1}{4\ln 2}\sqrt{\left(\frac{C_B \tau_{out}}{\Delta \nu}\right)^2 - \left(\frac{C_B}{\Delta \nu}\right)^4}\ , \tag{4.3}$$

where τ_{out} is the pulse duration measured after the fiber, while Δv and C_B are the frequency spectrum of the pulse and the transform-limited time-bandwidth product introduced in Chapter 2. For the measured output pulse duration of 3.2 ps, Eq. (4.3) yields a measured GDD of 129,000 fs^2. This measured value agrees quite well with the predicted value of 126,000 fs^2.

For nonlinear optical imaging, we generate femtosecond pulses from our wavelength-tunable oscillator, and thus the center wavelength can be tuned at or near the minimum dispersion wavelength of 753 nm to minimize dispersion of imaging pulses. However, with the CPA operating at a fixed wavelength of 780 nm, the microsurgery pulses clearly require dispersion pre-compensation to restore a femtosecond-regime pulse duration at the sample. This pre-compensation was achieved by modifying the compression stage of the CPA such that a suitable amount of positive dispersion was left in the pulse exiting the amplifier.

The best pre-compensation was achieved when delivering a 3.8 ps positively-chirped pulse into the fiber, which resulted in a 180 fs pulse after one meter of propagation. An autocorrelation of a pre-compensated pulse from the CPA after propagating through one meter of PBF is provided in Figure 4.5. Pre-compensating the pulse duration by stretching the input pulse also provides the added benefit of lowering the peak intensity being focused on the fiber tip during coupling of the light into the fiber. We found laser damage to the fiber tip during coupling to be the condition limiting the maximum pulse energy that we could couple into the fiber. Pre-stretching the laser pulse

from 140 fs to 3.8 ps increased the maximum energy we could deliver through the fiber from 400 nJ to 1.3 µJ without damaging the fiber tip.

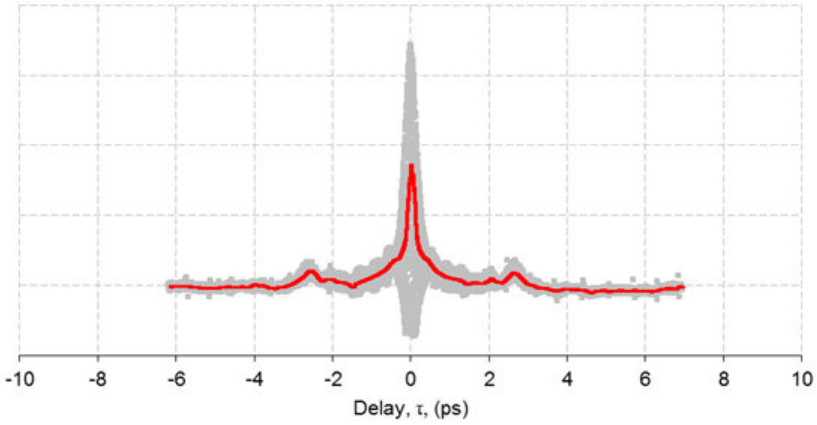

Figure 4.5. Autocorrelation trace at 780 nm after pre-compensation and propagation through one meter of PBF. Interferometric autocorrelation trace (grey) and the running average (red) of a pulse from the chirped pulse amplifier where the compression stage of the amplifier was adjusted to precompensate for the fiber dispersion, resulting in a recompressed pulse of 180 fs duration. Low energy side-lobes are present, likely due to the presence of higher-order dispersive effects in the fiber which were not compensated for in our arrangement.

In addition to dispersion characterization, we also characterized the beam profile to ensure the output laser beam was single mode. We also monitored the laser spectrum to ensure the laser beam exhibited no spectral broadening from self-phase modulation. For these measurements, we used a combination of a beam profiling camera (UP-680-12B, UNIQ) and software (LBA-PC, Spiricon) along with a spectrum analyzer (USB2000, Ocean Optics). Pulses from the Ti:Sapphire oscillator at 760 nm and 780 nm center wavelengths were delivered through one meter of PBF and collimated by a 0.23-pitch GRIN lens with 1.8 mm outer diameter. Beam profiling found the $1/e^2$ collimated beam waist and far field divergence half-angle to be 0.37 mm and 1.33 mrad at 760 nm.

At 780 nm, these values were measured to be 0.44 mm and 1.31 mrad. The expected divergence for a collimated Gaussian (TEM_{00}) beam is given by

$$\theta = \frac{\lambda}{\pi w_0}, \tag{4.4}$$

where θ here is the far field divergence half angle, λ is the center wavelength of the propagating laser light, and w_0 is the minimum beam radius. For the measured beam waists indicated above, the theoretical far field divergence angles for collimated Gaussian beams are 1.32 mrad at 760 nm and 1.12 mrad at 780 nm. The good agreement between the experimental and theoretical beam divergence angles indicate that the fiber-delivered beam is well collimated and predominantly in the TEM_{00} mode.

While monitoring the beam profile, we also adjusted the stability of the beam profile to transient motion of the fiber and to moderate bending. While holding the two ends of the fiber fixed, the beam profile showed no noticeable variations when perturbing the middle of the fiber with rapid movements or introducing bends as small as 5 inches in radius. Smaller bend radii were not tested. This insensitivity to bending makes this fiber an attractive candidate for clinical use, where the clinician will desire consistent performance despite the positioning of the probe. Furthermore, no spectral broadening was observed using the spectrometer for exiting pulse energies up to the maximum pulse energy of 1.3 µJ used in our experiments.

4.1.2: MEMS scanning mirror characterization

The MEMS device implemented in our first probe has a bare Si mirror measuring 500 × 500 μm^2 and was provided by our collaborators at the Solgaard group at Stanford University [167]. The device, illustrated in Figure 4.6, operates using banks of vertical interdigitated combs, which are driven outward by electrostatic forces. These forces create torsion along the mirror support beam and twist the mirror about this axis. The mirror is fabricated with both an inner and an outer axis oriented in a gimbaled fashion so that the mirror can rotate in two decoupled and orthogonal directions.

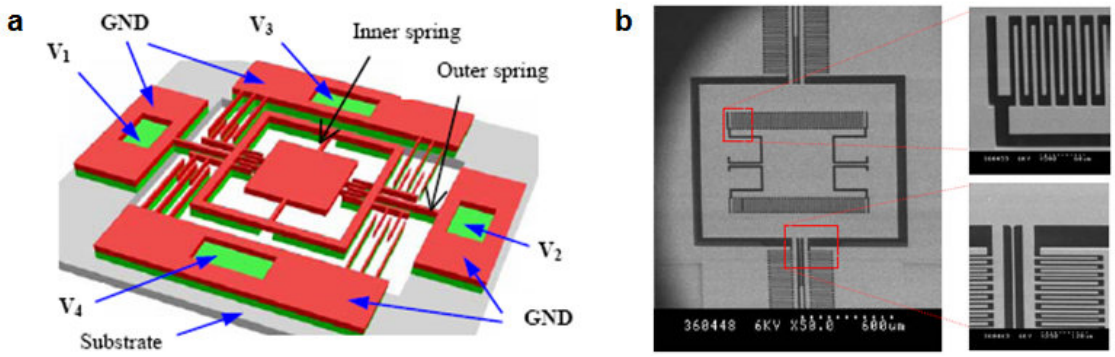

Figure 4.6. Detail images of the MEMS scanning mirror. a Illustration of the MEMS mirror architecture. The device utilizes a gimbaled support of a central mirror surface. Interdigitated comb banks are actuated through electrostatic forces to drive the mirror rotation. The driving electrodes and rotational torsion springs are labeled. **b** An SEM micrograph of a MEMS device of this design. The insets show detail of the vertical comb structures used to drive the mirror. Reproduced from [167].

For packaging into our first probe, the silicon-on-insulator chip containing the MEMS device was mounted onto a 9 mm × 7 mm leadless chip carrier. To characterize the mirror performance, we first investigated the static and dynamic deflection characteristics using a helium-neon laser reflecting off the MEMS mirror onto a screen 2.5 meters away. For static deflection, increasing voltage was applied to each electrode up to 180 V or until no more deflection was observed upon increasing voltage. Though MEMS scanning mirrors of this design have been shown to exhibit static optical deflections in excess of ±7°, imperfections in our device limited the measured static optical deflection to less than ±1° on the inner axis with negligible deflection measured using the outer axis.

We then measured dynamic scanning performance of the mirror by applying a sinusoidal voltage signal between zero and a peak voltage to opposing comb banks driven 180 degrees out of phase. In this manner, the device is driven to large deflections by exciting the resonant frequencies of the two axes. At a maximum driving voltage of 80 V_{peak}, The resonant frequencies of the outer and inner axes of the mirror were measured

to be 1.54 kHz ± 12 Hz and 2.73 kHz ± 40 Hz, with peak optical deflections of ±10.5° and ±10.0°, respectively. The stated bandwidths of the resonant peaks are measured at FWHM. For this MEMS scanning mirror, the mirror size and maximum deflection yield a maximum number of resolvable spots of approximately 333 × 317 by Eq. (3.14), which sets the upper bound on the number of resolvable spots possible for this prototype.

Lastly, we measured the reflectivity of the mirror using the collimated NIR laser beam from the PBF discussed in the previous section. The reflectivity of the bare Si MEMS mirror at 760 nm and 780 nm was found to be 30% for the largely depolarized light exiting the fiber.

4.2: PROBE DESIGN AND EXPERIMENTAL SETUP

In addition to the PBF and MEMS scanning mirror, a miniature objective lens, two relay lenses, and a dichroic mirror were selected to complete the optical system discussed in Chapter 3.1.3 (Figure 3.3) and shown here, as built, in Figure 4.7.

A GRIN lens with 0.46 NA (LGI830-1, Newport, Inc.) was chosen for use as the miniature objective lens. This GRIN lens is 0.23-pitch long, meaning that it acts as a positive singlet lens, and possesses a compact 1.8 mm outer diameter with a working distance of 210 µm. Despite the spherical aberrations that have been observed in such lenses, they have proven successful in many nonlinear optical endoscopes and their compact cylindrical shape make them easier to package.

For relay lenses, we chose a pair of aspherical lenses with 6.5 mm maximum outer diameter and 3.4× nominal beam expansion. Given the 7 × 9 mm^2 size of the chip carrier containing the MEMS scanning mirror, the relay lens diameters were chosen to be as close to 7 mm as possible to allow for the largest apertures without increasing the size of the prototype. To maximize resolution, the beam expansion ratio was chosen such that the 0.37 mm beam waist of the imaging laser is expanded to match the 1.26 mm clear aperture of the GRIN objective lens.

The dichroic mirror is a 5 × 5 mm^2 square dielectric mirror (Narrow Rejection Hot Mirror, High End Systems) which reflects > 99% of light between approximately 740 nm and 950 nm while transmitting > 90% of light between 395 nm and 690 nm for mixed polarization. A 5 mm glass prism with a silvered hypotenuse was used as a mirror to direct light from the relay lenses to the dichroic mirror, finishing out the optical system.

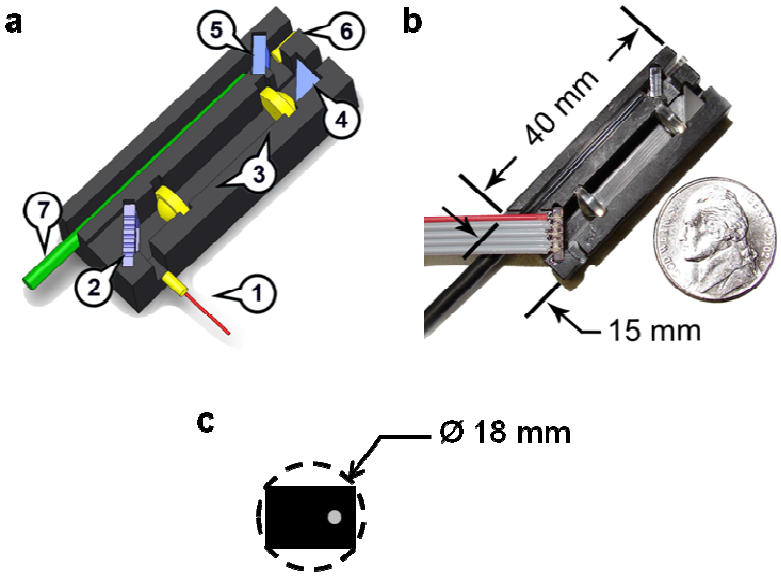

Figure 4.7. The 18-mm diameter probe for image-guided femtosecond laser microsurgery. a A computer rendering of the 10 × 15 × 40 mm^3 probe showing 1) air-core PBF and GRIN collimating lens, 2) two-axis MEMS scanner on a leadless chip carrier, 3) miniature aspheric relay lenses, 4) mirror, 5) dichroic mirror, 6) 0.46-NA GRIN objective lens, and 7) 2mm-core plastic optical fiber. **b** The photograph shows the miniature probe as built without the delivery fiber and the lid that was used to seal the probe. The PBF and its collimating GRIN lens were mounted separately and aligned to the probe during experiments. A United States Nickel is provided for size comparison. **c** Cartoon of the probe cross-section, illustrating the encircling diameter of 18 mm, which represents the smallest diameter housing that could be used to deliver this probe.

Figure 4.7 shows the individual components of the miniature optical system as packaged in a housing machined from Delrin® acetal resin polymer. We machined the housing, measuring at 10 × 15 × 40 mm^3, using a computer numerical controlled (CNC) milling station. The approximate finished dimension tolerance was 100 µm. The use of CNC facilitated rapid production of the prototype housing directly from a SolidWorks® computer model. Individual optical components are press-fit into the housing, as is a Delrin® lid which is used to seal the probe from stray light during use. The use of press-fit grooves for positioning of the optical components allows for simple fabrication and assembly of prototypes during refinement of the design, however the lack of positioning control in the final housing (e.g., adjustment screws or micropositioners) limits the ability to adjust component alignment after fabrication of the housing. This limitation was mitigated by the ability to rapidly mill revised housings as needed. With a circumscribing diameter of 18 mm, this first prototype is already small enough to be useful as a flexible surface probe for accessing many regions of the body, although it is still too large for endoscopic use.

Figure 4.8 presents the experimental setup used for testing the probe. We implemented the same fiber coupling and collimation system used during PBF characterization. Here, the probe is mounted inverted with the GRIN objective lens facing down with the sample holder positioned below on a three-axis piezoelectric translation stage. The fiber collimation system, consisting of fiber chuck and collimating GRIN lens, is mounted outside of the probe housing and aligned to direct the collimated laser light into the housing.

For imaging, a maximum average power of 120 mW near the 753 nm imaging wavelength could be delivered from high-repetition rate oscillator to the sample. The total transmission efficiency of the probe is about 12% as a result of a ~63% total transmission through one meter of PBF, the ~30% reflectance of the MEMS mirror, and the insertion losses of the remaining optics. For microsurgery, the maximum pulse energy deliverable from CPA system to the sample was 350 nJ. Above this pulse energy, the

laser intensity at the entrance to the PBF began to damage the fiber and decrease coupling efficiency.

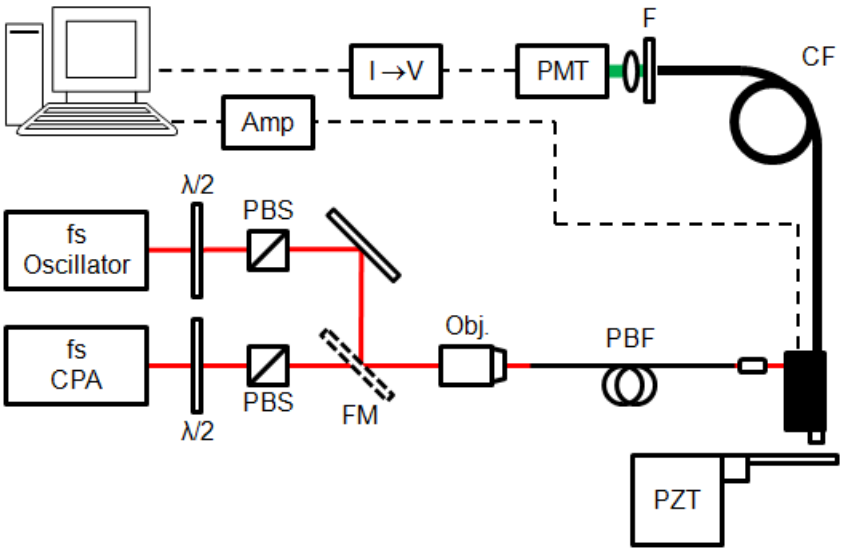

Figure 4.8. Experimental setup for testing the 18-mm diameter probe. For testing the first prototype, femtosecond laser pulses from a Ti:sapphire oscillator and pre-chirped picosecond pulses from a CPA were coupled into one meter of PBF, with selection between the lasers achieved using a flipping mirror mount. At the fiber output, the collimating GRIN lens was mounted independently and directed the laser light into the probe. A computer acquired the amplified photocurrent from the PMT, drove the MEMS scanning mirror, and reconstructed the resulting image. **λ/2**: half wave plate; **PBS**: polarizing beam splitter; **FM**: flipping mirror; **Obj.**: 0.25-NA objective lens; **PBF**: one meter of photonic bandgap fiber; **PZT**: piezoelectric translation stage; **CF**: one meter of plastic optical collection fiber; **F**: laser blocking filter; **PMT**: photomultiplier tube; **I→V**: current-to-voltage preamplifier; **Amp**: 200 V MEMS driving amplifier.

Collected fluorescence is delivered through 1 meter of the collection fiber and focused into a photomultiplier tube (PMT) (H7422-40, Hamamatsu) by a 4 mm focal length lens with a Schott BG38 filter blocking scattered laser light. The PMT photocurrent is amplified using a low-noise current preamplifier (SR570, Stanford

Research Systems) operating in high-bandwidth mode and sampling at 1 MHz. The amplified signal is read into a computer and a homebuilt LabView program through a data acquisition card (PCI-6115, National Instruments), which also shares duty with another data acquisition card (PCI-6711, National Instruments) for sending the driving signal to the MEMS. We use two cards simply because the PCI-6115 does not have enough output channels to drive the MEMS mirror independently. This signal is amplified by a custom built 10-channel amplifier (AgilOptics), which can supply up to 200 V at low driving currents, before being delivered to the MEMS device. Further details of the image reconstruction algorithms developed for the driving LabView program are discussed in the following section.

4.3: DEVELOPMENT AND IMPLEMENTATION OF A FAST-UPDATING AND NON-REPEATING LISSAJOUS IMAGE RECONSTRUCTION METHOD

The MEMS mirror used in the 18-mm image-guided microsurgery probe provides laser beam scanning only when actuated at its resonant frequencies. Resonant scanning scans the laser beam with two orthogonal sinusoids of comparable frequency, resulting in a mesh-like Lissajous pattern. Using traditional methods of Lissajous scanning, the frame rate must be reduced in order to achieve a dense scanning pattern that can acquire high resolution information evenly throughout the FOV. In this section, we present a new fast-updating method of Lissjous image reconstruction that provides increased temporal information at a high frame rate while still densely scanning the FOV. This section will introduce the conventional method of Lissajous image reconstruction, followed by a detailed description of our fast-updating method. We conclude this section with example images from the implementation of this method in the 18-mm probe.

4.3.1: Introduction to Lissajous scanning and image reconstruction

Most often, laser scanning microscopes scan the focused laser beam in a raster pattern, shown in Figure 4.9**a**, in which the image is created by the successive scanning

of parallel lines. The raster pattern provides the advantage of a uniformly illuminated FOV, in which each pixel receives nominally the same laser exposure, and requires only a simple image reconstruction algorithm. The creation of a raster pattern requires a fast scanning axis to scan each line and an orthogonally oriented slow axis, moving at the frame rate, to provide separation between each line to fill up each image. However, because our MEMS scanning mirror must be operated with each axis moving at resonance to achieve practical scanning angles, the common raster scanning pattern cannot be employed in our prototype.

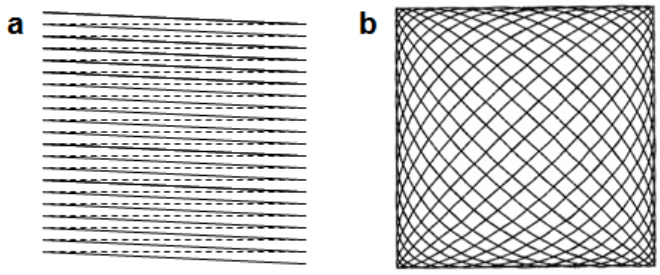

Figure 4.9. Comparison of laser scanning patterns for image reconstruction. a An illustration of a raster scanning pattern, which is commonly used in two-photon microscopes. In this pattern as it is shown here, the horizontal axis moves very rapidly for line-by-line acquisition while the vertical axis moves slowly at the frame rate. **b** Lissajous scanning moves both axes sinusoidally to cover the FOV, resulting in a mesh pattern. Note that in the Lissajous scan, the outside receives more laser coverage than the inner portions of the FOV and specific points are scanned repeatedly before the pattern is complete.

Driving the scanning mirror with both axes on resonance creates a Lissajous pattern, illustrated in Figure 4.9**b**, where the location (x, y) of the focused laser beam is given by the parametric equations:

$$x(t) = \frac{1}{2} X\left[\sin\left(2\pi f_x t + \phi_x\right) + 1\right] \tag{4.5}$$

and

$$y(t)=\frac{1}{2}Y\left[\sin\left(2\pi f_y t+\phi_y\right)+1\right]. \tag{4.6}$$

Here f and ϕ are the driving frequency and phase shift, respectively, in the x or y direction, and X and Y are the maximum extents of the field of view in x and y, respectively. For image reconstruction, Eqs. (4.5) and (4.6) describe the pixel location of each data sample where X and Y are in units of pixels. The pattern repeat rate, f_P, of a Lissajous pattern is given by

$$f_P=\frac{f_x}{n_x}=\frac{f_y}{n_y}, \tag{4.7}$$

where n_x and n_y are the smallest integer divisors that satisfy Eq. (4.7). Thus, for all real and rational scanning frequencies, the corresponding Lissajous pattern is stable and will repeat at a fixed rate. The integers n_x and n_y determine the number of cycles that occur in either the x or y direction, respectively, before the pattern repeats [129]. Larger values of n increase the number of lines scanned across the FOV during one completion of the Lissajous pattern.

Within the resonance bandwidth of the MEMS scanning mirror, the driving frequencies can be chosen to maximize the n values that satisfy Eq. (4.7), thereby increasing the line density of the image. From Eq. (4.7), it is clear that an increase in line density inherently reduces the pattern repeat rate. When the frame rate (f_F) is made equal to f_P, as is commonly done, there exists an intrinsic trade-off between sampling density and frame rate. Furthermore, because the Lissajous pattern is repeated once for each frame, regions of the image left unsampled by a sparse Lissajous pattern in one frame remain unsampled in subsequent frames and this information is lost. For illustration, Figure 4.10 displays single Lissajous-scanned frames where $f_F = f_P$ for several scanning frequency combinations and pixel sizes. In these examples, the driving frequencies are

restricted to the resonant scanning peaks of the MEMS scanning mirror used in the prototype: f_x = 1540 Hz with a 12 Hz FWHM bandwidth and f_y = 2730 Hz with a 40 Hz FWHM bandwidth. The images are compared quantitatively in Table 4.2.

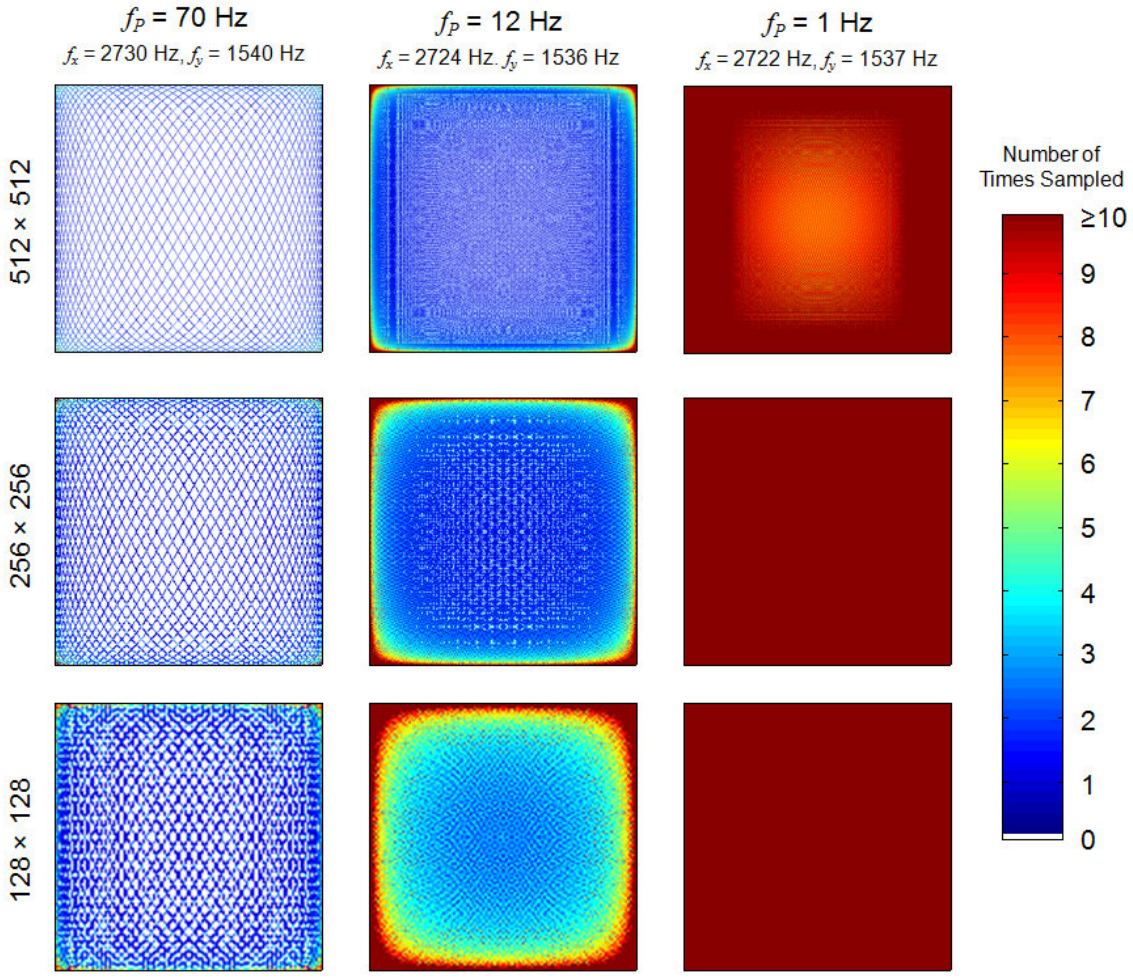

Figure 4.10. Conventional Lissajous reconstructions for various pattern repeat rates and pixel sizes. The color map represents the number of times a given pixel is sampled before one cycle of the Lissajous pattern completes. For the conventional case where $f_F = f_P$, this represents the number of times a pixel is sampled in each frame. White pixels denote unsampled regions of the image.

Table 4.2. Pixel sampling data for single frames in a traditional Lissajous-scanned image.

Scanning Frequencies (f_x, f_y) (Hz)	Frame Rate ($f_F = f_P$) (Hz)	Image size (pixels)	Pixels Sampled (%)	Pixels Sampled more than 10 times in a frame (%)
1540, 2730	70	512 × 512	17.4	0.0
		256 × 256	32.7	0.1
		128 × 128	54.5	0.5
1536, 2724	12	512 × 512	70.9	1.3
		256 × 256	95.2	3.7
		128 × 128	100	12.2
1537, 2722	1	512 × 512	100.0	70.5
		256 × 256	100.0	100.0
		128 × 128	100.0	100.0

In Figure 4.10, pixels that do not get sampled by the Lissajous pattern are shown white. To reduce these unsampled pixels, higher line densities, and subsequently lower frame rates, can be used and/or the relative pixel size can be increased. In either solution, pixels toward the outside of the image can be heavily oversampled (e.g., sampled ten or more times) in each frame. Moderate resampling of pixels can be useful in reducing noise when intensity values from different cycles within the same frame are averaged, however significant resampling of pixels provides little new spatial information despite the increased laser exposure to these oversampled regions.

The selection of the image pixel size also introduces several constraints. As seen in Figure 4.10, image reconstruction with a fewer number of pixels can reduce the number of unsampled pixels to achieve a completely filled image. For a given FOV and resolution, however, there is a minimum number of pixels that can be used before the

image resolution becomes limited by the pixel size. Using the Nyquist criterion, we desire at least two pixels per resolvable spot in our image. Thus for an example case of a 200 µm × 200 µm FOV and a 1 µm resolution, this criteria requires the reconstructed image consist of no fewer than 400 × 400 pixels. However, in addition to increasing the likelihood of unsampled pixels, increasing the number of pixels used in image reconstruction also increases the required data acquisition rate to avoid missing pixels at the center of the image. Explicitly, the pixel scanning speed can be expressed by the first derivatives of Eqs. (4.5) and (4.6),

$$\dot{x}(t) = \pi f_x X\left[\cos\left(2\pi f_x t + \phi_x\right)\right] \tag{4.8}$$

and

$$\dot{y}(t) = \pi f_y Y\left[\cos\left(2\pi f_y t + \phi_y\right)\right]. \tag{4.9}$$

When both axes are traveling at their maximum velocity, which occurs at the center of the image, the maximum scanning speed, v_{max}, in pixels/second is given by

$$v_{\max} = \pi P\sqrt{f_x^2 + f_y^2}\,, \tag{4.10}$$

for a square image in which $X = Y = P$. In the example case where $P = 400$, $f_x \approx 1540$ Hz and $f_y \approx 2730$ Hz, $v_{max} = 3.94\times10^6$ pixels/second. Therefore the data acquisition rate must equal or exceed 3.94 MHz to avoid missing pixels in the center of the image and thus the image size introduces hardware constraints in addition to resolution constraints.

Lastly, when the FOV is large relative to the focused laser spot size, sparsely sampled, fast-repeating patterns such as the 70 Hz pattern of Figure 4.10 may lose image information as a result of gaps in the scanned pattern on the sample. In these cases, increasing the pixel size will still reduce the number of unsampled pixels but will not change the density of the scanning pattern on the sample and thus will not recover any information that was not swept by the laser beam. Thus care needs to be taken in selecting the Lissajous pattern to ensure that the scanning pattern is dense enough such that no features of the sample may be missed by the laser beam.

As illustrated in Figure 4.10, it is possible to completely fill images with large numbers of pixels by selecting driving frequencies corresponding to a slowly repeating Lissajous pattern. However, for application in a clinical imaging system, the slow frame rate and inefficient use of laser dosage associated with large oversampling are both undesirable. While the 12 Hz updating pattern with a 256 × 256 pixel image size appears to be a good compromise, approximately 5% of the pixels towards the center of the image remain unsampled and will be unsampled in every frame, resulting in a small loss of information. What we desire is to achieve full coverage of the FOV, such as found with the 1 Hz updating pattern, but with the ability to capture dynamic information at a faster rate and to use the laser exposure more efficiently.

4.3.2: Our improved fast-updating Lissajous image reconstruction method

To improve upon this traditional approach to Lissajous scanning for clinical imaging applications, we have developed a new fast-updating Lissajous image reconstruction algorithm that uses a slowly repeating Lissajous pattern but updates the image at a frame rate much faster than the pattern repeat rate. Here, we simply take advantage of the fact that a Lissajous scanning pattern repeatedly samples across the entire extent of the FOV while acquiring information for a given frame. Thus information about the entire FOV can be extracted from a partially scanned frame.

In this new method, the image reconstruction algorithm tracks the pixel location continuously over time, rather than refreshing at the end of each frame. The location for the first pixel of each frame is dictated by the Lissajous trajectory and pixel location at the end of the preceding frame. The frame rate, f_F, is then set independently of f_P to optimize single-frame detail and imaging speed ($f_F > f_P$). In this manner, the number of oversampled pixels in a single frame is greatly reduced and the frame rate is increased for increased temporal resolution. Figure 4.11 illustrates this method where a 1 Hz Lissajous pattern created using f_x = 1537 Hz and f_y = 2722 is segmented into 10 frames for each complete Lissajous pattern. The result is a series of 10 Hz frames with reduced

oversampling that can capture faster dynamic events and can also be combined into the original 1 Hz Lissajous-scanned image. In this example, the frame rate was chosen such that each frame samples more than 84% of pixels and the percent of pixels sampled ten times or more is kept below 6%.

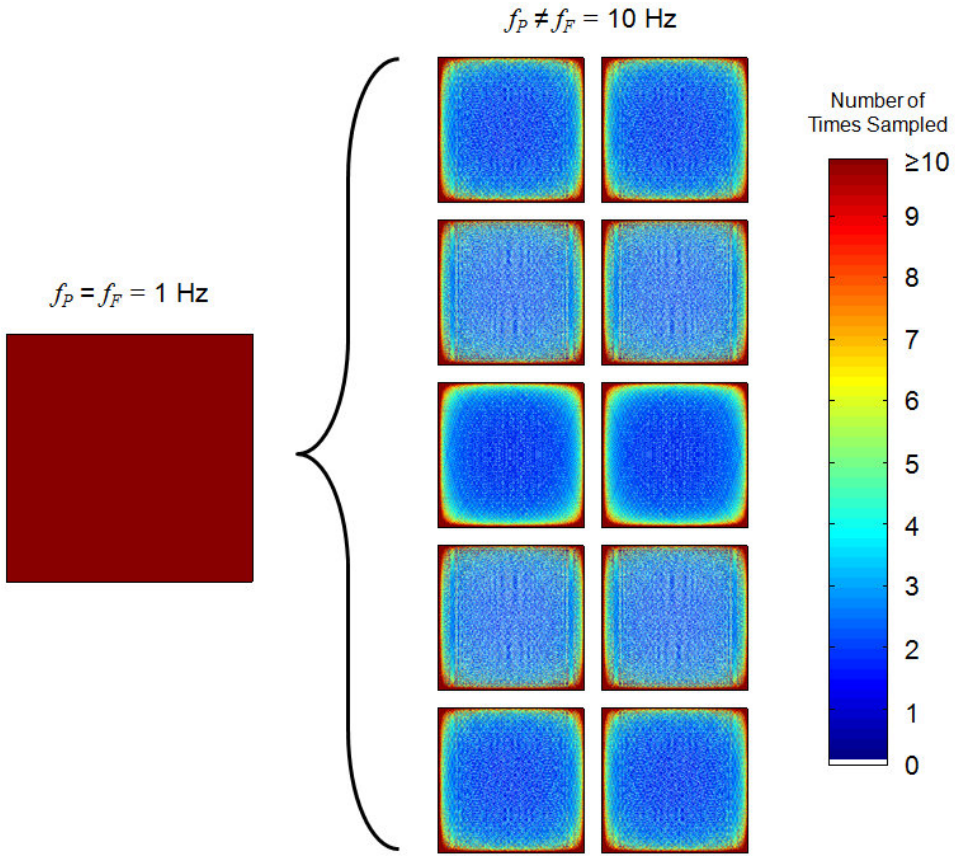

Figure 4.11. Illustrative representation of our fast-updating Lissajous image reconstruction method. The color map represents the number of times a given pixel was sampled before one cycle of the Lissajous pattern completed. In our method, a scanning pattern that would normally create the slowly updating (1 Hz) and oversampled image on the left is segmented into ten frames displayed at 10 Hz. The resulting 10 Hz images can capture faster events without motion artifacts and reduce oversampling to more efficiently use laser exposure.

Though each frame now contains more unsampled pixels than the corresponding image formed when $f_F = f_P$, the scanned pattern is changing between each subsequent frame, which means that unsampled pixels in one frame can be sampled in the following frame. Furthermore, due to the increased frame rate, the overall sampled pixel density can appear higher as the frame rate approaches the flicker fusion threshold of the human visual response [168].

Critically, *no information is lost from the traditional slower-displaying Lissajous image*. The information is simply separated and displayed into shorter time intervals to capture additional dynamic information. Thus, both the fast-updating, lower-pixel density image of our new algorithm and the slower, high pixel density image of the traditional algorithm can be viewed side-by-side during real-time image reconstruction.

4.3.3: Experimental implementation

To drive the scanning mirrors and handle image reconstruction, we developed a LabView program. This program generates driving signals for the MEMS scanning mirror and implements our fast-updating Lissajous image reconstruction algorithm to display the collected image data. Figure 4.12 provides a flow chart representing the basic program algorithm. The program generates two sinusoidal voltage waveforms using the driving frequency and driving voltage parameters given for each axis. Both *x*-axis and *y*-axis waveforms are then duplicated and the duplicated copies are phase-shifted 180º. The waveforms are then delivered out to the high-voltage amplifier through the analog voltage outputs of the PCI-6115 and PCI-6711 data acquisition cards. The clocks of the two data acquisition cards are locked over a Real-Time System Integration (RTSI) bus.

The voltage waveforms are also converted to pixel coordinates and used to map the incoming data to locations in the current frame. The amount of data to map into a given frame before moving to the following frame is determined by the frame rate. For driving the MEMS mirror in the 18-mm probe, we drive the mirror at f_x = 1537 Hz and f_y = 2722 Hz, and reconstruct and display each frame at a frame rate of 10 Hz. We selected

an image size of 256 × 256 pixels, in which over 90% of pixels in are sampled in each frame. The pre-amplifier used in our system limited acquisition speed to 1 MHz, resulting in some loss of pixels in the center of each frame. Because the exact locations of these pixels varied from frame to frame, however, their loss is mitigated when multiple frames are averaged.

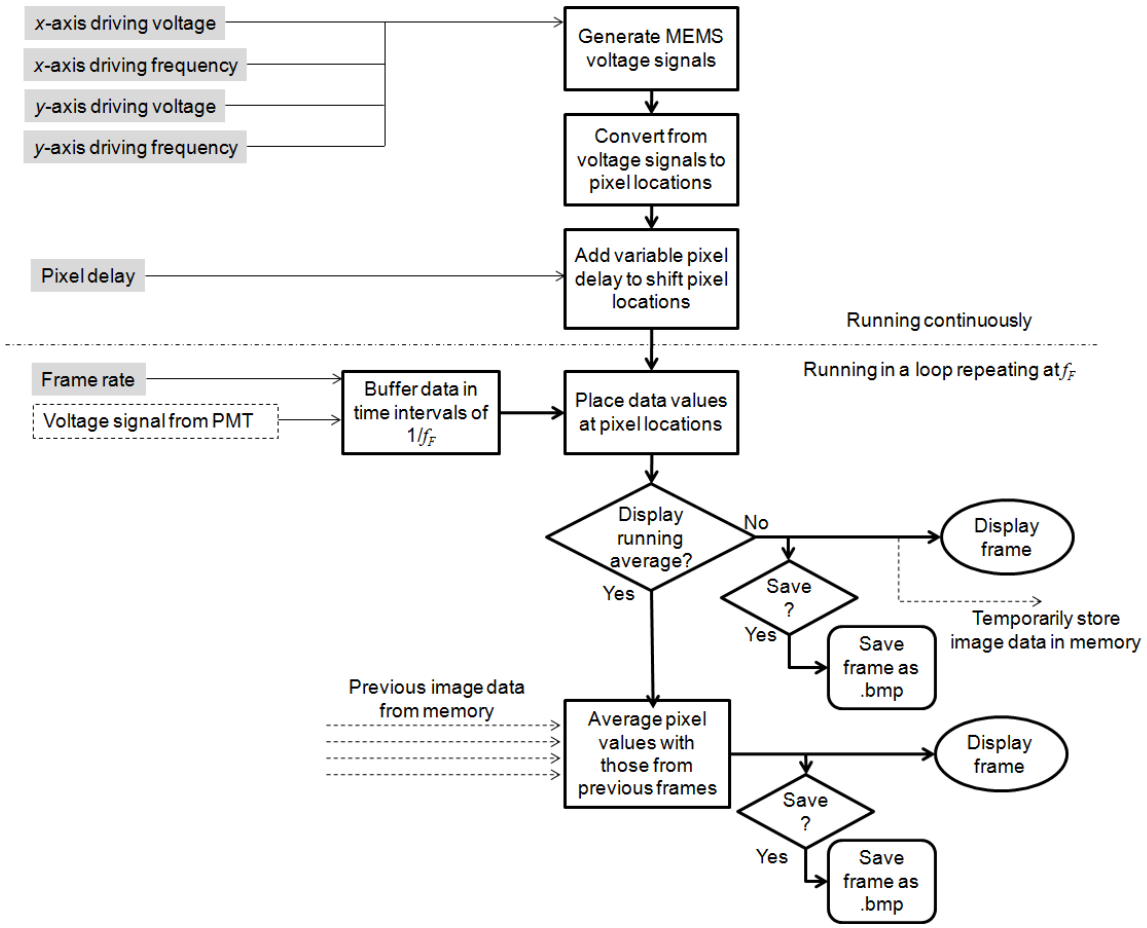

Figure 4.12. Flow chart illustrating our fast-updating Lissajous image reconstruction algorithm. User inputs are shaded gray and located on the left. User-selectable options are denoted by diamond process blocks. The MEMS driving signal and the data collection are synchronized by triggering from the same master clock in the software and by linking the data acquisition cards physically with a RTSI cable.

A real-time user-controlled pixel delay is used to shift the pixels along the Lissajous trajectory in order to compensate for the cumulative phase lag between the mirror driving signal and the true pixel location of the acquired data. An incorrect pixel shift leads to the formation of four ghost images of each object. The correct phase delay is then achieved by increasing the pixel offset until the ghost images merge into a single true image of the object. Using a real-time and variable phase shift compensation scheme, such as this pixel delay control, carries several advantages over using fixed phase delays generated from prior measurements of the MEMS mirror. While position sensitive detectors can be used to track the deflected laser beam and determine the phase delay between the position and the driving signal, this measurement would have to be investigated for each desired pair of driving voltages (i.e., each magnification). Additionally, we have found that the phase delay and deflection of the MEMS mirror inner axis is weakly dependent on the laser power incident on the mirror. We believe this dependence arises due to charge build-up and dissipation on the bare silicon mirror surface from the photoelectric effect. Due to this dependence, the phase delay would also have to be measured at each anticipated laser power. In contrast, the variable delay control in our program allows for real-time adjustments as necessary. Note that once the correct delay had been identified, it was found to be stable for all durations observed.

When a pixel location is repeatedly sampled during the construction of a frame, the program assigns the most recently sampled pixel value to that location, rather than averaging with the previous value. While averaging is preferred to help reduce noise in individual frames, pixel averaging at such a high data acquisition and display rate was found to be too computationally intensive to implement. This fact further underscores the utility of our image reconstruction methodology. In conventional reconstruction, where dense patterns are generally heavily oversampled the inability to average repeatedly sampled pixels during reconstruction would mean that the noise level would not be improved despite the inefficient resampling of every pixel. Thus the laser exposure is much more efficiently used when the data can be displayed rather than overwritten.

For greater image detail, we have also implemented a user-selectable “moving average” mode. When activated, the displayed image is averaged with the five preceding images to suppress noise and provide greater image detail. The image still updates at the specified frame rate, in this case 10 Hz, however the use of averaging begins to introduce mild motion artifacts for moving samples. This “moving average” image serves as a compromise between the high-speed dynamic information of the fast-updating image and the high detail of the traditional Lissajous image. Figure 4.13 shows two-photon fluorescence images taken with the 18-mm probe with and without the “moving average” mode, as well as after image post-processing. During post-processing, many frames could be averaged together to further reduce noise. Also, any isolated pixels that remained unsampled due to the 1 MHz sampling rate or any pixel noise can be easily filtered out using a Fourier-domain low-pass spatial filter.

Note in Figure 13 that the image illumination is fairly uniform across the FOV, rather than increasing at the edges where the laser dwell time is longer. This uniformity is inherent in this method of Lissajous image reconstruction, where the sampling rate is held constant. Because of the constant sampling rate, 1 MHz in the case of the 18-mm probe, and the constant laser repetition rate of 80 MHz, each pixel represents an integration of the signal that arises from 80 pulses, leading to a uniform displayed intensity.

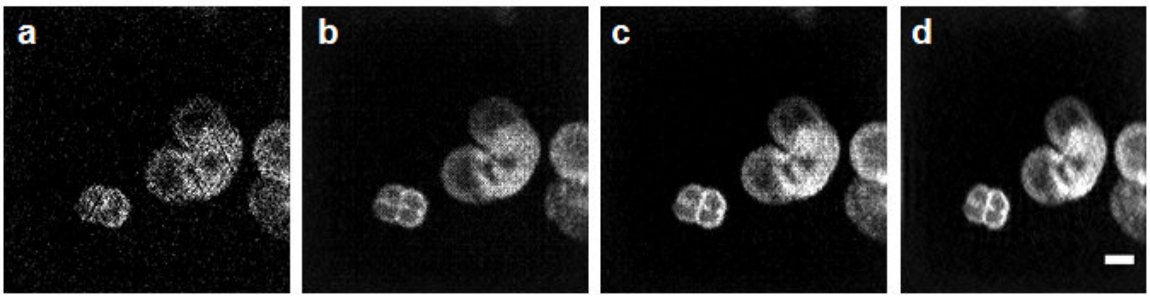

Figure 4.13. The imaging modes of the image-guided microsurgery probe software using our fast-updating Lissajous reconstruction algorithm. a An example of an unprocessed image frame of pollen grains taken with the 18-mm probe. **b** A running average mode is also available, in which the current frame is averaged with the 5 previous frames to provide greater detail. Though still updating at 10 Hz, this frame contains information from the previous 0.5 s. **c** Averaging of 10 raw frames (1 s average) conducted during post-processing. **d** Sub-resolution noise and zero-intensity pixels can be filtered out in post-processing as well, along with calibration of the pixel dimensions. Scale bar is 20 µm.

4.4: NONLINEAR IMAGING CHARACTERIZATION AND VALIDATION

To characterize the imaging performance of the 18-mm probe, we first measured the resolution and maximum field of view, followed by imaging of pollen grains for qualitative comparison with other devices.

The resolution of the prototype can be characterized by its point spread function (PSF). The PSF is essentially the impulse response of an imaging system, or put another way: the image formed from a point source object. For laser scanning optical microscopy systems, the PSF is equivalent to the focused laser spot that is scanned across the sample. This laser spot serves as the impulse response with which the sample is convolved. The PSF, and thus the focal spot size and shape, can be practically measured by imaging particles that are significantly smaller than the focal spot being measured.

To measure the 3D two-photon PSF of the probe, we imaged 100 nm fluorescent beads (F-8803, Invitrogen) suspended in an agar gel across a 40 × 40 × 100 μm^3 FOV. This agar-bead phantom consists of 10 µL of the stock bead solution (2% solids)

dispersed in 2 mL of 4% agar in water, which is then allowed to gel. During imaging, we acquired 50 frames at each of a series of planes along the optical axis, with 3.3 µm axial separation between planes. The axial movement was achieved by translating the sample using the piezoelectric stages. The images at each *z* location were averaged during post-processing to reduce noise. Lateral PSF measurements were taken by measuring the vertical and horizontal line profiles through the center of each bead at their respective focal planes, and fitting a Gaussian peak function to each profile. Axial PSF measurements were taken by measuring the maximum intensity of each bead at each imaging plane, and fitting a Gaussian peak function to the data for each bead.

To characterize the resolution, we measured the FWHM of the PSF, which corresponds to the Rayleigh resolution criterion. The FWHM of the Gaussian fits to the bead images (Figure 4.14) were 1.64±0.09 µm and 16.4±1.0 µm, for lateral and axial dimensions, respectively. The measurements were averaged across 10 beads and the reported errors correspond to the standard error of the mean. For comparison, the diffraction-limited FWHM values are 622 nm and 4.2 µm for lateral and axial resolution, respectively [165]. This resolution degradation relative to the diffraction limit has been previously attributed to spherical aberration from the GRIN objective lens and is similar in magnitude to what has been observed in other studies [128,130].

Epithelial cells form the most superficial layer of most body cavities and are thus likely targets for a femtosecond microsurgery endoscope. They can vary greatly in size but are frequently in the realm of 10 to 20 µm in diameter. Thus we see that the measured lateral resolution of this prototype is sufficient for visualization of sub-cellular structures. However the axial resolution reduces the optical sectioning capabilities and will degrade resolution in optically thick samples.

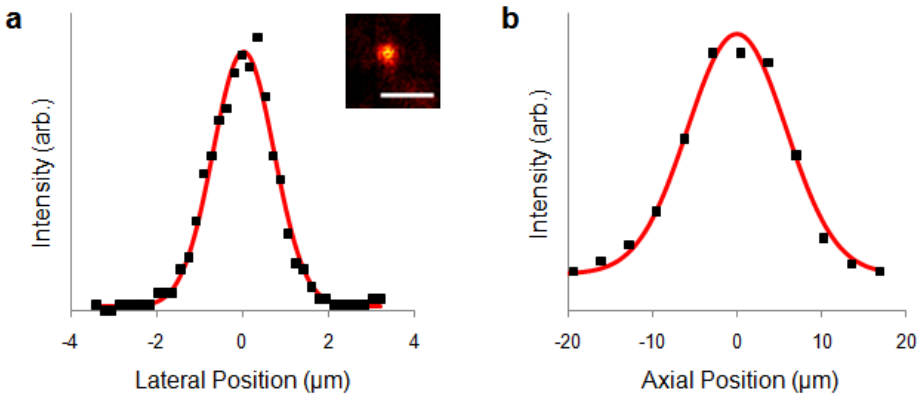

Figure 4.14. Example lateral and axial point spread function (PSF) measurements. a A representative PSF measurement showing the lateral resolution of the 18-mm probe. The inset image shows a single 100 nm bead used for PSF measurement, as imaged by the probe with 5 µm scale bar. **b** A representative axial PSF displaying the axial resolution. The raw data is shown in black and the Gaussian fit to the data is provided in red. The average FWHM of the lateral and axial PSFs are 1.64 µm and 16.4 µm, respectively.

The maximum extent and flatness of the FOV were investigated by imaging 1 µm fluorescent beads (F-8823, Invitrogen). Drying the beads onto a microscope slide provided a fairly uniform and flat sample. By translating the sample by known increments in the *x* and *y* directions using piezoelectric stages during imaging, we calibrated the image scale. Using peak driving voltage to the MEMS between 20 - 80 volts, the maximum extent of the FOV could be varied between 36 - 310 µm. The differences in voltage sensitivity between the mirror axes required unequal driving voltages for smaller FOVs. The maximum FOV is shown in Fig 4.15**a** wherein the image intensity appears constant over much of the field before rapidly decreasing at the edges.

The limiting aperture for the maximum FOV appeared to occur at the second relay lens in the beam path, where the beam is either clipped by the limit of the clear aperture or heavily degraded by off-axis aberrations at the extreme edge of the scan. When analyzed together, the maximum FOV of 310 µm and the lateral resolution of 1.64

µm yield an experimental number of resolvable spots of 189. The truncation of the maximum FOV and resolution degradation from aberrations both prevented the realization of the maximum theoretical *N* of ~330; however, this *N* value of 189 was still the second largest yet demonstrated for a fiber-coupled nonlinear imaging endoscope at the time of its publication [109], indicating the potential of this optical system. Since this time, two experimental *N* values as high as 700 (0.6 µm resolution, 420 µm FOV) have been reported using a fiber-scanner system with an aberration-corrected GRIN objective lens [139].

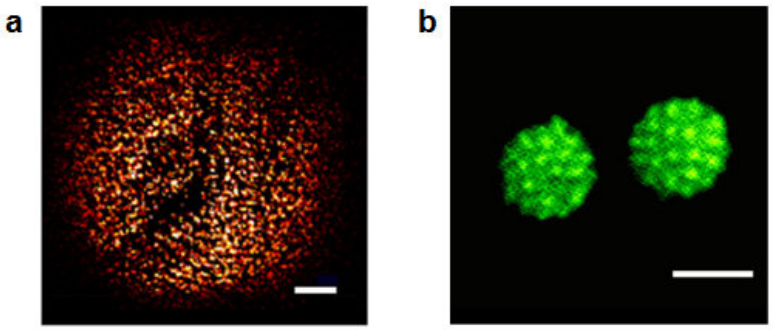

Figure 4.15. Two-photon fluorescence images used in characterization of the 18-mm probe. a An image of 1 µm fluorescent beads deposited on glass shows substantially uniform signal intensity, even at the maximum FOV, before dimming and ultimately truncating at a diameter of 310 µm. **b** The imaging resolution of the prototype is sufficient to detect the thin spike features covering the surface of these two pollen grains, however the clear resolution of each spike is somewhat degraded. The average powers at the sample were 8.2 mW for **a** and 9.0 mW for **b**. The displayed image in **a** is an average of 6 frames, corresponding to a 0.6 s acquisition time. The image in **b** is an average over 50 frames (5 seconds). Scale bars are 50 µm in **a** and 25 µm in **b**.

Lastly, we imaged a fixed sample of various pollen grains prepared on a microscope slide (30-4264, Carolina Biological Supply Co.) to demonstrate qualitative imaging capabilities. One of the pollen grain morphologies exhibits a spherical shell of thin protruding spikes, which provides an excellent challenge for imaging systems. As

seen in Figure 4.15**b**, the prototype microsurgery system is capable of resolving the spiky structure of the pollen grains, though clear resolution of the individual spikes remains a challenge. Imaging of the pollen grain required 9.0 mW of laser power at the sample. When compared with other published nonlinear imaging endoscopes that have imaged the same sample slide (see Table 2.3), our 18-mm probe required 3-4× less laser power to image, suggesting that the combined excitation and collection efficiency of our prototype exceeds that of these designs. Similarly, the 8.2 mW of laser power required to image the 1 µm beads is nearly a factor of 2× less than the other published study using a similar sample.

4.5: CELLULAR IMAGING AND ABLATION

The combined imaging and microsurgery capabilities of the probe were demonstrated using breast carcinoma cells grown in a single cell layer and labeled with the fluorescent cell viability dye, calcein AM. For these experiments, MDA-MB-468 breast carcinoma cells were cultured in complete L15 medium, then harvested via trypsinization and spun down at 200 g for 7 min before depositing them on a tissue culture dish in 2 mL Dulbecco's Phosphate Buffered Saline (DPBS). The cells were allowed to incubate for one hour at 37° C to begin adhering to the dish, at which point the DPBS was replaced with a solution of 14 µM calcein AM in fresh DPBS. Following further incubation for 30 min, the calcein solution was removed and replaced with fresh DPBS. Calcein AM is a cell-membrane permeable dye that indicates cell vitality when it is converted into fluorescent calcein by esterases found in living cells. Images obtained immediately after uptake and activation of the calcein, showed a uniform fluorescence in living cells.

During these experiments, the cells were imaged before and immediately following ablation. For microsurgery, the flipping mirror that directs the imaging beam was lowered to direct the microsurgery beam into the fiber while the imaging laser was blocked. The MEMS mirror was static and undeflected during microsurgery, thus

targeting the center of the FOV. By bringing the microsurgery beam collinearly with the imaging beam and triggering it through the imaging program, simultaneous imaging and microsurgery of off-axis targets is also possible with this system.

Figure 4.16 presents two-photon images of breast carcinoma cells before and after femtosecond laser microsurgery with a single pulse at 280 nJ pulse energy. Ablation of a targeted cell is evidenced by the loss of its fluorescence signal, where the abrupt signal loss suggests that the membrane of the targeted cell was ruptured, releasing all of the calcein dye. In this set of experiments, the pulse energy was increased incrementally from 160 nJ until loss of cellular fluorescence was observed at 280 nJ. Ablation using this energy level was found to be very repeatable. As only a single laser pulse was used in this experiment, we expect that the loss in fluorescence is due to ablation rather than photobleaching of the calcein inside the cell. Because the cells are much larger (~10-20 μm diameter) than the focal spot, longer exposures would be necessary to photobleach the total volume of the cell. Furthermore, the measured spot size from the PSF and the pulse duration measured after the fiber indicate that the peak irradiance at the focus exceeded 14 TW/cm^2 for a 280 nJ pulse, which is over 2× the predicted threshold for plasma-mediated ablation [17]. Additionally, increasing the brightness of the post-ablation imaging during post-processing revealed that some dimly fluorescent cell remnants are still present at the targeted cite (shown in the insets of Figure 4.16), which indicate that the cell was not merely knocked loose from the cell culture and ejected from the FOV. Note that the high precision of fs-laser ablation allowed disintegration of the target cell while adjacent cells remain intact.

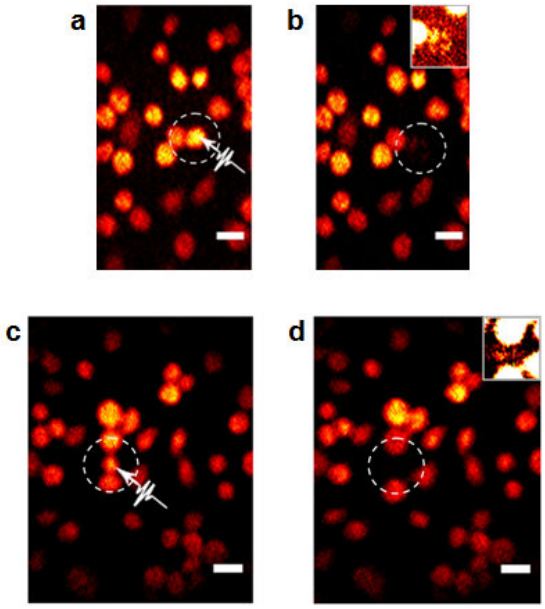

Figure 4.16. Combined two-photon microscopy and femtosecond laser microsurgery of a single layer of breast carcinoma cells. a, **c** Two photon images of a single layer of live breast carcinoma cells after uptake of calcein AM taken prior to irradiation with a high intensity microsurgery pulse. **b**, **d** The same FOVs as **a** and **c**, respectively, immediately after irradiation of a single cell with a single laser pulse at 280 nJ pulse energy. Average laser power used for imaging in both images was 10 mW. Both images were averaged over 5 seconds at 10 Hz frame rate and spatially filtered. Note that in both cases the targeted cell has lost fluorescence while the cell touching the targeted cell is left intact. Inset images in **b** and **d** show the targeted region with the image brightness greatly enhanced, showing remnants of the ablated cells. Scale bars are 20 μm.

We also investigated two-photon imaging and ablation of cells within a three-dimensional (3D) tissue phantom consisting of breast carcinoma cells embedded in a collagen matrix. This sample mimics tissue scattering properties and provides a means for testing sub-surface ablation.

For the phantom experiments, MDMBA468 breast carcinoma cells were cultured, harvested, and centrifuged as before, then resuspended in a solution of 14 μM calcein AM in DBPS. The cell suspension was then spun down again at 200 g for 7 min to

remove excess calcein AM and resuspended in a buffered solution of high concentration type I collagen (BD Biosciences). The collagen/cell mixture was pipetted into a 500 μm deep silicon isolator (Molecular Probes) and then incubated for 25 minutes to allow the solution to gel before imaging.

We imaged the carcinoma cell phantom with 17 mW average power measured at the sample while making axial steps of 6.6 μm by moving the sample on the piezoelectric stage. Figure 4.17 presents images where a cell approximately 125 μm deep was targeted for ablation. Here, 5000 pulses at 213 nJ per pulse were used as the scattering collagen media reduces the total energy reaching the focal plane. In this case, we again observed the immediate loss of cellular fluorescence after irradiation with the microsurgery laser while the cells closest to the target remain intact. Because the targeted cell is completely embedded in collagen, which restrains the motion of cells in 3D, these experiments provide further evidence that the immediate loss of fluorescence upon irradiation is due to ablation at the cell and not displacing the cell out of the FOV.

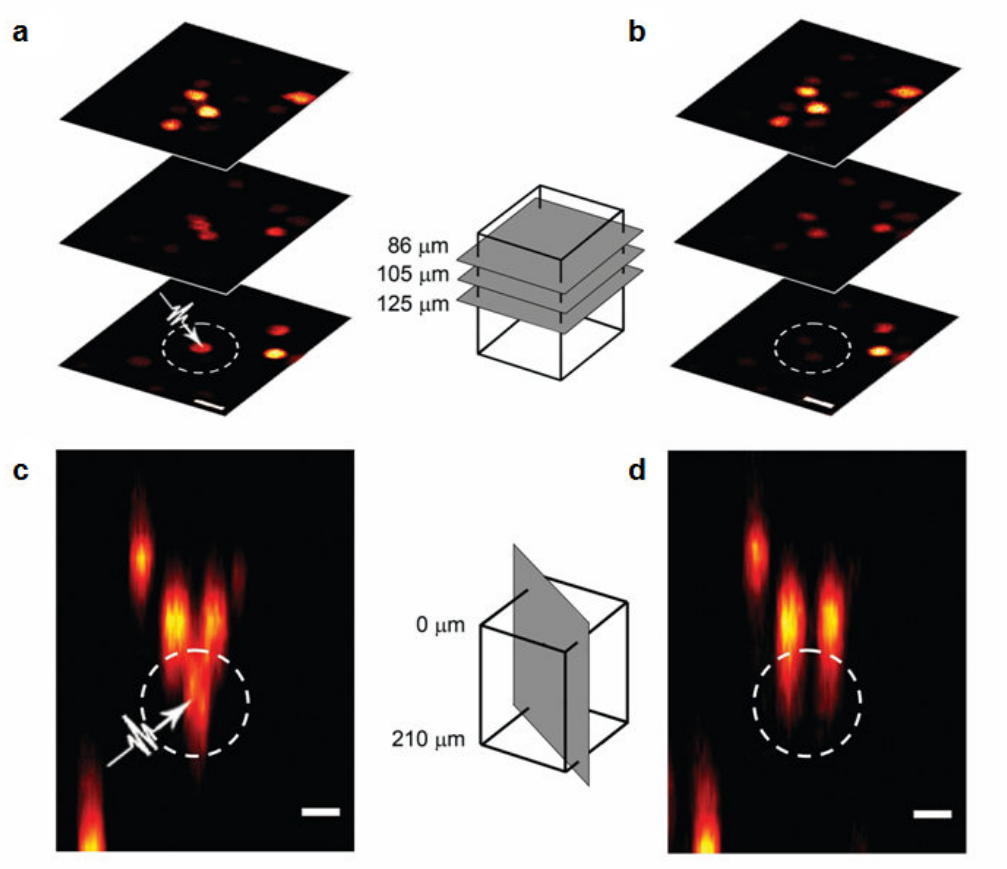

Figure 4.17. Combined two-photon microscopy and femtosecond laser microsurgery of breast carcinoma cells in a collagen tissue phantom. a Lateral slices with FOV of 116 × 160 µm^2 depicting a cell targeted for ablation as well as cells above it. The distance between the center of the targeted cell and those of the two cells above it is ~35 µm. **b** The same cells shown in **a** after irradiation of the targeted cell with 5000 pulses at 213 nJ pulse energy. **c, d** Vertical slice reconstruction through the same targeted cell and the cells above it before and after laser irradiation, respectively. Total imaging depth was 210 µm and the axial spacing between lateral slices was 6.6 µm. Scale bars are 20 µm.

In using lower pulse energies with many laser pulses, we take advantage of the widely known fact that the threshold for femtosecond laser ablation decreases as larger numbers of pulses are used as a result of an incubation effect. For example, when the number of pulses was increased from 1 to 1,000 for severing axons in the nematode *C.*

Elegans, Bourgeois and Ben-Yakar reduced the threshold from 9.6 TW/cm^2 to 1.8 TW/cm^2 [169]. Shen *et al*. [170] achieved ablation of individual mitochondria within cells with 1,000 pulses at 9.1 TW/cm^2, as estimated based on the reported NA of 1.4 and using $d = 0.925\lambda/NA$ [165]. Additionally, Tirlapur and König succeeded in optoporating cells using over one million pulses at 2.4 TW/cm^2 at an 80 MHz pulse repetition rate and NA of 1.3 [171]. For comparison, during ablation within the collagen tissue phantom, the 5000 pulses at 213 nJ correspond to ~11 TW/cm^2 per pulse. Given the scattering that occurs within the turbid tissue-like media of the phantom, the intensity used in this experiment compares well to the intensities used in other multiple-pulse experiments. In light of these results for both single- and multiple-pulse experiments, the observed cellular ablation threshold using the 18-mm prototype suggests that we were able to achieve femtosecond laser microsurgery with efficiency comparable to high-NA table-top systems.

The laser dosages used here for two-photon imaging are estimated to be at a safe level for cell vitality, which is crucial for sensitive clinical applications (see Table 4.3). Cell viability will depend on both the incident peak laser intensity and the number of pulses at this intensity that the cell receives. Thus for comparison, the number of overlapping consecutive pulses was estimated as well as the peak intensity. The number of overlapping pulses is defined here as the laser repetition rate divided by the product of the spot size and the scanning speed. For the 18-mm probe, the slow axis MEMS scanning frequency and the ~116 µm FOV of this experiment were used to arrive at a conservative estimate of scanning speed. Looking at peak intensity, the maximum average power used during cell imaging (17 mW used for imaging in the tissue phantom) corresponds to a peak intensity at the sample of ~13 GW/cm^2, which is below the maximum peak intensities found to be safe for long term two-photon imaging in recent studies [172-175]. In addition, the fast scanning speed used in the probe results in far fewer consecutive pulses delivered per spot at this intensity, which further reduces the

overall laser dosage to the sample when imaging with the probe. The favorable comparison shown in Table 4.3 suggests that the combined excitation and collection efficiency of the probe is sufficiently high to enable safe cellular two-photon imaging using conventional fluorophores.

Table 4.3. Comparison of imaging conditions proven not to affect cell viability to imaging conditions used in this study using the 18-mm probe.

	Other studies presenting threshold imaging conditions that do not impair normal cell function				
	König *et al.* [172], 1997	König *et al.* [173], 1999	Koester *et al.* [174], 1999	Hopt and Neher [175], 2001	This study
Peak Intensity [GW/cm^2]	34	61	78	27	13
Number of overlapping pulses while scanning	53,000	8,500	15,000	2,800	850

4.6: SUMMARY OF 18-MM PROBE VALIDATION

Using this initial prototype, we successfully demonstrated the potential for creating a fiber-coupled miniaturized probe that is capable of both nonlinear optical imaging and femtosecond laser microsurgery. Self-phase modulation and GVD were successfully managed to enable delivery of both amplified and unamplified femtosecond laser pulses over one meter of a single fiber, with peak laser intensities at the sample sufficient for both two-photon microscopy and optical breakdown. In addition to demonstrating the first fiber-coupled femtosecond laser microsurgery, the prototype provided nonlinear image guidance that equal or exceeding the state of the art in the experimental number of resolvable spots and combined excitation and collection efficiency.

There are several aspects of the prototype that require further development before a clinical femtosecond laser microsurgery probe can be realized. Foremost, to enable

endoscopic use, the overall device dimensions must be reduced without significantly compromising the optical performance. Also critical, the packaging of the system must incorporate the delivery fiber and collimating lens to enable truly flexibly decoupling the probe from the optical bench. To demonstrate clinical feasibility, a means of ablating large regions of cells over a short period of time should be demonstrated along with successful imaging of biological tissues. The ability to deliver even greater pulse energies to the sample would also help extend the clinical microsurgery potential, while an increase in deliverable power could potentially enable imaging of intrinsic fluorophores. The elongated axial resolution of the current prototype also needs to be addressed. Because the axial resolution is currently larger than most single cells, the optical sectioning abilities in tissue will be greatly degraded unless the axial resolution can be improved.

To address these issues, we developed an improved second-generation prototype based on the design of this 18-mm probe. The following chapters will first cover the in-depth design of the revised probe, followed by the characterization and demonstration of the imaging and ablation capabilities of this new system.

Chapter 5: Design of a Revised 9.6-mm Diameter Image-Guided Microsurgery Endoscope

The successful demonstration of imaging and microsurgery with our 18-mm probe is highly encouraging and illustrates the potential for a clinical femtosecond laser surgery endoscope. We now wish to refine the design of the 18-mm probe further towards a clinical practical tool through the development of a smaller second probe. As previously discussed, the general goals of this second-generation prototype are to reduce the packaged size, extend the microsurgery capabilities to enable ablation in tissue as well as rapid ablation of larger areas, and finally to enable imaging of intrinsic sources of nonlinear imaging signal. The new probe will utilize the same optical layout as the initial device so as to leverage our experiences from the 18-mm probe and to discover the limitations of this design.

This chapter will cover the design process for the second-generation prototype. We begin with the characterization and packaging solutions for the PBF and MEMS mirror, followed by investigation of miniature objective lens alternatives and the design and modeling of the remaining optical system. The chapter will conclude with the packaging design, followed by alignment and construction.

5.1: PHOTONIC BANDGAP FIBER CHARACTERIZATION AND PACKAGING

One of the goals of this new probe is to increase the maximum deliverable microsurgery pulse energy and the average laser power for imaging at the sample. One means to address this goal is to maximize the output through the PBF. During the development of the 18-mm probe, we found the microsurgery pulse energy to be limited by damage to the fiber tip during coupling, while imaging power was limited by the maximum output power of the Ti:sapphire oscillator combined with the coupling and attenuation losses. For the microsurgery laser, pre-chirping of the pulse increased the

damage threshold and thus the maximum deliverable microsurgery energy, and even higher pulse energies should be deliverable by pre-chirping the pulse to even longer pulse durations. Greater stretching of the pulse requires longer lengths of fiber to restore a femtosecond-scale pulse duration and the use of longer fiber will introduce even greater attenuation losses to the imaging laser. Thus the selection of the PBF length must be optimized to balance the deliverable laser energy of each laser system.

Figure 5.1 presents the estimated maximum microsurgery pulse energy and maximum imaging average power for increasing PBF lengths. In this estimation, we assumed an attenuation of 0.3 dB/m and a coupling efficiency of 65% using the fiber characterization results from Chapter 4, Section 4.1. To model the increase in deliverable pulse energy due to pre-chirping the pulse to longer pulse duration, τ, we interpolated the damage threshold measurements for fused silica made by Stuart *et al*. [22]. To summarize these measurements, Stuart *et al*. found the damage threshold of fused silica to scale with $\tau^{0.5}$ down to approximately 10 picosecond, below which the dependence becomes progressively weaker [22].

The model uses the observed damage threshold for one meter of PBF (1.3 µJ pulse energy) and the data of Stuart *et al*. to scale this threshold for longer pulses. If laser pulses with a larger spectral bandwidth were used, they would require larger pre-chirping prior to fiber delivery in order to compensate for the increased dispersion they would experience over a given length of fiber. The increased pulse duration would correspondingly increase the damage threshold at the fiber, and thus how much energy could be coupled into the fiber. Therefore, using a microsurgery laser source with a larger bandwidth provides another means for increasing the deliverable microsurgery energy. Larger spectral bandwidth would also result in a shorter pulse duration at the fiber exit when GDD is properly compensated for, thus increased care should be taken in this case to avoid unwanted nonlinear effects (such as SPM and self-focusing) and damage to optics.

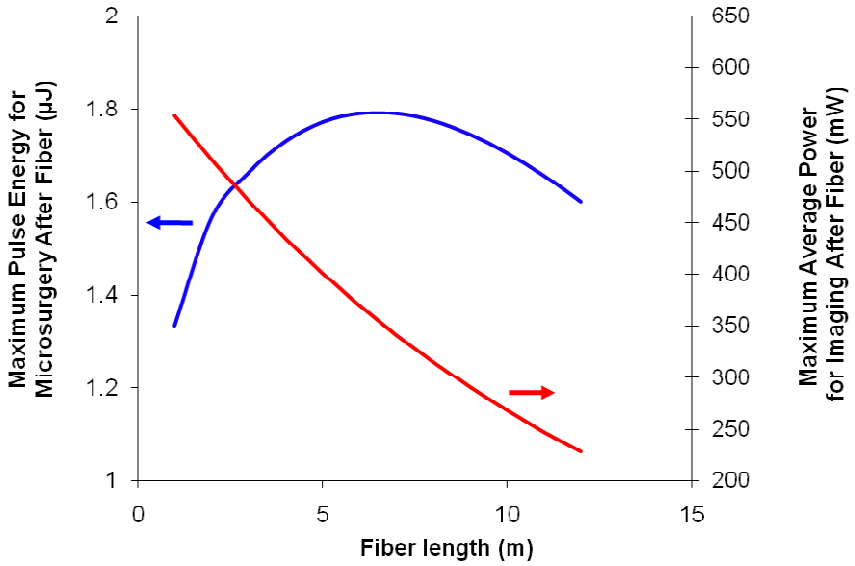

Figure 5.1. Estimated maximum deliverable microsurgery pulse energy and imaging laser average power for increasing lengths of photonic bandgap fiber. The data in blue represents the predicted maximum microsurgery pulse energy that can be delivered through the fiber with the current coupling optics. Data in red represents the maximum average laser power that can be delivered through the fiber for imaging is shown in red. The reflectivity of the MEMS mirror (30%) and any insertion losses from the remaining optics will reduce the transmission of both lasers through the probe to the sample. The curves shown reflect the 8 nm spectral bandwidth of the amplified pulses from the CPA, centered at 780 nm wavelength.

Increasing the wavelength of the surgery laser can also produce increased dispersion in this fiber, leading to greater pre-chirping and ultimately higher deliverable pulse energies. However, a shift to longer wavelengths will only be able to provide an incremental improvement using the air-core fiber in this study, as the fiber quickly becomes non-guiding above 800 nm.

Using the predictive model of Figure 5.1 to estimate the impact of fiber length, the maximum pulse energy that can be delivered through the PBF is approximately 1.8 µJ, achievable with a 6 meter fiber. Estimating 25% transmission through the probe due

to MEMS reflectivity and insertion losses from the remaining optics, the maximum deliverable pulse energy at the sample would be 460 nJ. To achieve higher pulse energy at the sample with our probe architecture, metallic coating of the MEMS mirror could triple the energy to ~1.4 µJ. An increase in fiber length also yields a decrease in available imaging power. At 6 meters, the maximum average power for imaging after the fiber would be reduced to 350 mW, yielding ~85 mW at the sample assuming the same 25% transmission.

To balance this trade-off, we have selected a PBF length of 3 meters. At this length, the maximum microsurgery pulse energy through the fiber should increase by 24% to approximately 1.7 µJ, (~420 nJ at the sample) while average power from the oscillator will drop only 13% to approximately 450 mW (~105 mW at the sample). This length was chosen to aid ablation inside more turbid samples and at greater depths without requiring large numbers of pulses, while maintaining nearly all of the imaging power to aid deep imaging and possibly enable visualization intrinsic fluorophores.

We measured the pulse widths before and after propagation through three meters of PBF using the same autocorrelation method described in Chapter 4, Section 4.1. Using the tunable Ti:sapphire oscillator at the minimum dispersion wavelength of 753 nm, we measured an output pulse duration of 280 fs, shown in Figure 5.2. Though the pulse was stretched to 2.3× the input pulse duration of 120 fs, this amount of dispersion is still less than is commonly experienced in many high-NA objective lenses and was thus deemed acceptable [176].

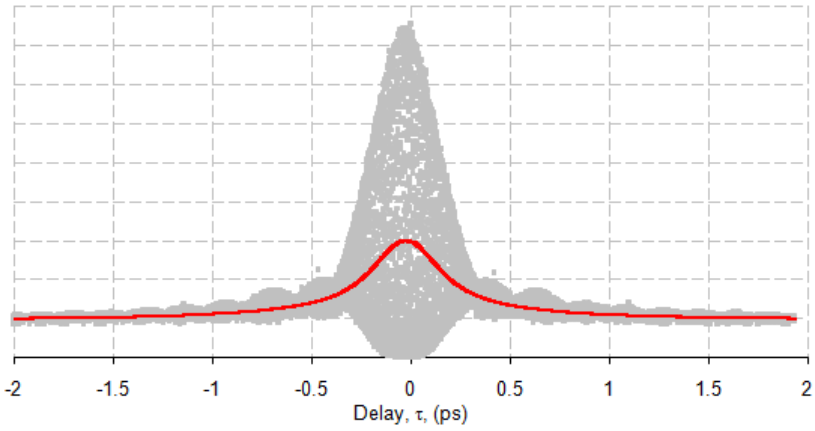

Figure 5.2. Autocorrelation trace at 753 nm center wavelength after propagation through three meters of PBF. An interferometric autocorrelation trace (grey) and the running average (red) for a 753 nm wavelength pulse of 280 fs duration FWHM, after propagating through three meters of PBF, for a 120 fs input pulse.

Increasing the fiber length from one to three meters triples the amount of GDD introduced to the microsurgery pulse and therefore requires pre-chirping the pulse to approximately 11 ps. The compressor stage of the CPA could not be easily adjusted to provide this much positive dispersion, so we constructed a dedicated pulse stretching system based on a single reflective grating first suggested by Martinez [177], shown in Figure 5.3. For this configuration, the GDD introduced to the pulse is [177]

$$\mathrm{GDD} = \frac{\lambda^2}{2\pi c}\frac{4\lambda}{cs^2\cos^2\theta_0}(f - z), \tag{5.1}$$

where $1/s$ is the groove spacing of the grating, θ_0 is the emerging angle of the beam off the grating, f is the focal length of the lens, and z is the separation between the grating and the lens, which can be varied. Detailed derivation of the pulse stretching design equations can be found in Martinez [177]. For our configuration, with a grating groove spacing of 1480 lines/mm, a lens focal length of 200 mm, and an emerging angle of ~35º, the GDD imparted to the laser pulse is 73,600 $\mathrm{fs}^2/\mathrm{cm} \times (f - z)$. Thus for the predicted

GDD of the fiber of 126,000 fs^2/m, three meters of fiber can be easily accommodated by setting *z* to approximately 183 mm.

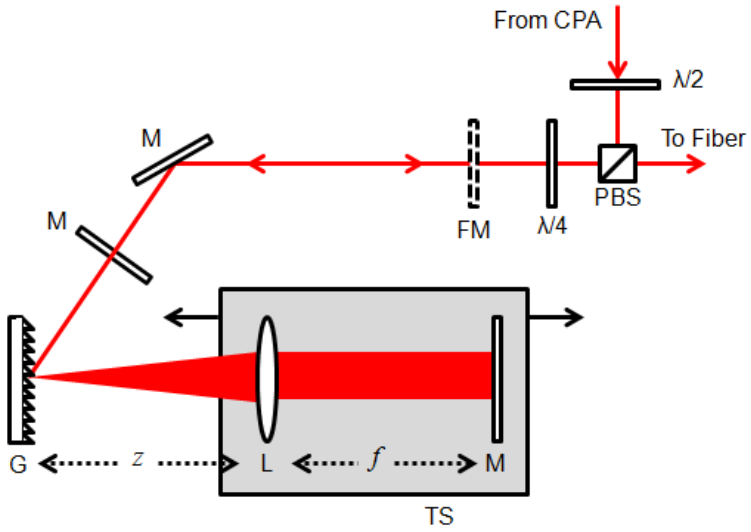

Figure 5.3. Top-down schematic of the single-grating pulse stretcher. **λ/2**: half wave plate; **PBS**: polarizing beam splitter; **λ/4**: quarter wave plate; **FM**: flipping mirror; **M**: mirror; **G**: gold reflection grating, 1480 lines/mm; **L**: 200-mm focal length lens; **TS**: linear translation stage. The lens provides a vertical displacement (out-of-plane in this diagram) in addition to collimating the diffracting beam. The translation stage provides control over the grating-lens separation, *z*.

Using this system with pulses from the CPA, a minimum pulse duration of 165 fs was measured after three meters of PBF for an input pulse duration of 11.5 ps. The corresponding autocorrelation traces are provided in Figure 5.4. With the 11.5 ps pulse, the maximum pulse energy that could be delivered to the output of three meters of PBF without damaging the proximal end of the fiber was found to be 1.6 µJ. This represents a 20% increase in deliverable energy compared to the 1.3 µJ that could be delivered through the one meter fiber used in the 18-mm probe.

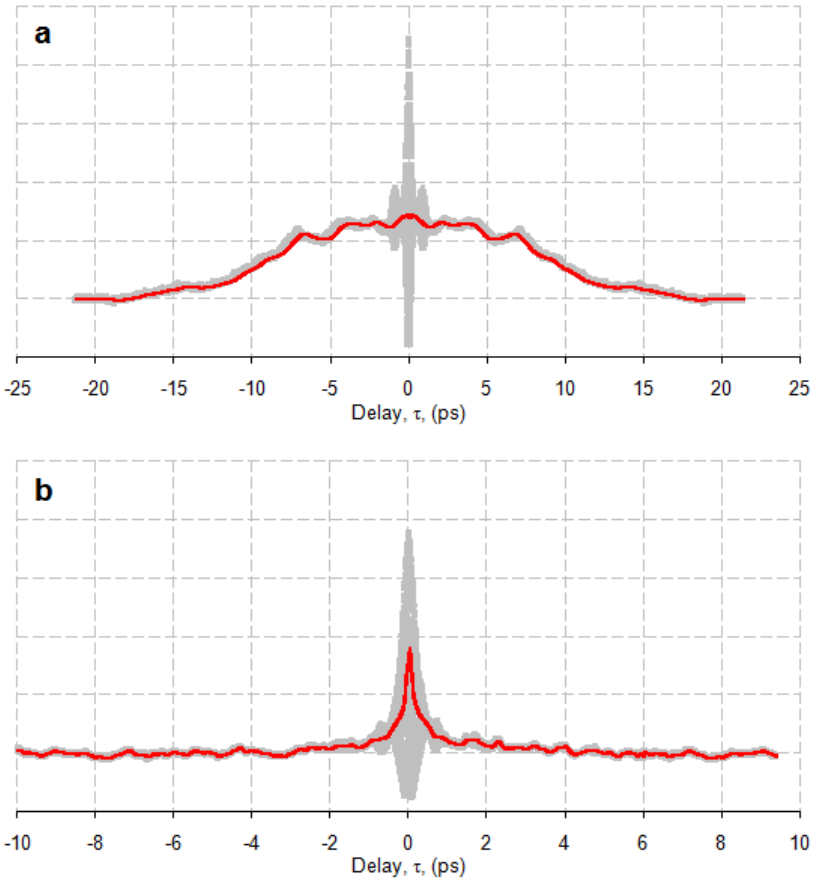

Figure 5.4. Autocorrelation traces before and after three meters of PBF using optimally pre-chirped pulses at 780 nm. a An interferometric autocorrelation trace (grey) and the running average (red) of a 780 nm wavelength pulse from the CPA, after pre-chirping to a pulse duration of 11.5 ps. **b** The corresponding trace for a pre-chirped 780 nm pulse after propagating through three meters of PBF. Here the pulse duration has compressed considerably down to 165 fs. Note change in scale between **a** and **b**.

Another design goal for the second probe is the shrinking and streamlining of the entire endoscopic system. For the PBF, this shrinking requires incorporating the collimating lens and the distal end of the PBF into the endoscope housing while minimizing the size of the collimation assembly. For this purpose, we have chosen a custom GRIN lens assembly (GRINTECH) which incorporates a 0.50 mm outer diameter

GRIN lens with a 0.5 mm right angle prism. The GRIN lens is designed to collimate the laser beam to a $1/e^2$ diameter of 425 µm with a working distance of 100 µm, while the prism reflects the beam by 90º through total internal reflection (TIR). This assembly provides a 15% increase in beam size relative to the 18-mm probe. An increase in beam diameter was shown in Chapter 3, Section 3.2 to increase the maximum number of resolvable spots while the 70% reduction in lens diameter aids the further miniaturization of the probe. The use of a right angle prism at the collimator output also enables packaging of the collimation assembly parallel to the axis of the endoscope with the fiber trailing behind to streamline the packaging, rather than orienting the fiber at a 90º angle as in the 18-mm probe.

To fix the lens-prism assembly to the distal end of the PBF, we have chosen to use a commercially available glass ferrule (Accu-Glass) to hold the PBF and a stainless steel tube to fix the lens-prism assembly to the ferrule. The ferrule is designed for mounting of single mode fiber and possesses an outer diameter of 1.0 mm with a 0.129 mm bore. The steel tubing has an inner diameter of 0.5 mm to match the outer diameter of the lens-prism assembly and an outer diameter of 1.0 mm to match that of the ferrule. After proper alignment, which will be discussed later, an ultraviolet light (UV)-curing epoxy can be used to bond the components together. The full assembly, illustrated in Figure 5.5, has an outer diameter of only 1 mm and a rigid length of 21 mm.

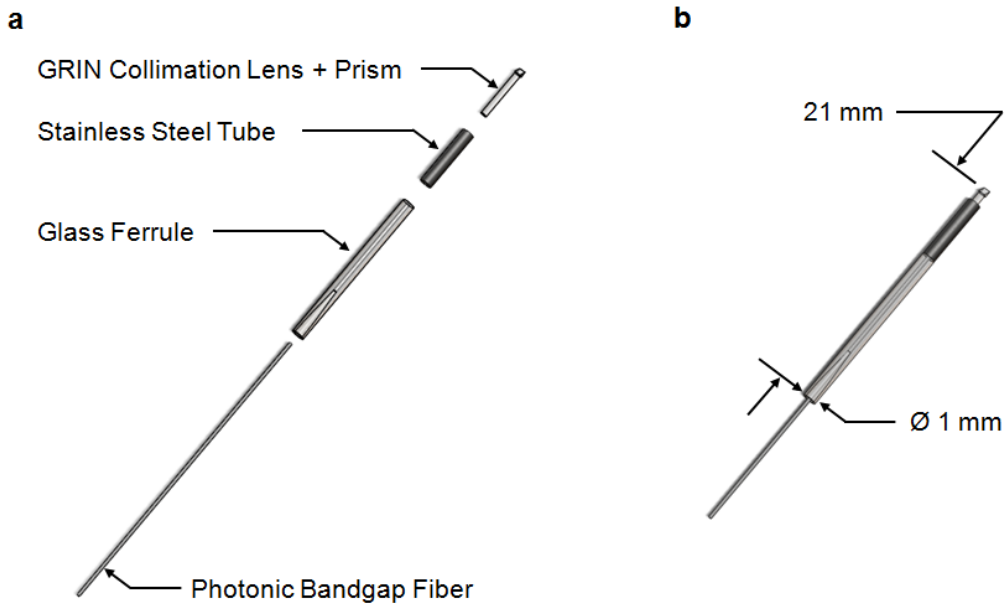

Figure 5.5. Illustration of photonic bandgap fiber collimation assembly. a An exploded view showing the individual elements of the collimation assembly designed for the second-generation microsurgery endoscope. **b** As designed, the completed collimation assembly has a diameter of 1 mm and produces a collimated beam with a 425 µm $1/e^2$ diameter. When assembled, the PBF protrudes into the stainless steel tube such that a 100 µm separation exists between the fiber tip and the GRIN lens.

5.2: MEMS SCANNING MIRROR CHARACTERIZATION AND PACKAGING

The MEMS scanning mirror provided for the second prototype is based on the same design used in the 18-mm probe. In this device, the mirror area is increased to 750 µm × 750 µm, while the total size of the MEMS chip is 3.0 mm × 3.2 mm. The mirror surface is bare silicon. Mirror deflection characterization was carried out following the protocol outlined in Chapter 4, Section 4.1, though this time care was taken not to exceed a peak dynamic driving voltage of 45 V because this device was reported to have a lower threshold for mechanical failure. The device did not display any measureable deflection under static voltage actuation, however dynamic actuation yielded resonant optical

deflections of ±7.1º and ±15.3º at resonant frequencies of 2.26 kHz and 0.98 kHz, for the inner and outer axes respectively. The bandwidth at FWHM of the inner and outer axes resonant deflection peaks are 100 Hz and 18 Hz, respectively.

In the 18-mm probe, the mounted MEMS mirror was the largest single element in the design. The leadless chip carrier used in the 18-mm probe, mounted at a 45º angle, occupied an area of 6.4 mm × 7 mm and thus limited the minimum size of the endoscope. To further miniaturize the endoscopic system for the second-generation prototype, a custom MEMS mount has been developed consisting of a 4.5 mm × 4.4 mm printed circuit board (PCB) with a total of five plated through-holes along two of the edges to provide wire-bonding contacts for the four voltage leads and the ground lead of the MEMS mirror. The through-holes allow the MEMS actuation wires to connect through the back of the PCB to help reduce the total packaged footprint. A photograph of the new PCB MEMS mount alongside the leadless chip carrier mount of the 18-mm probe is provided in Figure 5.6.

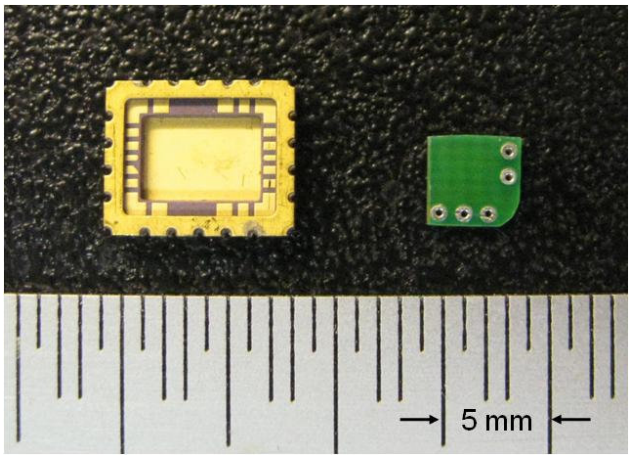

Figure 5.6 Photograph of MEMS scanning mirror mounts. The leadless chip carrier (left) that was used in the 18-mm probe. The large area of the chip carrier constituted a significant limitation to further miniaturization. For the second-generation prototype, a custom PCB (right) was designed to minimized the area required to mount the MEMS scanning mirror.

5.3: CHARACTERIZATION OF MINIATURE OBJECTIVE LENSES

The resolution of the 18-mm probe was not diffraction-limited and exhibited significant aberration. Since this aberration has been widely attributed to spherical aberration inherent to GRIN lenses, we wish to characterize a range of commercially available miniature lenses to determine the aberrations inherent to each lens. For this purpose, we have identified four lenses with diameters and numerical apertures suitable for use as a miniature objective lens at NIR wavelengths. The first lens (GT-LFRL-180-023-50, GRINTECH) is another GRIN lens with similar specifications to the previous objective lens. This lens utilizes a silver ion exchange to generate the radial refractive index gradient, rather than the thallium ion exchange used in the previous GRIN lens (manufactured by Nippon Sheet Glass (NSG)), and advertises improved aberration control. It should be noted that GRINTECH has recently offered a 0.65 NA compound GRIN lens with improved aberration correction that was not available at the time of testing [139]. The remaining three lenses (352150, 350140, and 372840; Lightpath

Technologies) are aspheric singlet lenses with numerical apertures ranging from 0.50 to 0.80. A summary of their relevant specifications is provided in Table 5.1.

Table 5.1. Comparison of commercially available lenses considered for use as the miniature objective lens.

	Numerical Aperture	Outer Diameter [mm]	Clear Aperture [mm]	Working Distance [mm]	Focal Length [mm]	Design Wavelength [nm]
Newport (NSG) LGI830-1[1]	0.46	1.8	1.26	0.21	1.38	830
GRINTECH GT-LFRL-180-023-50	0.49	1.8	1.62	0.23	1.78	810
Lightpath 352150	0.5	3.0	2.00	1.09	2.00	780
Lightpath 352140	0.55	2.4	1.60	0.88	1.45	780
Lightpath 370840	0.80	3.0	1.20	0.2	0.75	1550

NA: numerical aperture; OD: outer diameter; CA: clear aperture; WD: working distance; FL: focal length; λ_d: design wavelength. [1]The objective lens used in the original 18-mm probe is provided here for comparison.

To test the performance of these miniature lenses, we used a bench-top two-photon microscope. The experimental set up for this microscope is given in Figure 5.7. The laser oscillator, sample stage, and detection hardware are all identical to those used with the 18-mm probe, and further details of the microscope can be found in Durr *et al.* [123]. To test the imaging capabilities of each lens, an adapter was fabricated that allowed for mounting of each lens in place of the full-size objective lens. The PSF of each lens was then measured using a 100 nm bead-in-agar phantom following the protocols outlined in Chapter 4, Section 4.4. We ued the Ti:sapphire oscillator, tuned to a center wavelength of 753 nm, to match imaging conditions that are in the endoscope. Since the clear aperture dimensions of the lenses vary, the beam diameter at the back aperture was adjusted to approximately 4 mm ($1/e^2$). This ensured the truncation ratio for

each lens exceeded 2.0 and therefore each lens could be said to be equally overfilled [165]. The maximum scanning angle during imaging was held constant, except for the 0.80 NA lens where it was increased by 30%, to maintain a FOV between 25 µm and 50 µm for all lenses. This small FOV was desired so as to maintain a suitable number of pixels within each bead to provide a Gaussian fit. Point spread function measurements were taken from across the full FOV. No variations in PSF were identified over this fairly small FOV.

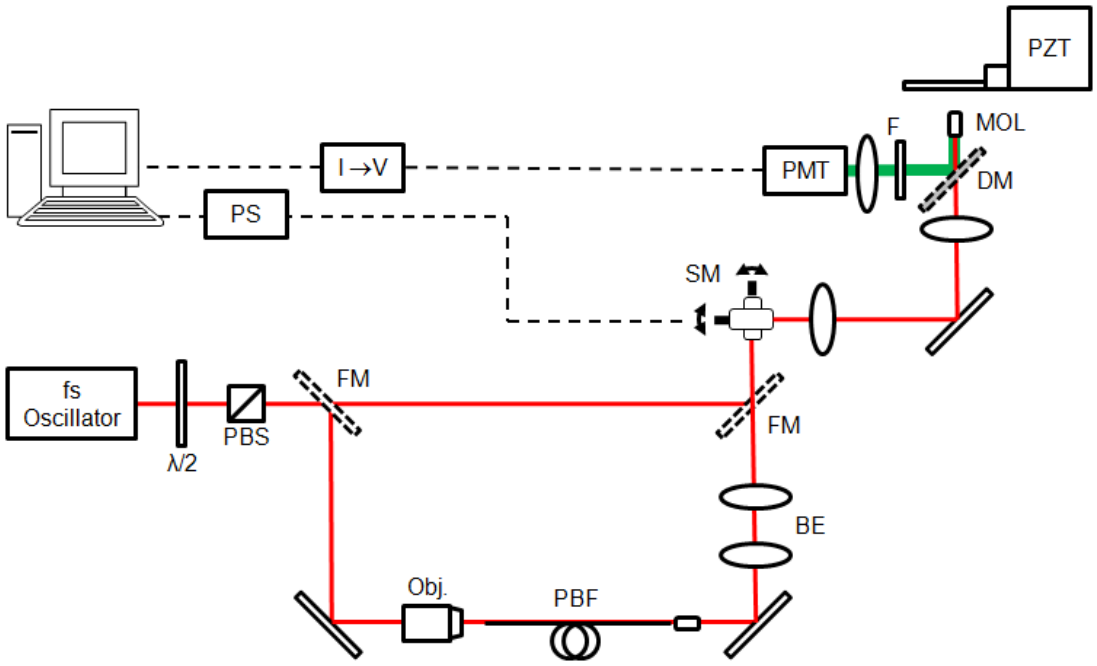

Figure 5.7. Experimental setup for measuring the PSF of miniature objective lenses. The system consists of a home-built inverted two-photon microscope in which a miniature lens is used in place of a traditional objective lens. Also, an optional beam path delivers the laser pulses through one meter of PBF. Care was taken to maintain a beam diameter at the back aperture of approximately 4 mm ($1/e^2$) for both optical paths. **λ/2**: half wave plate; **PBS**: polarizing beam splitter; **FM**: flipping mirror; **Obj**.: 0.25-NA objective lens; **PBF**: one meter of photonic bandgap fiber; **BE**: beam expander; **SM**: galvonemetric scanning mirrors; **DM**: dichroic mirror; **PZT**: piezoelectric translation stage; **MOL**: miniature objective lens; **F**: laser

blocking filter; **PMT**: photomultiplier tube; **I→V**: current-to-voltage preamplifier; **PS**: scanning mirror power supply.

The optimum beam quality in the endoscope is determined by the beam emerging from the PBF and collimating lens. Since GRIN lenses remain the optimum choice for achieving the smallest outer diameter of the fiber collimating assembly, we also repeated the PSF measurements using a beam delivered through one meter of PBF and collimated by the GRINTECH GRIN lens (GT-LFRL-180-023-50). The beam was again expanded to 4 mm to be consistent with the measurements made without the fiber.

In addition to the lenses being investigated, the PSF of the NSG GRIN lens used in the 18-mm probe was also measured for comparison. The results of the lateral and axial PSF measurements, with and without fiber delivery, are provided in Figure 5.8.

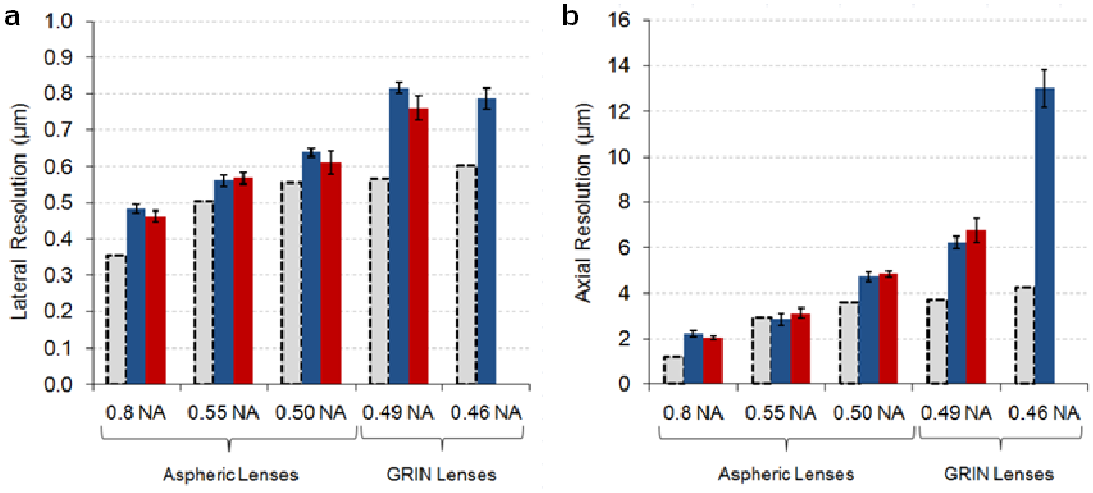

Figure 5.8. Lateral and axial resolution measurements for commercially available miniature lenses. The resolutions correspond to the FWHM of the lateral (**a**) or axial (**b**) PSF. Measurements taken with the free-space propagated beam are provided in blue. Measurements taken with a beam collimated by a GRIN lens after propagation through one meter of PBF are provided in red. The grey dashed bars denote the diffraction limit for the specified numerical aperture. Error bars correspond to the standard error of the mean (n = 12).

From Figure 5.8, the effect of fiber delivery and GRIN lens collimation appear to be insignificant. Given the 0.17 NA of the PBF and the 0.49 NA of the GRIN collimating lens, only a small portion of the full NA (and thus a small portion of the clear aperture) of the GRIN collimator is used during fiber collimation, which may explain why the GRIN lens aberrations does not affect the beam quality during fiber delivery.

When used as the objective lens, however, the influence of spherical aberrations in both the GRIN lenses is immediately apparent. The axial resolution of the NSG lens is approximately 3× larger than the diffraction limit. While the GRINTECH lens shows marked improvement in the axial resolution, it still remains far from diffraction-limited. Not surprisingly, the highest resolution is achieved using the 0.8 NA aspheric lens. This lens does not exhibit diffraction-limited performance, however, may be due to the large difference between the imaging wavelength of 753 nm and the lens design wavelength of 1550 nm. The 0.55 NA aspheric lens demonstrates diffraction-limited axial resolution with nearly diffraction-limited lateral resolution. This lens is a particularly attractive objective lens candidate due its smaller 2.4 mm diameter and long 0.88 mm working distance. The increased working distance can enable imaging through a cover slip or optical window, which would allow housing of the system inside of an endoscope insertion tube. From these measurements, both the 0.8 and the 0.55 NA aspheric lenses were identified as potential miniature objective lens candidates.

5.4: OPTICAL SYSTEM DESIGN

5.4.1: Analytical modeling

After identifying attractive candidates for miniature objective lenses and characterizing both the PBF and MEMS mirror, we investigated the potential optical systems that could be built around these components. The collimated beam diameter set by the design of the PBF collimation assembly and the scanning mirror aperture and deflection determined by the MEMS device determine the maximum number of

resolvable spots for the new probe. This upper value provides the limiting constraint on the optical design.

With the MEMS mirror oriented at 45º to the beam, the effective mirror aperture is 750 µm × 530 µm. By orienting the mirror such that the ±15.3º optical deflection is along the 530 µm axis and the ±7.1º optical deflection is along the 750 µm axis, a 425 µm beam waist at the mirror provides truncation ratios of 0.80 and 0.57, respectively. Oriented in this fashion, the difference in N for the two axes can be reduced. Using Eq. (3.8) and following the methodology used in Chapter 3, Section 3.2, the maximum number of resolvable spots for this system is 436 × 243. Note that the real optical system consists of a rectangular aperture and an under-filling round beam, while the equations used here are for a round aperture and a round beam, or a significantly overfilled rectangular aperture. As a result, the analytical model predicts slightly different resolutions along the two different axes due to the two different truncation ratios when the mirror is the limiting aperture. In reality, however, the beam only experiences these truncations along the two axes and elsewhere underfills the rectangular mirror aperture more significantly and we do not expect a measurably asymmetric resolution. Thus this maximum number of resolvable spots should be taken as an idealized design guideline rather than an absolute experimental target.

To begin modeling the optical system, we began by determining what the achievable fields of view and resolutions were for the various miniature objective lens candidates, given our collimated beam and MEMS mirror characteristics. To model these parameters, we calculated the FOV, lateral resolution and axial resolution for each lens. To explore the design space, we modeled varying relay lens pair magnifications from 1.25 to 4.75. As in Chapter 3, the equations used here utilize the thin lens and paraxial approximations and ignore all lens aberrations to estimate the "best case" performance limited only by diffraction. Plotting the calculated lateral resolution against the maximum FOV for each mirror axis (see Figs. 5.9**a** and 5.9**b**), we see that solutions for each

miniature objective lens collapse to a fixed linear slope over much of the plot. The slope corresponds to the number of resolvable spots, *N*, dictated by the mirror for that axis, as expected.

As beam expansion ratio increases, decreasing the FOV, the beam size at the back aperture of an objective lens increases. When the truncation ratio at the back aperture of the objective lens exceeds the truncation ratio at the mirror, the objective lens becomes the limiting aperture and the plot begins to deviate from the *N* calculated for the mirror. Note that the maximum *N*, given by the quotient of FOV over resolution, is decreased once the objective lens becomes the limiting aperture. Thus the optimal imaging performance is obtained by filling the scanning mirror more than the objective lens. This result may seem non-intuitive for those familiar with the design of bench-top microscope systems, where the objective lens is usually overfilled to maximize resolution and the beam is minimized on the scanner to avoid unnecessary energy loss. The scanning mirrors commonly used in bench-top systems, which usually have large scanning angles and large apertures, have *N* values much higher than needed for most imaging purposes [178]. In such systems, the number of resolvable spots can be partially sacrificed for increased resolution.

Figure 5.9 provides a map of the available design space, where the area above each curve contains designs allowed by diffraction theory and points along the curves represent diffraction-limited designs. The best resolution for each objective lens corresponds to a magnification of 4.75×, where the clear aperture of each objective lens is filled, while the worst resolution for each lens corresponds to the lowest magnification of 1.25× magnification. Over much of the design space, the choice of objective lens is not critical, as any lens can achieve the same design point given a suitable magnification from the relay lenses. For example, achieving a FOV of 475 µm × 220 µm FOV with the 0.55 NA aspheric objective lens requires a relay lens magnification of 1.625×. The predicted lateral resolutions along the outer and inner axes are 1.1 µm and 0.9 µm, respectively. The exact same resolution and FOV conditions can be achieved with the 0.8

NA objective lens, but would require a relay lens magnification of 0.906×. In this case, the beam diameter would actually need to be reduced, thus magnifying the scanning angle, to achieve such a large FOV with this lens.

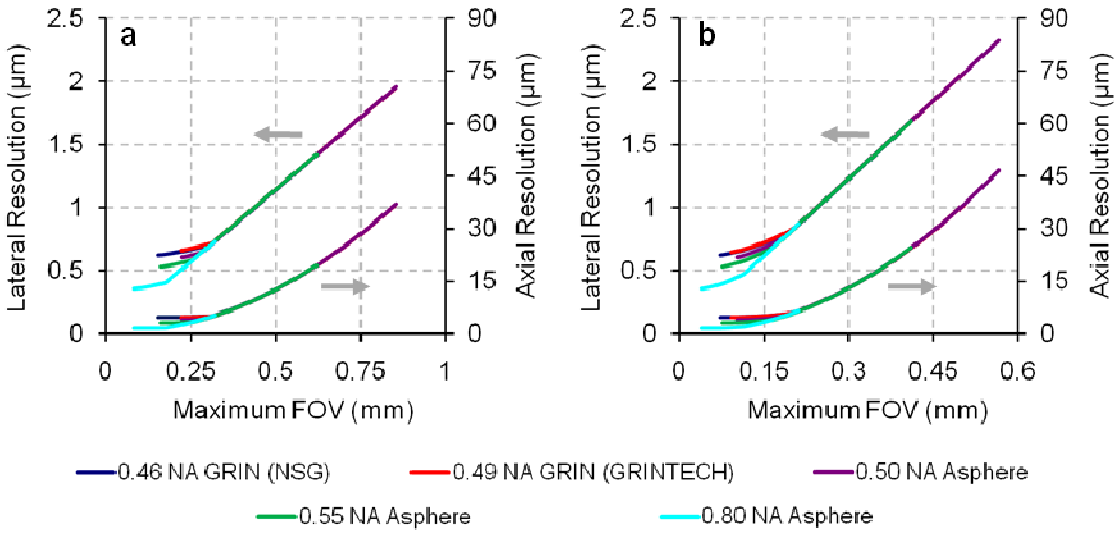

Figure 5.9. Calculated diffraction-limited lateral and axial resolution versus field of view for miniature objective lenses. Calculated diffraction-limited lateral and axial resolutions versus FOV for the specific collimated beam size and the MEMS mirror used in the new probe and the miniature objective lens candidates given in Table 1. The plots correspond to the outer and inner axes of the MEMS mirrors, **a** and **b** respectively. The optical deflection angles and effective apertures of the outer and inner mirror axes are ±15.3º and ±7.1º, and 530 µm and 750 µm, respectively. The collimated beam size of 425 µm corresponds to the 0.5-mm GRIN collimation lens used in the probe. The minimum resolution for each lens corresponds to a magnification of 4.75×, while the maximum resolution for each lens corresponds to a 1.25× magnification.

The axial resolution provides additional design guidance. Because the axial resolution depends nonlinearly on truncation ratio, the axial resolution grows much more rapidly as the objective lens is increasingly under-filled and thus provides a constraint on the design. For instance, from Figure 5.9**a**, one may be willing to shift the lateral

resolution from 0.9 µm to 1.5 µm to increase the maximum FOV from 390 µm to 655 µm, with little loss in resolvable features. However, the axial resolution curve predicts this would degrade the axial resolution from 7.8 µm to 21.8 µm, seriously impairing the optical sectioning capabilities of the endoscope.

This analytical model ignores all aberrations in the optical system. However the aberrations from the miniature objective lenses can be quite significant, as seen in Section 5.3, and the aberrations arising from off-axis scanning through the relay lenses must also be taken into account.

5.4.2: Numerical modeling with ZEMAX optical design software

To explore the impact of aberrations, we have constructed a computer-aided model of the new probe using ZEMAX optical design software. The ZEMAX model, shown in Figure 5.10, consists of an input beam, two relay lenses, a right angle prism, a dichroic mirror, and an objective lens. The prism and the dichroic mirror are modeled from commercially available optics (055-003, OptoSigma, and FF670-SDi01-4x5, Semrock, respectively). As the model describes only the laser delivery pathway of the endoscope, and not the emission collection pathway, only the reflective surface of the dichroic is modeled.

The input laser beam is defined by an entrance pupil diameter of 0.5303 mm, corresponding to the short effective aperture of the MEMS mirror at 45º, and an apodization factor of 1.5575, corresponding to a 425 µm beam diameter ($1/e^2$). The aperture conditions are set to the outer axis values because the ZEMAX Gaussian beam definition does not allow for a rectangular aperture in the Gaussian beam definition. Field angles of 0º, 7.1º, and 15.3º are modeled to explore the scanning angles of interest from the MEMS mirror. For the objective lens, the 0.55 NA aspheric lens was initially selected based on its combination of diffraction-limited performance and long working distance.

The ZEMAX software provides many different analysis tools with which to measure and optimize the performance of an optical design. Though the software

primarily operates through numerical ray tracing, it is also able to model aperture diffraction and diffraction-limited focusing. In the latter case, this is achieved by calculating the cumulative phase delay along each ray up to the exit pupil of the focusing lens. The phase delay of each ray is used to model the wavefront at the exit pupil, which is then propagated to the focus using either the fast Fourier transform (FFT) algorithm or the Huygens diffraction integral, depending on the requirements for accuracy and computing time.

For the microsurgery endoscope, we are most interested in maintaining a diffraction-limited focus across the entire FOV and thus the performance metrics chosen were the diffraction encircled energy (DEE), the Strehl ratio, and the root mean square (RMS) wavefront error at each field angle. In ZEMAX, the DEE is the plot of the percent of a beam's energy that lies inside a circle of increasing radius. Minimizing the DEE ensures the laser energy is being concentrated in as small a spot as possible at each field angle. Similarly, the software can calculate the predicted two-dimensional PSF using the Huygens diffraction integral, from which the two-photon excitation and SHG resolution can be deduced by multiplication of a factor of $1/\sqrt{2}$.

The Strehl ratio is the ratio of the intensity at the center of the simulated PSF to the peak intensity of the theoretical diffraction-limited PSF. This metric indicates how much energy is taken out of the central peak of the focus or how much the central peak is widened due to aberrations. By convention, a focus with a Strehl ratio of 0.8 or greater is taken to be qualitatively diffraction-limited [179], although clearly some energy is lost from the focus as the Strehl ratio decreases from unity.

Lastly, the RMS wavefront error is a measurement of the average error between the aberrated focusing wavefront and a perfectly spherical focusing wavefront. This metric is particularly useful in ZEMAX, because it is computed for all field angles up to the maximum design field angle, rather than just at the specific field angles specified by the user. This ensures that there are no scanning angles that yield localized aberrations

between the specified field angles. A RMS wavefront error of 0.07λ or less is commonly considered to be diffraction-limited [179].

To begin designing the optical system, we chose to start with commercially available aspheric lenses like those used in the first prototype. Specifically, we wished to identify a lens pair with a magnification between 1.8× and 2.5× and an outer diameter no larger than 3.5 mm. The diameter constraint is dictated by the desire to have the largest clear aperture possible without exceeding the size of the mounted MEMS mirror and thus increasing the packaged size of the prototype. For the 0.55 NA objective lens, these magnifications correspond to a maximum FOV at ±15.3º optical deflection of at least 310 µm with an axial resolution no worse than about 10 µm based upon the analytical model. Ultimately, the best lens pair we identified consisted of a 3 mm focal length lens (AC510, Anteryon) and a 6.1 mm focal length lens (352550, Lightpath Technologies) for a nominal magnification of 2.03×. Both lenses possess an outer diameter of 2.8 mm, though only the clear apertures of the lenses appear in the model. The optical layout for this system is shown below in Figure 5.10. The DEE and RMS wavefront error for the system are presented in Figure 5.11 and the PSF at each design scan angle are presented in Figure 5.12.

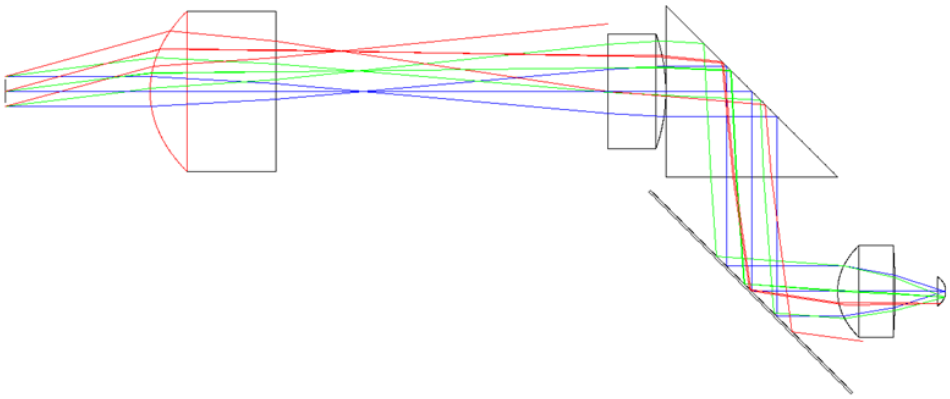

Figure 5.10. ZEMAX model of the new 9.6-mm probe design using a relay lens pair, consisting of commercially available aspheric lenses and 2.03× magnification. This optical layout displays the full ZEMAX model of the endoscope system, with the blue, green, and red rays corresponding to 0º, 7.1º, and 15.3º deflections from the MEMS mirror, respectively. The objective lens used is the 0.55 NA aspheric lens.

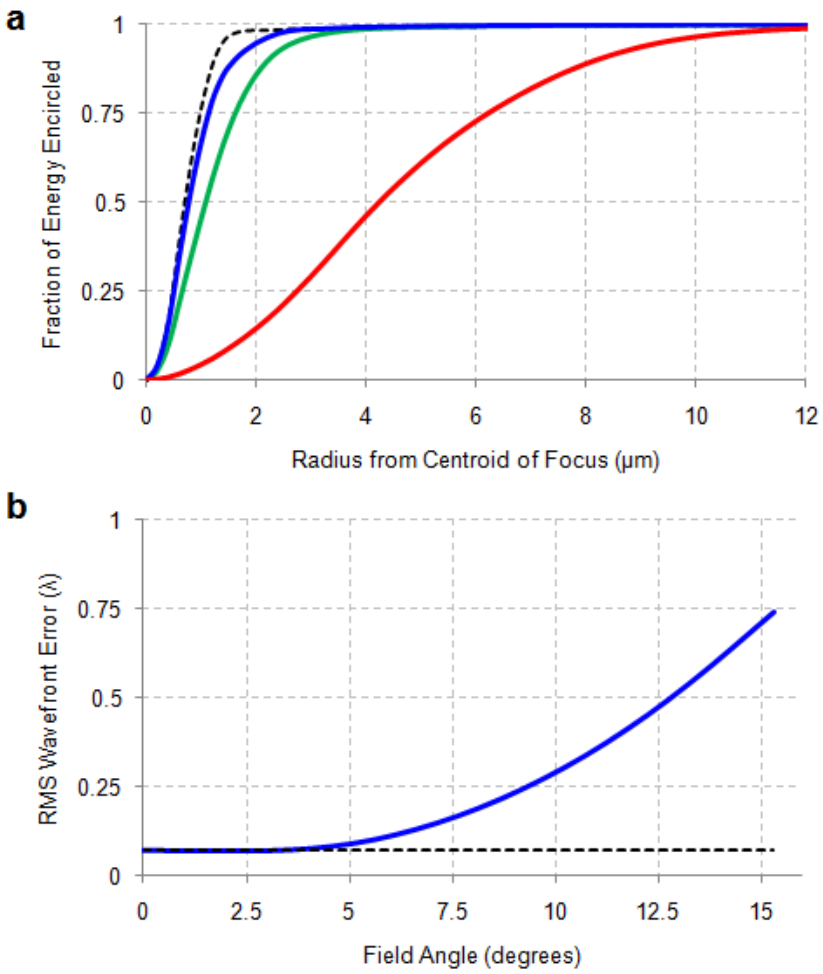

Figure 5.11. Optical performance of the optical system shown in Figure 5.10. a The diffraction encircled energy (DEE) at each field angle, where blue, green, and red lines correspond to 0º, 7.1º, and 15.3º field angles. The predicted DEE is nearly diffraction-limited at the FWHM for small field angles, but rapidly increases toward the maximum extent of the FOV. **b** The RMS wavefront error versus field angle. The RMS error remains near 0.07λ up to a field angle of approximately 5º, before off-axis aberrations become significant.

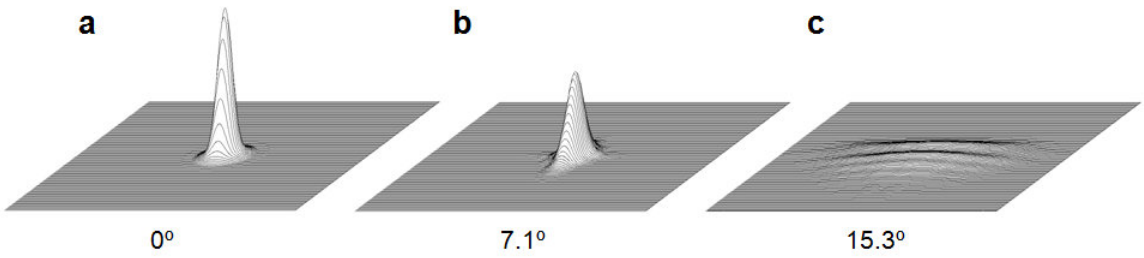

Figure 5.12. Point spread functions for the optical system shown in Figure 5.10. Each PSF is calculated using the Huygens diffraction integral and maximal values indicate Strehl ratio. The PSFs at 0º, 7.1º, and 15.3º are provided in **a**, **b**, and **c**, respectively. The modeled Strehl ratios at the 0º, 7.1º, and 15.3º field angles are 0.81, 0.47, and 0.036, respectively.

Using this relay lens pair yields a maximum FOV of approximately 415 µm × 210 µm but with significant curvature to the imaging plane. The peak-to-valley focal shift due to field curvature, Δ_z, is fairly large for this design at ± 42 µm. Additionally, Figure 5.11 clearly indicates the presence of strong aberrations arising from scanning the laser beam off the optical axis of the relay lenses. On axis, at a field angle of 0º, the system is nearly diffraction-limited with a predicted RMS wavefront error of 0.071λ and a predicted Strehl ratio of 0.81. From the DEE analysis, we see that the PSF has departed only slightly from the diffraction limit at the FWHM. The calculated PSF at the 0º field angle (provided in Figure 5.12**a**) predicts the on-axis imaging resolution to be approximately 0.922 µm. However, as the laser is scanned to greater angles, the wavefront error increases nonlinearly. At 7.1º, the maximum scanning extent of the inner axis of the MEMS mirror, the DEE appears the same however the Strehl ratio has dropped to 0.47. Though the DEE is normalized to unity, the lower Strehl ratio is clearly visible in the modeled PSF shown in Figure 5.12**b**. The resolution would not change significantly at this angle, however the excitation efficiency would decrease significantly. At the maximum field angle of 15.3º, wavefront error reaches approximately ¾λ and the PSF, shown in Figure 5.12**c**, contains very little energy. Based on this analysis, this optical system could provide near diffraction limited performance at the center of the FOV, with

the excitation efficiency decreasing by about 66% out to a FOV of 180 µm, much beyond which the excitation would be negligible.

The primary source of aberrations is astigmatism, arising from the scanning of the laser beam off-axis through the relay lens pair. The aspheric lenses used in the lens pair are designed primarily for collimating laser diodes and fiber-optics and therefore lack aberration correction for off-axis beams. Because the relay lens pair is critical to our endoscope design, we next endeavored to design a fully aberration-corrected lens pair.

The ZEMAX software package provides a powerful means of automated optical system design. Briefly, the user first builds a basic model of the optical system and then assigns variables to various parameters, such as lens curvature or thickness. Afterward, the user creates a "merit function" which consists of the performance metrics to be optimized (e.g., RMS wavefront error or DEE), target values for each metric, and relative weights to prioritize the metrics. The value of the merit function is given by the RMS of the difference between each performance metric and its target value, multiplied by its weight. The software can then optimize the system using a damped least-squares algorithm to progressively modify the variables until the merit function arrives at a local minimum. Initial investigation found that lens optimization of only the objective lens could not correct for aberrations across the entire scan range while still maintaining a realistic lens geometry. Thus we applied the automated design process to the relay lens pair to explore the possibility for diffraction-limited performance in our miniature optical system.

Using the ZEMAX software, we began with the commercially available relay lenses used in the initial model with their lens clear apertures increased to 3 mm to improve transmission of larger scan angles. To ensure the final lens designs could be easily manufactured, each lens was kept as a plano-convex lens with one aspherical surface. Also, since miniature aspheric lenses are often produced through a molding process, the glass types used in the commercially available lenses (N-BAK and CO550) were preserved as well.

Spherical aberrations arise when focusing into media of different indices of refraction, such as through microscope cover slips or into biological tissue. Clinical applications will require focusing into tissue and likely this device will be housed behind an optical window so that the system can be moved axially to adjust the focal plane. To account for any corresponding spherical aberrations at the focus, the sample was modeled as a microscope cover slip (BK7, n = 1.511) with seawater (n = 1.340) as the sample medium to approximate focusing in tissue through an optical window.

The radius of curvature, thickness, conic constant and aspheric constants of each lens were established as variables to be optimized, along with the distance between the relay lenses and the distance between the effective MEMS aperture and the first relay lens. We then constructed the merit function to optimize these variables to reach specified values of DEE at each field angle, with each weighted equally. By selecting DEE target values corresponding to different desired spot sizes, the software could be guided to optimize the relay lens pair for different magnifications.

In nonlinear optical imaging, a flat field of view is desirable, however not a strict requirement as most of the imaging is meant to occur inside the bulk of the samples. To improve the flatness of the FOV, the system was initially optimized with a flat image plane, so that the software would try to reach the target DEE everywhere on the flat image plane. Invariably, some curvature to the FOV would remain after optimization. To find the correct curvature and accurately represent the focus along the curved FOV, a second optimization was run using the same merit function but with the image plane curvature as the only variable. Using this method, the peak-to-valley focal shift, Δ_z, due to the FOV curvature was kept at 10 µm or less.

Using the design methodology outlined above, we optimized three different relay lens systems for use with the 0.55 NA aspheric objective lens. For each effective magnification, the minimum Strehl ratio across all design field angles, St_{min}, was maintained above 0.8 indicating nearly diffraction-limited performance. A similar lens pair was designed for the 0.80 NA aspheric objective lens to explore the potential to

achieve higher resolution while still seeking to maximize *N*. Table 5.2 displays a summary of the optical performance for each optical system design. Figure 5.13 plots these designs on the resolution versus FOV plot from Figure 5.9**a**. From Figure 5.13, we see that the analytical model provides an accurate guideline for the optimum imaging performance of the system and that the custom lens designs were able to converge very nearly to this limit imposed by diffraction.

Table 5.2. Summary of modelled optical system performance using optimized relay lens designs.

Objective Lens NA	M	FOV [µm]	Lateral Resolution [µm]	N_{model}	Δ_z [µm]	St_{min}
0.55	1.82	448 × 212	1.06	423	10	0.86
	1.98	396 × 192	0.962	412	10	0.85
	2.38	308 × 148	0.736	418	5	0.87
	2.32	297 × 142	0.741 – 5.23[1]	*NA*	18	0.04
		(85 × 85)	(0.741)	115	5	0.80
0.80	1.75	220 × 104	0.529	416	5	0.90

Values in grey correspond to commercially available spherical lens pair. The values in parentheses refer to the diffraction-limited portion of the field of view. *NA*: Not applicable due to rapid decrease in *St* across FOV. [1]Where aberrations induce an asymmetric PSF, the encircled energy radius corresponding to half the maximum energy is reported.

One goal of the second prototype is to enhance the imaging and microsurgery capabilities beyond those of the initial 18-mm probe. Reducing the focused spot size is a clear means to achieve this goal by reducing the energy required for ablation, improving the imaging resolution, and increasing the two-photon fluorescence excitation and SHG efficiencies. Though the design built around the 0.80 NA objective lens predicts an imaging resolution of approximately 530 nm, the short 200 µm working distance may

make future packaging of the system difficult and may limit the maximum imaging and ablation depths. For this reason, we chose to further pursue the 2.38× magnification design built around the 0.55 NA objective lens. The optical layout for this system is provide in Figure 5.14, with plots of the DEE and RMS wavefront error provided in Figure 5.15 and the PSF at the design field angles provided in Figure 5.16. As illustrated in Figs. 5.15 and 5.16, the optical design is very well corrected for aberrations across the entire FOV.

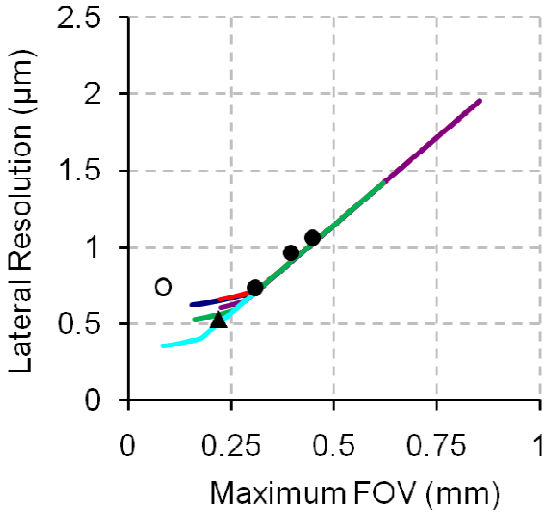

Figure 5.13. Comparison of optimized relay lens design systems with the analytical diffraction-limited model. The analytical model for the diffraction-limited lateral resolution vs. maximum FOV along the 530 µm effective dimension of the MEMS mirror is reproduced here from Figure 5.9**a**, with the ZEMAX models performances overlaid. By optimizing the design of the relay lenses to be aberration-corrected at varying magnifications, the ZEMAX designs approach the diffraction-limit predicted by the analytical model. The circles correspond to ZEMAX models utilizing the 0.55 NA aspheric objective lens (green line) while the triangle indicates the model using the 0.80 NA aspheric objective lens (turquoise line). The hollow marker corresponds to a model using commercially available spherical lenses for the relay lens pair (only the diffraction-limited region of the FOV is indicated).

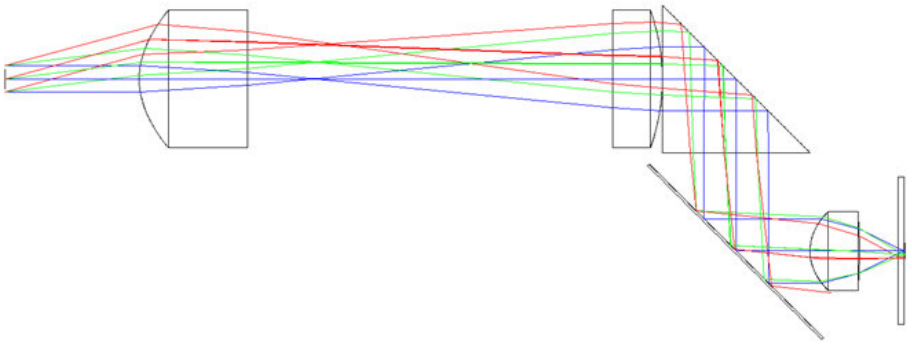

Figure 5.14. ZEMAX model of second-generation endoscope prototype using a custom-designed relay lens pair with 2.38× magnification. This optical layout displays the full ZEMAX model of the endoscope system, with the blue, green, and red rays corresponding to 0º, 7.1º, and 15.3º deflections from the MEMS mirror, respectively. The relay lenses used in this system provide correction of aberrations arising from off-axis scanning and refractive index mismatches at the sample. The objective lens used is the same 0.55 NA aspheric lens used previously.

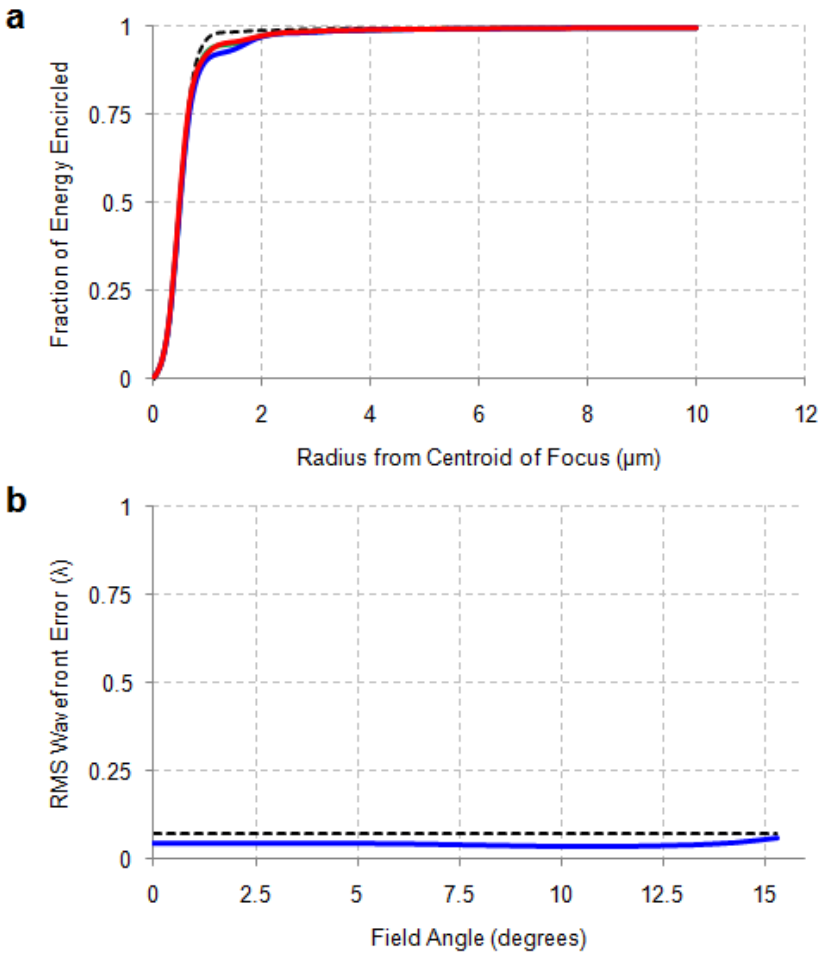

Figure 5.15. Diffraction-limited optical performance of the optical system shown in Figure 5.14. a The diffraction encircled energy at each field angle, where red, green, and blue lines correspond to 0º, 7.1º, and 15.3º field angles. Note that, for each field angle, the predicted DEE at FWHM is indistinguishable from the diffraction-limited value, shown here as a dashed line. **b** The RMS wavefront error versus field angle. The RMS error remains below 0.07λ across all field angles, and thus across the entire field of view.

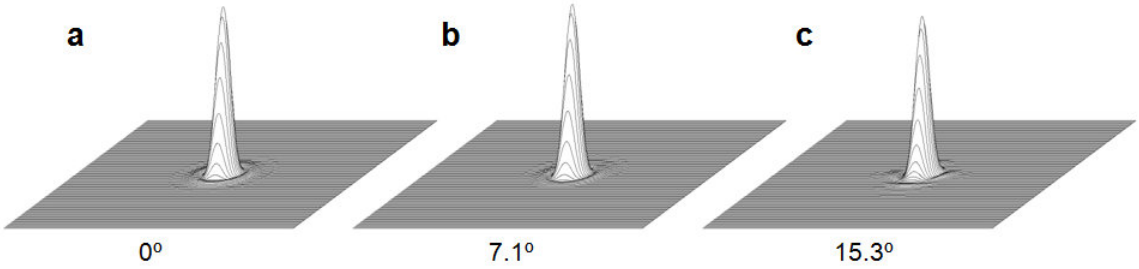

Figure 5.16. Point spread functions for the aberration-corrected relay lens pair system shown in Figure 5.14. Each PSF is calculated using the Huygens diffraction integral and maximal values indicate Strehl ratio. The PSFs at 0º, 7.1º, and 15.3º are provided in **a**, **b**, and **c**, respectively. The modeled Strehl ratios at the 0º, 7.1º, and 15.3º field angles are 0.93, 0.94, and 0.87, respectively.

To ensure this design was practical to manufacture, we analyzed the optical system for manufacturing and alignment tolerances. Using the ZEMAX software, tolerance sensitivity can be investigated by specifying the parameters subject to variation and the range of variation for each parameter. For example, lateral lens placement could be identified as a parameter and specified to vary ± 100 µm from the nominal position. The system can then use a Monte Carlo algorithm to randomly generate a series of optical systems in which all of the toleranced parameters have been perturbed within their specified range. The software models the optical performance (e.g., DEE, RMS wavefront error) for each Monte Carlo iteration. Additionally, the software can provide sensitivity analysis wherein each tolerance is investigated independently and the aggregate system performance is estimated by a root-sum-square method. This sensitivity analysis is useful in identifying which tolerance has the largest impact on the system performance, while the Monte Carlo method is useful in accurately predicting the overall system performance. We used both methods in analyzing the tolerance sensitivity of our model.

First, we assessed the sensitivity of our lens design to manufacturing tolerances and found that most specifications require only “commercial” level manufacturing, with

only decenter of the aspheric lens surfaces requiring “precision” manufacturing under conventional definitions [15]. There were no specifications requiring “high precision” tolerances. Using these tolerances, provided in Table 5.3, we used ZEMAX to generate 500 randomly perturbed systems and found over 98% of the models exhibit maximum RMS wavefront error below 0.069λ, with the worst system only exhibiting wavefront error of 0.077λ. Thus this lens design should be inexpensive for commercial mass production.

Table 5.3. Manufacturing tolerances sufficient for maintaining diffraction-limited performance.

Specification	Tolerance	Units
Radius	0.04	mm
Edge Thickness	0.1	mm
Wedge	60	arc sec
Decenter	0.01	mm
Surface Irregularity	2	fringes

For alignment tolerances, the lens tilt was allowed to vary ± 1.5º for each relay lens, while the lateral and axial positions of the lenses were allowed to vary by ± 50 µm and ± 100 µm, respectively. The working distance between the objective lens and the image plane was allowed to vary to account for a focal shift arising from axial movement of the relay lenses.

The impact of these combined tolerances can be seen in the overlay of the DEE and RMS wavefront error of 30 Monte Carlo-perturbed systems, provided in Figure 5.17. From the Monte Carlo-based results, the performance of the system appears to be robust to the tolerances specified. The system remains nearly diffraction-limited for all field

angles in many cases, with a handful of cases showing the onset of aberrations at field angles greater than 13º. Using the sensitivity analysis, the model predicts that the system is most sensitive to the tilt and lateral displacement of the first relay lens. By allowing the working distance to adjust for the best focus, axial variations in relay lens position have little effect on the imaging system. As the tolerance on lateral lens placement is loosened to ± 100 µm, the focused spot size at the periphery of the FOV was found to increase by up to 64%, indicating that lens alignment is the most stringent requirement. Based on this information, the lenses appear to have reasonable manufacturing requirements, while the packaging and alignment of this endoscope design should ensure that the required lens tilt and positioning tolerances be maintained.

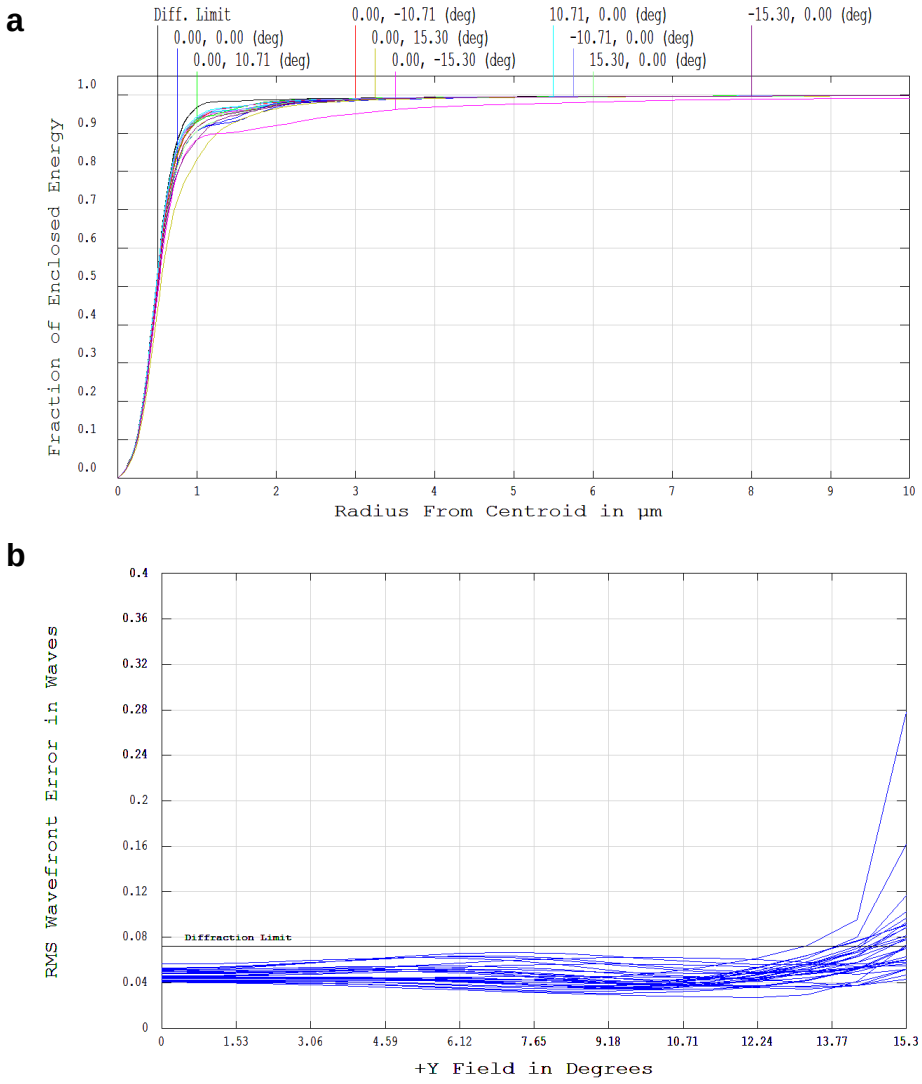

Figure 5.17. Effect of manufacturing and alignment tolerances on the optical performance of the optical system shown in Figure 5.15. a The diffraction encircled energy at each field angle. For all perturbations modeled, the system maintains near diffraction-limited performance at the FWHM. The furthest deviations from the diffraction limit appear at the largest field angles. **b** The RMS wavefront error versus field angle. In agreement with the DEE results in **a**, the design remains approximately diffraction-limited over much of the FOV, with departures from the diffraction limit only occurring above field angles of ~13º. A field angle of 13º corresponds to a FOV of roughly 260 µm.

The results of the lens design optimization demonstrate the potential for a fully miniaturized femtosecond laser microsurgery endoscope with robust aberration correction. Using current glass molding technologies, aspheric lenses of this size and complexity can be easily mass produced for commercial development. For this stage of prototype development, however, the production of low quantities of the custom lens designs is not cost effective. For our new probe, we have chosen to implement commercially available spherical lenses, each with 3 mm outer diameter (NT45-960 and NT48-648, Edmund Optics), to form an inexpensive relay lens pair with a nearly identical magnification of 2.32×. The optical layout of this system is provided in Figure 5.18 while the DEE and RMS wavefront plots are shown in Figure 5.19. The calculated PSFs for each specified field angle are given in Figure 5.20. The performance of this system is also compared to the aberration corrected models in Table 5.2 and Figure 5.13. For this model, the cover slip was removed from sample plane, since this design is not intended for incorporation into a commercial endoscope. The spherical lenses provide diffraction-limited performance at the center of the FOV, with predicted lateral and axial resolutions on-axis of 741 nm and 5.2 µm, respectively. These values agree with the lateral and axial resolutions predicted by the analytical diffraction model (760 nm and 5.6 µm, respectively) to within 10%. The maximal predicted FOV with this design is 297 µm × 142 µm. However off-axis aberrations, this time dominated by coma, increase drastically with increasing scanning angles similar to the stock aspheric lenses and only the central 85 µm maintains St $\geq$ 0.8. Though aberrated, this design provides an inexpensive means of verifying whether the theoretical performance of the ZEMAX model can be achieved experimentally prior to commissioning expensive custom lenses. Because these lenses possess similar dimensions and focal lengths to the custom lenses, the endoscope housing can be designed around these lenses and potentially reused with the custom lens design at a later date.

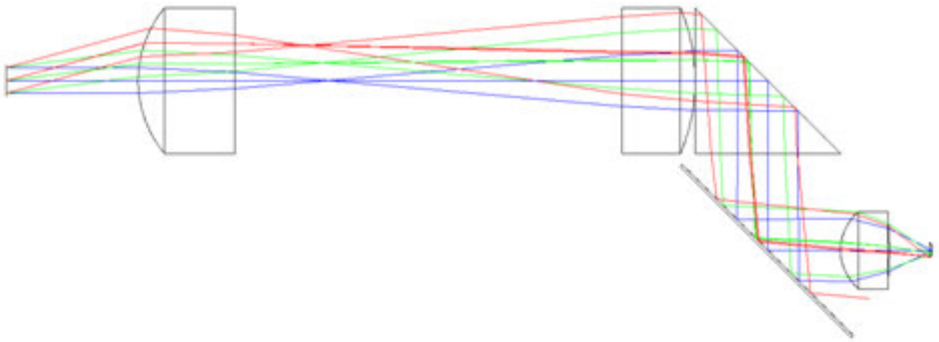

Figure 5.18. ZEMAX model of second-generation endoscope using a commercially available relay lens pair consisting of spherical lenses with 2.32× magnification. This optical layout displays the full ZEMAX model of the endoscope system, with the red, green, and blue rays corresponding to 0º, 7.1º, and 15.3º deflections from the MEMS mirror, respectively. The system is designed as a low-cost alternative to the optimized custom lens design shown in Figure 5.11.

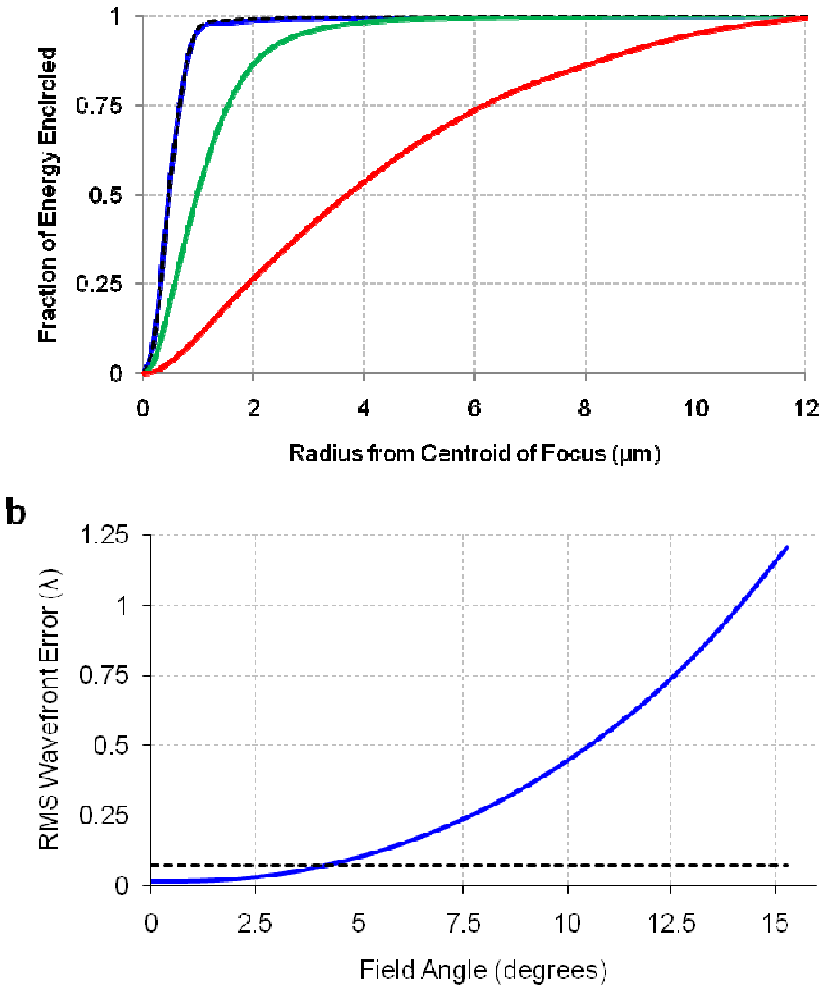

Figure 5.19. Optical performance of the optical system shown in Figure 5.18, utilizing inexpensive spherical lenses. a The diffraction encircled energy at each field angle, where red, green, and blue lines correspond to 0º, 7.1º, and 15.3º field angles. The predicted DEE clearly departs from the diffraction-limited value, shown here as a dashed line, as the scanning angle increases. **b** The RMS wavefront error versus field angle. The RMS error remains below 0.07λ up to a field angle of approximately 4.3º, corresponding to the central 85 µm of the FOV. At larger field angles, the RMS wavefront error increases dramatically.

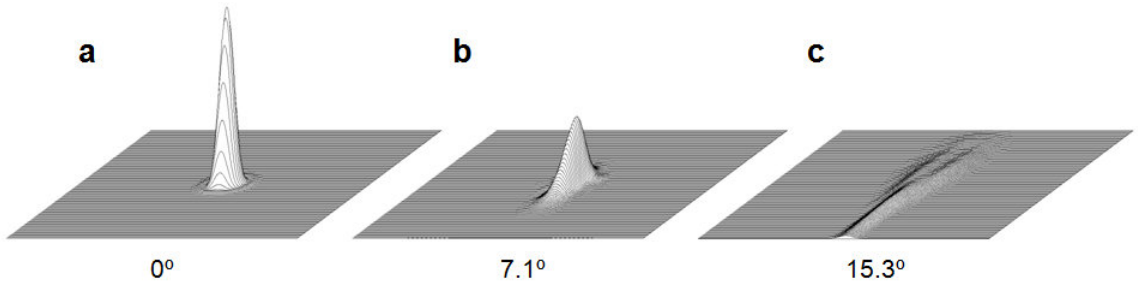

Figure 5.20. Point spread functions for the optical system shown in Figure 5.18. Each PSF is calculated using the Huygens diffraction integral and maximal values indicate Strehl ratio. The PSFs at 0º, 7.1º, and 15.3º are provided in **a**, **b**, and **c**, respectively. The Strehl ratios at 0º, 7.1º, and 15.3º field angles are 0.99, 0.36, and 0.04, respectively.

In addition to modeling the laser delivery pathway of the optical system, we built a separate model to analyze the collection pathway. This part of the pathway consists of all of the optical elements between the source of the emitted light and the PMT detector. Given the 2.4 mm outer diameter of the chosen objective lens, the same 2 mm-diameter collection fiber used in the 18-mm probe is utilized in the second-generation prototype without increasing the final packaged dimensions. A short pass dichroic mirror ($\lambda_{cut\text{-}off}$ = 670 nm; FF670-SDi01, Semrock) was selected to pass the emitted light and was modeled as a perfectly transmitting glass plate with the dichroic mirror's dimensions of 4 × 5 × 1 mm^3. The previous lens (f = 4.0 mm, 0.60 NA; C610TME-A, Thorlabs) directing the light from the collection fiber into the PMT (H7422-40, Hamamatsu) is reused as well. Specifically, the PMT cathode was modeled using a detector surface the same size as the PMT cathode inside an absorbing housing with the same dimensions as the PMT housing.

To approximate scattered light emitted from tissue, the sample, shown in Figure 5.21**a**, is modeled as a block of seawater (n = 1.340) with bulk scattering defined by a Henyey-Greenstein phase function using a mean scattering length of 29 µm and an anisotropy factor, g, of 0.75 [180]. The emitted light arising from two-photon fluorescence or SHG is modeled by a point source embedded inside the seawater block. The source is modeled as isotropically emitting 500,000 rays at a wavelength of 475 nm,

corresponding with the emission of many intrinsic fluorophores, such as NADH [181]. The depth of the source inside the sample can be varied while maintaining a fixed focal length from the objective lens to simulate increased imaging depth. The collection fiber is modeled by two concentric cylinders with inner and outer indices of refraction of 1.490 and 1.402, to match the total internal reflection properties of the actual fiber. As the model is only intended for comparison of relative collection efficiencies between design changes, rather than an absolute quantitative measurement, attenuation and bending in the collection fiber are ignored. Relative changes in collection efficiency can be determined by comparing the number of rays that reach the PMT cathode in this original model with the number of detected rays after any modifications.

As in the 18-mm probe, an air gap exists between the dichroic mirror and the entrance to the collection fiber, in which some scattered light may be lost, as seen in Figure 5.21**a**. To capture the lost light, we introduced a 45º bevel to the distal end of the collection fiber, shown in Figure 5.21**b**, allowing it to sit flush with the dichroic mirror.

Figure 5.21**c** displays the fraction of total emitted rays detected by the PMT for both the beveled and flat fiber tips with increasing imaging depth, normalized to the fraction detected when the focus is at the surface. When the focus is modeled to be at the surface of the sample, the emitted light is unscattered and is well collimated by the objective lens. Not surprisingly, this case results in the largest percentage of collected light. As imaging depth increases, more of the emitted light is scattered and accordingly fewer rays enter the objective lens. While both the flat and the beveled fiber tips exhibit decreasing collection efficiency as the imaging depth increases, the beveled fiber tip is less sensitive to increased scattering due to the closer interface between the fiber and the dichroic mirror. By creating a 45º bevel at the distal end of the collection fiber, this model predicts increases in collection efficiency up to 10% over the flat fiber tip at an imaging depth of 5 scattering lengths deep (145 μm). This modification should slightly help improve the collection efficiency of the new probe for sub-surface tissue imaging.

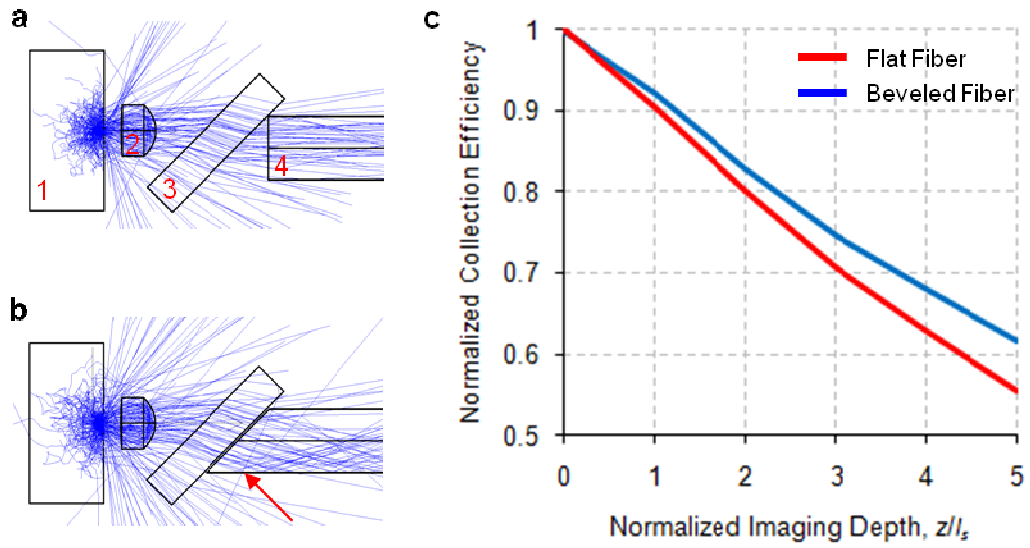

Figure 5.21. Detailed view of the distal end of the collection efficiency model. a The model utilizes (1) an scattering tissue block containing a point source as the sample, (2) the 0.55 NA aspheric objective lens, (3) the Semrock dichroic mirror, and (4) the 2 mm plastic optical collection fiber. **b** The addition of a 45º bevel (red arrow) enables the collection fiber to sit flush with the dicrhoic mirror, enhancing collection of scattered rays. **c** The impact of the beveled fiber tip on the number of rays detected from the PMT for varying imaging depths, where depth has been normalized by scattering length.

The optimization of the collection pathway completes the design and modeling of the entire optical system of the second-generation microsurgery endoscope. The complete optical system is displayed in Figure 5.22. Because this optical system is based on the layout of the 18-mm probe, the system includes many independent, miniature optics which need to be accurately aligned to each other. The alignment of the optics is largely dictated by the packaging of the system, which is discussed in the following section.

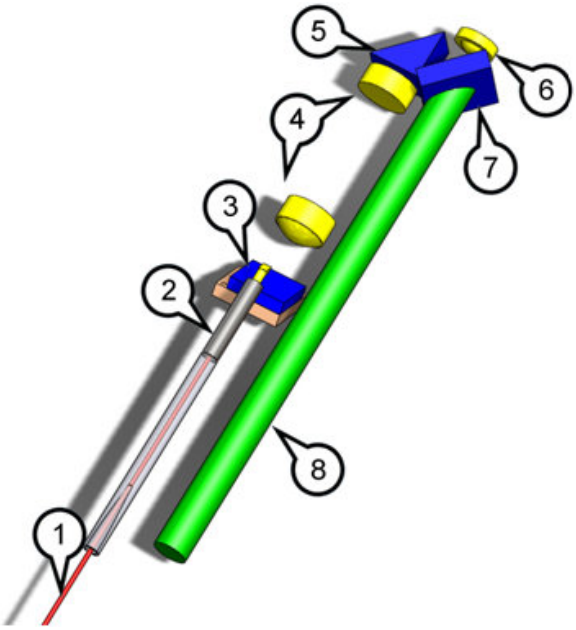

Figure 5.22. Optical system of the new 9.6-mm femtosecond laser microsurgery endoscope probe. This rendering includes all of the optical components designed for the second-generation prototype. Lenses are displayed in yellow and mirrors in blue. The components include: (1) three meters of PBF; (2) the fiber collimation assembly; (3) a two-axis MEMS scanning mirror; (4) a pair of spherical relay lenses with 2.32× magnification; (5) a right angle TIR prism; (6) a 0.55 NA aspheric objective lens; (7) a dichroic mirror; and (8) one meter of 2 mm core plastic optical fiber.

5.5: PACKAGING DESIGN

The packaging of the optical system determines the final outer dimensions of the endoscope and also how the optics can be aligned to each other. For active alignment, where each optic must be carefully placed in its correct location and orientation by some form of micromanipulator, the packaging must provide each optic sufficient degrees of freedom to allow for movement of the optic and access for the micromanipulator. Conversely, in passive alignment the optical element is aligned by the shape of the package, such as a press-fit into a tightly toleranced hole or centered by gravity into a v-groove. Active alignment requires a high degree of control over the manipulation and

fixation of each optic while passive alignment places the burden of accuracy on the fabrication of the housing design. The 18-mm probe primarily utilized passive alignment, with each optical component press-fit into precision machined slots while the collimated laser beam was actively aligned into the housing.

For the second-generation prototype, we initially considered several designs. A flat silicon optical table with lithography-etched grooves would provide high-precision location of the lenses, however lens tilt would be difficult to control and grooves may obscure the lower portion of the lens clear apertures. Also, the orientation of the MEMS scanning mirror mount and fiber collimation assembly shown in Figure 5.22 is difficult to achieve on a flat plate. At the other end of the spectrum, a single block in which each component is press-fit, similar to the first prototype, requires high-precision fabrication of complex geometries and does not allow for fine tuning of alignment during construction to compensate for inaccuracies in fabrication. For these reasons, a hybrid active-passive approach was chosen, resulting in a modular packaging design shown in Figure 5.23. In this design, the optics are divided into three sub-housings: the MEMS mirror housing, the relay lens pair housing, and the objective lens housing. Within each module, the optics are aligned predominantly through passive means by precision slots and holes, after which the subsystems can be easily aligned to each other through active micromanipulation.

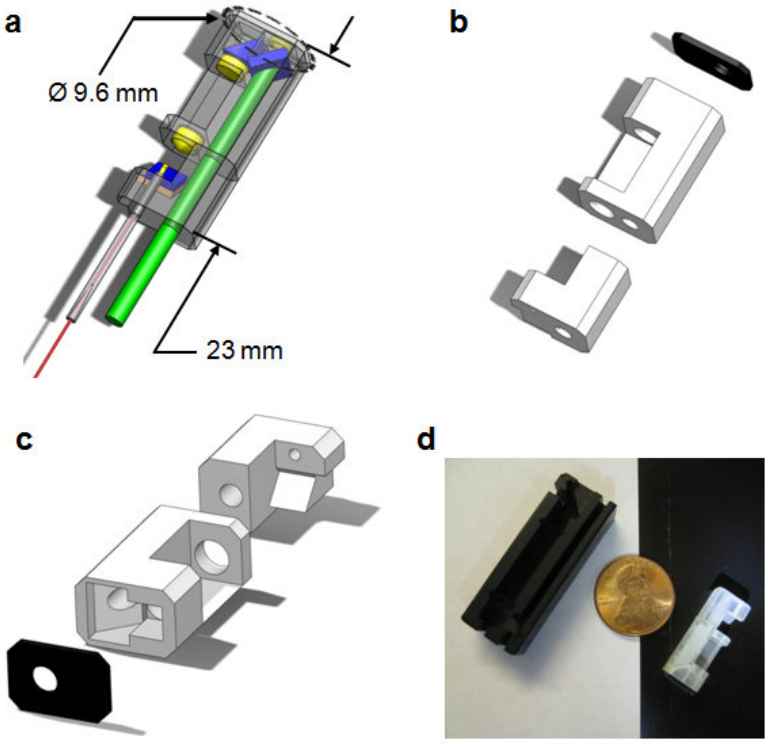

Figure 5.23. Packaging design for the new 9.6-mm diameter microsurgery and microscopy endoscope. a The packaged endoscope is shown transparently overlaid with the optical system of the endoscope, shown in Figure5.22. The assembled endoscope design has a circumscribing diameter of 9.6 mm and a rigid length of 23 mm. **b** An exploded view of the endoscope housing, showing each module separately. **c** An alternate perspective of the exploded view, showing details of the complex geometry used for alignment of the optics. **d** Photograph showing the housing of the 18-mm probe beside the housing for the 9.6-mm probe. A US penny is shown for scale.

Because the MEMS mirror and relay lens housings contain complex geometries that would be difficult to produce by milling processes, the housings were specified for manufacture with ProJet Ultra High Definition 3D printing, a high-precision rapid-prototyping technique. This technique is capable of quickly producing small polymer parts with a typical accuracy of 25 – 50 µm. The objective lens housing is essentially a thin plate with a press-fit hole to mount the miniature objective lens. This piece is

designed to be manufactured from Delrin® acetyl resin on a high-precision end mill, to take advantage of the material's higher stiffness.

To ensure the accuracy of the relay lens placement, which was found to be the most critical alignment item in the ZEMAX model, the press-fit holes for the relay lenses were specified slightly smaller than the 3 mm lens diameters and are to be finished out to exact dimensions with a high-speed drill. Passive alignment was chosen over active alignment for the lateral and angular relay lens positioning because the small scale of the lenses and packaging made access with micromanipulators difficult and because the edge thickness of the lenses are long enough to ensure < 1.5º angular deviation in a tightly toleranced press-fit. Axial lens positioning, which was found to be significantly less critical, can be achieved actively by adjusting the lens' positions axially inside their respective holes while monitoring beam collimation. Details of the alignment procedure are provided in the next section.

This design reduces the outer dimensions of the new endoscope to 6.0 mm × 8.8 mm × 23.0 mm. The circumscribing diameter of this design has been reduced to 9.6 mm, nearly half the 18.0 mm of the intial prototype, while the rigid length has been decreased by 43%. The improved miniaturization and packaging enables this design to be flexibly delivered to the oral cavity, to a wide range of open intraoperative sites, or delivered through the insertion tube of most commercial colonoscopes as a custom endoscope.

5.6: ENDOSCOPE ALIGNMENT AND CONSTRUCTION

The construction of the 9.6-mm probe consisted of the alignment of several sub-assemblies of increasing size which were finally aligned to each other while using laser beam profiling to monitor beam quality. To construct the fiber collimation lens assembly, the custom GRIN collimation lens and prism were first inserted into a 5 mm length of the 1 mm outer diameter stainless steel tube. The lens was then fixed in place by distributing a small amount of UV-curing epoxy where the exposed sides of the lens interface with the steel tube. The mounted GRIN lens and steel tube were then held fixed on an optical

table while the glass ferrule and PBF were aligned to the steel tube with micrometer control of *x*-, *y*-, and *z*-axes, as well as pitch and yaw angles. Collimation of the laser light was achieved by adjusting the axial position of the PBF inside the glass ferrule using a second translation stage while monitoring the beam waist at various distances from the collimating lens. Once optimum alignment and collimation were achieved, a small amount of UV-curing epoxy was applied to the perimeter of the junction between the glass ferrule and the steel tube and also to the PBF where it exits the back of the ferrule. A photograph of the complete collimation assembly is provided in Figure 5.24.

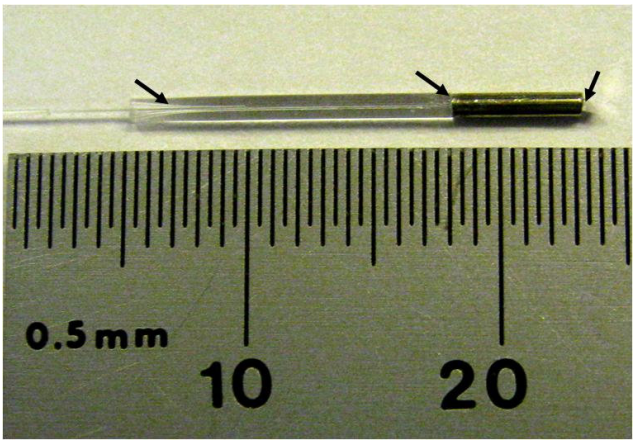

Figure 5.24. Photograph of the finished fiber collimation assembly. Once aligned, the assembly was sealed together using small drops (≤0.5 µL) of UV-curing epoxy where indicated by the black arrows.

During alignment of the collimation assembly, the best collimation yielded a beam diameter ($1/e^2$) of 405 µm, close to the design specification of 425 µm. The far-field beam divergence half-angle was measured to be 2.59 mrad, more than twice the diffraction-limited divergence half-angle of 1.10 mrad. This increased beam divergence is likely because we are utilizing the full clear aperture of the 500 µm GRIN collimating lens, and thus spherical aberration in the lens will be more noticeable than when using the larger 1.8 mm GRIN collimating lens of the first prototype.

During application and curing of the UV-curing epoxy, the beam profile was observed to undergo distortion and then settle at a smaller collimated beam waist of 320 µm. The divergence half-angle decreased slightly to 2.11 mrad, only 40% larger than the 1.51 mrad diffraction-limited half-angle for this beam waist. That the divergence angle moved closer to the diffraction limit as less of the lens aperture was filled by the collimated beam supports the theory that the increased divergence stems from spherical aberration in the lens. This change in collimated beam waist also accompanied a drop in the transmitted energy across the three-meter PBF and collimation assembly from 53% before the curing of the epoxy to 33% afterward. Even though the amount of epoxy applied was small (~0.5 µL), the viscosity of the uncured epoxy is very low and most likely a sufficient volume of epoxy wicked into the inside of the steel tubing during curing. Because the steel tube significantly blocks the UV curing lamp, the epoxy did not cure before capillary forces had distributed the epoxy into the space between the fiber and the collimating lens. Improper curing of this epoxy due to the opacity of the steel tube is likely responsible for the drop in transmitted energy. This issue will need to be addressed in future prototypes.

To package the MEMS scanning mirror, the silicon chip containing the MEMS device was first transferred mounted to the custom PCB using double-sided tape. We then wire-bonded the voltage actuator leads and the ground lead to the PCB bonding pads. During wire-bonding, we found it difficult to achieve a reliable bond between the silver wire and the leadless solder of the PCB, so small gold pads were glued over the PCB bond pads using conductive silver paint.

To mount the MEMS chip and PCB to the MEMS module of the endoscope package, we constructed a specialized alignment system. First, a helium neon (HeNe) reference laser was reflected off a one inch mirror onto a screen three meters away. The mirror was leveled to be completely flat with respect to the optical table. We then replaced the one inch mirror with the PCB-mounted MEMS chip, held by a pair of locking tweezers and controlled by a 6-axis translation stage. Using the reference laser,

the angle of the MEMS chip was adjusted until the projected laser spot matched the previous spot made by the flat mirror, indicating that the MEMS chip was level. Next, the linear controls of the translation stage were adjusted to lower the PCB onto the MEMS mirror module of the endoscope housing, which was mounted in a 45º clamping mount (VC1, Thorlabs) such that the MEMS mounting surface was also level with the table. To fix the PCB to the housing, a drop of cyanoacrylate epoxy was placed on the mounting surface of the housing. To ensure accurate placement of the PCB, the entire process was conducted under a stereoscope. After successful mounting of the PCB, the wires carrying the MEMS mirror driving signal were attached to the plated through-holes on the back of PCB using conductive silver epoxy. The far side of the wires connected to a custom-built junction box connecting each voltage lead to a BNC terminal and linking the common grounds, with a switch to control power to the mirror.

We next mounted the fiber collimation assembly into the MEMS mirror module of the housing and aligned the collimated laser beam to the MEMS scanning mirror. The fiber collimation assembly was aligned through its mounting hole using a 5-axis translation stage, after which the assembly was rotated until the beam was centered on the MEMS mirror. The inner axis of the MEMS mirror was actuated to verify that the laser beam was centered on the mirror surface of the MEMS chip before sealing the collimation assembly in place with cynaoacrylate epoxy.

For the relay lens module of the endoscope package, the relay lenses were each pressed into their appropriate holes and inspected under a stereo scope to ensure they were not tilted with respect to the optical axis. The relay lens housing was then aligned to the collimated beam from the MEMS mirror housing to check that the beam was collimated emerging from the relay lenses. The lens separation was then adjusted slightly as necessary using a small cotton swab to optimize the beam collimation. The collimated beam diameter after expansion through the relay lenses was measured to be 1,000 µm, very near the design specification of 986 µm. The increased beam divergence from the collimator and the ability to actively align the relay lens separation allowed us to achieve

a beam diameter after expansion close to the design value despite the smaller beam diameter from the collimator. The measured divergence half-angle of 1.19 mrad is further from the divergence half-angle predicted by the diffraction of 0.48 mrad, however. In the ZEMAX model, moderately increased divergence due to axial separation of the relay lenses resulted primarily in shift in the focal plane with minimal degradation to the imaging resolution. After best collimation was achieved, the lenses were fixed into place using a small amount of UV-curing epoxy placed around the perimeter of each lens.

During collimation, significant high-frequency and axially symmetric ripples were observed superimposed upon the Gaussian spatial profile of the beam (Figure 5.25). The highest spatial frequencies were observed close to the second relay lens, with decreasing spatial frequencies as the observation distance increased. A clean Gaussian profile was recovered for distances larger than the Rayleigh range.

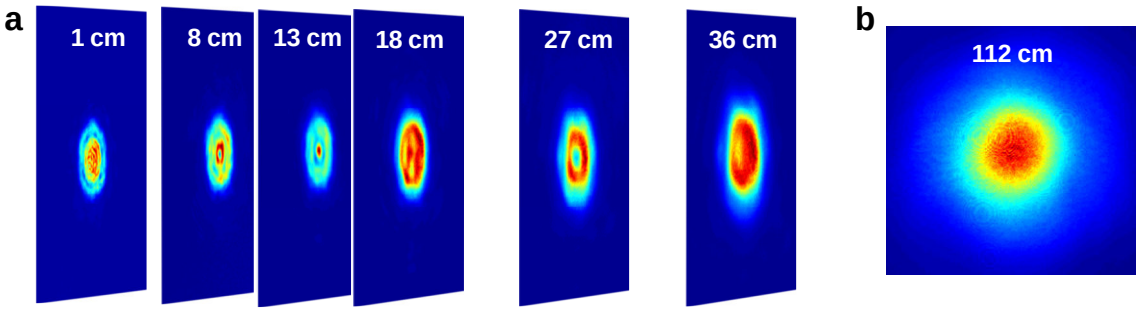

Figure 5.25. Beam profile evolution after expansion by the miniature relay lens pair. a Series of beam profiles taken at increasing distances from the second relay lens. The distance is noted in each frame and image separations are scaled accordingly. The beam profile at 1 cm displays high-frequency ripples across the profile, which decrease in spatial frequency as distance increases, similar to diffraction from a circular aperture. This pattern was repeatable even with large diameter (1 inch) lenses. **b** Outside the Rayleigh range (~1 m), a Gaussian profile is recovered.

The ripple pattern follows the behavior of diffraction arising from the aperture of the second relay lens, however this diffraction is unlikely given the 1.00 mm beam diameter and the 2.7 mm minimum clear aperture specified for the lens. Replacing the relay lens module with a 35 mm focal length one inch diameter lens, the collimated beam from the MEMS module displayed the same behavior. Therefore, we suspect that phenomenon is a beam quality issue arising from the issues in the fiber collimation assembly.

When a laser beam is focused, high spatial frequencies the beam profile will result a distribution of energy out of the central focus spot and into low-energy rings. This is a result of the Fourier transform properties of a lens [162]. To estimate how much energy would be lost from the focal spot due to the ripple pattern we observed, we wrote a MATLAB script to analyze the Fourier transform of the capture beam profile. This analysis estimated an 18% reduction in the peak intensity.

With the relay lenses fixed in place, the right angle prism and dichroic mirror were pressed into their appropriate places in the relay lens module. The relay lens module was then realigned to the MEMS mirror module. During this process, the angle of the collimated laser beam was monitored to ensure that the right angle prism and the dichroic mirror were both mounted vertically and at 45º with respect to the beam path. With alignment verified, the prism and the dichroic were both fixed in place with UV-curing epoxy and the MEMS mirror module was bonded to the relay lens module using cyanoacrylate epoxy around the junction of the two modules.

The objective lens was pressed into the Delrin® nosepiece of the endoscope and inspected under stereoscope to ensure that the lens was not tilted, which would result in astigmatism. This nosepiece was aligned to the rest of the endoscope using a 5-axis translation stage. The beam profiler was used to ensure that the placement of the lens did not alter the angle of the emerging laser light and that the far-field beam profile was Gaussian. Once in place, the nosepiece was fixed to the rest of the endoscope using cyanoacrylate epoxy.

Lastly, the collection fiber was installed in the endoscope, taking care to ensure that the beveled angle of the collection fiber was oriented parallel to the dichroic mirror. We then used cyanoacrylate epoxy to seal the fiber in place, completing the construction of the 9.6-mm microsurgery endoscope.

5.7: SUMMARY OF 9.6-MM ENDOSCOPE DESIGN

In designing the 9.6-mm probe, we established design goals of reducing the packaged size, extend the microsurgery capabilities and enabling imaging of intrinsic sources of nonlinear imaging signal by optimizing the optical system of the 18-mm probe. The finished probe has been reduced in size by nearly a factor of two along every dimension, resulting in a 9.6 mm circumscribing diameter that would allow flexible delivery into the oral cavity or an intraoperative surgical site, or allow for delivery through the insertion tube of most commercial colonoscopes. Analytical and numerical design analysis, along with experimental testing of miniature objective lenses, showed that the resolution could be improved and the FOV increased, even within the smaller packaged size of the new prototype. Chapter 6 will cover the characterization and demonstration of this new prototype with the aim of demonstrating improved imaging and microsurgery capabilities.

Chapter 6: Characterization of the 9.6-mm Probe

We have constructed a 9.6-mm diameter probe of the femtosecond laser microsurgery endoscope with the goals of:

- Decreasing the size of the system to enable future endoscopic use
- Improving the resolution and fluorescence collection efficiency to enable tissue imaging
- Improving the microsurgery capabilities to enable both delivery of high energy pulses for ablation in tissue. .

Using the design methodology covered in the previous chapter, we have successfully reduced and streamlined the packaged size of this optical system such that it can now be incorporated into a custom endoscope and access a variety of clinical sites. In this chapter, we will investigate the imaging and ablation capabilities of this new prototype.

We begin by illustrating improvements made to the data acquisition and image reconstruction methods, followed by determining the focused laser spot size, and thus resolution, by measuring the PSF. In addition to the PSF, we will determine our maximum FOV and compare our experimental imaging capabilities with the performance predicted by our ZEMAX modeling. Additionally, we will image standard benchmark samples, such as pollen grains, to qualitative explore the imaging capabilities and allow comparison with other published nonlinear optical endoscopy systems. To finish the imaging characterization, we will explore our ability to identify morphology and image intrinsic signals in tissue.

Finally, we will explore the microsurgery capabilities of the new endoscope. To achieve rapid ablation over larger areas, we will introduce a new technique called plasmonic laser nanosurgery (PLN), in which bio-conjugated gold nanospheres will be used to aid imaging and ablation of cultured breast carcinoma cells. This technique not

only provides molecularly-specific imaging contrast to aid diagnosis, but also greatly reduces the ablation threshold of the labeled cancer cells.

6.1: CHARACTERIZATION OF IMAGING CAPABILITIES

The experimental setup used to demonstrate the new prototype (shown in Figure 6.1) is nearly identical to the setup used in Chapter 4, Section 4.2, with two key improvements. First, the microsurgery laser can pass through a single-grating pulse stretching system which pre-chirps pulses from the CPA to approximately 11.5 ps to compensate for dispersion in the PBF. Second, the 1 MHz current-to-voltage preamplifier used in the previous system was replaced with a high-speed current-to-voltage preamplifier (DHPCA-100, FEMTO Messtechnik). Operated in "High Gain" mode at a bandwidth setting of 14 MHz, the new preamplifier is able to provide twice the transimpedance gain of the previous preamplifier while sampling at 4 MHz. Using this increased sampling speed, the new endoscope captures 512 × 512 pixel images, increased from 256 × 256 pixels, without any missed pixels at the center of the FOV due to under-sampling. This increases the quality of the individual frames while ensuring that the Nyquist sampling theorem is upheld for all achievable FOV. Based on the resonant performance of the new MEMS scanning mirror, the mirror is driven at scanning frequencies of f_x = 2,263 Hz and f_y = 979 Hz to create a dense Lissajous pattern with a pattern repeat rate of 1 Hz. Using the image reconstruction algorithm discussed in Chapter 4, Section 4.3, we display images at a frame rate of 7 Hz to balance increased temporal resolution with single-frame image quality. At 7 Hz, between 75.7% and 76.4% of pixels are sampled in every frame, providing a good balance between single frame pixel sampling and imaging speed with good frame-to-frame consistency.

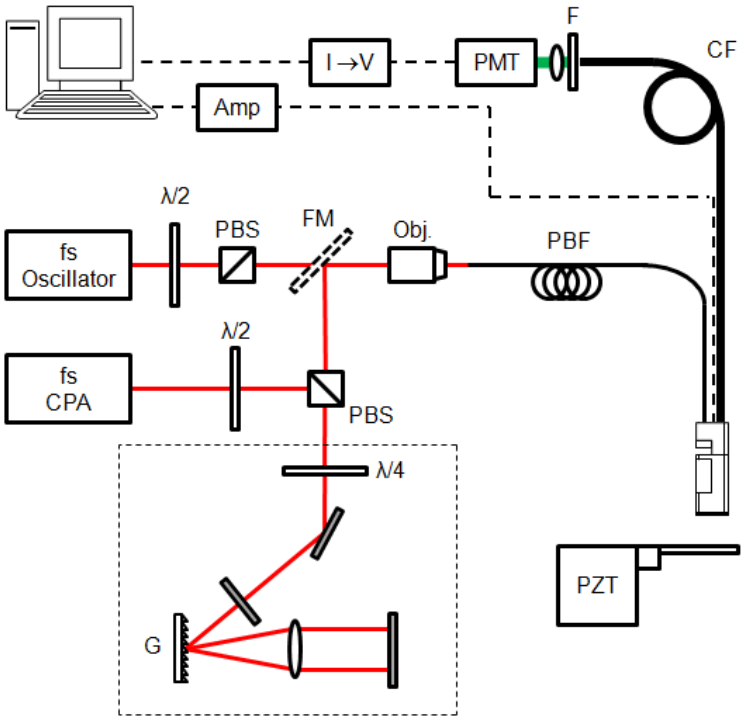

Figure 6.1. Experimental setup for testing the 9.6-mm probe. The experimental setup consisted of the prototype mounted inverted above a piezoelectric sample holder, similar to the testing of the first prototype. This new system includes a single-grating pulse stretcher for pre-chirping the microsurgery pulses, which is boxed in by the thin dashed line. **λ/2**: half wave plate; **PBS**: polarizing beam splitter; **λ/4**: quarter wave plate; **G**: reflective grating; **FM**: flipping mirror; **Obj**.: 0.25-NA objective lens; **PBF**: three meters of photonic bandgap fiber; **PZT**: piezoelectric translation stage; **CF**: one meter of plastic optical collection fiber; **F**: laser blocking filter; **PMT**: photomultiplier tube; **I→V**: current-to-voltage preamplifier; **Amp**: 200 V MEMS driving amplifier.

The improvement in image quality due to the new sampling and image acquisition settings can be seen in comparing images of 1 µm fluorescent beads dried on a microscope slide. Figure 6.2**a** shows a raw frame taken at a 7 Hz frame rate with an image size of 512 × 512 pixel images and a 4 MHz sampling rate using the new high-speed preamplifier. Figure 6.2**c** presents approximately the same FOV imaged with 256 × 256 pixels with data acquisition rate of 1 MHz using the original SRS preamplifier. The

image taken at 4 MHz samples more pixels in the center of the FOV, providing greater detail. Given the 110 µm × 110 µm FOV, the Nyquist sampling theorem is still satisfied with 256 × 256 pixels, however Figure 6.2**a** still appears to provide better resolution of single beads in the raw frames due to the insufficient sampling speed in Figure 6.2**c**. Even after acquiring seven frames to acquire the full Lissajous pattern, the 512 × 512 pixel image (Figure 6.2**b**) with the 4 MHz sampling rate provides noticeable improvement in signal-to-noise ratio when compared with the previous methodology (Figure 6.2**d**). As a result, the new endoscope requires less averaging of raw frames for producing low noise images.

Similarly, Figure 6.3 illustrates the ability of the 9.6-mm probe to capture increased dynamic information using the fast-updating Lissajous image reconstruction algorithm developed in Chapter 4, Section 4.3. In this experiment, 1 µm fluorescent beads (F-8823, Invitrogen) were dried onto a glass slide, after which a drop of water was placed over the beads. The water allowed some of the beads to become unfixed from the slide and move freely around the sample to provide movement. In the frames produced at 7 Hz using our method (Figure 6.3**a**), the motion is captured and the independent motion of each bead and agglomerate can be tracked across the three second acquisition time. The white circles in Figure 6.3**a** track an individual bead's trajectory from the entrance at the right of the FOV to its exit at the left. In the frames reconstructed using the traditional Lissajous reconstruction method (Figure 6.3**b**), where the frame rate equals the pattern repeat rate of 1 Hz, the temporal resolution is insufficient to identify the entry and exit points of the highlighted bead. Also, the crisp outline of the moving agglomerated beads is degraded by motion artifacts.

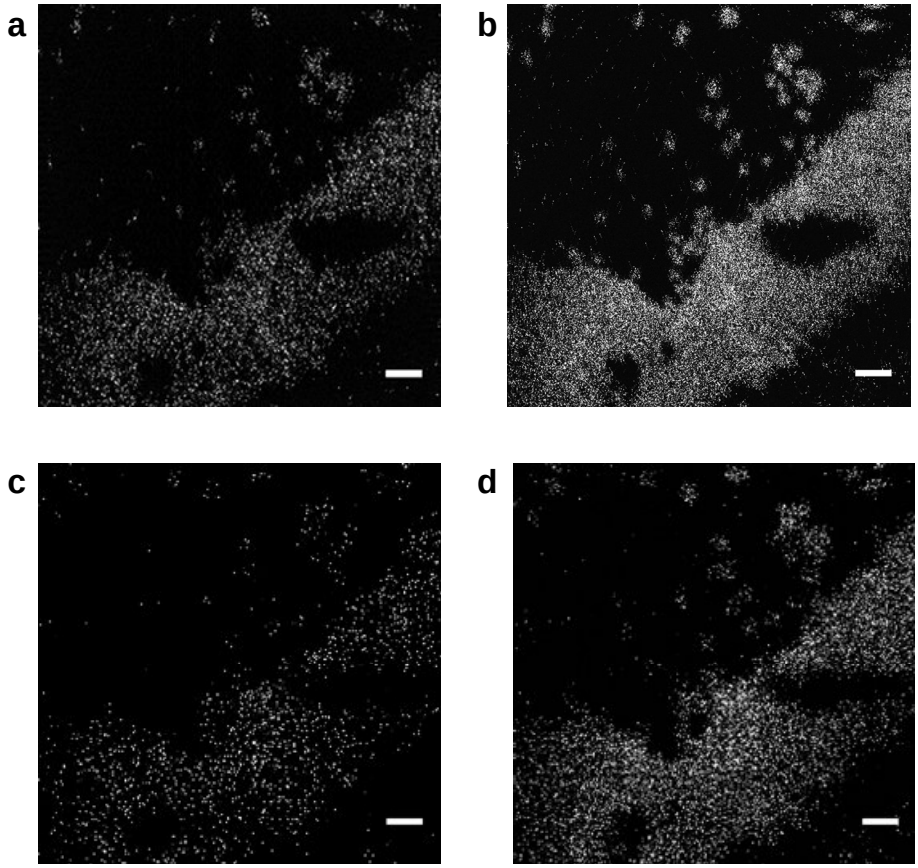

Figure 6.2. Comparison of new image sampling and reconstruction parameters with those of the previous prototype. a and **b**, A single raw frame and the maximum intensity projection of 7 frames, respectively, of agglomerated 1 µm fluorescent beads on glass taken with the 9.6-mm probe using a 512 × 512 pixel image size and sampling at 4 MHz with the FEMTO Messtechnik preamplifier. **c** and **d**, A single raw frame and the maximum intensity projection of 7 frames, respectively, taken with the 9.6-mm probe using the previous 256 × 256 pixel image size and sampling at 1 MHz with the SRS preamplifier. A slight shift of the FOV between the top and bottom image sets can be observed, which occurred while changing the preamplifier hardware in between images. Average laser power at the sample was 9 mW. Scale bars are 10 µm.

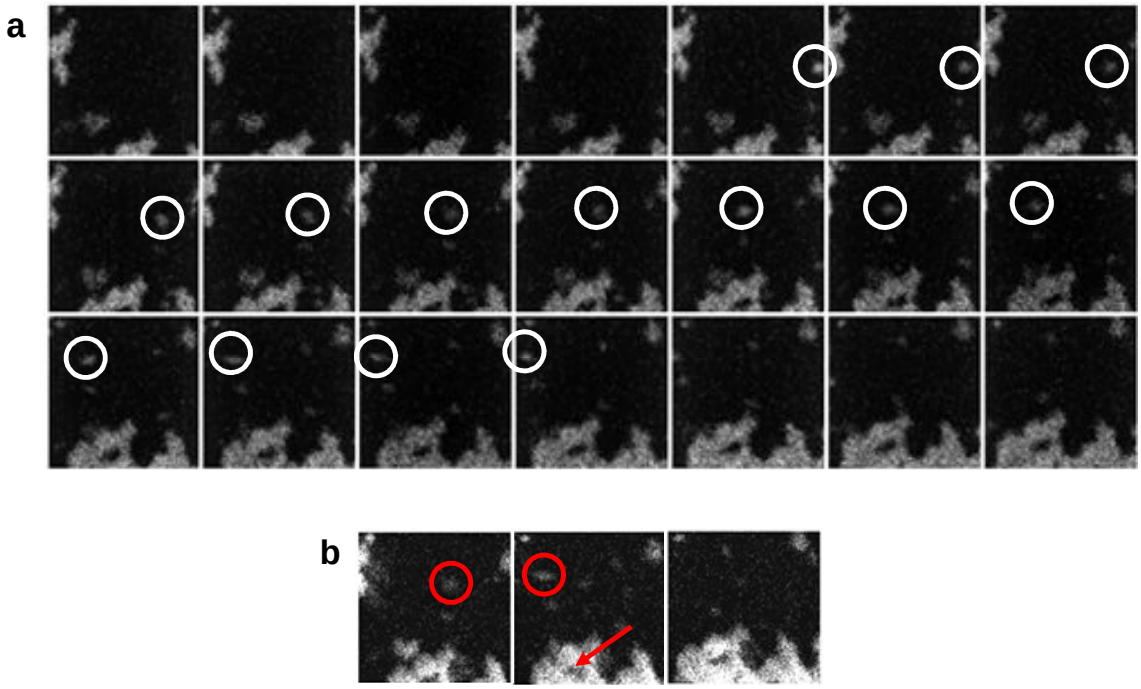

Figure 6.3. Comparison of time-elapse images using our fast-updating Lissajous image reconstruction method and using the traditional method. a A series of images of 1 µm fluorescent beads taken at 7 frames per second using our fast-updating Lissajous image reconstruction algorithm and the 9.6-mm endoscope. The beads were allowed to dry and then hydrated with water so that some beads and agglomerates move freely. **b** The corresponding traditional Lissajous-scanned images, updating at 1 frame per second, for the same data set. The white circles in **a** highlight a freely flowing single bead travelling across the FOV. Its trajectory can be clearly identified. The red circles in **b** highlight the same bead. The red arrow denotes one of the noticeable motion artifacts encountered using the traditional image reconstruction method. Single frame FOV is 35 µm × 35 µm and the average laser power at the sample is 10 mW.

Using the new prototype endoscope in this experimental setup, we can deliver a maximum average power of 60 mW to the sample from the Ti:sapphire oscillator for imaging and, based on our measured transmission efficiency, a maximum pulse energy of 180 nJ from the CPA for microsurgery. These values fall short of the maximum imaging

power and microsurgery energy predicted in Chapter 5 and are also significantly less than those of the 18-mm probe. The primary cause of this decreased transmittance is the added attenuation of the fiber collimation assembly, as discussed in the previous chapter. In addition to addressing this issue in future designs, the use of metallic coated MEMS mirrors will triple the transmittance of future endoscopes based upon our design. The lower deliverable laser powers for imaging and microsurgery can be partially offset by improvements to the resolution as well.

We experimentally measured the PSF of the new prototype using a bead-in-agar phantom similar to the samples used in the previous chapters. For this sample, we utilized 500 nm fluorescent beads (F-8813, Invitrogen) to improve the signal-to-noise ratio of our measurements. We took measurements over a 160 µm FOV to attempt to detect the off-axis aberrations predicted by the ZEMAX model. The average power of the laser at the sample was 27 mW.

The FWHM of the Gaussian fits to the lateral and axial PSFs are 1.32 µm ± 0.03 µm and 9.92 µm ± 0.40 µm, respectively. The measurements are averaged across 12 beads and the reported errors correspond to the standard error of the mean. Representative PSF measurements are provided in Figure 6.4. There was no statistically significant difference in PSF size for beads measured at different locations in the FOV, suggesting that the any aberrations arising on-axis in the 9.6-mm probe are sufficiently larger than those predicted by ZEMAX over a 150 µm FOV. While the 500 nm beads used in this experiment are significantly larger than the 100 nm beads used in our previous PSF measurements, we found the change in FWHM spot size due to deconvolution of the 500 nm bead to be less than 5% and so these measurements do not include deconvolution. There was no measurable asymmetry in the lateral PSF shape, though the analytical model predicted that some asymmetry may be present due to the rectangular effective aperture of the MEMS mirror. The lack of observed asymmetry is

because the PSF is not diffraction-limited and aberrations mask any small asymmetry that would otherwise be present.

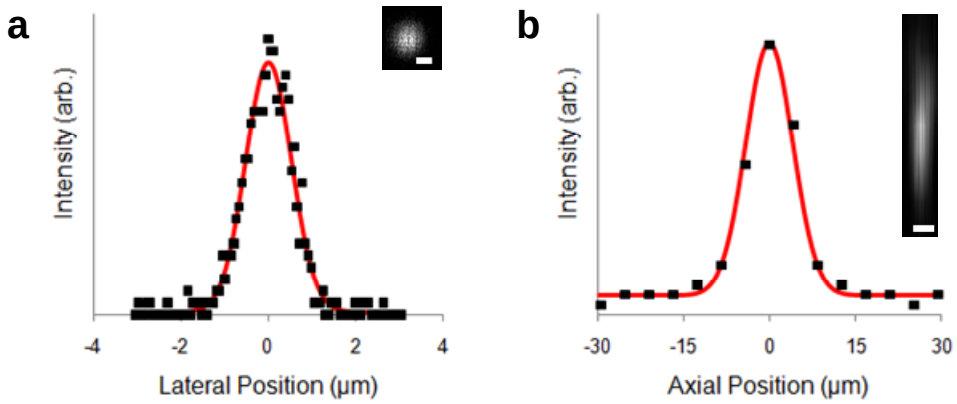

Figure 6.4. Example lateral and axial point spread function measurements for the 9.6-mm probe. a A representative PSF measurement showing the lateral resolution of the 18-mm probe. The inset image shows a single 500 nm bead used for PSF measurement, as imaged by the probe with 1 μm scale bar. **b** A representative axial PSF displaying the axial resolution. The inset image shows a *x-z* plane reconstruction showing the axial profile of a single 500 nm bead with 1 μm scale bar. The raw data is shown in black and the Gaussian fit to the data is provided in red. The average FWHM of the lateral and axial PSFs are 1.32 μm and 9.92 μm, respectively.

The measured PSF represents a notable improvement over the previous 18-mm probe, with a 20% decrease in lateral spot size and a 40% decrease in axial spot size. The measured PSF is significantly larger than the PSF predicted by the ZEMAX model, however. The model predicted that with a perfect Gaussian beam and ideal alignment the optimum lateral and axial resolutions at the center of the FOV would be 0.74 μm and 5.2 μm, respectively. Based on the beam profiling measurements taken during alignment of the prototype, the departure of the measured resolutions from the predicted values is most likely attributable to the spherical aberration and beam quality issues arising from the fiber collimation assembly. To avoid these aberrations, future designs should incorporate

a collimation assembly design that utilizes a larger aperture collimating lens and prevents the introduction of epoxy into the air space between the fiber and the lens. Despite not being diffraction-limited, however, the measured improvement in axial resolution will greatly improve the optical sectioning capabilities of this probe.

As with the previous endoscope, we imaged the slide of fixed pollen grains to provide qualitative visualization of resolution improvement and also a benchmark with which to compare the combined excitation and collection efficiency. Using the 9.6-mm probe, we imaged the same species of pollen grain as with the 18-mm probe, demonstrating that the spikes along the outer shell are now clearly resolved (see Figs. 6.5**a**-**c**). When comparing these pollen images with those taken using the 18-mm probe (reproduced in Figure 6.5**d**), the improved lateral and axial resolutions of the new prototype can be clearly seen. The spikes along the periphery of the pollen grains are better resolved with the new prototype due to the improvement in lateral resolution, while the improved axial resolution provides increased optical sectioning, which is evident in the series of axially spaced images provided in Figure 6.5**d**.

The average laser power used to image the pollen grains was in the range of 9.8-25 mW, slightly higher than the 9.0 mW used in the 18-mm probe. This increase in required power is most likely because longer axial resolution of the 18-mm probe excites more fluorescent molecules than the 9.6-mm probe in thicker samples. For a flat sample, the 10.0 mW average laser power used to image the 1 µm beads in Figure 6.3 is also slightly higher the 8.2 mW used to image the dried 1 µm beads with the 18-mm probe in Figure 4.15. This slight increase in imaging powers suggests that the combined excitation and collection efficiency of the 9.6-mm probe is comparable to the 18-mm probe for minimally scattering samples. Most likely, the increased excitation efficiency that would be expected from the smaller focused spot size is offset by the ~18% decrease in peak intensity anticipated by the Fourier analysis of the collimated beam profile (Chapter 5, Section 5.6). As with the 18-mm probe, this new 9.6-mm probe is able to image standard samples such as pollen grains and fluorescent beads using lower laser powers than the

other published devices listed in Table 2.1. This proves that we were able to conserve the high excitation and collection efficiency of the 18-mm probe even while reducing the packaged size by almost 50%.

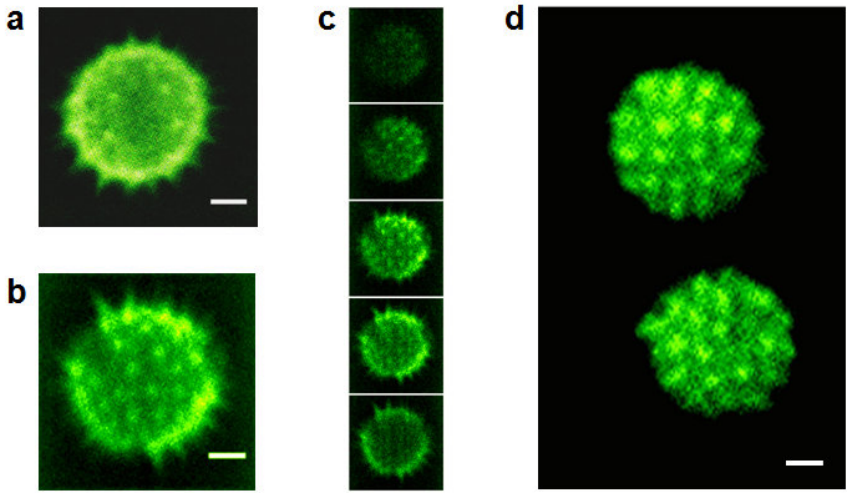

Figure 6.5. Comparison of two-photon fluorescence images of pollen grains taken with the two femtosecond laser microsurgery endoscope probes. a, **b** Representative images of pollen grains taken with the 9.6-mm probe. Due to improved optical sectioning, images are depth projections of axially spaced images to show 3D detail. The axial step between images is 4.2 µm with 14 frames (2 seconds) averaged at each step. Average laser power at the sample is 9.8 mW in **a** and 25 mW in **b**. **c** A series of axially spaced images used to construct the image shown in **b**, demonstrating the optical sectioning power of the new prototype. **d** Image of two pollen grains taken with the first 18-mm probe, provided for comparison. Average laser power was 9.0 mW at the sample with averaging at a single axial location over 50 frames (5 seconds).Scale bars are 5 µm.

Using a peak driving voltage of 45 V to both axes of the MEMS mirror, we imaged the rhodamine-stained tissue paper of Figure 6.2 to determine the maximum FOV (see Figure 6.6). At this driving voltage and using 7 mW average laser power, the maximal FOV of the 9.6-mm probe was measured to be 225 µm × 180 µm. The ZEMAX

predicted FOV (380 µm × 150 µm) is larger along the MEMS outer axis than the measured FOV, while the other axis is slightly shorter. The differences likely arise from changes in the quality of the electrical connections during wire-bonding and packaging. At two sides of the periphery of the FOV, the signal level decreases. The region of the FOV that provides the greatest signal is approximately 130 µm × 100 µm. That the area of best signal is not centered in the image suggests some misalignment in the probe, as it is unlikely that aberrations decrease at larger scan angles for a well-aligned probe. Despite the use of beam profiling and active alignment, one or more optics is likely sufficiently off-axis to produce this effect. Future devices will need to develop more stringent alignment techniques to achieve optimal performance. Lastly, a scanning device with static deflection capabilities might be used to compensate for this type of misalignment by providing a constant offset to the FOV.

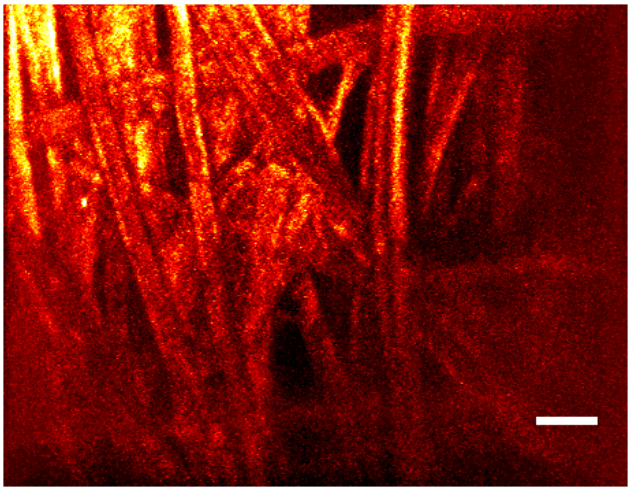

Figure 6.6. Maximum intensity depth projection image of rhodamine-stained lens paper showing maximum FOV. A peak driving voltage of 45 V was delivered to each actuator on the MEMS device to achieve the maximum FOV without risking damage to the MEMS scanning mirror. A depth stack of 135 µm total depth with 4.2 µm steps was taken to ensure that the presence of field curvature was accommodated. 14 frames were averaged at each step. Loss in resolution and signal intensity is observed along two sides of the FOV. The optimal resolution appears to be achieved over an area of roughly 130 µm × 100 µm, while the total FOV of the image is 210 µm × 160 µm. Average laser power at the sample was 7 mW and the scale bar is 20 µm.

To complete the characterization of the imaging capabilities, we investigated the ability of the new endoscope to visualize morphological features inside biological tissue and to utilize intrinsic sources of contrast such as SHG and autofluorescence. The first sample investigated is rat tail tendon. Rat tail tendon is a common nonlinear optical microscopy sample because it consists of dense and highly aligned collagen fibers that act as a strong source of intrinsic SHG and, to a lesser degree, autofluorescence. The sample was prepared from a tail harvested from a Sprague Dawley rat, after the animal had been euthanized as required for an unrelated approved research protocol at the Animal Resource Center of The University of Texas at Austin. After harvesting of the tail, the tail was then delivered to our lab in room-temperature saline, sections of tendon

were removed, and placed on a microscope slide in saline for imaging. Using the 9.6-mm probe, the fibrous structure of the rat tail tendon can be clearly visualized in Figure 6.7, without the introduction of exogenous contrast agents. The images in Figure 6.7 were acquired using an average power of 20 mW, which is 2.75× less than the 55 mW used by Wu *et al*. [140], providing further evidence that the combined excitation and collection efficiency of this prototype compares well with published systems. The successful imaging of the collagen-rich rat tail tendon demonstrates the potential to conduct nonlinear optical imaging based solely on intrinsic sources of contrast with our new 9.6-mm probe.

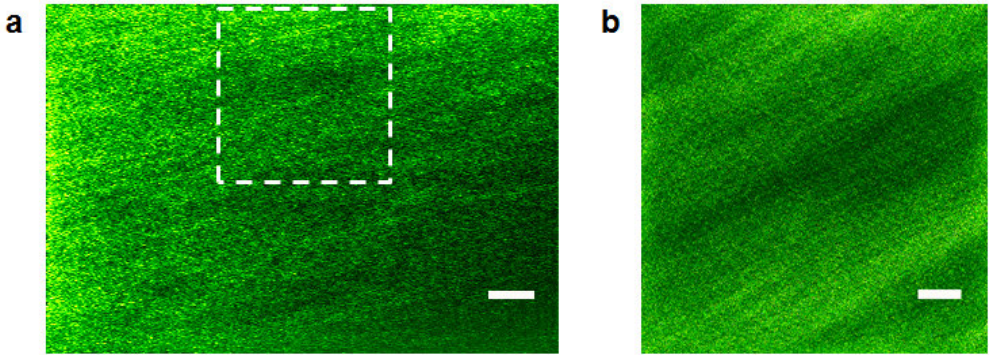

Figure 6.7. SHG images of rat tail tendon taken with the 9.6-mm femtosecond laser microsurgery and imaging probe. a At a FOV of 110 µm × 75 µm, the high degree of orientation in the fiber can be seen. The dashed white box represents the size of the 40 µm × 40 µm FOV shown in **b**. The average laser power at the sample was 20 mW and the scale bars are 10 µm and 5 µm in **a** and **b**, respectively. Both images are 14 frame averages.

In addition to rat tail tendon, we tested the capabilities of the 9.6-mm probe to image the epithelial layer of porcine vocal fold. Vocal fold tissue is of particular clinical interest because the treatment of scarred vocal folds presents a major clinical challenge as well as a unique application for femtosecond laser microsurgery that will be explored in the following chapter. Porcine larynx was obtained from a local slaughterhouse and

brought to our lab for dissection. After dissection, the superior vocal fold was excised. Initial imaging of the unlabeled vocal fold did not produce sufficient autofluorescent signal for imaging at approximately three hours after initial excision from the pig. To enhance the imaging signal, we then incubated the excised vocal fold in a 5 mL solution of phosphate-buffered saline (PBS) containing 5 μM Hoechst 3342 for 45 minutes. Hoechst 33342 is a cell-permeable dye which binds to DNA to provide nuclear contrast. Nuclear stains are preferable to cytoplasmic stains such as calcein AM for tissue imaging with our probes, as distinguishing the boundaries of closely packed cells with uniform fluorescence is difficult with an axial resolution $\geq$ 10 μm. The two-photon excitation spectrum of Hoechst 3342 (λ_{ex} ~ 650-750 nm) is better suited for the endoscope than those of the two other commonly used nuclear stains, 4",6"-diamidino-2-phenylindole (DAPI, λ_{ex} ~ 780-810 nm) and acridine orange (λ_{ex} ~ 780-900 nm) [182,183]. After incubation, the vocal fold sample was placed on a microscope slide and kept moist with PBS during imaging with the prototype (see Figure 6.8).

The images of the stained vocal fold clearly delineate the nuclei in the outermost cell layers of the epithelium and provide morphological information about nuclear size, cell density, and the surface contours of the vocal fold. Using an average power of 35 mW, only a one to two cell layers are clearly visible. Below these cells, the imaging power was increased up to the maximum deliverable power of 60 mW, however negligible increase in signal was observed. We believe this is because the Hoechst stain was unable to penetrate further into the tissue during incubation. The available literature on Hoechst staining pertains mostly to staining of thin tissue sections and cell cultures, and there is little information regarding the penetration of the dye through intact tissue. If the penetration of the dye proves to be limiting, clinical applications of the femtosecond laser microsurgery endoscope requiring exogenous contrast will need to identify a stain with improved penetration, as well as the desired excitation, emission, and binding characteristics.

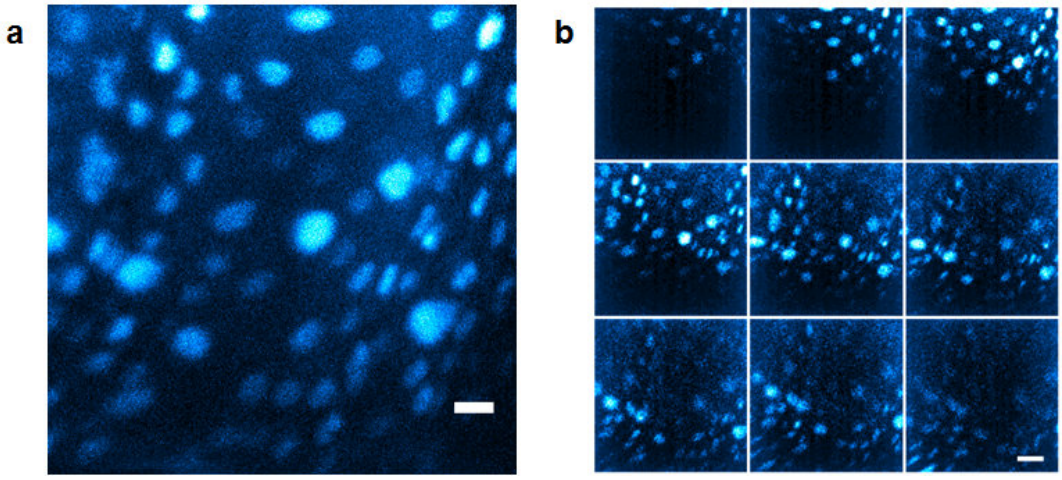

Figure 6.8. TPEF images of Hoechst 3342-stained porcine vocal fold epithelium taken with the 9.6-mm probe. a Maximum intensity depth projection from a series of images taken 4.2 µm apart axially, 14 frames averaged at each step. Total imaging depth is approximately 67 µm. **b** Montage of selected frames from the depth stack, showing the contour of the epithelium. Axial step between displayed images is 8.4 µm. Average laser power at the sample was 35 mW, scale bars are 10 µm in **a** and 20 µm in **b**.

We opted not to test microsurgery using the 9.6-mm probe as a result of concerns for damaging the fiber collimation assembly with amplified laser pulses. The drop in laser transmission that was observed after sealing the fiber collimation assembly has limited the maximum deliverable laser energy to the sample to an estimated 195 nJ per pulse. Given the decrease in lateral $1/e^2$ spot size to ~3.2 µm, from the 3.9 µm $1/e^2$ focal spot size of the 18-mm probe, 195 nJ should be sufficient for single pulse cell ablation with the 9.6-mm probe. However, most likely the drop in transmission and the accompanying distortions to the beam profile that occurred after sealing the collimation assembly are a result of UV-curing epoxy seeping into the fiber collimation assembly and occupying the space between the fiber and the collimating lens. If this is the case, the laser light enters the cured epoxy immediately upon exiting the fiber, at a beam diameter equal to the 6 µm core size of the fiber. With the measured transmission, delivering a 195

nJ pulse to the sample requires delivering a 1.6 µJ pulse to the exit of the fiber, where the 6 µm spot size would create a fluence of 5.7 J/cm^2. Since this is well above the damage threshold for glass of 2 J/cm^2 for NIR femtosecond laser pulses, it is highly likely that the epoxy would become ablated at the interface with the fiber and produce unpredictable and irreversible changes to the beam quality. For this reason, we have chosen to avoid delivering amplified laser pulses for microsurgery with the 9.6-mm probe, and instead we develop a new means of rapid cellular ablation using the plasmonic optical near-field enhancement of gold nanoparticles.

6.2: PLASMONIC LASER NANOSURGERY OF GOLD METAL NANOPARTICLE-LABELED CANCER CELLS FOR RAPID NON-THERMAL CELL DEATH

Though the maximum deliverable pulse energy in our 9.6-mm endoscope has ultimately proven to be limited in comparison to the 18-mm probe, our goal of enabling rapid ablation of larger areas of cells can still be achieved through the use of bio-conjugated gold nanoparticles. Recently, bio-conjugated gold nanoparticles have attracted attention as a means for enhancing the signal level and for providing molecularly specific contrast in nonlinear optical imaging through multiphoton-induced luminescence [122,123,184]. By conjugating such nanoparticles to ligands for receptors known to be over-expressed in particular pathologies, the particles enable selective visualization of diseased cells and may be useful in guiding treatment.

We have recently proposed and demonstrated that the same gold nanospheres and laser system can also be used as precise treatment agents, selectively disrupting the cellular membranes of labeled cells at laser fluences known to be safe for healthy cell types [185] and can lead to cell death. Cell death is caused by exciting plasmonic gold nanospheres using ultrafast laser pulses, where the ultrafast pulses are enhanced in the near-field of nanoparticles. The use of femtosecond laser pulses prevents thermal side effects that can lead to collateral tissue damage. Meanwhile, the use of the nanoparticles' near-field enhancement leads to focusing laser intensity to nano-volumes and further

improves the precision of femtosecond laser ablation beyond the diffraction limit. An additional benefit of this method is that it relaxes the requirements for laser guidance and tight focusing because damage will selectively occur wherever particles are bound. We term this nanoparticle-mediated ablation technique plasmonic laser nanoablation (PLN) [186,187]. The synergistic combination of molecularly-specific image enhancement and selective therapy suggest that gold nanospheres may present a promising modality for guided treatment of small cancerous cell masses in sensitive areas, such as neural tissue.

The clinical application of PLN requires the parallel development of flexible miniature imaging devices capable of delivering ultrafast laser pulses inside the body or to intraoperative surgical sites, such as our femtosecond laser microsurgery and microscopy probes. The use of bio-conjugated gold nanospheres for luminescent imaging and plasmonic ablation are particularly complimentary to our miniaturized microsurgical system as they enhance both the imaging and microsurgical capabilities.

In this section, we present preliminary results demonstrating combined multphoton luminescence imaging and plasmonic laser nanosurgery of gold nanosphere-labeled cancer cells using 9.6-mm image-guided microsurgery probe.

6.5.1: Experimental methods

For these experiments, we fabricated 50 nm diameter gold nanospheres using the Turkevich method. Specifically, the gold spheres possess a mean diameter of 49 nm and a standard deviation of 3.4 nm. The mean ellipticity of the particles is 1.22. Anti-epithelial growth factor receptor (αEGFR) antibodies are directly physisorbed to the particle surface with final average molar ratio of antibodies to particles of 1:630.

Carcinoma cells (MDA-MB-468) are cultured on cover slips that are also functionalized with αEGFR antibodies to bind the cells strongly to the glass substrate and ensure cells are not washed off during subsequent labeling steps. The nanoparticle bio-conjugate solution is allowed to interact with the cultured cells for 20 minutes at room temperature, followed by two washes with phosphate-buffered saline prior to use with the

endoscope prototype. Dark field light microscopy and multiphoton luminescence images from a bench-top microscope illustrate the degree of labeling (Figure 6.9**a**).

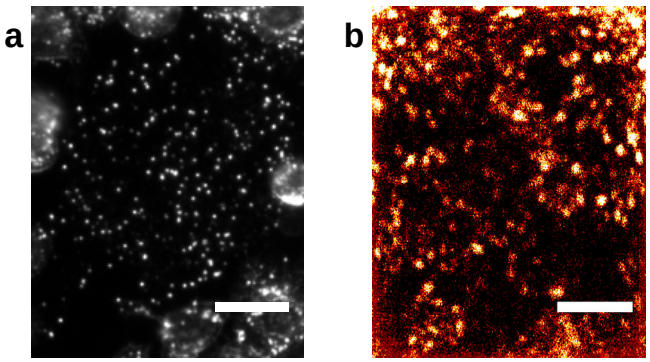

Figure 6.9. Image of breast carcinoma cells labeled with 50 nm gold nanospheres. a Dark field microscopy image of gold-nanosphere labeled cells, where the bright punctuate objects are the nanospheres. From this image, the degree of labeling can be observed. **b** Two-photon luminescence image of gold nanosphere-labeled breast carcinoma cells taken with the 9.6-mm probe. This image is an average of 14 frames (two seconds). The average laser power at the sample is 16.5 mW. Scale bars are 20 µm.

Using the 9.6-mm probe, we acquired an image of each cell culture using the multiphoton luminescence of the labeled cancer cells. This image serves to verify the success of the labeling protocol and to locate the focal plane on the cell layer. To enhance the signal to noise ratio of the images, images were acquired for two seconds and averaged using an average laser power at the sample of 16.5 mW. After imaging, the sample is translated 200 µm at a time to a series of new fields of view, irradiating each field for two seconds at decreasing laser fluences to determine the threshold for PLN.

The average powers delivered to the sample in our experiment are 25.2, 18.9, 12.6, 9.5, and 6.3 mW. The $1/e^2$ diameter of the focal spot in our 9.6-mm probe is 3.17 µm, based on the earlier PSF measurements, so these fluences correspond to 4.0, 3.0, 2.0, 1.5, and 1.0 mJ/cm^2. On either end of the series of irradiated FOV, we also irradiate a

FOV for ten seconds at 7 mJ/cm^2 to act as fiduciary marks with which to identify our experimental series later under wide-field fluorescence microscopy.

For preliminary investigation into the mechanism of cell death, after multiphoton luminescence imaging of one sample we add 100 µL of 10 kDa fluorescein isothiocyanate (FITC)-dextran solution to the cells at a concentration of 25 mg FITC-dextran to 25 mL PBS. The 10 kDa FITC-dextran is membrane impermeable and thus is used to indicate disruption of cell membranes due to PLN. We conduct a similar irradiation series using 3.0, 2.0, 1.5, 1.0, and 0.5 mJ/cm^2 to correlate the threshold for cell death with the threshold for membrane optoporation.

After the irradiation of each field, the sample is washed twice with PBS to remove extracellular FITC-dextran (if used) and then immersed in 14 µM calcein red-orange acetoxymethyl ester (AM) for 10 minutes at room temperature. After two more washes with PBS, we image the cells under a wide-field fluorescence microscope (BX51, Olympus) using filter sets for FITC and tetramethyl rhodamine isothiocyanate (TRITC) to isolate the FITC and calcein red-orange signals, respectively. Using this protocol, the dead cells can be identified as those displaying a lack of red-orange emission. For the FITC-labeled cells, cells that are transiently optoporated during irradiation will produce yellow-green fluorescent emission due to the uptake of FITC-dextran when viewed with the FITC filter. Cells that are permanently optoporated will not express any dye.

6.5.2: Results and Discussion

A representative multiphoton luminescence image of nanoparticle-labeled carcinoma cells taken with the 9.6-mm probe is provided in Figure 6.9**b** where the circular shape of the labeled cells can be observed. Due to the ~10 µm axial resolution of our probe, some remaining unbound nanoparticles can be observed on the substrate surface as well. For comparison, we also labeled a culture of the carcinoma cells using only calcein AM, with no nanoparticles, following the protocol outlined in Chapter 4, Section 4.5 and found that imaging these cells with the 9.6-mm probe required 13.5 mW

average laser power at the sample. The 13.5 mW average power is comparable to the 16.5 mW average laser power used to image the nanoparticle-labeled cells, demonstrating that the gold nanoparticle bio-conjugates provide signal as bright as traditional organic dyes while providing enhanced molecular specificity. These laser powers are well below the powers required to image intrinsic fluorophores with the 9.6-mm probe, indicating that labeling gold nanoparticles to cancer cells with disease-specific antibodies has the potential to enable high-contrast diagnostic imaging.

Figure 6.10**a** shows a wide-field fluorescence microscopy image of labeled cells after 2 seconds irradiation with the 9.6-mm probe at a series of different laser fluences. At a fluence of 4.0 mJ/cm^2, we observe near total cell death within a 105 µm × 110 µm region. This area is within one to two cell widths of the 80 µm × 90 µm imaging field of view. At 3.0 mJ/cm^2, the region of cell death decreases slightly below the imaging field of view. At 2.0 mJ/cm^2, only eleven cells in the central portion of the irradiated area show an absence of calcein red-orange activation, indicating that the threshold for cell death lies near this fluence. Below 2.0 mJ/cm^2, no cell death is observed.

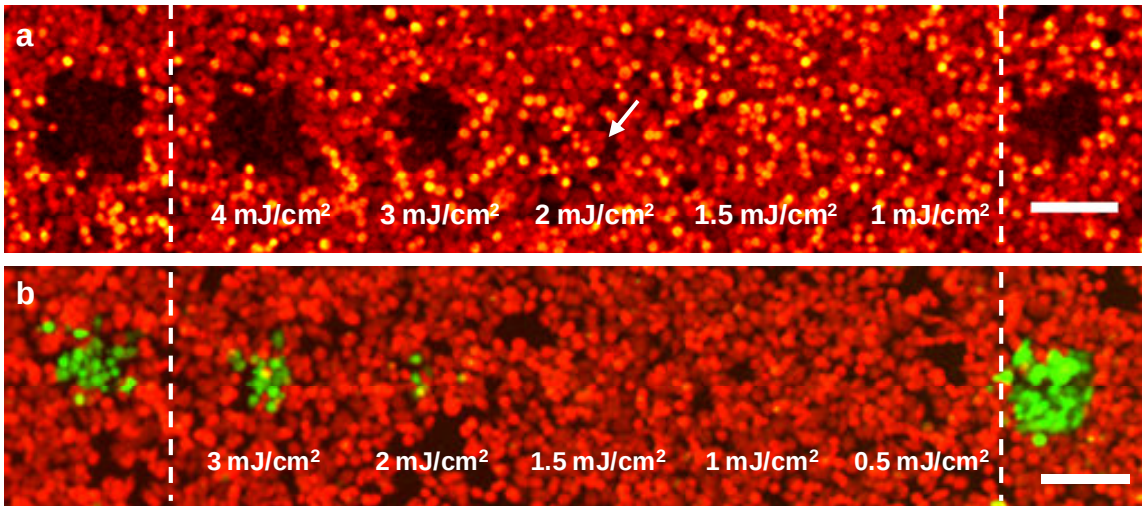

Figure 6.10. Wide field fluorescence microscopy images of gold nanoparticle-labeled breast carcinoma cells after PLN with the 9.6-mm probe in two different experiments. The regions between the dashed white lines denote the experimental data set where the cells were irradiated with different fluences for 2 seconds. Outside the dashed lines, areas were irradiated with 7 mJ/cm^2 for 10 seconds, to serve as fiduciary markers delineating the experimental series. **a** Wide-field fluorescence microscopy using only the introduction of calcein red AM after femtosecond laser irradiation to distinguish dead cells. Near total cell death is observed at 4 mJ/cm^2, while only a few cells are killed at 2 mJ/cm^2. **b** With FITC-dextran present during femtosecond laser irradiation, transiently porated cells exhibit green fluorescence. Cell death and FITC-dextran uptake were found to be correlated for all fluence levels. Again only few cells are porated and killed at 2 mJ/cm^2, while widespread poration and death is noted at 3 mJ/cm^2. Scale bars are 100 µm.

The 16.5 mW average laser power used during imaging corresponds to a fluence of approximately 2.6 mJ/cm^2, which is above the fluence observed to cause cell death. Indeed, during post-irradiation wide field fluorescence microscopy, the imaged area was consistently observed to contain dead cells. For the proposed application of image-guided therapy, that cellular death is concomitant with imaging is acceptable, as only diseased cells are heavily labeled. To enable imaging without harming the viability of the labeled

cells, for purely diagnostic purposes for example, will require further enhancement of the collection efficiency of the probe.

When FITC-dextran was introduced to the cells prior to irradiation, the same cell death trends are observed (Figure 6.10**b**). Irradiation at 3.0 mJ/cm^2 leads to cellular uptake of FITC-dextran over the majority of the irradiated area indicated by green cells, while irradiation at 2.0 mJ/cm^2 shows significantly less uptake of FITC-dextran, in this case only by six cells near the center of the irradiated area out of approximately 70 cells. No uptake of FITC-dextran is observed for fluences below 2.0 mJ/cm^2. Correlating the images of FITC emission with those of the calcein emission, we find that cellular uptake of FITC-dextran within the irradiated regions is appears to be accompanied by cell death over the range of fluences investigated. This 1:1 correspondence strongly suggests that the part of the mechanism of cell death during irradiation is transient cell membrane disruption which we attribute to the presence of the membrane-conjugated gold nanoparticles. Because our axial focal volume is large enough to encompass the full height of a cell, the transient optoporation that the cell experiences during irradiation likely covers the entire surface area of the cell, which appears to be sufficient for causing cell death without causing permanent disruption of the membrane.

Interestingly, the onset of cell death observed at 2.0 mJ/cm^2 remained limited to the central portion of the irradiated area. As the Lissajous scanning pattern reaches maximum speed at the center of the field of view and slows significantly when changing directions at the periphery, the peripheral cells receive a larger number of overlapping pulses during scanning and could be expected to exhibit a lower threshold for cell death. That this trend was not observed indicates that fluence ultimately plays a stronger role in determining cell death than the number of pulses received.

Cell death from PLN also appears to occur well below the death threshold for healthy cells. Assuming a pulse duration at the sample near 280 fs, the 4.0 mJ/cm^2 fluence that was observed to reliably kill near 100% of cells in two seconds corresponds to a peak intensity of approximately 13 GW/cm^2. Similar to what was shown with the 18-

mm probe, this intensity is 2-6× lower than the intensities that have been demonstrated to impair viability of healthy cells in previously published studies [172-175], while the RMS number of overlapping pulses is less by a factor of 3.8-7.2×. This comparison indicates that 4.0 mJ/cm^2 could be used to selectively destroy labeled cells without collateral damage to unlabeled healthy cells. This is further supported by the clear boundaries observed for PLN at this fluence where cell death is limited to the irradiated area. This low fluence and high degree of damage confinement make PLN an attractive potential tool for cleaning up tumor margins around sensitive tissue, for example along the spinal cord.

The 13 GW/cm^2 intensity used here for PLN is approximately three orders of magnitude lower than the peak intensities used for cellular ablation with our 18-mm microsurgery probe [109]. It is this vastly decreased intensity threshold that enables the use of a single laser oscillator for imaging and therapy and eliminates the need for a laser amplifier. The elimination of the chirped pulse amplifier used with our previous probe greatly reduces the overall size, cost, and complexity of the complete imaging and microsurgical system, making it more attractive for clinical adoption. Thus the use of PLN with bio-conjugated gold nanoparticles provides an alternative approach to femtosecond laser microsurgery and may ease the degree of laser guidance necessary to avoid damaging healthy tissue. Size and cost can also be addressed by utilizing a single amplified fiber laser system for both imaging and ablation [110], and the next chapter will discuss the development of a new femtosecond laser treatment application based upon a single fiber laser platform.

Chapter 7: Developing Application – Treatment of Scarred Vocal Folds

Thus far, our development of a femtosecond laser microsurgery endoscope has been driven by the general need for flexible delivery of high intensity femtosecond laser pulses to enable a wide range of potential clinical applications. Further development of this microsurgical tool into a clinical device will need to be focused on a specific clinical application to ensure that the final device can achieve a defined clinical outcome. The most desirable application is a clinical problem which can only be addressed by the unique capabilities of femtosecond laser microsurgery, such as the ability to create cuts inside the bulk of tissue or to ablate with minimal thermal or mechanical side effects. Furthermore, the desired outcome should be achievable using laser parameters we have found to be attainable in a miniaturized and fiber-coupled optical system.

We have recently begun development of one particularly attractive clinical application, which is the treatment of vocal fold scarring. This chapter will cover the bench-top exploration of this application, demonstrating the feasibility of creating clinically useful voids in porcine vocal fold using laser energies and scanning speeds that can be achieved in endoscopic systems. The chapter will first summarize the problem of vocal fold scarring, then describe the unique experimental procedure, and finally present femtosecond laser ablated sub-epithelial voids in vocal fold tissue, as verified by *in situ* nonlinear optical imaging and follow-up histology.

7.1: BACKGROUND

Vocal fold scarring, resulting from disease, mechanical stress from overuse, or post-surgical healing, reduces the mechanical compliance of vocal fold tissue and is a major cause of voice disorders. It is estimated that between 2 to 6 million people in the U.S. alone suffer from chronic voice impairment due to vocal fold scarring [188]. Unfortunately, there currently exists no reliable treatment for restoring proper phonation

in scarred vocal folds. One treatment method that has shown promise utilizes the injection of soft biomaterials aimed at restoring the proper viscoelasticity to the tissue [189]. In scarred vocal fold tissue, the density of the tissue and the required injection pressure impair proper localization of the injected material in the desired tissue layer, reducing the effectiveness of the injection treatment. To enhance treatment effectiveness, we are investigating a technique to ablate sub-epithelial planar voids in vocal fold tissue using femtosecond laser pulses to localize injected material.

Vocal fold tissue has a layered structure that consists of the epithelium at the outermost layer followed by the lamina propria and the vocalis muscle. The lamina propria is divided into the superficial, intermediate, and deep lamina propria layers. The superficial lamina propria (SLP) has a band of collagen that is highly aligned along the length of the vocal fold in its superficial aspect [190]. The layer below the collagen band consists largely of elastic fibers (primarily elaunin and oxytalan) in a random arrangement along with amorphous ground substance (consisting largely of proteoglycans and glycosaminoglycans) [189]. As a result, the SLP is often described as having a “jelly-like” viscoelasticity. The SLP and the epithelial layer make up the mucosa, which is the vibratory outer layer of the vocal fold responsible for phonation. During the wound healing response, scar tissue can replace the mucosal layer. The scar tissue consists predominantly of collagen and fibronectin, both of which increase the stiffness of the mucosa and lead to dysphonia [191]. The proposed treatment method focuses on injecting soft biomaterials, such as hydrogels and microgels, to mimic the mechanical properties of healthy tissue, or to use biologically active materials, such as hyaluronic acid, which can limit collagen formation [191,192]. Direct injection of such materials in scarred vocal fold leads to a localization of biomaterial around the point of injection and often significant backtracking from the injection site due to low tissue permeability and the high injection pressures required. It is hypothesized that the creation of a planar void in the SLP, covering the approximate width and length of the active area of the mucosa affected by scarring (estimated to be maximally 3×10 mm^2), will provide

a space for the injected material to fill, thus reducing the required injection pressure and improving localization of the material throughout the targeted layer.

Focused ultrafast laser pulses are uniquely suited for creating the sub-surface void due to their ability to create confined ablation beneath the surface of scattering tissue. Furthermore, the high degree of damage confinement is especially important when working with delicate tissue such as vocal folds and may serve to prevent any new scar formation. Recently, successful femtosecond laser microsurgery of vocal fold tissue has been demonstrated, showing the potential for sub-surface ablation confined within the sub-layers of the lamina propria [68]. Additionally, scar tissue consists predominantly of collagen fibers, which we provide a strong SHG signal that we have successfully imaged with our latest femtosecond laser microsurgery endoscope. The use of low-energy femtosecond laser pulses for imaging can provide a means for visualizing the region of surgery with the identical field of view and resolution of the surgical laser.

With the development of our two prototype femtosecond laser microsurgery endoscopes, the door is now open for the development of new surgical applications of femtosecond laser pulses, such as the laryngeal surgical technique proposed here. For these initial exploratory experiments, we investigated the creation of thin voids within *ex vivo* porcine vocal fold samples using a bench-top microscope system [110]. We ensured that the desired voids could be created using laser parameters (e.g., spot size, scanning speed and pulse energy) that are readily achievable in miniaturized, fiber-based optical systems and also using a single compact laser system suitable for use in a clinical environment.

7.2: EXPERIMENTAL SETUP

For these experiments, we used a home-built, bench-top laser-scanning microscope with microsurgery and nonlinear imaging capabilities, shown in Figure 7.1. For both microsurgery and nonlinear imaging, we use a 500 kHz repetition rate erbium-doped fiber laser (Discovery, Raydiance Inc.). When frequency-doubled, the laser

produces 750 fs pulses at 776 nm and a maximum pulse energy of 2.5 µJ. The laser is delivered into a laser scanning microscope and focused at the sample with a 0.75-NA, 20× air objective (Nikon Plan Apo 20×/0.75) for both multiphoton imaging and femtosecond laser microsurgery. We measured the focused spot size of the laser beam by imaging 100 nm fluorescent beads suspended in agar gel and measuring the point spread function (PSF) using the PSF protocol from Chapter 4, Section 4.4. To better simulate the focusing conditions below the epithelial layer, the PSF was measured between imaging depths of 60 to 120 µm. The average lateral full width at half maximum (FWHM) of the two-photon PSF was found to be 0.78 µm, which corresponds to a 1.88 µm $1/e^2$ diameter of the intensity distribution. ZEMAX modeling of the 9.6 -mm probe showed that this focused spot size is readily attainable in miniaturized femtosecond laser surgery probes. For microsurgery, the laser beam was scanned by the *x*-axis of a pair of galvonometric scanning mirrors (Cambridge Technologies, Inc.), while the sample was translated using precision stepper-motor stages (NanoMax MAX343, Thorlabs, Inc.) in the *y*-axis.

The duration of surgery is a key factor in development of a clinical technique. Our goal was to minimize ablation duration while using low pulse energies that are deliverable through a fiber-coupled miniature optical system. The duration of ablation depends on the beam scanning speed and thus the degree to which sequential pulses overlap each other (or the distance between sequential pulses) at the focal plane. The degree of pulse-to-pulse overlap, on the other hand, determines both the ablation volume and the speed of ablation, two competing parameters that require optimization. A high degree of overlapping increases pulse-to-pulse accumulation effects providing the desired extent of tissue ablation at lower pulse energies. For a fixed repetition rate, increasing pulse overlap decreases the speed of ablation, thus increasing the time required for ablating a given region. We therefore chose to perform our experiments using 4 overlapping pulses by deflecting the laser beam such that 75% of the focused spot diameter overlapped the spot of the previous pulse. The length of the line scanned by the galvo-mirror on the tissue was chosen to be 300 µm, which is readily achievable with our

18-mm probe [109]. Our earlier ZEMAX modeling suggests that this scanning range can even be extended in future devices without compromising the focal spot size. To achieve 75% pulse-to-pulse overlap with the 300 µm field of view, the mirror scanning speed was 390 Hz, and the translation speed of the *y*-axis was 0.72 mm/s.

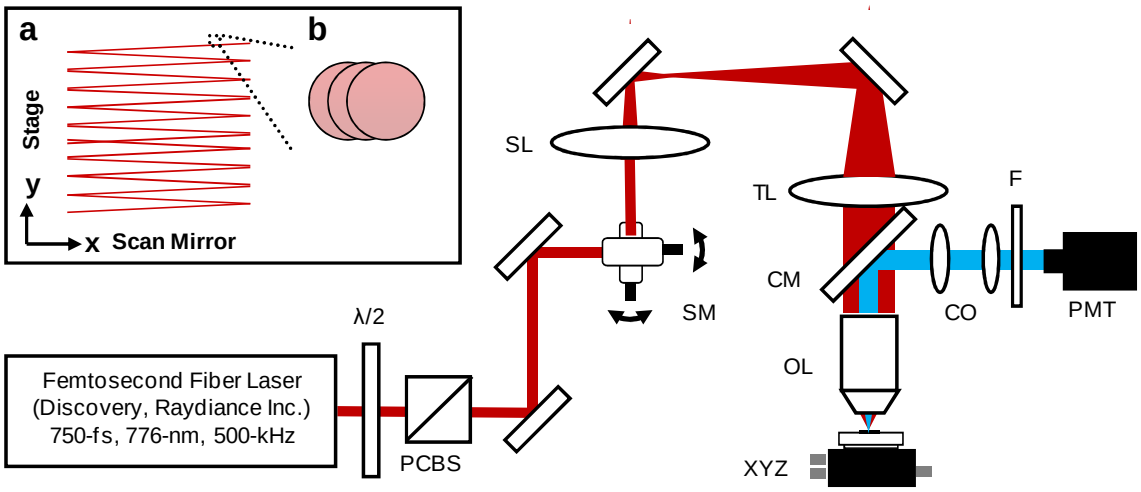

Figure 7.1. Schematic representation of the bench-top microsurgery microscope system used for combined imaging and microsurgery. Femtosecond laser pulses are delivered from a compact fiber laser system to a half-wave plate (λ/2) and polarizing cube beamsplitter (PCBS) for energy attenuation. The beam is scanned by galvanometric scanning mirrors (SM) through a scan lens (SL) and tube lens (TL) which image the mirrors to the back aperture of a 0.75-NA 20x objective lens (OL). The laser is used to either ablate or image the sample on a three-axis motorized stage (XYZ). Emitted light is redirected by a cold mirror (CM) through collection optics (CO) and a laser-blocking filter (F) to the photomultiplier tube (PMT). The PMT, stage, and scanning mirrors communicate with a personal computer via data acquisition cards, not shown. Inset: **a** Schematic of the laser scanning pattern at the sample during microsurgery. Translation of the sample stage provides beam scanning in the *y* direction. For imaging, a similar raster pattern is employed with the scanning mirrors provide beam scanning in both *x* and *y* directions. **b** Illustration of the degree of overlap between subsequent laser pulses during imaging and microsurgery.

For multiphoton imaging, the laser beam was scanned over a 550×550 μm^2 field of view using both axes of the scanning mirrors. We separated the emitted light from the laser light by a cold mirror (HT-1.00, CVI Laser), directed it into a PMT (H7422-40, Hamamatsu) and reconstructed the signal into 512 × 512 pixel images at a frame rate of 0.75 frames per second. This imaging speed roughly corresponds to the same 75% pulse-to-pulse overlap used during surgery. We chose to keep the laser scanning speed approximately equal for both microsurgery and imaging because most miniaturized beam scanning systems rely upon resonant actuation and exhibit optimum deflection at a fixed frequency. The use of the same scanning speed for both imaging and surgery was chosen to demonstrate that both functions could be achieved using a single resonant scanning device in the future.

During imaging, we occasionally performed simultaneous two-photon excited fluorescence (TPEF) and SHG imaging using our wavelength-tunable Ti:sapphire oscillator set to 870 nm excitation wavelength and a bandpass filter (436/20 nm) inserted before the PMT. The filter effectively blocks the majority of TPEF signal generated at this wavelength while passing any frequency-doubled signal generated by SHG. This protocol enables us to determine whether the source of our signal is fluorescent or SHG in nature. We used the wavelength-tunable laser simply to access the pass-band of the filter currently used in our lab.

We acquired frozen whole porcine airway specimens from a local slaughterhouse, after which the larynx was isolated and thawed in a room-temperature saline bath. Porcine vocal folds have a layered lamina propria very similar in organization and constituents to human vocal folds. Preliminary nonlinear imaging and histology of the superior vocal fold showed the presence of a prominent collagen band at the uppermost extent of the SLP, which was not identified in the inferior fold. Because scarred human vocal fold consists of dense collagen, we chose the superficial vocal fold for our experiments so as to better model the structural components and sources of nonlinear image signal we expect to find in the first few hundred microns of scarred human vocal

fold. Additionally, recent studies suggest that the superior vocal fold may play the dominant role in porcine phonation, similar to the inferior or "true" vocal fold in humans [193]. After excision, the vocal fold was placed in saline and covered by a glass cover slip to flatten the upper surface. The cover slip acted to gently flatten the surface of the sample so that a uniform plane could be accessed for experimentation. In a clinical application, the glass cover slip would be akin to having the window of a microsurgery probe in contact with the sample, thus helping to maintain a constant depth of ablation. As a result of the freezing process, little cellular autofluorescence was present from which the surface of the sample could be identified during imaging. To ensure proper identification of the tissue surface, 5 µL of a solution of 1 µm fluorescent beads in saline (0.002% solids after dilution in PBS, F-8823, Invitrogen) was deposited onto the tissue surface prior to placement of the cover slip. Samples that were to be examined by follow-up histology were placed in 10 mL 10% formalin (SF98-4, Fisher) immediately after ablation and TPEF/SHG imaging and stored at 4º C for at least 48 hours prior to delivery for histology preparation, paraffin embedding, sectioning, and hematoxylin and eosin (H & E) staining (TherapeUTex; Austin, Texas).

7.3: SUB-EPITHELIAL VOID FORMATION AT VARYING FLUENCES

We used nonlinear imaging to target the ablation within the desired tissue architecture of the vocal folds before the ablation and to verify the success of the ablation after the procedure. Figure 7.2 shows a representative image stack through the vocal fold mucosa of one sample before ablation. The tissue surface was readily identified by the presence of the fluorescent beads (Figure 7.2**a**). As imaging depth was increased, we detected SHG signal which appeared to correspond to highly organized and dense collagen fibers. The depth at which collagen first appeared varied significantly between samples, ranging from 24 µm to 55 µm below the surface (Figure 7.2**b**), while the depth at which the image plane was entirely within the collagen varied between 60 µm and 75 µm below the surface (Figure 7.2**c**).

We verified whether the fibers were indeed collagen, rather than elastin using the SHG differentiation protocol described earlier. The images with and without the filter at constant imaging power demonstrated equal signal intensity, indicating that the signal source was SHG and not TPEF; collagen fibers are well known sources of SHG, while nonlinear optical signal from elastin fibers is due to the more broadband TPEF [194]. The identification of a large amount of collagen highly-oriented along the length of the vocal fold is consistent with the structure of the upper SLP in porcine vocal fold [195]. We therefore determined the collagen interface to be the interface of the epithelial and SLP layers and chose it as our desired plane of ablation.

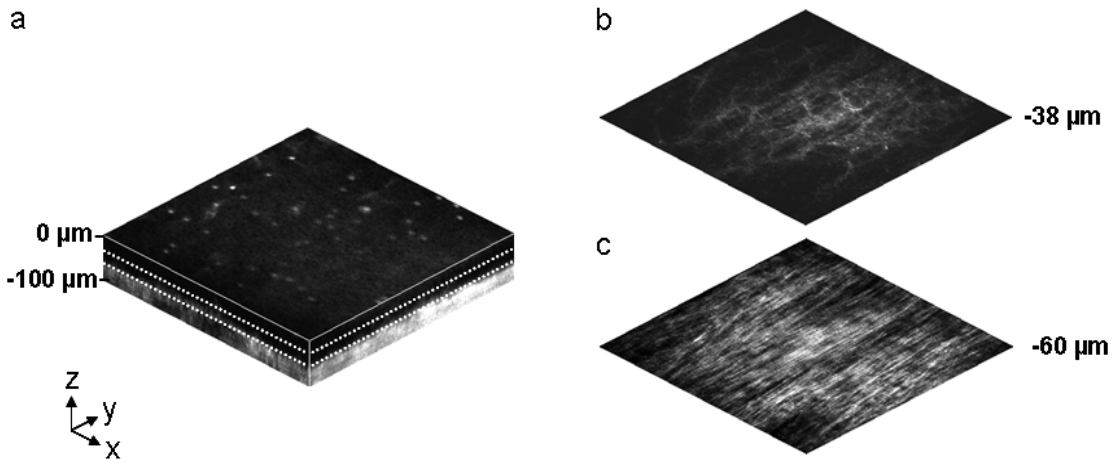

Figure 7.2. Representative nonlinear images of excised porcine vocal fold mucosa. a Three dimensional reconstruction of the image stack. Each image comprises a five-frame average and the separation between each image is 2 µm. The punctuated bright spots on the surface are the fluorescent beads that were placed for surface identification. Total imaging depth is 100 µm and lateral field of view is 550 × 550 μm^2. Dotted lines in **a** represent the planes shown in **b** and **c**, at depths of 38 µm and 60 µm below the surface, respectively. The average laser power during imaging was 0.85 mW at the surface, gradually increasing to 4.35 mW at a depth of 100 µm below the surface. In **c**, the imaging plane is entirely within the collagen and the straight, strongly aligned fibers can be clearly seen.

We investigated sub-surface void formation by irradiating a series of 300 µm × 300 µm squares at the epithelium-SLP interface using pulse energies of 50, 100, 500, and 750 nJ. These pulse energies correspond to fluences of approximately 1.8, 3.6, 18, and 27 J/cm^2, respectively. The size of the ablation was chosen so that the entire region of interest could be visualized before and after ablation using the 550 µm × 550 µm field of view of the multiphoton microscope. In some cases, nonlinear imaging 1 minute after ablation revealed a region or regions of signal loss. We considered these dark regions as the location of the photo-disrupted area and classified them as voids or bubbles. Because the source of the collagen imaging signal is SHG, we can rule out photobleaching as the cause of lost signal in this region. Furthermore, we observed deflection of the surrounding collagen in cases of larger voids, supporting the view that bubble expansion occurred rather than a photochemical depolymerization of collagen.

Figure 7.3 presents a representative example of a sample ablated with 100 nJ pulses. While we did not observe any noticeable tissue modification using 50 nJ pulses, irradiation with 100 nJ pulses produced a very thin plane of induced luminescence around the irradiated region and occasionally small localized voids within that region. Figure 7.3 shows the induced luminescence after ablation with 100 nJ laser pulses. When a notch filter was employed to filter out broadband fluorescent emission as before, this luminescence signal could not be detected. The broadband nature of the luminescence signal indicates that it is fluorescent in nature rather than due to an enhancement or generation of second harmonic signal. This luminescent border appeared long-lived and could still be observed one hour after ablation. Though the mechanism behind the increased luminescence has yet to be determined, this phenomenon has been observed by several other groups using fluorescence imaging to visualize femtosecond laser ablation of tissue [107,196,197].

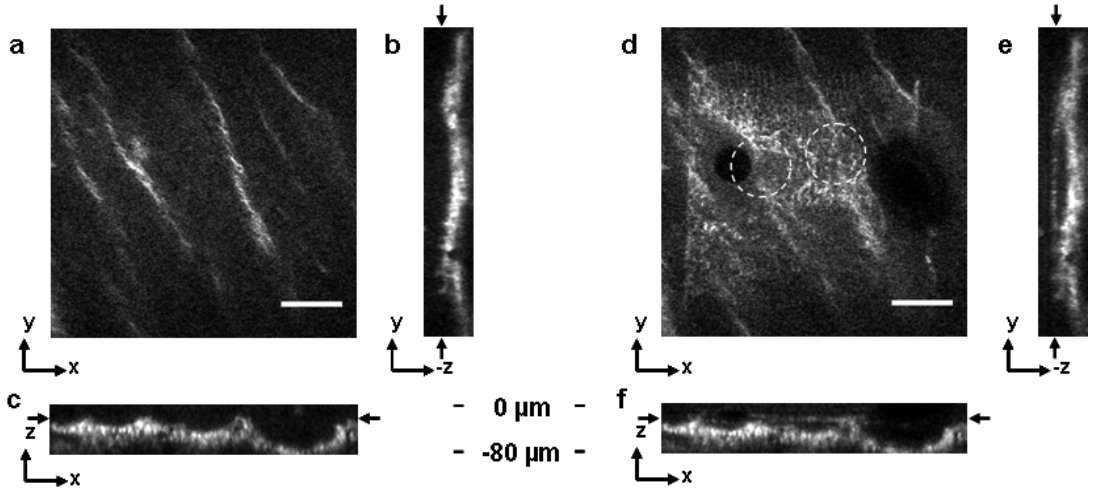

Figure 7.3. Irradiation using 100 nJ pulses. a Second harmonic generation images of collagen structure show the plane, 30 µm below the surface, targeted for ablation just prior to irradiation. **d** The same field of view, 1 minute after irradiation with 100 nJ pulses. Cross section images through the centerlines of **a** and **d** are provided in **b** and **c**, and **e** and **f**, respectively. Arrows in cross section images indicate the imaging planes of **a** and **d**. In **d**, note both the square region of induced luminescence corresponding to the size of the ablated region and the two circular regions resulting from localized bubble nucleation during irradiation. Two dashed circles highlight what appear to be disrupted collagen fibers, suggesting a thin sub-resolution plane may have been disrupted at this energy. Imaging depth in both sets of images is 80 µm. Scale bars are 100 µm.

At low laser fluences near the damage threshold, the extent of ablation can be smaller than the spot size of the focused laser beam. When imaging resolution is similar to that of surgery, it is expected that near-threshold voids, created with 100 nJ pulses for example, would be difficult to identify since they would be below the image resolution. Accordingly, we did not observe any single large void with 100 nJ laser pulses, but instead we occasionally observed small voids in the tissue. These voids most often occurred at the beginning or end of the ablation region and likely resulted from these areas receiving increased exposure. Less frequently, small bubbles were observed in the middle of the region of ablation. These bubbles were likely a result of inhomogeneities in

the tissue that gave rise to a slightly lower breakdown threshold at certain locations. Both cases can be seen in the example shown in Figure 7.3**d**. The presence of induced luminescence and occasional bubble nucleation indicates that the tissue was modified when using pulses as low as 100 nJ. However whether or not the scanned regions were entirely ablated at this energy or less will require a secondary means of verification, such as histology.

Higher pulse energies generally resulted in the formation of larger voids within the tissue. Using 500 and 750 nJ pulses, large voids were created, covering the scanned region of ablation and extending above and below the plane of ablation. We theorize that these large voids are caused by long-lasting bubbles created at the plane of ablation that then merge and expand, displacing the tissue above and below the ablation plane. The formation of bubbles that expand beyond the focal volume is consistent with femtosecond laser ablation well above the optical breakdown threshold. Increased pulse energy beyond the threshold leads to increased maximum bubble diameter. The larger amount of vaporized biomolecules produces a volume of gas which cannot be condensed and must diffuse out, leading to longer bubble lifetimes [17].

Figure 7.4 illustrates a representative example using 500 nJ pulses. In this case, the sub-surface void has maximum dimensions in the ablation plane of 350 µm × 390 µm, and has a maximum height of 90 µm. In one case, shown in Figure 7.5, a similar void created by scanning 750 nJ pulses was then monitored continuously for 45 minutes after ablation. The void was initially measured to be approximately 350 µm × 400 µm in the targeted ablation plane and extended 40 µm and 45 µm above and below this plane, respectively.

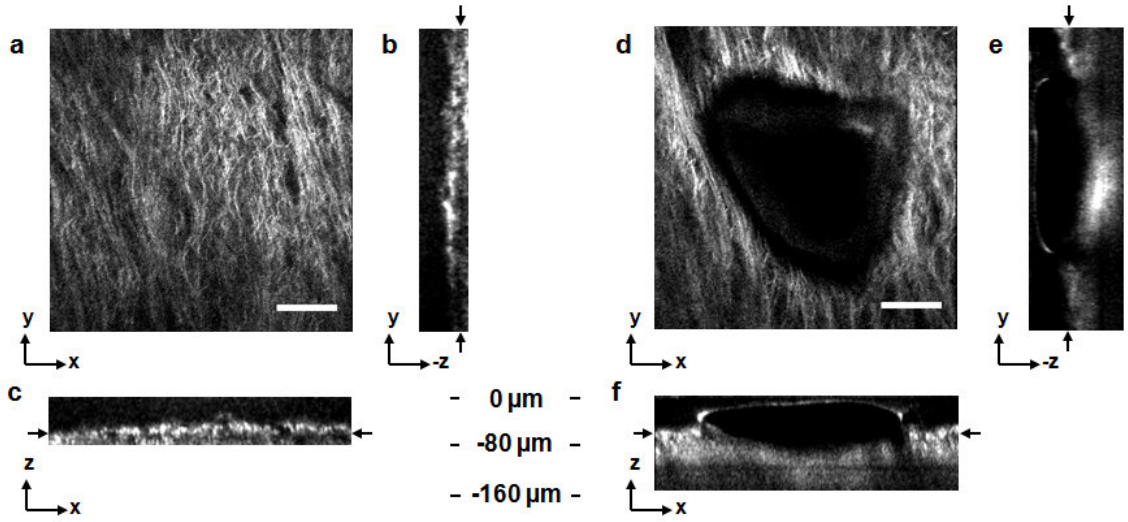

Figure 7.4. Sub-surface void formation with 500 nJ pulses. a SHG images of collagen structure show the plane, 60 µm below the surface, targeted for ablation just prior to irradiation. **d** The same field of view, ~1 minute after irradiation with 500 nJ pulses. Cross sections through the centerlines of **a** and **d** are provided in **b** and **c**, and **e** and **f**, respectively. Arrows in cross section images indicate the imaging planes of **a** and **d**. In **e** and **f**, the induced luminescence at the periphery of the ablated void is apparent. Total imaging depth in **c** and **b** was 80 µm. In **e** and **f**, imaging depth increased to 160 µm to fully capture the void. Scale bar is 100 µm.

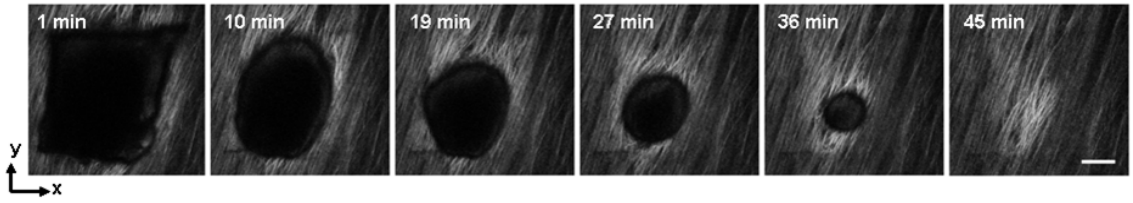

Figure 7.5. Time-lapse images after ablation by 750 nJ pulses. Images show the x-y plane located 15 µm below the targeted ablation plane. Time stamps in the upper left corner denote the time elapsed since irradiation. In the first image, a large void is observed, corresponding roughly to the size and shape of irradiation but clearly extending below the targeted ablation plane. As time progresses, the void appears to recede, allowing the displaced collagen to relax and return to the field of view. Corresponding *x-y* plane and cross section views of the ablation plane after the 45 minutes are shown in Figure 6. Scale bar is 100 µm.

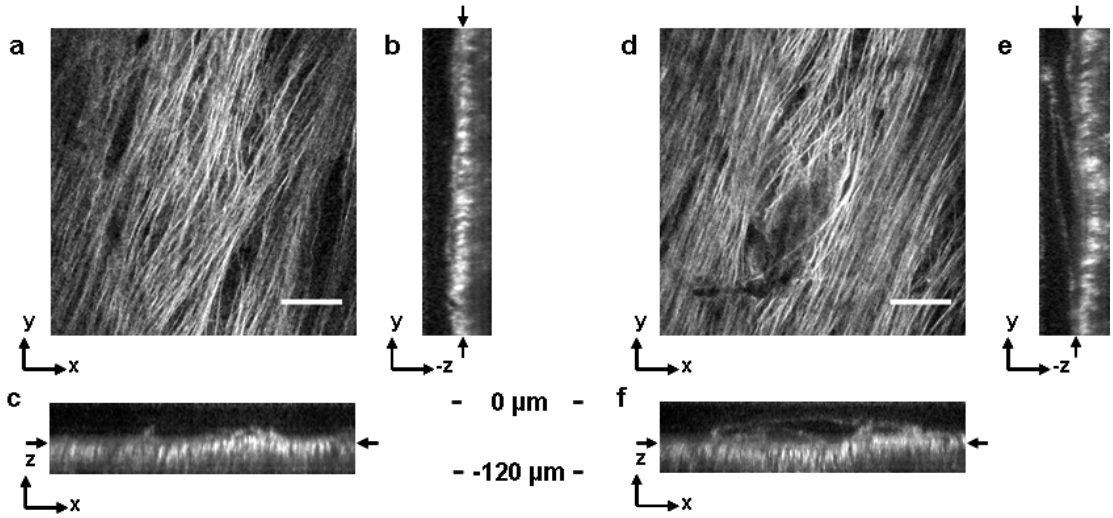

Figure 7.6. Sub-surface void formation with 750 nJ pulse. a Second harmonic generation images of collagen structure show the plane, 65 µm below the surface, targeted for ablation just prior to irradiation. **d** The plane targeted for ablation approximately 45 minutes after irradiation, once the void had mostly collapsed. Cross sections through the centerlines of **a** and **d** are provided in **b** and **c**, and **e** and **f**, respectively. Arrows in cross section images indicate the imaging planes of **a** and **d**. After irradiation with 750 nJ pulses, a large void was observed which then collapsed over 45 minutes, shown in Figure 7.5. Note that in **e** and **f**, the induced luminescence at the periphery of the ablated void is apparent. Also, note the tilting of the void in the *y*-*z* plane in **e**. During ablation, laser scanning progressed in the positive *y* direction. The apparent rise of the ablation during the ablation process is attributed to the interaction of incoming laser pulses with the pre-existing bubble from previous pulses. Total imaging depth in both sets of images is 120 µm. Scale bar is 100 µm.

Over the next 45 minutes, the bubble was observed to collapse until it measured only 40 µm at its thickest point. The remaining void, shown in Figure 7.6, covered an area of approximately 320 µm × 350 µm, similar to the target dimensions. However the planar void exhibited a tilt out of the plane of ablation toward the surface of the tissue. Over the 350 µm extent of the ablation, the void rose just over 50 µm and nearly breaks the plane of the tissue surface. We did not observe any tilt in the induced luminescence of

the 100 nJ cases, which rules out tilting of the sample stage as the source of tilt in the ablated void. This tilt is likely caused by incoming surgery pulses interacting with the long-lasting bubbles created with the previous, high-energy pulses, leading to refraction and an incremental focal shift.

Lastly, we ablated a series of voids using 500 nJ pulses, spaced 100 µm apart, at a fixed depth of 100 µm beneath the surface to examine by follow-up histology. In this series, the targeted void dimensions were 200 µm × 300 µm. The appearance of the voids identified in histology (Figure 7.7) correlate well with the *in situ* images taken using nonlinear optical imaging. Figures 7.7**a** presents a cross-sectional image reconstructed from nonlinear optical images of one void in the series, taken approximately 25 minutes after ablation. From this image, the void appears to be localized entirely within the collagen layer, with a centerline depth of 97 µm and a length of 215 µm. Estimated uncertainty on the measurements from image size calibration is approximately ± 2 µm. The same void was identified during follow-up histology (Figure 7.7**b**), exhibiting similar epithelial morphology and measured centerline depth and length of 99 µm and 175 µm, respectively. For histological analysis, the estimated uncertainty is approximately ± 1 µm. The histological measurements agree well with the *in situ* measurements considering that the tissue is expected to contract during the histology preparation. In this histology image, no visible modification was identified in the cell layers above the ablated void. Another void in the series (Figure 7.7**c**) occurred underneath a thinner portion of epithelium and even separated a small number of epithelial cells. Interestingly, the void beneath the thinner section of epithelium is much thicker, indicating that the reduced epithelial scattering allowed more energy to reach the focal plane, subsequently increasing void dimensions. By cutting into a small part of the epithelial layer, this void provided further evidence that the spaces identified in histology are in fact ablated voids (rather than, perhaps, an abnormally shallow blood vessel). To

ensure the epithelium is not disrupted in clinical use, future voids should be created at deeper depths below the tissue surface.

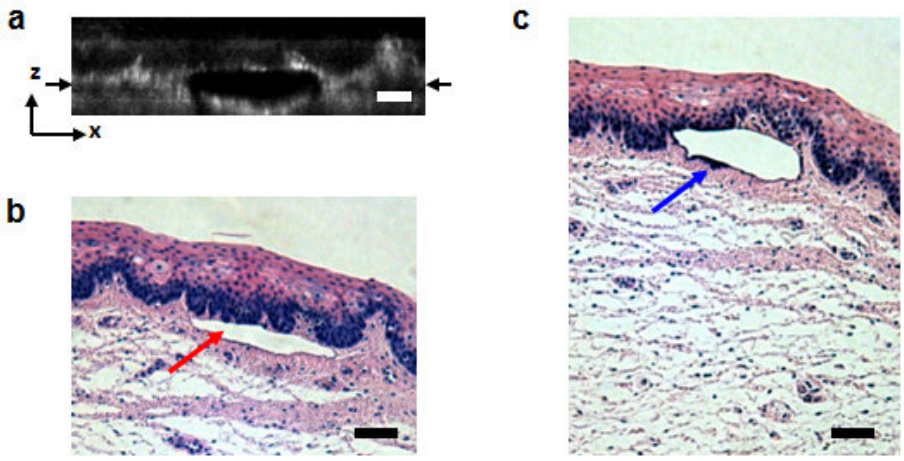

Figure 7.7. Histological follow-up of voids created with 500 nJ pulses. **a** Cross-sectional second harmonic generation image of a void ablated approximately 100 µm beneath the tissue surface. Black arrows denote the plane targeted for ablation. **b** Follow-up histology of the void shown in **a**. Red arrow indicates sub-epithelial void created by femtosecond laser ablation. **c** Histology section of a different void in the series. Blue arrow indicates small section of epithelial nuclei that were separated out of the epithelium during femtosecond laser ablation. Note the thicker void and the thinner epithelium in comparison with **c**. Histology images are stained by H & E. All scale bars are 50 µm.

7.4: DISCUSSION AND SUMMARY OF RESULTS

The imaging and void formation observed in these experiments demonstrate the potential for a femtosecond laser-assisted microsurgery/imaging technique for vocal fold restoration. By utilizing the damage confinement properties of femtosecond laser ablation, planar voids could be created near the epithelium-SLP boundary which may be able to aid in the localization of injected biomaterials. Using lower energy pulses from the same laser system for nonlinear optical imaging of the sample, the structure and orientation of collagen fibers can be clearly distinguished. In addition to determining the

tissue type at a given depth, this ability may be useful in identifying scarring in the vocal fold, where scarring is expected to manifest as dense but less organized collagen infiltrating throughout the SLP. Additionally, the induced luminescence phenomenon that we observed always accompanied void formation and was localized in the 3D periphery of the ablated region. In clinical applications, it may be possible to use the induced luminescence as a signal source to determine the extent of successful ablation. For this use, further histology of near-threshold ablations or a better understanding of the induced luminescence mechanism may be required to ensure that the presence of induced luminescence always indicates successful ablation. It is possible that, just below the ablation threshold, the energy is sufficient for generation of luminescence but not ablation.

Ablation using larger pulse energies well above the optical breakdown threshold produced voids that expanded significantly above and below the plane of ablation. Creating large voids may be advantageous for localizing injected materials as they should increase the likelihood of correctly locating the void during injection. In the envisioned application, the biomaterial is expected to track away from and along the injection needle during injection until it encounters the void, which will then fill selectively as it is the path of least resistance. In the case of the 750 nJ-irradiated void shown in Figs. 7.5 and 7.6, the void was observed to have mostly collapsed after 45 minutes, which provides more than ample time for injection. The interaction of surgery pulses with an expanding bubble from previous pulses appears to have caused the ablated void to rise away from the plane of ablation toward the tissue surface. This tilt needs to be avoided for clinical applications, as it would prevent localization of the void in a consistent tissue layer over the 10 mm maximum anticipated ablation length. To reduce this source of tilting of the ablation plane, the pulse energy can be decreased, as shown in the 100 nJ case, or the slow-axis speed of ablation can be increased to provide more separation between lines of ablation. The second option is most likely preferable for clinical application where the clinician may wish to ensure continuous ablation and a larger void.

As previously mentioned, by maintaining a constant beam scanning speed for imaging and ablation, a single resonant scanning device could be used to provide beam scanning within a clinical manifestation of this technique. Many miniaturized scanning systems, such as micro-electromechanical system (MEMS) mirrors and piezoelectric fiber scanners, exhibit optimum deflection on resonance and the use of a single scanning device can greatly reduce complexity and final packaging size. The ablation dimensions are also consistent with the field of view of our initial 18-mm femtosecond laser microsurgery probe. The maximum pulse energy deliverable by this first device was 350 nJ, however the use of a reflective coating on the MEMS scanning mirror would easily increase the maximum energy to over 900 nJ. As seen in the 9.6-mm probe, some further increase in deliverable energy can also be achieved through increased stretching of the pulse prior to fiber coupling to avoid damage to the fiber tip. A longer length of air-core fiber can then be used to ensure proper re-compression of the pulse at the sample. The objective lens used in this study provided a measured spot size of 1.88 µm inside an agar phantom at the depths we investigated in our study. For comparison, the PSF measurements from the 0.8-NA miniaturized aspheric lens with 3 mm diameter taken in our table-top microscope achieve a 1.1 µm $1/e^2$ focal spot diameter (Chapter 5, Section 5.3), indicating that these spot sizes can be readily achieved in miniaturized femtosecond laser systems.

Using the scanning parameters and pulse repetition rate of 500 kHz employed in this study, a 3 × 10 mm^2 area could be ablated in just over two minutes, which is considered acceptable for clinical use. For comparison, the same scanning parameters coupled with a 1 kHz rate common to most chirped-pulse amplification (CPA) systems would require almost 20 hours to ablate the same region, making these systems unrealistic for clinical microsurgery or imaging with regard to this application. Pulse repetition rates of hundreds of kilohertz are well-suited for this application, as these systems can easily be used for both imaging and microsurgery above optical breakdown. Similarly, as discussed previously in Chapter 2, the 750 fs pulse duration is preferable to

the 100-200 fs pulse duration from our CPA laser source, as the ablation thresholds are predicted to be very similar but the peak intensity has been reduced nearly 7-fold, leading to decreased self-focusing and SPM. Also, fiber laser systems such as the one used in this study are particularly well-suited for clinical applications, since they are often much more compact and robust than CPA systems.

We have successfully demonstrated the use of a single, compact, high repetition-rate femtosecond laser system for imaging and microsurgery of porcine vocal fold as a first step towards the development of an ultrafast laser-assisted method of treating scarred vocal folds in humans. These preliminary experiments show that large long-lasting sub-surface voids can be created and that collagen fiber organization can be clearly resolved, all using laser conditions achievable in a miniaturized fiber-based probe. Future steps will include follow-up histology to investigate near-threshold ablation conditions and a systematic study of the maximum achievable ablation depth using endoscope-compatible laser parameters. The soft and pliable structure of healthy vocal fold make it a poor model for testing the effect of the voids on injection pressure and localization of injectables. The next phase of the study will incorporate animal scar models so that we may gauge the ultimate clinical outcome achievable with the femtosecond laser ablated voids.

Chapter 8: Conclusion

As illustrated in the preceding chapters, femtosecond laser pulses achieve unrivaled microsurgical precision by developing extremely high peak intensity with relatively low total pulse energy. Despite a wide range of clinical advantages and applications that have been identified in bench-top studies, clinical development of femtosecond laser microsurgery outside of ophthalmology has remained in its infancy. The lack of a means to flexibly deliver the high-intensity laser light to areas of interest and guide it with suitable precision has constituted a serious hurdle to further clinical development. In response, this dissertation has detailed my research and development of the first fiber-coupled femtosecond laser microsurgery and microscopy probes.

Using the enabling technologies of air-core photonic bandgap fibers and microelectromechanical scanning mirrors, we constructed an 18-mm diameter probe capable of delivering both amplified and unamplified femtosecond laser pulses for nonlinear optical imaging and cellular microsurgery. With this probe, we achieved the first known demonstration of femtosecond laser microsurgery through an optical fiber by ablating selected carcinoma cells within cell cultures and collagen tissue phantoms. In these studies, the precision of femtosecond laser microsurgery was shown to be preserved by ablating individual cells without damage to neighboring cells in contact with or superficial to the targeted cell.

For image guidance, imaging of benchmark microscopy samples demonstrated two-photon microscopy using average laser powers 2-4× lower than the current state-of-the art nonlinear optical endomicroscopes, confirming the high combined excitation and collection efficiency of this probe design. Due to this efficiency, the imaging powers required for imaging fluorescently labeled cells with this probe were shown to be within safe limits for cell viability, based upon comparison with other published studies.

Additionally, we developed a fast-displaying Lissajous image reconstruction technique which enables extraction of increased temporal resolution from slow-scanning Lissajous patterns without discarding any information from the conventional Lissajous-scanned image. This technique reduces motion artifacts, allows for improved determination and tracking of the focal plane, and more efficiently utilizes laser exposure. All of which are beneficial for clinical microscopy applications.

During development and testing of the 18-mm probe, several areas for improvement were identified. First, clinical utility of the probe depends on the ability to flexibly decouple the probe from the optical table, allowing the device to be delivered to the clinical site of interest. In the 18-mm probe, the separate mounting and collimation of the air-core fiber made this impractical. Secondly, the 18-mm diameter of the probe prevented access to many internal body locations, limiting its regions of application to surface tissues, some oral cavity locations, and some intraoperative sites. Third, the long 16.4 µm axial focal length, due in large part to spherical aberration inherent in the GRIN objective lens, greatly degraded the imaging capabilities in dense samples such as tissue.

To address these issues, we designed and constructed a second femtosecond laser microsurgery and microscopy probe with improved resolution and nearly half the diameter of the first probe. This probe also incorporated all of the elements into one package with all fibers and wires trailing back along the optical axis. As a result, the new 9.6-mm diameter probe is sufficiently compact to allow access to the entire oral cavity and to the larynx, to a larger number of intraoperative sites, or to the colon through the insertion tube of a commercial colonoscope.

During the design process, we identified the limiting aspects of the optical design including the aberrations inherent in various miniature objective lenses and the aberrations induced during off-axis scanning through miniature relay optics, and found ways to mitigate or eliminate both. Using computer aided lens design techniques, we created a diffraction-limited miniaturized probe design that utilized only two custom lens elements, both of which could be easily fabricated for commercial development.

During testing of the 9.6-mm probe, we demonstrated axial resolution improvement of 40% to 9.92 µm, which proved to be sufficient to resolve collagen fiber bundles in rat tail tendon and stained nuclei in porcine vocal fold tissue. By utilizing second harmonic generation of collagen, the rat tail imaging was achieved using solely intrinsic sources of image contrast, demonstrating the potential for label-free image guidance with the 9.6-mm probe.

As an alternative means for creating precise and targeted cell death, we also provided preliminary demonstration of plasmonic laser nanosurgery through the 9.6-mm probe using the optical near-field enhancement of gold nanoparticles. This technique enables imaging and microsurgery of selected cells at greatly reduced laser irradiances, thus generating imaging contrast and therapeutic specificity at the same time. Using this technique, the laser systems used for imaging and therapy are combined, greatly reducing the ultimate cost, complexity, and size of the complete clinical system. By using molecularly targeted nanoparticles to provide therapeutic specificity, the PLN technique eases the burden of precise surgical guidance and could potentially simplify microsurgery in complex and delicate environments such as around neural tissue.

This 9.6-mm probe design can access many clinical areas with the incorporation of a suitable outer housing and the design is easily modified to accommodate a side-viewing orientation, rather than the current forward-viewing orientation, as required. Each clinical application, however, will have its own distinct requirements and will likely require its own specific probe design.

To begin exploring specific clinical applications, we conducted a bench-top study of a new concept for the treatment of scarred vocal folds. This application presents an ideal niche for clinical development of femtosecond laser microsurgery because it presents a currently unsolved problem in which the ability to cut inside of tissue without cutting through tissue may uniquely enhance treatment efficacy. Using bench-top studies, we demonstrated that imaging of collagen and creation of voids could be achieved

beneath the epithelium of porcine vocal fold using a focused spot size, scanning speed, and pulse energy that are achievable with our general probe design.

For this study, we also demonstrated that nonlinear optical imaging and microsurgery through optical breakdown could be achieved using a compact fiber laser source. This system is compact and robust to enable integration into a clinical environment and significantly cheaper than the chirped pulse amplification system used during our probe development. By operating at a high repetition rate (500 kHz), we achieved ablation speeds suitable to treat a totally scarred vocal fold in only a few minutes. Meanwhile, the pulse duration of the system is optimized to mitigate self-focusing and self-phase modulation effects while maintaining a low ablation threshold of the sample.

Further development of this application will require design and construction of a laryngeal probe capable of scanning ~ 3 mm × 10 mm areas at the sample and interfacing with the larynx *in vivo* for animal studies. For such large scanning areas, new scanning modalities will need to be explored, such as rotational scanning via micromotors. Meanwhile, improved packaging will be required to handle operation in a clinical environment. To ensure sufficient energy can be delivered, either metallization or elimination of the MEMS scanning mirror will also likely be required.

Looking forward, endoscopic femtosecond laser microsurgery can be further developed towards a host of clinical applications. Based on the experience gained through the design and testing of our two microsurgery probes, a number of points have been identified that should be considered as development continues.

Femtosecond laser sources remain the largest and most expensive element of a clinical femtosecond laser microsurgery system and are often the limiting factor in determining maximum deliverable laser energy and maximum ablation speed. Future femtosecond laser microsurgery systems will benefit from utilizing amplified fiber laser systems, such as the one used in our vocal fold study. Such systems can provide repetition rates in the hundreds of kilohertz which serves to greatly enhance ablation

speed, in comparison with CPA systems, while enabling practical nonlinear optical imaging with the same single laser source. In general, amplified fiber laser systems are significantly smaller and easier to maintain than CPA systems, making them better suited for clinical environments. Also, many amplified femtosecond fiber lasers generate pulses with durations slightly below 1 ps, which is desirable for minimizing nonlinear effects and GVD, while still enabling nonlinear optical imaging and optical breakdown with low pulse energy. Owing to the high repetition rate of these systems, the maximum pulse energy that can be delivered for microsurgery is lower than that for CPAs and may become the limiting factor in determining maximum microsurgical pulse energy at the sample. As a result, pulse pre-chirping of fiber laser systems, when required, should utilize prism-based pre-chirping systems which have much higher energy efficiency than grating-based systems, like the one used to characterize our three meter PBF.

As we have shown, bio-conjugated nanoparticles can also be used for PLN, thereby enabling imaging and microsurgery with a single laser source as well. While we have demonstrated several advantages of this technique, most significantly to initiate cell death at laser powers that are safe for unlabeled cells, clinical development of PLN will face additional hurdles associated with labeling specificity, particle delivery, and federal regulatory clearance that are unique to nanoparticle-based treatments.

For the optical system, designing for a moderate effective numerical aperture (~0.5 – 0.75) for the objective lens is desirable, keeping in mind that it is the total optical system rather than simply the objective lens that determines the effective NA. Low effective NAs require larger pulse energies for ablation that can be difficult to deliver through single-mode air-core fibers, can lead to self-focusing, and, when nonlinear optical imaging is used for guidance, can degrade axial resolution to the point that tissue imaging becomes impossible. To achieve very high NAs, however, the maximum FOV must be sacrificed as limited by the number of resolvable spots of the scanning device and a higher NA objective lens must be used, decreasing the available working distance.

Furthermore, smaller spot sizes require slower scanning speeds if continuous ablation is desired.

Within the optical system, care needs to be taken to avoid utilizing the full aperture of GRIN lenses to maintain optimum beam quality. Bench-top testing of commercially available miniature objective lenses confirmed that GRIN lenses introduce a significant amount of spherical aberration when their full apertures are used. While we avoided this source of aberration in the objective of our 9.6-mm endoscope, we still encountered aberrations that likely arose from the 0.50 mm diameter GRIN collimating lens. Future devices will need to employ larger diameter, larger NA GRIN collimating lenses or small diameter (~2 mm) aspheric lenses, either of which will increase the diameter of the collimating assembly. Revised assembly techniques should also be developed to eliminate excess epoxy degrading beam quality and energy transmittance, as experienced in our 9.6-mm probe.

Lastly, as previously mentioned, future devices based around MEMS mirror scanning should utilize a thin aluminum coating on the active surface of the MEMS mirror to boost reflectivity. In contrast to using longer lengths of PBF with increased microsurgery pulse pre-chirping, which necessitates a trade-off between maximum microsurgery and imaging laser energies, metallic coated MEMS mirrors can bolster the transmitted energy of both laser systems by 300% at NIR wavelengths without adding significant cost or complexity to the optical system.

Alternatively, the MEMS mirror may ultimately be eliminated for some applications. For applications requiring delivery through the accessory channel of a commercial endoscope, further miniaturization to a diameter below 5 mm is necessary. Even with the minimal footprint of the PCB used to mount the MEMS mirror in the 9.6-mm diameter design, the diameter required to package the MEMS mirror alone exceeds 5 mm. As a result, future femtosecond laser microsurgery probes designed for accessory channel delivery should be built around an alternate means of beam scanning, such as a piezoelectric fiber scanning element. The same is true for probes designed for

applications of the inner ear or entry through the nasal passages. Such systems have the benefit of eliminating reflective losses from silicon scanning mirrors and have shown strong performance as imaging-only endomicroscopes [138-140].

Lastly, for some applications, nonlinear optical imaging may not be the appropriate means of surgical guidance. For applications of bone ablation, for example, laser-induced breakdown spectroscopy may provide a spectral “fingerprint” elucidating whether the material being ablated is bone or soft tissue, while OCT might provide accurate feedback regarding the depth and surface quality of ablation. Even when microscopic surgical guidance is required, the two-photon fluorescent signal from most intrinsic tissue fluorophores is so weak that effective imaging with fiber-coupled probes proves quite difficult. Since the introduction of exogenous contrast agents such as fluorescent dyes or metal nanoparticles is not always practical, future applications should also pursue alternative imaging technologies such as NIR reflectance confocal microscopy and OCT as other means of image guidance.

Based on the results of this body of work, fiber-optic femtosecond laser microsurgery is not only feasible but can occupy a unique place among clinical microsurgery techniques. The enabling technologies, including the laser sources, fiber optics, and scanning devices, continue to develop, which will expand the capabilities of the microsurgical endoscopes and probes while decreasing their cost. Meanwhile, new clinical applications continue to be identified that take advantage of the unique properties of ultrafast laser optical breakdown to provide treatment options that are otherwise impossible. With these initial niche applications, fiber-optic femtosecond laser microsurgery can gain entry into the operating room, paving the way for clinical acceptance in a wider range of applications.

References

1. T. H. Maiman, "Stimulated Optical Radiation in Ruby," Nature **187,** 493-494 (1960).

2. C. H. Townes, "Optical Masers and Their Possible Applications to Biology," Biophys. J. **2,** 325-329 (1962).

3. M. Bessis, F. Gires, G. Mayer, and G. Nomarski, "Irradiation des organites cellulaires a l'aide d'un LASER a rubis," C. R. l'Academie. Sci. **255,** 1010 (1962).

4. N. M. Saks, and C. A. Roth, "Ruby Laser as a Microsurgical Instrument," Science **141,** 46-47 (1963).

5. R. L. Amy, and R. Storb, "Selective mitochondrial damage by a ruby laser microbeam: an electron microscope study," Science **150,** 756-758 (1965).

6. M. W. Berns, R. S. Olson, and D. E. Rounds, "In vitro Production of Chromosomal Lesions with an Argon Laser Microbeam," Nature **221,** 74-75 (1969).

7. M. M. Zaret, G. M. Breinin, H. Schmidt, H. Ripps, I. M. Siegel, and L. R. Solon, "Ocular Lesions Produced by an Optical Maser (Laser)," Science **134,** 1525-1526 (1961).

8. L. Goldman, D. J. Blaney, D. J. Kindel, D. Richfield, and E. K. Franke, "Pathology of the Effect of the Laser Beam on the Skin," Nature **197,** 912-914 (1963).

9. L. Goldman, P. Hornby, R. Meyer, and B. Goldman, "Impact of the Laser on Dental Caries," Nature **203,** 417-417 (1964).

10. V. Magidson, J. Loncarek, P. Hergert, C. L. Rieder, and A. Khodjakov, "Laser Microsurgery in the GFP Era: A Cell Biologist's Perspective," Methods in Cell Biology **82,** 239-266 (2007).

11. F. Fankhauser, and S. Kwasniewska, *Lasers in Ophthalmology—Basic, Diagnostic, and Surgical Aspects: A Review* (Kugler Publications, The Hague, Netherlands, 2003).

12. E. L. Tanzi, J. R. Lupton, and T. S. Alster, "Lasers in dermatology: Four decades of progress," Journal of the American Academy of Dermatology **49,** 1-31 (2003).

13. R. H. Ossoff, J. A. Coleman, M. S. Courey, J. A. Duncavage, J. A. Werkhaven, and L. Reinisch, "Clinical applications of lasers in otolaryngology - head and neck surgery," Lasers in Surgery and Medicine **15,** 217-248 (1994).

14. A. Vogel, and V. Venugopalan, "Mechanisms of Pulsed Laser Ablation of Biological Tissues," Chemical Reviews **103,** 577-644 (2003).

15. L. S. Bass, and M. R. Treat, "Laser tissue welding: A comprehensive review of current and future," Lasers in Surgery and Medicine **17,** 315-349 (1995).

16. A. P. Joglekar, H. H. Liu, E. Meyhofer, G. Mourou, and A. J. Hunt, "Optics at critical intensity: Applications to nanomorphing," PNAS **101,** 5856-5861 (2004).

17. A. Vogel, J. Noack, G. Hüttman, and G. Paltauf, "Mechanisms of femtosecond laser nanosurgery of cells and tissues," Applied Physics B **81,** 1015-1047 (2005).

18. A. Ben-Yakar, and F. Bourgeois, "Ultrafast laser nanosurgery in microfluidics for genome-wide screenings," Curr. Opin. Biotechnol. **20,** 100-105 (2009).

19. U. K. Tirlapur, K. König, C. Peuckert, R. Krieg, and K.-J. Halbhuber, "Femtosecond near-infrared laser pulses elicit generation of reactive oxygen species in mammalian cells leading to apoptosis-like death," Exp. Cell Res. **263,** 88-97 (2001).

20. B. Boudaiffa, P. Cloutier, D. Hunting, M. A. Huels, and L. Sanche, "Resonant Formation of DNA Strand Breaks by Low-Energy (3- to 20- eV) Electrons," Science **287,** 1658-1660 (2000).

21. L. R. Koller, *Ultraviolet Radiation* (J. Wiley, New York, 1965).

22. B. C. Stuart, M. D. Feit, A. M. Rubenchik, B. W. Shore, and M. D. Perry, "Laser-induced damage in dielectrics with nanosecond to subpicosecond pulses," Phys. Rev. Lett. **74,** 2248-2251 (1995).

23. C. Schaffer, A. Brodeur, and E. mazur, "Laser-induced breakdown and damage in bulk transparent materials induced by tightly focused femtosecond laser pulses," Meas. Sci. Technol. **12,** 1784-1794 (2001).

24. G. Olivié, D. Giguère, F. Vidal, T. Ozaki, J. C. Kieffer, O. Nada, and I. Brunette, "Wavelength dependence of femtosecond laser ablation threshold of corneal stroma," Opt. Express **16,** 4121-4129 (2008).

25. R. Y. Chiao, E. Garmire, and C. H. Townes, "Self-Trapping of Optical Beams," Phys. Rev. Lett. **13,** 479 (1964).

26. P. L. Kelley, "Self-Focusing of Optical Beams," Phys. Rev. Lett. **15,** 1005 (1965).

27. E. T. J. Nibbering, M. A. Franco, B. S. Prade, G. Grillon, C. Le Blanc, and A. Mysyrowicz, "Measurement of the nonlinear refractive index of transparent

materials by spectral analysis after nonlinear propagation," Opt. Commun. **119,** 479-484 (1995).

28. M. Miclea, U. Skrzypczak, S. Faust, F. Fankhauser, H. Graener, and G. Seifert, "Nonlinear refractive index of porcine cornea studied by z-scan and self-focusing during femtosecond laser processing," Opt. Express **18,** 3700-3707.

29. Y. R. Shen, *The Principles of Nonlinear Optics* (John Wiley & Sons, Inc., New York, NY, 1984).

30. C. L. Arnold, A. Heisterkamp, W. Ertmer, and H. Lubatschowski, "Streak formation as side effect of optical breakdown during processing the bulk of transparent Kerr media with ultra-short laser pulses," Appl. Phys. B **80,** 247-253 (2005).

31. A. Heisterkamp, T. Ripken, T. Mamom, W. Drommer, H. Welling, W. Ertmer, and H. Lubatschowski, "Nonlinear side effects of fs pulses inside corneal tissue during photodisruption," Applied Physics B-Lasers and Optics **74,** 419-425 (2002).

32. M. Han, L. Zickler, M. Walter, G. Giese, F. Loesel, and J. F. Bille, "Noninvasive evaluation of mini-invasive femtosecond laser refractive surgery," in *Commercial and Biomedical Applications of Ultrafast Lasers IV*, (SPIE, San Jose, Ca, USA, 2004), pp. 55-65.

33. L. Sudrie, A. Couairon, M. Franco, B. Lamouroux, B. Prade, S. Tzortzakis, and A. Mysyrowicz, "Femtosecond Laser-Induced Damage and Filamentary Propagation in Fused Silica," Phys. Rev. Lett. **89,** 186601 (2002).

34. Tse, Christine, Zohdy, J. Marwa, Y. E. Jing Yong, O'Donnell, and Matthew, "Penetration and Precision of Subsurface Photodisruption in Porcine Skin Tissue With Infrared Femtosecond Laser Pulses," Anglais **55,** 8 (2008).

35. C. B. Schaffer, A. Brodeur, J. F. García, and E. Mazur, "Micromachining bulk glass by use of femtosecond laser pulses with nanojoule energy," Opt. Lett. **26,** 93-95 (2001).

36. V. Nuzzo, M. Savoldelli, J. M. Legeais, and K. Plamann, "Self-focusing and spherical aberrations in corneal tissue during photodisruption by femtosecond laser," JBO **15,** - (2010).

37. D. Stern, R. W. Schoenlein, C. A. Puliafito, E. T. Dobi, R. Birngruber, and J. G. Fujimoto, "Corneal Ablation by Nanosecond, Picosecond, and Femtosecond Lasers at 532 and 625 Nm," Archives of Ophthalmology **107,** 587-592 (1989).

38. W. Kautek, S. Mitterer, J. Krüger, W. Husinsky, and G. Grabner, "Femtosecond-pulse laser ablation of human corneas," Appl. Phys. A **58,** 513-518 (1994).

39. F. H. Loesel, J. P. Fischer, M. H. Gotz, C. Horvath, T. Juhasz, F. Noack, N. Suhm, and J. F. Bille, "Non-thermal ablation of neural tissue with femtosecond laser pulses," Applied Physics B-Lasers and Optics **66,** 121-128 (1998).

40. J. Neev, L. B. D. Silva, M. D. Feit, M. D. Perry, A. M. Rubenchik, and B. C. Stuart, "Ultrashort Pulse Lasers for Hard Tissue Ablation," IEEE J. Sel. Top. Quantum Electron. **2,** 790-800 (1996).

41. I. Ratkay-Traub, I. E. Ferincz, T. Juhasz, R. M. Kurtz, and R. R. Krueger, "First clinical results with the femtosecond neodynium-glass laser in refractive surgery," Journal of Refractive Surgery **19,** 94-103 (2003).

42. K. Stonecipher, T. S. Ignacio, and M. Stonecipher, "Advances in refractive surgery: microkeratome and femtosecond laser flap creation in relation to safety, efficacy, predictability, and biomechanical stability," Current Opinion in Ophthalmology **17,** 368-372 (2006).

43. S. G. Slade, "The use of the femtosecond laser in the customization of corneal flaps in laser in situ keratomileusis," Current Opinion in Ophthalmology **18,** 314-317 (2007).

44. H. Lubatschowski, "Overview of commercially available femtosecond lasers in refractive surgery," Journal of Refractive Surgery **24,** 102-107 (2008).

45. S. G. Slade, "Applications for the femtosecond laser in corneal surgery," Current Opinion in Ophthalmology **18,** 338-341 (2007).

46. B. Seitz, A. Langenbucher, C. Hofmann-Rummelt, U. Schlötzer-Schrehardt, and G. O. H. Naumann, "Nonmechanical posterior lamellar keratoplasty using the femtosecond laser (femto-plak) for corneal endothelial decompensation," American Journal of Ophthalmology **136,** 769-772 (2003).

47. S. I. M. D. Mian, H. K. M. D. Soong, S. V. M. D. Patel, T. M. D. Ignacio, and T. P. Juhasz, "In Vivo Femtosecond Laser-Assisted Posterior Lamellar Keratoplasty in Rabbits," Cornea **25,** 1205-1209 (2006).

48. L. Buratto, and E. Böhm, "The Use of the Femtosecond Laser in Penetrating Keratoplasty," American Journal of Ophthalmology **143,** 737-742.e731 (2007).

49. T. S. Ignacio, T. B. Nguyen, R. S. Chuck, R. M. Kurtz, and M. A. Sarayba, "Top Hat Wound Configuration for Penetrating Keratoplasty Using the Femtosecond Laser: A Laboratory Model," Cornea **25,** 336-340 (2006).

50. M. Farid, M. Kim, and R. F. Steinert, "Results of Penetrating Keratoplasty Performed with a Femtosecond Laser Zigzag Incision Initial Report," Ophthalmology **114,** 2208-2212.e2204 (2007).

51. F. W. Price Jr, and M. O. Price, "Femtosecond Laser Shaped Penetrating Keratoplasty: One-year Results Utilizing a Top-hat Configuration," American Journal of Ophthalmology **145,** 210-214.e212 (2008).

52. H. K. Soong, and J. B. Malta, "Femtosecond Lasers in Ophthalmology," American Journal of Ophthalmology **147,** 189-197 (2009).

53. Y. S. Rabinowitz, X. Li, T. S. Ignacio, and E. Maguen, "INTACS Inserts Using the Femtosecond Laser Compared to the Mechanical Spreader in the Treatment of Keratoconus," Journal of Refractive Surgery **22,** 764-771 (2006).

54. A. Ertan, G. Kamburoglu, and M. Bahadir, "Intacs insertion with the femtosecond laser for the management of keratoconus - One-year results," Journal of Cataract and Refractive Surgery **32,** 2039-2042 (2006).

55. M. H. Shabayek, and J. L. Alió, "Intrastromal Corneal Ring Segment Implantation by Femtosecond Laser for Keratoconus Correction," Ophthalmology **114,** 1643-1652 (2007).

56. E. Coskunseven, G. D. Kymionis, N. S. Tsiklis, S. Atun, E. Arslan, M. R. Jankov, and I. G. Pallikaris, "One-Year Results of Intrastromal Corneal Ring Segment Implantation (KeraRing) using Femtosecond Laser in Patients with Keratoconus," American journal of ophthalmology **145,** 775-779.e771 (2008).

57. S. Yoo, G. Kymionis, T. O'Brien, T. Ide, W. Culbertson, and E. Alfonso, "Femtosecond-assisted diagnostic corneal biopsy (FAB) in keratitis," Graefe's Archive for Clinical and Experimental Ophthalmology **246,** 759-762 (2008).

58. J. H. Kim, J. H. Yum, D. Lee, and S. H. Oh, "Novel technique of corneal biopsy by using a femtosecond laser in infectious ulcers," Cornea **27,** 363-365 (2008).

59. H. Louis, P. Helene, M. Frederic, C. John, and R. Bernard, "Correction of Postkeratoplasty Astigmatism by Femtosecond Laser Compared with Mechanized Astigmatic Keratotomy," American journal of ophthalmology **147,** 779-787.e771 (2009).

60. M. Blum, K. Kunert, S. Nolte, S. Riehemann, M. Palme, T. Peschel, M. Dick, and H. Dick, "Presbyopietherapie mit Femtosekundenlaser," Der Ophthalmologe **103,** 1014-1019 (2006).

61. T. Ripken, U. Oberheide, M. Fromm, S. Schumacher, G. Gerten, and H. Lubatschowski, "fs-Laser induced elasticity changes to improve presbyopic lens accommodation," Graefe's Archive for Clinical and Experimental Ophthalmology **246,** 897-906 (2008).

62. S. Schumacher, M. Fromm, U. Oberheide, G. Gerten, A. Wegener, and H. Lubatschowski, "In Vivo Application and Imaging of Intralenticular Femtosecond Laser Pulses for the Restoration of Accommodation," Journal of Refractive Surgery **24,** 991-995 (2008).

63. S. Schumacher, U. Oberheide, M. Fromm, T. Ripken, W. Ertmer, G. Gerten, A. Wegener, and H. Lubatschowski, "Femtosecond laser induced flexibility change of human donor lenses," Vision Research **49,** 1853-1859 (2009).

64. M. A. Sarayba, R. M. Kurtz, T. T. B. Nguyen, T. Ignacio, M. Mansoori, P. M. Sweet, and R. S. Chuck, "Femtosecond laser-assisted intracorneal keratoprosthesis implantation - A laboratory model," Cornea **24,** 1010-1014 (2005).

65. Z. Nagy, A. Takacs, T. Filkorn, and M. Sarayba, "Initial clinical evaluation of an intraocular femtosecond laser in cataract surgery," J Refract Surg **25,** 1053-1060 (2009).

66. K. S. Frederickson, W. E. White, R. G. Wheeland, and D. R. Slaughter, "Precise Ablation of Skin With Reduced Collateral Damage Using the Femtosecond-Pulsed, Terawatt Titanium-Sapphire Laser," Arch Dermatol **129,** 989-993 (1993).

67. N. Nishimura, C. B. Schaffer, E. H. Li, and E. Mazur, "Tissue ablation with 100-fs and 200-ps laser pulses," Proceedings of the 20th Annual International Conference of the IEEE Engineering in Medicine and Biology Society **20,** 1703-1706 (1998).

68. H. Wisweh, U. Merkel, A. K. Huller, K. Lurben, and H. Lubatschowski, "Optical coherence tomography monitoring of vocal fold femtosecond laser microsurgery " in *Therapeutic Laser Applications and Laser-Tissue Interaction III*, A. Vogel, ed. (2007), p. 63207.

69. H. Huang, and Z. Guo, "Human dermis separation via ultra-short pulsed laser plasma-mediated ablation," J. Phys. D: Appl. Phys. **42,** 165204 (2009).

70. H. Huang, and Z. Guo, "Ultrashort pulsed laser ablation and stripping of freeze-dried dermis," Lasers in Medical Science **25,** 517-524 (2010).

71. Loesel, H. F, Niemz, H. M, Bille, F. J, Juhasz, and T, *Laser-induced optical breakdown on hard and soft tissues and its dependence on the pulse duration : Experiment and model* (Institute of Electrical and Electronics Engineers, New York, NY, ETATS-UNIS, 1996).

72. J. Wahrburg, K.-U. Schmidt, M. H. Götz, K. Kappings, and S. Gölz, "Concept of a novel laser probe for minimal invasive applications in neurosurgery," Mechatronics **6,** 479-489 (1996).

73. M. H. Goetz, and et al., "Computer-guided laser probe for ablation of brain tumours with ultrashort laser pulses," Physics in Medicine and Biology **44,** N119 (1999).

74. J. Nguyen, J. Ferdman, M. Zhou, D. Huland, S. Saqqa, J. Ma, N. Nishimura, T. Schwartz, and C. Schaffer, "Femtosecond laser ablation as a subsurface light scalpel to alter seizure propagation dynamics," *American Society of Lasers in Medicine and Surgery Annual Meeting*, (Phoenix, Arizona, 2010).

75. A. Moritz, and F. Beer, *Oral laser application* (Quintessence, London, 2006).

76. J. Neev, L.-H. L. Liaw, D. V. Raney, J. T. Fujishige, P. D. Ho, and M. W. Berns, "Selectivity, efficiency, and surface characteristics of hard dental tissues ablated with ArF pulsed excimer lasers," Lasers in Surgery and Medicine **11,** 499-510 (1991).

77. J. Pelagalli, C. B. Gimbel, R. T. Hansen, A. Swett, and D. W. Winn, "Investigational Study of the Use of Er:YAG Laser Versus Dental Drill for Caries Removal and Cavity Preparationâ€" Phase I," Journal of Clinical Laser Medicine & Surgery **15,** 109-115 (1997).

78. L. Zach, and G. Cohen, "Pulp response to externally applied heat," Oral Surgery, Oral Medicine, Oral Pathology **19,** 515-530 (1965).

79. K. Ulrich, and H. Raimund, "Experimental studies of the application of the Er:YAG laser on dental hard substances: II. Light microscopic and SEM investigations," Lasers in Surgery and Medicine **9,** 345-351 (1989).

80. B. Gokce, B. Ozpinar, C. Artunc, and G. Aksoy, "Laser use vs. handpiece for tooth preparation: A preliminary in vitro study," Journal of Laser Applications **21,** 63-66 (2009).

81. O. Feuerstein, D. Palanker, A. Fuxbrunner, A. Lewis, and D. Deutsch, "Effect of the ArF excimer laser on human enamel," Lasers in Surgery and Medicine **12,** 471-477 (1992).

82. R. Boehm, J. Rich, J. Webster, and S. Janke, "Thermal stress effects and surface cracking associated with laser use on human teeth," J Biomech Eng **99,** 189-194 (1977).

83. H. H. K. Xu, J. R. Kelly, S. Jahanmir, V. P. Thompson, and E. D. Rekow, "Enamel subsurface damage due to tooth preparation with diamonds," J. Dent. Res. **76,** 1698-1706 (1997).

84. B.-M. Kim, M. D. Feit, A. M. Rubenchik, E. J. Joslin, P. M. Celliers, J. Eichler, and L. B. Da Silva, "Influence of pulse duration on ultrashort laser pulse ablation of biological tissues," JBO **6,** 332-338 (2001).

85. A. V. Rode, E. G. Gamaly, B. Luther-Davies, B. T. Taylor, J. Dawes, A. Chan, R. M. Lowe, and P. Hannaford, "Subpicosecond laser ablation of dental enamel," J. Appl. Phys. **92,** 2153-2158 (2002).

86. J. Krüger, W. Kautek, and H. Newesely, "Femtosecond-pulse laser ablation of dental hydroxyapatite and single-crystalline fluoroapatite," Appl. Phys. A **69,** S403-S407 (1999).

87. M. H. Niemz, A. Kasenbacher, M. Strassl, A. Bäcker, A. Beyertt, D. Nickel, and A. Giesen, "Tooth ablation using a CPA-free thin disk femtosecond laser system," Appl. Phys. B **79,** 269-271 (2004).

88. J. Serbin, T. Bauer, C. Fallnich, A. Kasenbacher, and W. H. Arnold, "Femtosecond lasers as novel tool in dental surgery," Appl. Surf. Sci. **197,** 737-740 (2002).

89. L. R. Friesen, C. M. Cobb, J. W. Rapley, L. Forgas-Brockman, and P. Spencer, "Laser Irradiation of Bone: II. Healing Response Following Treatment by CO2 and Nd:YAG Lasers," Journal of Periodontology **70,** 75-83 (1999).

90. E. K. Gardner, J. Dornhoffer, and S. Ferguson, "Photoacoustic Effects of Carbon Dioxide Lasers in Stapes Surgery: Quantification in a Temporal Bone Model."

91. J. Neev, J. S. Nelson, M. Critelli, J. L. McCullough, E. Cheung, W. A. Carrasco, A. M. Rubenchik, L. B. D. Silva, M. D. Perry, and B. C. Stuart, "Ablation of human nail by pulsed lasers," Lasers in Surgery and Medicine **21,** 186-192 (1997).

92. B. Girard, D. Yu, M. R. Armstrong, B. C. Wilson, C. M. L. Clokie, and R. J. D. Miller, "Effects of femtosecond laser irradiation on osseous tissues," Lasers in Surgery and Medicine **39,** 273-285 (2007).

93. K. Ozono, and M. Obara, "Tailored ablation processing of advanced biomedical hydroxyapatite by femtosecond laser pulses," Appl. Phys. A **77,** 303-306 (2003).

94. B. Girard, M. Cloutier, D. J. Wilson, C. M. L. Clokie, R. J. D. Miller, and B. C. Wilson, "Microtomographic analysis of healing of femtosecond laser bone calvarial wounds compared to mechanical instruments in mice with and without application of BMP-7," Lasers in Surgery and Medicine **39,** 458-467 (2007).

95. W. B. Armstrong, J. A. Neev, L. B. D. Silva, A. M. Rubenchik, and B. C. Stuart, "Ultrashort pulse laser ossicular ablation and stapedotomy in cadaveric bone," Lasers in Surgery and Medicine **30,** 216-220 (2002).

96. J. Ilgner, M. Wehner, J. Lorenzen, M. Bovi, and M. Westhofen, "Morphological effects of nanosecond- and femtosecond-pulsed laser ablation on human middle ear ossicles," JBO **11,** 014004 (2006).

97. R. G. McCaughey, H. Sun, V. S. Rothholtz, T. Juhasz, and B. J. F. Wong, "Femtosecond laser ablation of the stapes," JBO **14,** 024040-024046 (2009).

98. B. J. F. Wong, M. R. Dickinson, M. W. Berns, and J. Neev, "Identification of Photoacoustic Transients during Pulsed Laser Ablation of the Human Temporal Bone: An Experimental Model," Journal of Clinical Laser Medicine & Surgery **14,** 385-392 (1996).

99. Y. Liu, and M. Niemz, "Ablation of femural bone with femtosecond laser pulses—a feasibility study," Lasers in Medical Science **22,** 171-174 (2007).

100. J. Qiu, J. M. H. Teichman, T. Wang, J. Neev, R. D. Glickman, K. F. Chan, and T. E. Milner, "Femtosecond laser lithotripsy: feasibility and ablation mechanism," JBO **15,** 028001-028005 (2010).

101. J. Qiu, J. Neev, T. Wang, D. Gomez, and T. E. Milner, "Fiber delivery system for ablation of hard and soft tissues using near-infrared femtosecond laser pulses," *American Society for Lasers in Medicine and Surgery Annual Conference*, (Phoenix, Arizona, 2010).

102. Y. Matsuura, M. Miyagi, K. Shihoyama, and M. Kawachi, "Delivery of femtosecond pulses by flexible hollow fibers," J. Appl. Phys. **91,** 887-889 (2002).

103. B. M. Kim, M. D. Feit, A. M. Rubenchik, B. M. Mammini, and L. B. Da Silva, "Optical feedback signal for ultrashort laser pulse ablation of tissue," Appl. Surf. Sci. **127-129,** 857-862 (1998).

104. O. Kermani, W. Fabian, and H. Lubatschowski, "Real-Time Optical Coherence Tomography-Guided Femtosecond Laser Sub-Bowman Keratomileusis on Human Donor Eyes," American Journal of Ophthalmology **146,** 42-45 (2008).

105. V. Nuzzo, K. Plamann, M. Savoldelli, M. Merano, D. Donate, O. Albert, P. F. G. Rodriguez, G. Mourou, and J.-M. Legeais, "In situ monitoring of second-harmonic generation in human corneas to compensate for femtosecond laser pulse attenuation in keratoplasty," JBO **12,** 064032-064011 (2007).

106. M. Han, L. Zickler, G. Giese, M. Walter, F. H. Loesel, and J. F. Bille, "Second-harmonic imaging of cornea after intrastromal femtosecond laser ablation," JBO **9,** 760-766 (2004).

107. K. König, O. Krauss, and I. Riemann, "Intratissue Surgery With 80 MHz Nanojoule Femtosecond Laser Pulses in the Near Infrared," Opt. Express **10,** 171-176 (2002).

108. M. Mogensen, L. Thrane, T. M. Jørgensen, P. E. Andersen, and G. B. E. Jemec, "OCT imaging of skin cancer and other dermatological diseases," Journal of Biophotonics **2,** 442-451 (2009).

109. C. L. Hoy, N. J. Durr, P. Chen, W. Piyawattanametha, H. Ra, O. Solgaard, and A. Ben-Yakar, "Miniaturized probe for femtosecond laser microsurgery and two-photon imaging," Opt. Express **16,** 9996-10005 (2008).

110. C. L. Hoy, W. N. Everett, J. Kobler, and A. Ben-Yakar, "Toward endoscopic ultrafast laser microsurgery of vocal folds," Proc. SPIE **7548,** 754831-754839 (2010).

111. P. Theer, M. Hasan, T., and W. Denk, "Two-photon imaging to a depth of 1000μm in living brains by use of a Ti:Al_2O_3 regenerative amplifier," Opt. Lett. **28,** 1022-1024 (2003).

112. P. Theer, and W. Denk, "On the fundamental imaging-depth limit in two-photon microscopy," J. Opt. Soc. Am. A **23,** 3139-3149 (2006).

113. W. R. Zipfel, R. M. Williams, and W. W. Webb, "Nonlinear magic: multiphoton microscopy in the biosciences," Nat. Biotechnol. **21,** 1368-1376 (2003).

114. I. Freund, and M. Deutsch, "2^{ND}-Harmonic Microscopy of Biological Tissue," Opt. Lett. **11,** 94-96 (1986).

115. R. M. Williams, W. R. Zipfel, and W. W. Webb, "Interpreting Second-Harmonic Generation Images of Collagen I Fibrils," **88,** 1377-1386 (2005).

116. M. C. Skala, J. M. Squirrell, K. M. Vrotsos, J. C. Eickhoff, A. Gendron-Fitzpatrick, K. W. Eliceiri, and N. Ramanujam, "Multiphoton microscopy of endogenous fluorescence differentiates normal, precancerous, and cancerous squamous epithelial tissues," Cancer Res. **65,** 1180-1186 (2005).

117. P. Wilder-Smith, K. Osann, N. Hanna, N. El Abbadi, M. Brenner, D. Messadi, and T. Krasieva, "In vivo multiphoton fluorescence imaging: A novel approach to oral malignancy," Lasers in Surgery and Medicine **35,** 96-103 (2004).

118. J. Leppert, J. Krajewski, S. R. Kantelhardt, S. Schlaffer, N. Petkus, E. Reusche, G. Hüttmann, and A. Giese, "Multiphoton Excitation of Autofluorescence for Microscopy of Glioma Tissue," Neurosurgery **58,** 759-767 (2005).

119. S. J. Lin, S. H. Jee, C. J. Kuo, R. J. Wu, W. C. Lin, J. S. Chen, Y. H. Liao, C. J. Hsu, T. F. Tsai, Y. F. Chen, and C. Y. Dong, "Discrimination of basal cell

carcinoma from normal dermal stroma by quantitative multiphoton imaging," Opt. Lett. **31,** 2756-2758 (2006).

120. M. C. Skala, K. M. Riching, A. Gendron-Fitzpatrick, J. Eickhoff, K. W. Eliceiri, and J. G. White, "*In vivo* multiphoton microscopy of NADH and FAD redox states, fluorescence lifetimes, and cellular morphology in precancerous epithelia," PNAS **104,** 19494-19499 (2007).

121. E. Dimitrow, M. Ziemer, M. J. Koehler, J. Norgauer, K. Konig, P. Elsner, and M. Kaatz, "Sensitivity and Specificity of Multiphoton Laser Tomography for In Vivo and Ex Vivo Diagnosis of Malignant Melanoma," J. Invest. Dermatol. **129,** 1752-1758 (2009).

122. H. F. Wang, T. B. Huff, D. A. Zweifel, W. He, P. S. Low, A. Wei, and J. X. Cheng, "In vitro and in vivo two-photon luminescence imaging of single gold nanorods," PNAS **102,** 15752-15756 (2005).

123. N. J. Durr, T. Larson, D. K. Smith, B. A. Korgel, K. Sokolov, and A. Ben-Yakar, "Two-photon luminescence imaging of cancer cells using molecularly targeted gold nanorods," Nano Lett. ***7,*** 941-945 (2007).

124. W. Denk, K. R. Delaney, A. Gelperin, D. Kleinfeld, B. W. Strowbridge, D. W. Tank, and R. Yuste, "Anatomical and functional imaging of neurons using 2-photon laser scanning microscopy," Journal of Neuroscience Methods **54,** 151-162 (1994).

125. C. Stosiek, O. Garaschuk, K. Holthoff, and A. Konnerth, "In vivo two-photon calcium imaging of neuronal networks," PNAS **100,** 7319-7324 (2003).

126. E. B. Brown, R. B. Campbell, Y. Tsuzuki, L. Xu, P. Carmeliet, D. Fukumura, and R. K. Jain, "In vivo measurement of gene expression, angiogenesis and

physiological function in tumors using multiphoton laser scanning microscopy," Nature Medicine **7,** 864-868 (2001).

127. S. M. Ameer-Beg, P. R. Barber, R. J. Hodgkiss, R. J. Locke, R. G. Newman, G. M. Tozer, B. Vojnovic, and J. Wilson, "Application of multiphoton steady state and lifetime imaging to mapping of tumor vascular architecture in vivo," Proc. SPIE **4620,** 85-95 (2002).

128. M. J. Levene, D. A. Dombeck, K. A. Kasischke, R. P. Molloy, and W. W. Webb, "In Vivo Multiphoton Microscopy of Deep Brain Tissue," J. Neurophysiol. **91,** 1908-1912 (2004).

129. F. Helmchen, M. S. Fee, D. W. Tank, and W. Denk, "A miniature head-mounted two-photon microscope: high-resolution brain imaging in freely moving animals," Neuron **31,** 903-912 (2001).

130. J. C. Jung, and M. J. Schnitzer, "Multiphoton endoscopy," Opt. Lett. **28,** 902-904 (2003).

131. W. Göbel, J. N. D. Kerr, A. Nimmerjahn, and F. Helmchen, "Miniaturized two-photon microscope based on a flexible coherent fiber bundle and a gradient-index lens objective," Opt. Lett. **29,** 2521-2523 (2004).

132. B. A. Flusberg, J. C. Jung, E. D. Cocker, E. P. Anderson, and M. J. Schnitzer, "*In vivo* brain imaging using a portable 3.9 gram two-photon fluorescence microendoscope," Opt. Lett. **30,** 2272-2274 (2005).

133. W. Piyawattanametha, E. D. Cocker, R. P. J. Barretto, J. C. Jung, B. A. Flusberg, H. Ra, O. Solgaard, and M. J. Schnitzer, "A portable two-photon fluorescence microendoscope based on a two-dimensional scanning mirror," in *IEEE/LEOS*

International Conference on Optical MEMS and Nanophotonics, (Hualien, Taiwan, 2007).

134. C. J. Englebrecht, R. S. Johnston, E. J. Seibel, and F. Helmchen, "Ultra-compact fiber-optic two-photon microscope for functional fluorescence imaging *in vivo*," Opt. Express **16,** 5556-5564 (2008).

135. W. Piyawattanametha, E. D. Cocker, L. D. Burns, R. P. J. Barretto, J. C. Jung, H. Ra, O. Solgaard, and M. J. Schnitzer, "In vivo brain imaging using a portable 2.9 g two-photon microscope based on a microelectromechanical systems scanning mirror," Opt. Lett. **34,** 2309-2311 (2009).

136. M. T. Myaing, D. J. MacDonald, and X. Li, "Fiber-optic scanning two-photon fluorescence endoscope," Opt. Lett. **31,** 1076-1078 (2006).

137. L. Fu, A. Jain, C. Cranfield, H. Xie, and M. Gu, "Three-dimensional nonlinear optical endoscopy," JBO Lett. **12,** 0405011-04050113 (2007).

138. H. Bao, J. Allen, R. Pattie, R. Vance, and M. Gu, "Fast handheld two-photon fluorescence microendoscope with a 475 μm × 475 μm field of view for in vivo imaging," Opt. Lett. **33,** 1333-1335 (2008).

139. R. Le Harzic, M. Weinigel, I. Riemann, K. König, and B. Messerschmidt, "Nonlinear optical endoscope based on a compact two axes piezo scanner and a miniature objective lens," Opt. Express **16,** 20588-20596 (2008).

140. Y. Wu, Y. Leng, J. Xi, and X. Li, "Scanning all-fiber-optic endomicroscopy system for 3D nonlinear optical imaging of biological tissues," Opt. Express **17,** 7907-7915 (2009).

141. S. Tang, W. Jung, D. McCormick, T. Xie, J. Su, Y.-C. Ahn, B. J. Tromberg, and Z. Chen, "Design and implementation of fiber-based multiphoton endoscopy with microelectromechanical systems scanning," JBO **14,** 034005-034007 (2009).

142. H. Bao, and M. Gu, "A 0.4-mm-diameter probe for nonlinear optical imaging," Opt. Express **17,** 10098-10104 (2009).

143. C. L. Hoy, and A. Ben-Yakar, "Optical design and testing of a 9.6 mm-diameter femtosecond laser microsurgery probe," *Manuscript in preparation.*

144. A. F. Gmitro, and D. Aziz, "Confocal Microscopy through a Fiberoptic Imaging Bundle," Opt. Lett. **18,** 565-567 (1993).

145. C. P. Lin, and R. H. Webb, "Fiber-coupled multiplexed confocal microscope," Opt. Lett. **25,** 954-956 (2000).

146. J. Knittel, L. Schnieder, G. Buess, B. Messerschmidt, and T. Possner, "Endoscope-compatible confocal microscope using a gradient index-lens system," Opt. Commun. **188,** 267-273 (2001).

147. C. Liang, M. R. Descour, K. B. Sung, and R. Richards-Kortum, "Fiber confocal reflectance microscope (FCRM) for in-vivo imaging," Opt. Express **9,** 821-830 (2001).

148. E. Laemmel, M. Genet, G. Le Goualher, A. Perchant, J. F. Le Gargasson, and E. Vicaut, "Fibered confocal fluorescence microscopy (Cell-viZio (TM)) facilitates extended imaging in the field of microcirculation - A comparison with intravital microscopy," Journal of Vascular Research **41,** 400-411 (2004).

149. G. Liu, T. Xie, I. V. Tomov, J. Su, L. Yu, J. Zhang, B. J. Tromberg, and Z. Chen, "Rotational multiphoton endoscopy with a 1 μm fiber laser system," Opt. Lett. **34,** 2249-2251 (2009).

150. M. A. Green, and M. J. Keevers, "Optical-Properties of Intrinsic Silicon at 300 K," Progress in Photovoltaics **3,** 189-192 (1995).

151. M. T. Myaing, J. Y. Ye, T. B. Norris, T. Thomas, J. R. Baker, W. J. Wadsworth, G. Bouwmans, J. C. Knight, and P. S. J. Russell, "Enhanced two-photon biosensing with double-clad photonic crystal fibers," Opt. Lett. **28,** 1224-1226 (2003).

152. D. G. Ouzounov, K. D. Moll, M. A. Foster, W. R. Zipfel, W. W. Webb, and A. L. Gaeta, "Delivery of nanojoule femtosecond pulses through large-core microstructured fibers," Opt. Lett. **27,** 1513-1515 (2002).

153. W. Gobel, A. Nimmerjahn, and F. Helmchen, "Distortion-free delivery of nanojoule femtosecond pulses from a Ti : sapphire laser through a hollow-core photonic crystal fiber," Opt. Lett. **29,** 1285-1287 (2004).

154. L. Fu, and M. Gu, "Fibre-optic nonlinear optical microscopy and endoscopy," Journal of Microscopy **226,** 195-206 (2007).

155. Y. Kremer, J. F. Léger, R. Lapole, N. Honnorat, Y. Candela, S. Dieudonné, and L. Bourdieu, "A spatio-temporally compensated acousto-optic scanner for two-photon microscopy providing large field of view," Opt. Express **16,** 10066-10076 (2008).

156. B. A. Flusberg, E. D. Cocker, W. Piyawattanametha, J. C. Jung, E. L. M. Cheung, and M. J. Schnitzer, "Fiber-optic fluorescence imaging," Nature Methods **2,** 941-950 (2005).

157. C. M. Brown, P. G. Reinhall, S. Karasawa, and E. J. Seibel, "Optomechanical design and fabrication of resonant microscanners for a scanning fiber endoscope," Opt. Eng. **45,** 043001-043010 (2006).

158. J. C. Jung, A. D. Mehta, E. Aksay, R. Stepnoski, and M. J. Schnitzer, "In vivo mammalian brain imaging using one- and two-photon fluorescence microendoscopy," J. Neurophysiol. **92,** 3121-3133 (2004).

159. K. König, A. Ehlers, I. Riemann, S. Schenkl, R. Bückle, and M. Kaatz, "Clinical Two-Photon Microendoscopy," Microsc. Res. Tech. **70,** 398-402 (2007).

160. R. H. Webb, "Optics for Laser Rasters," Appl. Opt. **23,** 3680-3683 (1984).

161. W. J. Smith, *Modern optical engineering; the design of optical systems* (McGraw-Hill, New York, 1966).

162. J. W. Goodman, *Introduction to Fourier Optics* (Roberts & Co., Englewood, 2005).

163. W. Piyawattanametha, R. P. J. Barretto, T. H. Ko, B. A. Flusberg, E. D. Cocker, H. Ra, D. Lee, O. Solgaard, and M. J. Schnitzer, "Fast-scanning two-photon fluorescence imaging based on a microelectromechanical systems two-dimensional scanning mirror," Opt. Lett. **31,** 2018-2020 (2006).

164. K. C. Maitland, H. J. Shin, H. Ra, D. Lee, O. Solgaard, and R. Richards-Kortum, "Single fiber confocal microscope with a two-axis gimbaled MEMS scanner for cellular imaging," Opt. Express **14,** 8604-8612 (2006).

165. H. Urey, "Spot size, depth-of-focus, and diffraction ring intensity formulas for truncated Gaussian beams," Appl. Opt. **43,** 620-625 (2004).

166. J. K. Ranka, A. L. Gaeta, A. Baltuska, M. S. Pshenichnikov, and D. A. Wiersma, "Autocorrelation measurement of 6-fs pulses based on the two-photon-induced photocurrent in a GaAsP photodiode," Optics Letters **22,** 1344-1346 (1997).

167. D. Lee, and O. Solgaard, "Two-axis gimbaled microscanner in double SOI layers actuated by self-aligned vertical electrostatic combdrive," in *Proceedings of the Solid-State Sensors, Actuators and Microsystems Workshop, Hilton Head Island*, (Hilton Head Island, South Carolina, 2004), pp. 352-355.

168. C. Landis, "Determinants of the Critical Flicker-Fusion Threshold," Physiol. Rev. **34,** 259-286 (1954).

169. F. Bourgeois, and A. Ben-Yakar, "Femtosecond laser nanoaxotomy properties and their effect on axonal recovery in *C. Elegans*," Opt. Express **15,** 8521-8531 (2007).

170. N. Shen, D. Datta, C. B. Schaffer, P. LeDuc, D. E. Ingber, and E. Mazur, "Ablation of cytoskeletal filaments and mitochondria in live cells using a femtosecond laser nanoscissor," Mech. Chem. Biosyst. **2,** 17-25 (2005).

171. U. K. Tirlapur, and K. König, "Targeted transfection by femtosecond laser," Nature **418,** 290-291 (2002).

172. K. König, P. T. C. So, W. W. Mantulin, and E. Gratton, "Cellular response to near-infrared femtosecond laser pulses in two-photon microscopes " Opt. Lett. **22,** 135-136 (1997).

173. K. König, T. W. Becker, P. Fischer, I. Riemann, and K. J. Halbhuber, "Pulse-length dependence of cellular response to intense near-infrared laser pulses in multiphoton microscopes," Opt. Lett. **24,** 113-115 (1999).

174. H. J. Koester, D. Baur, R. Uhl, and S. W. Hell, "Ca2+ fluorescence imaging with pico- and femtosecond two-photon excitation: Signal and photodamage," Biophys. J. **77,** 2226-2236 (1999).

175. A. Hopt, and E. Neher, "Highly nonlinear photodamage in two-photon fluorescence microscopy," Biophys. J. **80,** 2029-2036 (2001).

176. J. B. Guild, C. Xu, and W. W. Webb, "Measurement of group delay dispersion of high numerical aperture objective lenses using two-photon excited fluorescence," Appl. Opt. **36,** 397-401 (1997).

177. O. E. Martinez, "3000 times grating compressor with positive group velocity dispersion: application to fiber compensation in 1.3 –1.6 μm region," IEEE J. Quantum Electron. **23,** 549-564 (1987).

178. W. Piyawattanametha, R. P. J. Barretto, T. H. Ko, B. A. Flusberg, E. D. Cocker, H. Ra, D. Lee, O. Solgaard, and M. J. Schnitzer, "Fast-scanning two-photon fluorescence imaging based on a microelectromechanical systems two-dimensional scanning mirror," Opt. Lett. **31,** 2018-2020 (2006).

179. R. R. Shannon, *The Art and Science of Optical Design* (Cambridge University Press, Cambridge, UK, 1997).

180. E. Salomatina, B. Jiang, J. Novak, and A. N. Yaroslavsky, "Optical properties of normal and cancerous human skin in the visible and near-infrared spectral range," JBO **11,** (2006).

181. R. Drezek, K. Sokolov, U. Utzinger, I. Boiko, A. Malpica, M. Follen, and R. Richards-Kortum, "Understanding the contributions of NADH and collagen to cervical tissue fluorescence spectra: Modeling, measurements, and implications," JBO **6,** 385-396 (2001).

182. F. Bestvater, E. Spiess, G. Stobrawa, M. Hacker, T. Feurer, T. Porwol, U. Berchner-Pfannschmidt, C. Wotzlaw, and H. Acker, "Two-photon fluorescence absorption and emission spectra of dyes relevant for cell imaging," Journal of Microscopy **208,** 108-115 (2002).

183. T. R. Neu, U. Kuhlicke, and J. R. Lawrence, "Assessment of Fluorochromes for Two-Photon Laser Scanning Microscopy of Biofilms," Appl. Environ. Microbiol. **68,** 901-909 (2002).

184. R. A. Farrer, F. L. Butterfield, V. W. Chen, and J. T. Fourkas, "Highly Efficient Multiphoton-Absorption-Induced Luminescence from Gold Nanoparticles," Nano Lett. **5,** 1139-1142 (2005).

185. A. Ben-Yakar, D. Eversole, and O. Ekici, "Spherical and Anisotropic Gold Nanoparticles in Plasmonic Laser Phototherapy of Cancer," in *Non-Magnetic Metallic Nanomaterials for Life Sciences*, C. Kumar, ed. (John Wiley & Sons, Weinheim, 2008), pp. 493-539.

186. D. Eversole, B. Luk'yanchuk, and A. Ben-Yakar, "Plasmonic laser nanoablation of silicon by the scattering of femtosecond pulses near gold nanospheres," Applied Physics A **89,** 283-291 (2007).

187. R. K. Harrison, and A. Ben-Yakar, "Role of near-field enhancement in plasmonic laser nanoablation using gold nanorods on a silicon substrate," Opt. Express **18,** 22556-22571.

188. L. O. Ramig, and K. Verdolini, "Treatment efficacy: Voice disorders," Journal of Speech Language and Hearing Research **41,** S101-S116 (1998).

189. S. Hirano, "Current treatment of vocal fold scarring," Current Opinion in Otolaryngology & Head and Neck Surgery **13,** 143-147 (2005).

190. T. H. Hammond, R. X. Zhou, E. H. Hammond, A. Pawlak, and S. D. Gray, "The intermediate layer: A morphologic study of the elastin and hyaluronic acid constituents of normal human vocal folds," Journal of Voice **11,** 59-66 (1997).

191. M. S. Hahn, B. A. Teply, M. M. Stevens, S. M. Zeitels, and R. Langer, "Collagen composite hydrogels for vocal fold lamina propria restoration," Biomaterials **27,** 1104-1109 (2006).

192. X. Q. Jia, Y. Yeo, R. J. Clifton, T. Jiao, D. S. Kohane, J. B. Kobler, S. M. Zeitels, and R. Langer, "Hyaluronic acid-based microgels and microgel networks for vocal fold regeneration," Biomacromolecules **7,** 3336-3344 (2006).

193. F. Alipour, and S. Jaiswal, "Phonatory characteristics of excised pig, sheep, and cow larynges," Journal of the Acoustical Society of America **123,** 4572-4581 (2008).

194. A. Zoumi, X. Lu, G. S. Kassab, and B. J. Tromberg, "Imaging Coronary Artery Microstructure Using Second-Harmonic and Two-Photon Fluorescence Microscopy," **87,** 2778-2786 (2004).

195. C. Boudoux, S. C. Leuin, W. Y. Oh, M. J. Suter, A. E. Desjardins, B. J. Vakoc, B. E. Bouma, C. J. Hartnick, and G. J. Tearney, "Preliminary Evaluation of Noninvasive Microscopic Imaging Techniques for the Study of Vocal Fold Development," Journal of Voice **23,** 269-276 (2009).

196. J. A. Galbraith, and M. Terasaki, "Controlled damage in thick specimens by multiphoton excitation," Mol. Biol. Cell **14,** 1808-1817 (2003).

197. B. G. Wang, I. Riemann, H. Schubert, D. Schweitzer, K. Konig, and K. J. Halbhuber, "Multiphoton microscopy for monitoring intratissue femtosecond laser surgery effects," Lasers in Surgery and Medicine **39,** 527-533 (2007).

Vita

Christopher Luk Hoy was born in Bremerton, Washington on September 21, 1982 to Jeffrey Craig Hoy and Elizabeth Willson Hoy. In 2000, he graduated from James Madison High School in Vienna, Virginia. Christopher then studied mechanical engineering at Virginia Polytechnic Institute and State University (Virginia Tech), graduating *cum laude* in 2004 with a Bachelor of Science in Mechanical Engineering and Minor in Mathematics. Christopher was introduced to the field of biomedical optics upon joining the Ben-Yakar group at the University of Texas at Austin later in 2004, receiving a Master of Science in Engineering in 2007.

Permanent address: 2324 Wind River Trail, Cheyenne, WY 82009

This dissertation was typed by the author.